Identifying mechanisms underlying the pathogenesis of age-associated periventricular white matter lesions

by

Motaz Mohammed Fadul

Submitted for the degree of Doctor of Philosophy (PhD)

Sheffield Institute for Translational Neuroscience

University of Sheffield

December 2020

ACKNOWLEDGEMENT

There are so many people whom I would like to thank. First and foremost, I would like to acknowledge my father, Mohammed, and mother, Nadia, for their continuous help and unconditional support. Thank you for believing in me which made me achieve this goal and they have always encouraged me to the best I can be.

Thank you, Sara, my wonderful wife and my best friend, I am so blessed to have your love and support behind all my endeavours. She has been extremely supportive even when she was also busy doing her PhD. We have been through this together. Thank you to my son Mohammed (Hamoodi), who witnessed all this journey since he was one and a half year old, you have been my comfort zone and I would like to say sorry for being grumpy whilst I wrote this thesis.

Thank you to my supervisors, Dr Julie Simpson and Prof Stephen Wharton for their guidance and support throughout my PhD.

I would like to express my sincere gratitude to Dr Julie Simpson, as she always believed in me and for her continuous encouragement, help, guidance and reassurance throughout this adventure.

I would like to thank Dr Paul Heath, with his RNA analysis expertise. I gained valuable knowledge on transcriptomic analysis of NanoString and Microarrays. I

would also like to thank Dr Jonathan Cooper-Knock for his help in computational deconvolution analysis.

Thank you to the Neuropathology research group and all SITraN staff for their support and help. Thank you to Dr Rachel Waller, Dr Irina Vázquez-Villaseñor, Dr Hemant Mistry, Catherine Gelsthorpe, Lynne Baxter and Daniel Fillingham.

To King Abdulaziz University in Saudi Arabia for funding this project, and for sponsoring my postgraduate studies.

Thank you to all donors and their families for considering donating their tissue to scientific research; without you, we were not able to do this work.

PUBLICATION

Fadul, M.M.; Heath, P.R.; Cooper-Knock, J.; Kurz, J.M.; Al-Azzawi, H.A.; Ali, Z.; Smith, T.; Matthews, F.E.; Brayne, C.; Wharton, S.B.; Simpson, J.E., on behalf of the Cognitive Function and Ageing Neuropathology Study Group; Transcriptomic Analysis of Age-Associated Periventricular Lesions Reveals Dysregulation of the Immune Response. Int. J. Mol. Sci. 2020, 21, 7924.

POSTER PRESENTATIONS

Fadul, M.M., Brayne, C, Matthews, F.E., Ince, P., Wharton, S.B., Simpson, J.E. Characterising the microglial profile of age-associated confluent white matter lesions. Alzheimer's Research United Kingdom, March 2018, London.

Fadul, M.M., Heath, P., Cooper-Knock, J., Wharton, S.B., Simpson, J.E. The role of microglia in the pathogenesis of age-associated white matter lesions. Dementia Futures, July **2018**, Sheffield.

Fadul, M.M., Heath, P., Cooper-Knock, J., Brayne, C., Matthews, F.E., Wharton, S.B., Simpson, J.E. A microarray analysis approach to identify mechanisms underlying the pathogenesis of age-associated periventricular white matter lesions. XIV European Meeting on Glial Cells in Health and Disease, July **2019**, Porto.

ABSTRACT

Age-associated white matter lesions (WML) appear as hyperintense signals on T2-weighted magnetic resonance imaging (MRI) scans and are associated with dementia and cognitive decline. Based on their anatomical location, WML are classified into deep subcortical lesions (DSCL), which are associated with high levels of CD68$^+$ amoeboid microglia; periventricular lesions (PVL), which are characterised by increased levels of MHC II$^+$ immune activated microglia; and confluent lesions which encompass both periventricular and deep subcortical regions.

As the microglial phenotype is significantly different in PVL compared to DSCL, the profile of CD68$^+$ and MHC-II$^+$ microglia in confluent lesions was immunohistologically assessed to test the hypothesis that confluent lesions arise as a result of combined PVL and DSCL spread. The immunoreactive profile of microglia within confluent lesions was classified into four lesion subtypes with distinct staining patterns: MHC II$^+$ and CD68$^+$ microglia primarily associated with the periventricular region and deep subcortical region, respectively; MHC II$^+$ microglia predominantly throughout all regions; CD68$^+$ microglia predominantly throughout all regions; a mix of both CD68$^+$ and MHC II$^+$ microglia present throughout the confluent lesions. The current study demonstrates a range of confluent lesion subtypes which may reflect a spread of DSCL pathology, PVL lesion pathology or both, suggesting that a variety of mechanisms may be associated with the pathogenesis of confluent lesions.

While transcriptomic profiling of DSCL has previously been performed to identify the underlying mechanisms associated with the formation of these lesions, the current study is the first in the field to employ this approach to identify gene expression changes which may underlie the formation of PVL. Interestingly, histological characterisation of radiologically control white matter identified a subgroup of control cases which displayed intact myelin, but also high levels of MHC-II^{+} microglia and were subsequently reclassified as "pre-lesional". The current study characterised the gene expression profile of age-associated periventricular white matter using two independent approaches, namely microarray analysis and Nanostring. The research presented in this thesis suggests that established PVL are part of a continuous spectrum of white matter injury. Bioinformatic analysis of the datasets revealed both "pre-lesions" and established PVL are associated with the significant down-regulation of an immune response. Furthermore, increased signalling pathways in "pre-lesions", including calcium and glutamate signalling, may indicate a neuroprotective mechanism to prevent the formation of PVL.

Table of Contents

LIST OF FIGURES

LIST OF TABLES

Abbreviations

Ab	Antibody
ABC-HRP	Avidin-biotinylated complex-horse radish peroxidase
ACTB	Actin cytoplasmic 1
AD	Alzheimer's Disease
AKT3	V-akt murine thymoma viral oncogene homolog 3
AMPA	α-Amino-3-hydroxy-5-methyl-4-isoxazolepropionic acid
ATP	Adenosine triphosphate
Aβ	Amyloid Beta
BBB	Blood brain barrier
BCSFB	Blood-cerebrospinal fluid barrier
BDNF	Brain-derived Neurotrophic Factor
BST2	CD317, tetherin
CAA	Cerebral Amyloid Angiopathy
CACNA1E	Calcium voltage-gated channel subunit alpha 1E
CAMK2A	Calcium/calmodulin-dependent protein kinase II alpha
CAMK2B	Calcium/calmodulin-dependent protein kinase II beta
CAMK4	Calcium/calmodulin-dependent protein kinase IV
cAMP	Cyclic adenosine 3′,5′-monophosphate
CCL2	C-C motif chemokine ligand 2
CCL3	C-C motif chemokine ligand 3
CCL4	C-C motif chemokine ligand 4
CCR5	C-C motif chemokine receptor 5 (gene/pseudogene
CD163	CD163 molecule, Scavenger Receptor Cysteine-Rich Type 1 Protein M130
CD274	Cluster of differentiation 274, programmed death-ligand 1
CD74	CD74 HLA class II histocompatibility antigen gamma chain
CD80	Cluster of differentiation 80, B7-1
CD86	Cluster of differentiation 86, B7-2
CD8A	CD8a molecule, T-cell surface glycoprotein CD8 alpha chain
CFAS	Cognitive Function and Ageing Study
cGMP	Cyclic guanosine monophosphate
CNS	Central Nervous System

COL6A3	Collagen type VI alpha 3 chain
cRNA	Complementary RNA
CSF	Cerebrospinal Fluid
CSNK1A1	Casein kinase 1, alpha 1
CT	Computed Tomography
CX3CR1	C-X3-C motif chemokine receptor 1
CXCL	Chemokine CXC Ligand
CXCR	Chemokine CXC Receptor
CYBB	Cytochrome b-245, beta polypeptide
CyTOF	Cytometry by time-of-flight
DAB	3,3'-Diaminobenzidine tetrahydrochloride
DAM	Disease-associated microglia
DAVID	Database for Annotation Visualisation and Integrated Discovery
DEG	Differentially Expressed Genes
DEPC	Diethylpyrocarbonate
dH_2O	Distilled water
DNA	Deoxyribonucleic acid
DPX	Dibutylphthalate Polystyrene Xylene
ds-DNA	Double Stranded Deoxyribonucleic acid
DSC	Deep Subcortical Region
DSCL	Deep Subcortical Lesion
dT	Oligonucleotide
dUTP	Deoxyuridine Triphosphate
EAE	Experimental autoimmune encephalomyelitis
EDTA	Ethylenediaminetetraacetic acid
ENTPD1	Ectonucleoside triphosphate diphosphohydrolase 1, CD39
EPSTI1	Epithelial stromal interaction protein 1
EtOH	Ethanol
FC	Fold Change
FCER1G	Fc fragment of IgE receptor Ig
FCGR1A	Fc fragment of immunoglobulin gamma Fc receptor 1A
FCGR2A	Fc fragment of immunoglobulin gamma Fc receptor 2A
FFPE	Formalin Fixed Paraffin Embedded
FGL2	Fibrinogen like 2

FLAIR	Fluid-attenuated inversion recovery
fM	Femtomolar
FOV	Field of view
FPR1	Formyl peptide receptor 1
FU	Fluorescence unit
GABA	Gamma-Aminobutyric Acid
GABRA4	Gamma-aminobutyric acid (GABA) A receptor, alpha 4
GABRA5	Gamma-aminobutyric acid (GABA) A receptor, alpha 5
GAPDH	Glyceraldehyde-3-phosphate dehydrogenase
GBP5	Guanylate-binding protein 5
GDNF	Glial cell-Derived Neurotrophic Factor
GEO	Gene Expression Omnibus
GLUR	Glutamate ionotropic receptor
GO	Gene Ontology
GRIA2	Glutamate receptor, ionotropic, AMPA 2
GRIN1	Glutamate receptor, ionotropic, N-methyl D-aspartate 1
GRM5	Glutamatergic synaptic signalling, including glutamate receptor, metabotropic 5
H&E	Haematoxylin and eosin
H_2O_2	Hydrogen Peroxide
HAVCR2	Hepatitis A virus cellular receptor 2
HLA	Human leukocyte antigen
HLA-DMB	Major histocompatibility complex, class II, DM beta
HLA-DPA1	Major histocompatibility complex, class II, DP alpha 1
HLA-DPB1	Major histocompatibility complex, class II, DP beta 1
HLA-DQB1	Major histocompatibility complex, class II, DP beta 1
HLA-DRA	Major histocompatibility complex, class II, DR alpha
Hrs	Hours
HSP	Heat shock proteins
HSP-70	70-kDa heat shock protein
HSP-90	90-kDa heat shock protein
HSP90AA1	Heat shock protein 90 alpha family class A member 1
HSPA1L	Heat shock protein family A (Hsp70) member 1 like
HSPA8	Heat shock protein family A (Hsp70) member 8

Iba-1	Ionized calcium-binding Adaptor Molecule 1
ICH	Intracerebral haemorrhage
IFI35	Interferon induced protein 35
IFI44	Interferon induced protein 44
IFI44L	Interferon induced protein 44-like
IFIT1	Interferon induced protein with tetratricopeptide repeats 1
IFIT3	Interferon induced protein with tetratricopeptide repeats 3
IFN-γ	Interferon Gamma
IFNAR1	Interferon alpha and beta receptor subunit 1
IgG	Immunoglobulin G
IGSF6	Immunoglobulin superfamily member 6
IHC	Immunohistochemistry
IKBKB	Inhibitor of nuclear factor kappa B kinase subunit beta
IL	Interleukin
IL1A	Interleukin 1 alpha
IL1B	Interleukin 1 Beta
ILT7	Immunoglobulin-like transcript 7
IMPaLA	Integrated Molecular Pathway Level Analysis
IRF7	Interferon regulatory factor 7
IRF9	Interferon regulatory factor 9
ISG15	Interferon-stimulated gene 15
ITGAX	Integrin, alpha X (complement component 3 receptor 4 subunit), CD11c
IVT	*In Vitro* Transcription
JUN	Jun proto-oncogene, AP-1 transcription factor subunit
KEGG	Kyoto Encyclopedia of Genes and Genomes
KW	Kruskal-Wallis Test
LCM	Laser Capture Microdissection
LCP2	Lymphocyte cytosolic protein 2
LFB	Luxol Fast Blue
LUHMES	Lund Human Mesencephalic
LvC	Lesion versus Control
LY6E	lymphocyte antigen 6E
MAPK	Mitogen-activated protein kinase
MAS	MicroArray Suite 5.0

MBP	Myelin Basic Protein
mg	milligram
MHC-II	Major Histocompatibility Class II
MID	Middle Region
MIF	Macrophage migratory inhibitory factor
Min	Minute
MM	Master Mix
MND	Motor neuron diseases
MRC1	Mannose receptor C-type 1
MRI	Magnetic Resonance Imaging
mRNA	Messenger RNA
MS4A6A	Membrane spanning 4-domains A6A
MSR1	Macrophage scavenger receptor 1
mW	milliwatts
MX1	MX dynamin like GTPase 1
n/a	Not available
NAWM	Normal Appearing White Matter
NFT	Neurofibrillary Tangles
NFκB	Nuclear Factor Kappa B
NMDAR	N-Methyl-D-aspartic acid or N-Methyl-D-aspartate receptor
NO	Nitric Oxide
NTC	No Template Control
OAS1	2'-5'-oligoadenylate synthetase 1
OAS2	2'-5'-oligoadenylate synthetase 2
OAS3	2'-5'-oligoadenylate synthetase 3
OPC	Oligodendrocyte Precursor Cells
PCA	Principal Component Analysis
PD	Parkinson's disease
PHF21A	PHD finger protein 21A
PI3K	Phosphatidylinositol 3-kinase
PLP	Proteolipid Protein
PMD	Post-mortem Delay
PTGS2	Prostaglandin-Endoperoxide Synthase 2, COX-2
PV	Periventricular region

PvC	Pre-lesion versus Control
PvL	Pre-lesion versus Lesion
PVL	Periventricular Lesion
QC	Quality control
R^2	Correlation coefficient
REC	Research Ethical Committee
RIN	RNA Integrity Number
RLE	Relative Log Expression
RNA-Seq	Ribonucleic acid-Sequencing
ROS	Reactive Oxygen Species
RPLP0	60S acidic ribosomal protein P0
rpm	Revolutions per minute
RSAD2	Radical S-adenosyl methionine domain containing 2
RT	Room Temperature
RXRA	Retinoid X receptor alpha
SAMSN1	SAM domain, SH3 domain and nuclear localisation signals 1
SD	Standard Deviation
SLAMF8	SLAM family member 8
snRNA-seq	Single-cellRNA-sequencing
ss-cDNA	Single Stranded cDNA
SVD	Small Vessel Disease
TAC	Transcriptomic Analysis Console
TAE	Tris-Acetate-EDTA
TBS	Tris Buffered Saline
TdT	Terminal deoxynucleotidyl transferase
TFEC	Transcription factor EC
TGF-β	Transforming Growth Factor-Beta
TIMD4	T Cell Immunoglobulin and Mucin Domain Containing 4
TNF-α	Tumour Necrosis Factor α
TREM 2	Triggering Receptor Expressed on Myeloid cells 2
TYROBP	Tyrosine kinase-binding protein
UBE2L6	Ubiquitin conjugating enzyme E2 L6
UDG	Uracil-DNA glycosylase
USP	Ubiquitin Specific Protease

USP18	Ubiquitin specific peptidase 18
VaD	Vascular Dementia
Vs	Versus
WM	White Matter
WMC	White Matter Change
WMH	White Matter Hyperintensities
WML	White Matter Lesion
XAF1	XIAP-associated factor 1
Y	Year
ZO-1	Zona Occludin-1
β-actin	Beta-actin
κ	Kappa
µl	Microliter
µm	Micrometre
μm^2	Square Micron

CHAPTER 1: AGE-ASSOCIATED WHITE MATTER LESIONS

1.1 Introduction

Age-associated white matter lesions (WML) appear as hyperintensities on T2-weighted magnetic resonance imaging (MRI) scans (Prins & Scheltens, 2015). Different terminologies have been used in the literature to describe these hyperintensities, including white matter changes (WMC) and white matter hyperintensities (WMH). In 1986, Hachinski and colleagues used *Leukoaraiosis* (from the greek "leuko" meaning "white" and "araiosis" meaning "rarefaction") as a descriptive term for the intensities found on computed tomography (CT) (Hachinski *et al.*, 1986). The current study will refer to these hyperintensities as WML.

There are few truly ageing population-representative neuropathology cohorts worldwide. In the UK, the Cognitive Function and Ageing Study (CFAS) is a large-scale study of the ageing population that also has a population-representative brain donor cohort (Ince, 2001; Wharton *et al.*, 2011). Population-representative studies, such as CFAS and others, have shown that while WMLs are commonly observed in healthy elderly people aged 65 and older, they are also associated with neurological diseases, such as Alzheimer's disease (AD) (Lee *et al.*, 2016), and vascular dementia (Hu *et al.*, 2021). Age-associated WMLs, clinically manifest as cognitive impairment (Prins *et al.*, 2005), dementia (Fernando & Ince, 2004; Matthews *et al.*, 2009; Debette & Markus, 2010), depression (O'Brien *et al.*, 1996; Lee *et al.*, 2015), gait dysfunction (De Laat *et al.*, 2011; Rosario *et al.*, 2016) and/or balance disturbance (Baezner *et al.*, 2008; Veselý *et al.*, 2016). Increasing age is the most common risk factor for WML formation (Basile *et al.*, 2006; Zhuang *et al.*, 2018; Garnier-Crussard *et al.*, 2020). However, more risk factors for the development of these white matter

hyperintensities have been found, including hypertension and cardiovascular disease (de Leeuw *et al.*, 2002; Verhaaren *et al.*, 2013; Zhao *et al.*, 2019), while smoking and increased age are the most predictive factors for the progression of WML (Van Dijk *et al.*, 2008; Garnier-Crussard *et al.*, 2020).

1.2 The brain vasculature

The major arteries responsible for supplying blood to the brain are the internal carotid arteries, and the vertebral arteries. The basilar artery arises from the distal union of the two vertebral arteries, forming the vertebrobasilar arterial system. Vertebrobasilar stroke, arising from occlusion of large vessels in this system, usually leads to major disability or death. However, many vertebrobasilar lesions arise from small vessel disease. The basilar artery and internal carotid arteries connect to the Circle of Willis, which forms an anastomotic ring enabling perfusion of the cerebral hemispheres via three major arteries: the anterior, middle and posterior cerebral arteries (Cipolla, 2009).

Cerebral white matter is primarily supplied by the medullary artery which is a branch of the vertebral arteries and distributes in the cerebral parenchyma, subdividing into superficial cerebral and basal perforating arteries (Akashi *et al.*, 2017). White matter in the periventricular white matter mainly receives its blood supply through the long perforating branches of the cerebral pial and ventriculofugal blood vessels. Ventriculofugal vessels arise from the striatal arteries' terminal branches or the choroidal artery (Rowbotham & Little, 1965; Van Den Bergh, 1969; Pantoni & Garcia, 1997). These vessels sparsely coincide to form

a blood supply watershed, making the periventricular white matter vulnerable to ischaemia. In contrast, the subcortical white matter primarily receives its blood supply via the long perforating branches of the medullary arteries, which arise from the cortical branches of the middle cerebral artery, which often have a long and tortuous course. These characteristics also make the subcortical white matter vulnerable to hypoxic-ischemic damage (Rowbotham & Little, 1965; Pantoni & Garcia, 1997; Akashi *et al.*, 2017) (Figure 1.1).

1.2.1 Brain barriers

In the brain, two major barriers protect the CNS, namely, the blood-brain barrier (BBB), and the blood-cerebrospinal fluid barrier (BCSFB). These barriers regulate the exchange between the circulation and the CNS (Saunders *et al.*, 2013), and function to maintain brain homeostasis (Segarra *et al.*, 2021). The BBB is mainly composed of cerebral endothelial cells which express tight junction proteins, smooth muscle cells, pericytes and astrocytes (Graves & Baker, 2020; Kadry *et al.*, 2020), and plays a major role in inhibiting the passage of blood-borne molecules into the CNS.

In contrast, the blood-cerebrospinal fluid barrier is composed of choroid plexus epithelial cells in the ventricles which, similar to the BBB endothelial cells, express tight junction proteins, and inhibit the paracellular movement of water soluble molecules across the barrier (Engelhardt & Sorokin, 2009; Saunders *et al.*, 2016; Solár *et al.*, 2020).

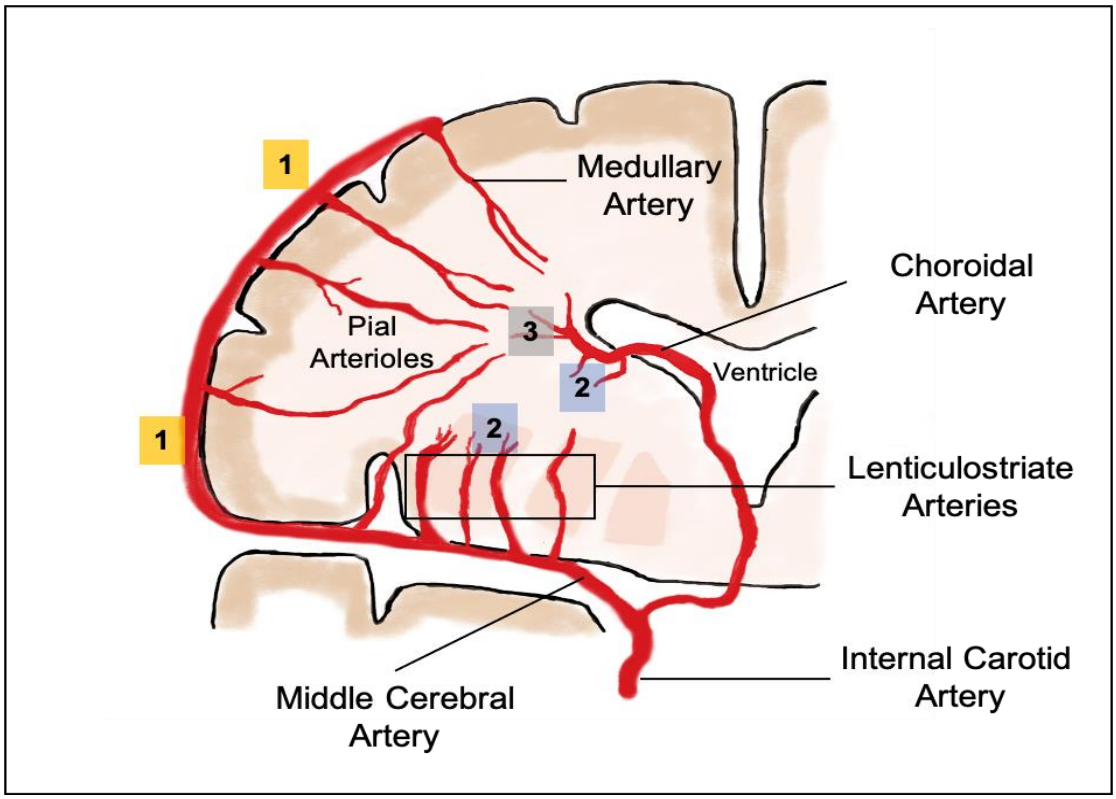

Figure 1.1 Periventricular and deep subcortical white matter arterial supply

The periventricular white matter is supplied by the pial arterioles which originate from the cortical arteries (1) and the ventriculofugal vessels (2), arising either from the subependymal arteries (3), which branch from the choroidal artery, or from the striatal arteries' terminal branches. The deep subcortical region is supplied by long perforating branches of the medullary arteries which arises from the cortical branches of the middle cerebral artery. Adapted from (Medrano Martorell *et al.*, 2012; Funaki & Miyamoto, 2021).

1.3 White matter lesions (WML)

1.3.1 Classification

Many studies classify white matter hyperintensities into two major categories based on their anatomical location (Figure 1.2): periventricular white matter lesions which are located adjacent to the ventricular system (PVL) and deep subcortical lesions, which are located in the deep white matter (DSCL), distant from the ventricles (De Groot *et al.*, 2002; Kim *et al.*, 2008; Wharton *et al.*, 2011). Numerous visual rating scales used in clinical settings are based on this distinction (Fazekas *et al.*, 1987; Scheltens *et al.*, 1993; Ylikoski *et al.*, 1993). Population-based studies have shown that around 90% of the ageing population have PVL, while DSCL are found in around 60% of the over 65s (de Leeuw, 2001). Lesions tend to extend to become more confluent (Figure 1.2. B) (Barkhof & Scheltens, 2006), but whether these represent the spread of PVL or DSCL or both is currently unknown.

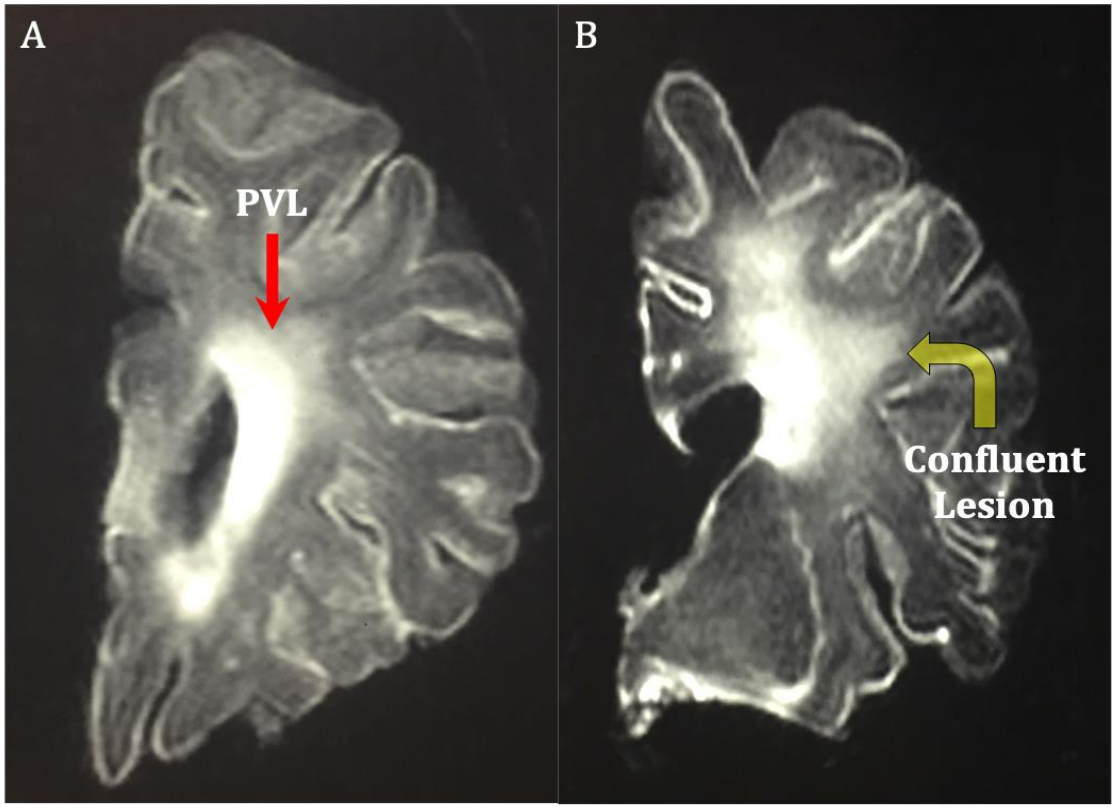

Figure 1.2 MRI detection of age-associated WML

Depending on their anatomical location, age-associated WML are classified as (A) periventricular lesions (PVL, red arrow) or deep subcortical lesions (DSCL). Extensive WML encompassing both periventricular and deep subcortical regions are classified as confluent lesions (B).

1.3.2 Clinical manifestation

1.3.2.1 WML and cognition:

Cognitive dysfunction is a common clinical feature in people with WML and is thought to be associated with cerebral small vessel disease (SVD) (Prins & Scheltens, 2015). In the ageing brain, vascular pathologies have been reported in 71% of non-demented individuals compared to 84% of patients with dementia. PVL are common in demented (95%) ageing population compared to non-demented (87%), while DSCL are less common (60% in non-demented compared to 73% in demented) (Matthews *et al.*, 2009). While these WML are a common feature of the ageing brain, they have been identified as a significant independent risk factor for dementia (Fernando & Ince, 2004; Matthews *et al.*, 2009).

Increased WML volumes are associated with the increasing risk of cognitive impairment and dementia (Prins & Scheltens, 2015). However, it should be acknowledged that there are conflicting reports regarding the association between WML subtypes and cognitive impairment. Several studies indicate that PVL, but not DSCL, are directly related to deterioration in cognition and are associated with an increased risk of dementia (De Groot *et al.*, 2002; Prins *et al.*, 2004; van den Heuvel *et al.*, 2006). Conversely, other studies have shown that both PVL and DSCL have a similar impact on cognitive decline (Burns *et al.*, 2005).

1.3.2.2 Depression

Assessment of the presence and severity of PVL and DSCL in a large population-based study of 1077 elderly people revealed that cerebral white matter changes, in particular DSCL, are linked to symptoms of depression (de Groot *et al.*, 2000).

Furthermore, increases in the volume of DSCL have been shown to increase the risk of late-life depression (Chen *et al.*, 2006).

1.3.3 Pathological correlates of WML

Both PVL and DSCL share some similar histopathological features, including myelin attenuation, axonal damage, astrogliosis and microglial activation (Gouw *et al.*, 2011; Schmidt *et al.*, 2011; Wharton *et al.*, 2015); however, it should be noted that each WML subtype also has distinct features.

PVL are characterised histologically by ventricular ependymal denudation and subependymal dense astrogliosis (Fernando *et al.*, 2006). This disruption in the ependymal lining may lead to abnormal leakage of cerebrospinal fluid (CSF) into the periventricular white matter area, and initiate or exacerbate lesional pathology (Scheltens *et al.*, 1995; Simpson *et al.*, 2007a). While numbers of remyelinating oligodendrocyte progenitor cells (OPC) are significantly increased at the border of PVL, it has been suggested that the dense astrogliosis associated with these lesions may prevent remyelination (Simpson *et al.*, 2007a). Microglia in PVL have a ramified morphology and an immune-activated phenotype, associated with the significant increase in major histocompatibility complex-II (MHC II) expression (Simpson *et al.*, 2007b).

In striking contrast to PVL, the microglia in DSCL are large, round and amoeboid in morphology with increased expression of the lysosomal marker CD68 (Fernando *et*

al., 2006). These differences in microglial morphologies suggest microglia play different roles in the pathogenesis of DSCL and PVL (as discussed below).

1.3.4 Proposed Mechanisms of WML formation

While the precise mechanism(s) underlying the pathogenesis of WML remains unknown; however, several hypotheses have been suggested. These include (i) chronic cerebral hypoperfusion leading to a hypoxic environment (Tomimoto *et al.*, 2003; Duncombe *et al.*, 2017), (ii) blood-brain barrier dysfunction resulting in the extravasation and accumulation of plasma proteins which stimulate a neuroinflammatory response (Simpson *et al.*, 2007a), (iii) cortical pathology preceding and underlying WML formation (Leys *et al.*, 1991; Huang *et al.*, 2007; McAleese *et al.*, 2017).

1.3.4.1 Hypoperfusion/Hypoxia

The prevalence of WML in the ageing population is increased by vascular risk factors such as hypertension (Dufouil *et al.*, 2001; Van Dijk *et al.*, 2004), hyperlipidaemia and a previous history of stroke (Sonohara *et al.*, 2008). The resulting reduction in cerebral blood flow leads to tissue damage and is associated with the formation of WML (Marstrand *et al.*, 2002; Makedonov *et al.*, 2013; Wong *et al.*, 2019).

Cerebral hypoperfusion results in a hypoxic environment, a feature of both PVL and DSCL, evidenced by the increased expression and nuclear translocation of hypoxia-inducible transcription factors, and the increased expression of several hypoxia-associated proteins including matrix metalloproteinase-7 (Fernando *et al.*, 2006).

While detected in both PVL and DSCL, these findings are predominantly associated with DSCL (Fernando *et al.*, 2006). Differences in the vascular supply of both lesion types could contribute to these differences. The WM is supplied by arteries that do not anastomose, which increases the susceptibility to ischemia (Auriel *et al.*, 2012). The periventricular white matter is supplied by long, penetrating arterioles, forming a watershed area that makes it vulnerable to ischemic injury (Prins & Scheltens, 2015).

In contrast, the deep subcortical white matter is supplied by small arteries which are more prone to arteriolosclerotic vascular changes and are highly susceptible to hypoxic damage (Rowbotham & Little, 1965; Pantoni & Garcia, 1995; Simpson *et al.*, 2009; Xiong & Mok, 2011). The majority of studies have mainly focused on the impact of arterial alterations on the formation of WML, with less attention to the role venous pathology plays. Those studies investigating venules in the periventricular white matter have shown an association between severe periventricular vascular collagenosis and WML (Moody *et al.*, 1995; Black *et al.*, 2009; Keith *et al.*, 2017).

The rat model of cerebral hypoperfusion is a widely used and robust experimental model, where the common carotid arteries of rats are bilaterally occluded (Washida *et al.*, 2019). This model exhibits cognitive impairment in addition to white matter pathology resembling cerebral WML (Farkas *et al.*, 2004). These studies support the hypoxia/hypoperfusion hypothesis, strongly suggesting that a reduction in cerebral blood flow leads to microglial activation and demyelination, and that hypoperfusion

plays a major role in the development and pathogenesis of age-associated WML (Fernando *et al.*, 2006; Schmidt *et al.*, 2011).

1.3.4.2 Blood Brain Barrier (BBB) dysfunction

The BBB is highly selective in its ability to regulate the movement of molecules from the blood to the CNS, and vice versa (Stevenson *et al.*, 1986; Furuse *et al.*, 1993; Zhao *et al.*, 2015). Disruption of the BBB is a common feature of normal ageing (Montagne *et al.*, 2015) and neurodegenerative diseases, including Alzheimer's disease (Halliday *et al.*, 2016). While the expression of tight junction proteins (TJP), including zona occludens-1 (ZO-1), claudin-5 and occludin are not significantly different in WML compared to radiologically normal WM, BBB dysfunction is a prominent feature of age-associated WM pathology (Simpson *et al.*, 2010; Hainsworth *et al.*, 2017). Post-mortem studies suggest that BBB dysfunction plays a role in the pathogenesis of WML, showing that the accumulation of plasma proteins, such as albumin, thrombin, and fibrinogen is a prominent feature of WML (Simpson *et al.*, 2007a; Winkler *et al.*, 2014; Hainsworth *et al.*, 2017). Under normal conditions, serum proteins are excluded from the CNS. However, BBB dysfunction and the leakage of these proteins, some of which are neurotoxic, induces inflammatory processes and/or causes oedema that consequently leads to hypoperfusion (Winkler *et al.*, 2014).

The presence of clasmatodendritic astrocytes is considered as a marker of BBB dysfunction. These astrocytes are characterised by large rounded cell bodies with beaded processes, resembling the morphology of amoeboid microglia, and have been demonstrated in WML (Tomimoto *et al.*, 1997; Simpson *et al.*, 2007a). In

particular, clasmatodendritic astrocytes are a prominent feature of age-associated PVL (Simpson *et al.*, 2007a) and frontal white matter of post-stroke dementia patients (Chen *et al.*, 2016a; Freeze *et al.*, 2020), suggesting a correlation between BBB dysfunction and cognitive impairment.

In addition to post-mortem studies, the rat model of chronic cerebral hypoperfusion supports the hypothesis that dysfunction of the BBB contributes to white matter pathology (Ueno *et al.*, 2002; Lee *et al.*, 2017). However, while the majority of the literature supports a role for BBB dysfunction in WM pathology, it should be noted that an MRI study suggests that BBB dysfunction is not related to the pathogenesis of WML (Wahlund & Bronge, 2000).

1.3.4.3 Cortical Pathology

Cortical pathologies such as AD have been suggested to contribute to the development of WML (McAleese *et al.*, 2017). AD is neuropathologically characterised by the presence of neurofibrillary tangles (NFT) of hyperphosphorylated tau that may lead to axonal damage and myelin loss as part of the neurodegenerative process (Huang *et al.*, 2007; McAleese *et al.*, 2015).

CAA is associated with the abnormal deposition of β-amyloid (Aβ) within vascular walls, including the leptomeningeal blood vessels that supply the cortex. It has been suggested that CAA affects the vascular supply to the WM and causes ischaemia which leads to the formation of WML (Vinters *et al.*, 2000; Weller *et al.*, 2015). Recently, a study revealed that periventricular white matter hyperintensities are associated with elevated cerebral amyloid, and CAA pathology is an independent

predictor for the formation of periventricular white matter hyperintensities with age (Marnane *et al.*, 2016).

In conclusion, hypoperfusion/hypoxia, disruption of BBB and cortical pathologies are considered as important factors that play a major role in the development of WML.

1.3.5 WML arise in a field effect of pathology

Histological analysis of radiologically normal-appearing white matter (NAWM) has identified subtle pathological abnormalities, including an increase in MHC-II^{+} microglia, extending beyond the lesion, suggesting these lesions may arise in a field effect of pathology (Simpson *et al.*, 2007b; Wardlaw *et al.*, 2015; Wharton *et al.*, 2015). Whole-genome RNA microarray analysis of the radiologically normal area surrounding the lesion revealed 419 genes were significantly, differentially expressed and included genes mainly associated with immune function, cell cycle and ion transport (Simpson *et al.*, 2009). Furthermore, histological characterisation has revealed a significant increase in oxidative DNA damage associated with glia in the normal-appearing white matter from lesional cases, demonstrating pathology extends beyond the established lesion (Al-Mashhadi *et al.*, 2015). Recently, a study revealed radiological changes in the white matter surrounding lesions, indicating changes in the white matter microstructures (Vangberg *et al.*, 2019).

1.4 Vascular dementia (VaD)

White matter is highly sensitive to vascular disruptions, including cerebrovascular injuries (Black *et al.*, 2009; Iadecola, 2013). Disruption to the cerebral vasculature results in a reduction of brain function impacting cognitive ability, forgetfulness and problem-solving (Sachdev *et al.*, 2004). Vascular dementia is the second most common cause of dementia, which may be caused by a stroke or small vessel disease (Kalaria, 2018).

1.4.1 Large vessel disease

Large vessel disease, such as atherosclerosis, is characterised by the abnormal deposition of lipid, plasma proteins and plaques in the walls of large arteries leading to a reduction in blood flow. A population-based post-mortem study conducted on 600 cases found that the odds ratio for dementia increased significantly with internal carotid artery atherosclerosis (Suemoto *et al.*, 2011).

1.4.2 Small vessel disease

Small vessel disease (SVD) is a frequent finding on both MRI and CT, which reflects a range of pathological features associated with the small vessels of the brain (Pantoni, 2010), including arterioles and capillaries (Pantoni, 2010; Wardlaw *et al.*, 2013). SVD may arise due to either arteriolosclerosis which is mainly associated with vascular risk factors such as hypertension and atherosclerosis (Vermeer *et al.*, 2003; Giwa *et al.*, 2012; Prins & Scheltens, 2015) or due to the presence of cerebral amyloid angiopathy (CAA). CAA is characterised by the abnormal deposition of β-amyloid (Aβ) in the walls of arteries and arterioles (Biffi & Greenberg, 2011), leading

to occlusion of the vascular lumen, and eventually resulting in ischemia. CAA is an important factor for the progression of cognitive decline in old age population (Boyle *et al.*, 2015; Case *et al.*, 2016).

Lacunar infarcts arise due to acute occlusion of small vessels and appear as focal hyperintensities on MRI scans. Cerebral microbleeds are another neuroimaging marker of SVD, associated with the rupture of vessels and resulting in intracerebral haemorrhage (ICH) (Caceres & Goldstein, 2012). ICH, which is a type of haemorrhagic stroke, may lead to injury of both grey and white matter and is associated with an increase in the risk of developing dementia (Corraini *et al.*, 2017). Recently, a retrospective study revealed that the progression rate of WML is higher in patients with a history of ICH (Chen *et al.*, 2018), supporting other studies which suggest ICH may underlie the pathogenesis of WML (Román *et al.*, 2002; Weller *et al.*, 2015).

1.5 Alzheimer's disease

Alzheimer's disease (AD) is the most common age-related neurodegenerative disease and is characterised by progressive neurodegeneration and memory loss (Selkoe, 2001). Late stages of this disease are associated with dementia, together with behavioural changes and motor deficits (DeTure & Dickson, 2019).

AD is neuropathologically characterised by the extracellular deposition of β-amyloid (Aβ) protein in the form of diffuse and neuritic plaques, and the intracellular accumulation of hyperphosphorylated tau protein in neurofibrillary tangles (NFT)

(Vickers *et al.*, 2015). These characteristic features are associated with neuronal death, loss of synapses and glial activation, which eventually contribute to cognitive decline in a progressive fashion (DeTure & Dickson, 2019). The hippocampus and entorhinal cortex are the first regions in AD to be affected by these neuropathological changes, which later spread to involve limbic and isocortical regions (Braak & Braak, 1991).

1.6 Microglia

Microglia, first described by Rio-Hortega in 1919, are the resident brain macrophage (Rio-Hortega & P, 1919). They play a significant role in maintaining homeostasis within the CNS and share similar functions with tissue macrophages, including immune surveillance, antigen presentation, and phagocytosis of cell debris (Nimmerjahn *et al.*, 2005; Teeling & Perry, 2009; Hashemiaghdam & Mroczek, 2020).

Under normal resting conditions, microglia are ramified in morphology with small cell bodies and multiple processes. The motile processes of microglia constantly extend and retract to survey their surroundings (Nimmerjahn *et al.*, 2005). These cells become activated by various triggers such as trauma, ischemia and neurodegeneration (Luo *et al.*, 2010). Immunoglobulins and the leakage of other plasma proteins into the brain parenchyma also activate microglia (Lu *et al.*, 2001). Once activated, these cells can retract their processes and transform to become amoeboid in shape with a large cell body, and thicker processes, in addition to

functional changes and rapid migration to the site of injury (Nimmerjahn *et al.*, 2005; Lynch *et al.*, 2010).

1.6.1 Microglial activation (including primed microglia)

Several factors determine the behaviour of microglia in the CNS, which can exert either neuroprotective and neurotoxic effects based on the type of injury, pathological environment and the activated microglial phenotype (Luo *et al.*, 2010; Tang & Le, 2016).

Microglia have historically been suggested to adopt two distinct phenotypes based on the mechanism of activation (Figure 1.3): "classically" activated microglia, also known as pro-inflammatory (M1) and "alternatively" activated microglia, also known as an anti-inflammatory (M2).

The classically activated M1 phenotype is induced by interferon-gamma (IFN-γ) and lipopolysaccharide (LPS) (Boche *et al.*, 2013; Satoh, 2018), which can, in turn, induce detrimental damage to the surrounding tissue by releasing pro-inflammatory cytokines, including tumour necrosis factor-alpha (TNF-α), interleukin-1-beta (IL-1β) (Tang & Le, 2016), nitric oxide (NO) (Block *et al.*, 2007) and free radicals, such as reactive oxygen species (ROS) (Nakagawa & Chiba, 2014). In contrast, the alternatively activated M2 phenotype is induced following the exposure to interleukin 4 (IL-4) and is associated with the release of anti-inflammatory cytokines and plays a role in repair processes (Yang *et al.*, 2016). M2 microglia serve as an inhibitor of the inflammatory response, clear cellular debris, and secrete

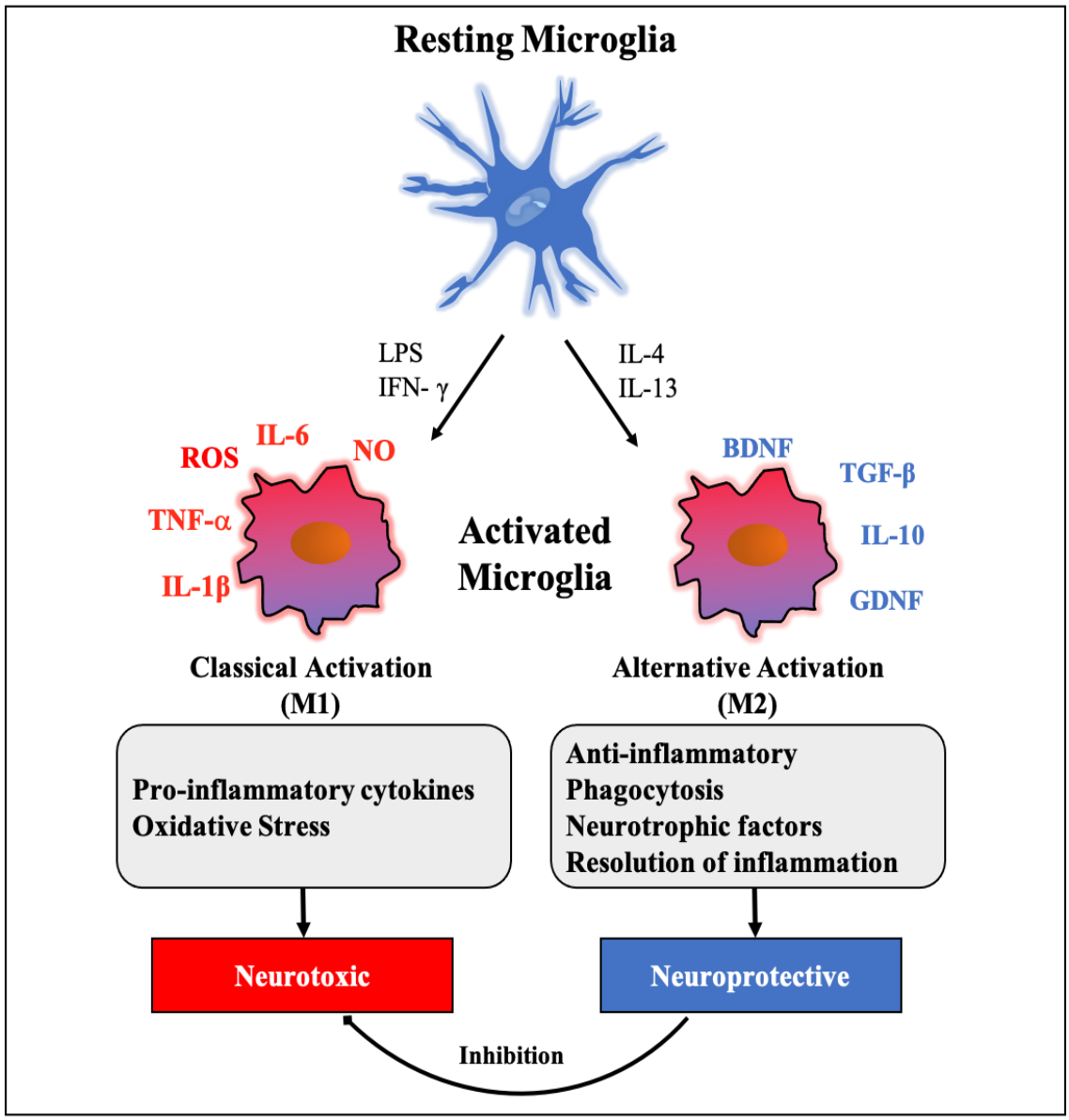

Figure 1.3 Activated microglial phenotypes

Classically activated microglia (M1) adopt a mainly neurotoxic phenotype, as they release pro-inflammatory cytokines such as interleukin-1-beta (IL-1β), nitric oxide (NO) and reactive oxygen species (ROS). In contrast, alternatively activated microglia (M2) adapt a neuroprotective phenotype, releasing neurotrophic factors such as, glial cell-derived neurotrophic factor (GDNF) and IL-10, which are mainly neuroprotective and involved in the phagocytic mechanism of cellular debris in the brain. Adapted from (Nakagawa & Chiba, 2014; Hu *et al.*, 2015).

neurotrophic factors, such as brain-derived neurotrophic factor (BDNF) and glial cell-derived neurotrophic factor (GDNF) (Jiao *et al.*, 2018), helping in the reduction of both demyelination and oligodendrocyte injury (Miron *et al.*, 2013).

It should be noted that this simple classification of M1/M2 phenotypes was originally defined in peripheral macrophages to explain the pro- and anti-inflammatory states of infiltrating monocyte-derived macrophages, and was mainly observed in animal studies (Mills *et al.*, 2000). Microglia are considered among the most versatile cells in the body. They are characterised by the ability to shift into different activation states, including in response to ageing, trauma, infections, ischemia, and neurodegenerative diseases, which are not limited to the M1/M2 classification (Ransohoff, 2016). This classification represents extreme states, and it is likely that both states, as well as intermediate forms, will be present in the ageing brain. Characterisation of the microglial activation states associated with ageing WM pathology may provide evidence of a critical role of these cells in WML formation.

Transcriptomic profiling of microglia faces several challenges. Gene expression studies on total tissue extracts will include a heterogeneous population of cells, which likely mask cell-specific changes in the transcriptome and requires identifying genes associated with the cell of interest. A study using animal models of EAE, ALS and Huntington's, developed a protocol to separate the microglial population from other CNS cells and infiltrating myeloid cells using single-cell mass spectrometry [cytometry by time-of-flight (CyTOF)]. The microglial population were distinguished using a panel of specific cell surface markers, including CD45,

CD11b, BST2 (CD317), MHC-II, CD39 and CD86. Activated microglia highly expressed MHC-II, CD86, TREM2, CD274 and CD80. However, the inactivated group lack the expression of these markers and only express BST2 (CD317) (Ajami *et al.*, 2018), which diminishes the expression of inflammatory genes (Polyak *et al.*, 2013). These findings can be employed to study microglial heterogeneity in transcriptomic profiling studies, as examining co-expressed genes will aid in identifying activated and inactivated microglia.

single-cell RNA-sequencing (snRNA-seq) profiling of microglia in human post-mortem tissue has revealed differences in the microglial phenotype depending on their location. Microglia in the white matter express higher levels of MHC-II related HLA-DR and CD68 than the grey matter (Sankowski *et al.*, 2019). Furthermore, the subventricular zone of the white matter contains a distinct microglial phenotype compared to other brain regions, with microglia in this region expressing high levels of microglial activation markers, including CD68, CD86, CD45, CX3CR1, CD11c, CD64 and HLA-DR (Böttcher *et al.*, 2019). Together these findings demonstrate the diversity of microglia between different brain regions.

1.6.2 Microglia in the ageing brain

Ageing is the greatest risk factor for the development of many neurodegenerative diseases, and no cell is safe from the ageing effects, including microglia (von Bernhardi, 2007). Innate immune activation occurs during brain ageing and is associated with cognitive decline. Microglia become primed during neurodegeneration, neuroinflammation and as part of the normal ageing process.

Primed microglia were first described in animal models associated with prion diseases (Combrinck *et al.*, 2002). Primed microglia have a lower activation threshold, and when stimulated, they produce an exaggerated inflammatory response, which may contribute to neurodegeneration and cognitive impairment (Perry & Holmes, 2014). In ageing mice, LPS administration leads to an exaggerated neuroinflammatory response, including increased cytokine expression (Godbout *et al.*, 2005). Similarly, excessive pro-inflammatory IL-1B is produced following LPS administration , mainly derived from primed microglia (Henry *et al.*, 2009).

Ageing murine studies indicate a disturbance in the microglial functions, including a reduction in surveillance, phagocytosis, and a delayed response to injury (Floden & Combs, 2011; Hefendehl *et al.*, 2014). Primed microglia shift toward the neurotoxic activation phenotype (M1) (Hu *et al.*, 2012), resulting in increased production and secretion of pro-inflammatory cytokines such as IL-6, IL-1β, and TNF-α (Cunningham *et al.*, 2009) and an increase of ROS production alongside an increased phagocytic activity in the earlier stages of priming, which is reduced over time (Koellhoffer *et al.*, 2017; Angelova & Brown, 2019). The release of these neurotoxic factors can lead to more microglial priming, forming a positive feedback loop (Li *et al.*, 2018). Furthermore, ageing animal models are associated with an increased expression of CD68 (Godbout *et al.*, 2005), co-stimulatory molecule CD86 (B7) (Griffin *et al.*, 2006) and MHC II (Henry *et al.*, 2009). Increased expression of CD68 in aged microglia is one of the hallmarks of ageing, together with an increased lipofuscin accumulation in mice (Safaiyan *et al.*, 2016) and human microglia (Moreno-García *et al.*, 2018). Lipofuscin, which are insoluble lipid debris, is a lysosomal aggregate that accumulates in the microglia (Singh Kushwaha *et al.*,

2018), leading to reduction/impairment of microglial homeostatic functions, including myelin clearance and phagocytosis (Kakimura *et al.*, 2002).

It should be noted that animal findings do not necessarily translate to human diseases. Microglia in humans are heterogeneous and may not reflect the findings of animal models. In addition, genetically engineered animal models do not recapitulate the whole profile of the disease, which may lead to misinterpretation of the data. Yet, some aspects of these models are helpful to understand the mechanisms underlying pathological diseases to be translated into humans. For example, transcriptomic profiling of human and murine microglia reveals an overlap in immune function genes, but has identified that age-associated gene expression changes show little overlap between the two species (Galatro *et al.*, 2017).

Microglia in the ageing brain display changes in their morphology, which is reflected by hypertrophied cell bodies and shorter, twisted and fragmented processes, these changes have been referred to as senescent or dystrophic microglia (Streit *et al.*, 2004). These microglia found to have reduced surveillance (Davies *et al.*, 2017), alongside a significant reduction in processing speed, motility and cellular migration (Damani *et al.*, 2011; Hefendehl *et al.*, 2014) leading to a failure in responding correctly to stimuli.

1.6.3 The role of microglia in the formation of WML

Microglial activation and changes in microglial morphology are a prominent feature of both PVL and DSCL; however, there are striking differences between both lesion types which suggest variation in underlying pathological mechanisms. As discussed above, the amoeboid morphology of $CD68^+$ microglia in DSCL suggests that these microglia play a role in demyelination, phagocytosis and the removal of myelin breakdown debris (Simpson *et al.*, 2007b). In contrast, microglia in the PVL have a mainly ramified morphology with significantly increased expression of MHC II and the co-stimulatory molecule CD86 (B7-2) and CD40, suggesting these lesions are associated with an ongoing immune activation process (Simpson *et al.*, 2007a). Whether the microglia have adapted an M1 or an M2 phenotype within these lesion types is currently unknown.

In addition to significantly increased levels of MHC II^+ microglia within the PVL, the radiologically NAWM from lesional cases have also been shown to contain significantly higher levels of MHC II^+ microglia than control WM from non-lesional cases (Simpson *et al.*, 2007b). This finding demonstrates that the radiologically NAWM is histologically abnormal, but it is still unknown whether these microglia are contributing to lesion progression or inhibiting lesion spread.

As discussed earlier, cerebral hypoperfusion together with disruption of the BBB plays a major role in the formation of age-associated WML (Figure 1.4), which may lead to the activation of microglia and subsequent pro-inflammatory response

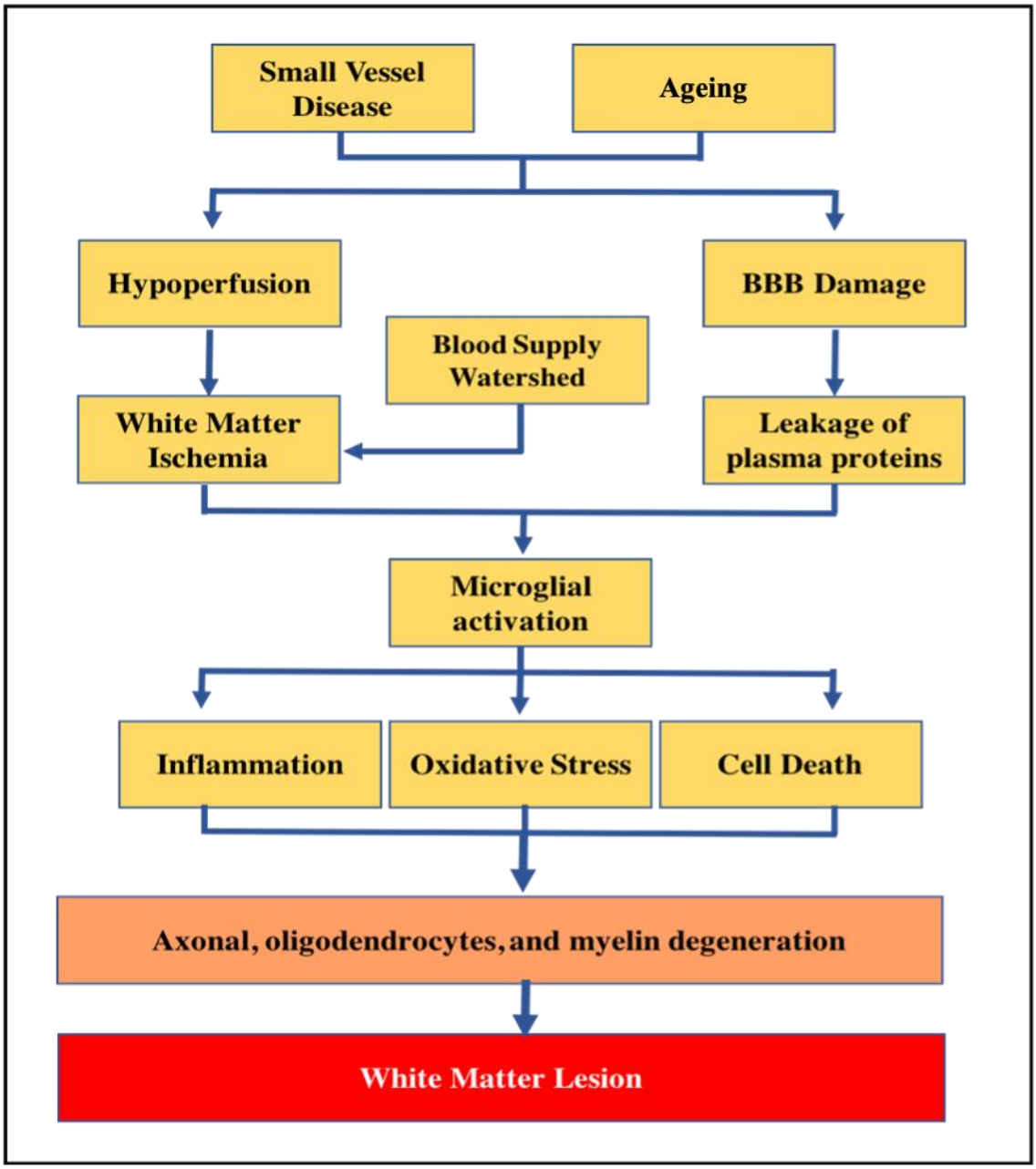

Figure 1.4 Pathway for the formation of WML

This figure illustrates the proposed mechanisms for the development of white matter lesions. Small vessel disease and ageing are the main factors affecting the cellular processes in the brain, leading to cerebral hypoperfusion and leakage of plasma proteins into the white matter. These processes were suggested to activate glial cells in the white matter. Microglial activation may result in multiple pathological processes, including subsequent pro-inflammatory response, oxidative stress and cellular death resulting in degeneration of axons, myelin, and oligodendrocytes depletion, which eventually leading to demyelination and development of white matter lesions. Adapted from (Wharton *et al.*, 2015; Lin *et al.*, 2017).

characterised by the formation of ROS including hydrogen peroxide, free radicals and NO (Merrill *et al.*, 1993; Park *et al.*, 2002). An imbalance between the formation of ROS and their removal by antioxidants leads to the accumulation of ROS, giving rise to oxidative stress. Oligodendrocytes and axons are highly susceptible to oxidative stress (Merrill *et al.*, 1993; Giacci *et al.*, 2018), which can result in oligodendrocyte depletion, and disrupt their maturation, impacting their role in myelination (French *et al.*, 2009).

Secretion of pro-inflammatory cytokines by microglia may directly impact the integrity of the BBB, leading to the accumulation of plasma proteins into the brain (Rosenberg, 2009; Shigemoto-Mogami *et al.*, 2018). This increased production and secretion of pro-inflammatory mediators may also activate surrounding glia, and impact on axonal function (Rosenberg, 2009; Winkler *et al.*, 2014). In addition to increased production and expression of pro-inflammatory mediators, activated microglia are also responsible for the secretion of damaging molecules such as lysosomal proteases, including cathepsins, which are a family of protein degrading enzymes. Transcriptomic profiling of DSCL indicates that cathepsins are highly expressed by amoeboid microglia, suggesting that these molecules play a role in myelin degradation and the pathogenesis of WML (Simpson *et al.*, 2009; Liu *et al.*, 2019b).

1.7 Hypothesis and aims

The role of microglia in age-associated white lesion pathogenesis is currently unknown; therefore, this project will test the following hypotheses:

(i) Confluent lesions arise as a result of combined PVL and DSCL spread.

(ii) Microglia within PVL adapt a neurotoxic M1 phenotype which promotes axonal damage and results in cognitive decline in the ageing population.

(iii) The mechanisms underlying the pathogenesis of PVL are different to DSCL.

This research aims to:

i. Characterise the microglial phenotype of confluent lesions, specifically assessing the immunoreactive profile of MHC-II and CD68, to determine if confluent lesions arise as a spread of PVL, DSCL or both.

ii. Characterise the gene expression profile of age-associated PVL using microarray analysis to identify significant changes in biologically relevant functional groups and pathways using DAVID.

iii. Perform bioinformatics analysis using EnrichR and computational microglial deconvolution of the bioinformatic datasets to identify microglial-specific transcriptomic changes.

iv. To validate a key panel of candidate gene expression changes identified in the microarray analysis using an independent approach, namely NanoString nCounter, and to confirm the differential expression of the proteins encoded by a panel of key gene changes using immunohistochemistry.

CHAPTER 2: CHARACTERISATION OF THE MICROGLIAL PHENOTYPE IN AGE-ASSOCIATED CONFLUENT WHITE MATTER LESIONS

2.1 Introduction

To date, the majority of dementia research has focussed on cortical pathology. AD is neuropathologically characterised by β-amyloid (Aβ) plaques and neurofibrillary tangles composed of hyperphosphorylated tau. The amyloid hypothesis currently dominates the AD field, proposing that Aβ and its oligomers are central to neuronal damage (Hardy & Selkoe, 2002). This hypothesis has given rise to research to identify treatments that remove Aβ; however, clinical trials aimed at removing pathogenic Aβ have all failed to slow disease progression (Honig *et al.*, 2018; Sun & Benet, 2020). In contrast, the myelin model of AD proposes that cerebral white matter pathology triggers an adaptive response that initiates the deposition of Aβ and tau (Bartzokis, 2011). In support of this model, which suggests cortical pathology occurs as a downstream event in AD, MRI of patients has shown that WMH are prominent early features of both late-onset (Brickman, 2013) and hereditary AD (Lee *et al.*, 2016). Moreover, WML are an independent risk factor for dementia (Matthews *et al.*, 2009), and form secondary to vascular pathology, including SVD, as discussed in detail in Chapter 1.

WML are broadly classified based on their neuroanatomical location into PVL and DSCL. However, it should be noted that extensive WML encompassing both periventricular and deep subcortical regions are classified as confluent lesions (Barkhof & Scheltens, 2006). These WML are further subdivided into punctate, early confluent and confluent lesions based on their detection by MRI (Fazekas *et al.*, 1988; Schmidt *et al.*, 1992). Confluent lesions are clinically relevant and are associated with an increased risk for the development of cognitive impairment and

dementia (Srikanth *et al.*, 2010; Callisaya *et al.*, 2015). White matter tracts throughout the brain connect cortical and subcortical regions into functional units that play a role in cognition and emotion; therefore cognitive ability is as reliant on brain connectivity as it is on neuronal activity (Filley & Fields, 2016).

While a number of studies have focussed on MRI assessment of WML in ageing and dementia patients (Wahlund *et al.*, 1996; Fernando *et al.*, 2004; Kim *et al.*, 2008), research has also been performed to histologically characterise these lesions in ageing population-representative neuropathology cohorts, such as CFAS. CFAS is a prospective longitudinal study of an ageing population-representative cohort. The study began in 1989 when over 18,000 people aged 65 and older were selected from GP registers and invited to participate in the study. The study participants were located in six different centres across the UK, representing north and south, urban and rural areas (Brayne *et al.*, 2006). The participants underwent regular cognitive testing and completed questionnaires regarding their lifestyle, medication and general health, enabling longitudinal data to be collected. A subgroup of around 550 participants donated their brain to the CFAS neuropathology study which has enabled assessment of the molecular and cellular pathologies of brain ageing, frailty and dementia to be evaluated (Wharton *et al.*, 2011).

Microglia exist in a quiescent state with a ramified morphology in the healthy brain, constantly surveying their environment to maintain homeostasis. In response to an insult or infection, microglia become activated and can change their morphology to adopt a larger, amoeboid morphology. Microglial activation is a complex and dynamic action, and reactive microglia display different cell surface and

intracellular markers, secrete different factors and perform different functions depending on their activation phenotype. M1 microglia express the distinctive markers CD74, CD40, CD86, CCR7 (Peferoen *et al.*, 2015), whereas M2 microglia are associated with the expression of mannose receptor and CCL22 (Peferoen *et al.*, 2015; Liu *et al.*, 2018). These microglial states are predominantly defined by cytokine expression patterns as evidenced in animal and human studies (Boche *et al.*, 2013). Microglia with an M1 phenotype are regarded as pro-inflammatory, while those with an M2 phenotype are regarded as an anti-inflammatory. However, it should be noted that (as discussed in Chapter 1) these states were originally defined in peripheral macrophages, and the extent to which this applies to microglia is less certain. These states are 2 extremes and it is generally accepted that the phenotype of activated microglia exists along a spectrum between these two poles (Boche *et al.*, 2013).

Current microglial markers include Iba-1, CD68 and MHC II. Ionized calcium-binding adaptor molecule (Iba-1) is a member of calcium-binding proteins which interacts with actin molecules and is mainly located in the cytoplasm of microglia (Ohsawa *et al.*, 2004). This marker is widely used as a microglial pan-marker which immunolabels both ramified and amoeboid microglial phenotypes in WML (Walker & Lue, 2015; Korzhevskii & Kirik, 2016). However, a recent study by Waller *et al.* reported that not all microglia are Iba-1^{+}, and demonstrated the presence of Iba-1^{-} microglia in DSCL (Waller *et al.*, 2019). HLA-DR class II molecules of the major histocompatibility complex (MHC-II) play a major role in antigen processing and presentation and are expressed by immune-activated microglia. Histological assessment of MHC-II expression in age–associated WML has demonstrated that

PVL contain significantly higher levels of MHC-II$^+$ microglia than DSCL (Simpson *et al.*, 2007b). Interestingly, the radiologically normal-appearing white matter from lesional cases contains significantly higher levels of these immune activated microglia than control white matter from non-lesional cases, demonstrating that microglial pathology extends beyond the WML itself. CD68 is a lysosomal-associated membrane protein (Ramprasad *et al.*, 1996) used to identify microglia with a phagocytic phenotype (Zotova *et al.*, 2011). In contrast to the PVL which contain high levels of immune activated microglia, DSCL contains significantly elevated levels of CD68$^+$ microglia with an amoeboid, phagocytic phenotype.

While the histological evaluation of WM pathology in the CFAS cohort has identified significant differences in the microglial profile of PVL compared to DSCL, to date the microglial profile of confluent lesions in the CFAS neuropathology cohort is unknown.

2.1.1 Hypothesis and aims:

We hypothesise that confluent white matter lesions arise as a result of the combined spread of PVL and DSCL.

To test this hypothesis, this chapter aims to:

(i) Characterise the microglial immunoreactive profile of MHC II and CD68 expression in confluent lesions.

(ii) Quantify the percentage area immunoreactivity across the periventricular, middle and deep subcortical regions, to determine if these lesions comprise a gradient of microglial phenotypes.

2.2 Materials and methods

2.2.1 MRI guided sampling of confluent lesions

Post-mortem brain tissue was obtained from the CFAS, following multi-centre research ethics committee (REC) approval (REC Reference number 15/SW/0246). Cases were identified by two independent, experienced radiologists who examined the MRI of formalin fixed coronal slices from three distinct anatomical levels of each brain (Newcastle coronal brain map reference levels 10/12, 19/20 and 24/25), and scored WML using a modified Schelten's rating, as shown in Table 2-1 (Scheltens *et al.*, 1993; Fernando *et al.*, 2004). Based on these scores, and using post mortem MRI as a guide, 18 confluent lesions from 16 cases were sampled from the formalin fixed hemisphere with a mean age of 87.9 years (standard deviation (SD) 6.3 years; range 87-101), post-mortem delay (PMD) mean of 39.6 hrs (SD 41.2; range 17-164 hrs), and mean brain pH of 6.36 (SD 0.32; range 6.5-7.04) (Table 2-2).

Table 2-1 A modified Scheltens rating scale for PVL and DSCL (Scheltens *et al.*, 1993)

Periventricular lesions (PVL)	***Deep subcortical lesions (DSCL)***
0 Absent	0 No abnormality
1 ≤5 mm	1 <4 mm; n < 6
2 >5 mm - ≤10 mm	2 <4 mm; n ≥ 6
3 >10 mm	3 4-10 mm; n ≤ 6
	4 4-10 mm; n ≥ 6
	5 >10 mm
	6 Confluent lesion

Table 2-2 Details of cases used in the confluent lesion study

Case Number	Age	Gender	PMD (Hrs)	pH
CASE 1	87	F	17	6.50
CASE 2	101	F	5	5.97
CASE 3	84	F	36	7.04
CASE 4	91	F	35	5.97
CASE 5	94	F	35	6.43
CASE 6	91	F	36	6.50
CASE 7 (BLOCK 1)	80	M	20	6.18
CASE 7 (BLOCK 2)				
CASE 8 (BLOCK 1)	89	M	46	6.42
CASE 8 (BLOCK 2)				
CASE 9	82	F	N/A	N/A
CASE 10	86	F	N/A	N/A
CASE 11	94	F	N/A	N/A
CASE 12	90	F	72	N/A
CASE 13	77	F	7	6.23
CASE 14	82	M	164	N/A
CASE 15	89	F	19	N/A
CASE 16	90	F	24	N/A

PMD, Post-Mortem Delay; Hrs, Hours; M, Male; F, Female.

2.2.2 Characterisation of the microglial phenotype in confluent lesions

2.2.2.1 Pre-treatment of FFPE sections

FFPE sections (5µm) were prepared using a microtome, collected onto charged slides (Leica, UK) and dried overnight in an oven at 60°C. All steps were carried out at room temperature (RT) unless otherwise stated. Sections were dewaxed in xylene (2x5 min), rehydrated to water using a graded series of ethanol (EtOH) (100%, 95%, 70%, for 5 minutes each). Sections were placed in 3% Hydrogen Peroxide (H_2O_2)/methanol (Fisher Chemicals, Loughborough, UK) for 20 minutes at room temperature (RT) to block endogenous peroxidase activity and then briefly washed with tap water. Antigen retrieval was required to unmask the antigen binding site in the FFPE tissue and was performed by microwaving the sections for 10 minutes at maximum power (800 watts) (model NN-E255W, Panasonic, Franklin Park, IL, USA) in 10mM Tri-Sodium Citrate buffer (TSC, pH6.5). The sections were cooled to RT by placing them in running tap water.

2.2.3 Immunohistochemistry (IHC)

IHC is a biochemical technique used to detect specific antigens in tissue sections and occurs via binding of a specific primary antibody to the antigen of interest. The signal from the primary antibody (Ab) is amplified through a species-specific secondary antibody and the introduction of peroxidase enzyme via an avidin biotinylated complex (ABC). This process enhances and amplifies the signals to be easily visualised using a microscope.

Following antigen retrieval, IHC was performed on the sections using the Vectastain Elite Mouse IgG kit (Vector Laboratories, Peterborough, UK), using solution preparations as outlined in Table 2-3. Sections were covered with 1.5% normal horse blocking solution for 30 minutes at RT; then, following removal of blocking solution, incubated with the primary antibody (diluted in blocking solution) for one hour at RT (all antibody details are shown in Table 2-4). After rinsing slides with Tris-buffered saline (TBS, 50mM Tris, 150mM NaCl, pH 7.6) for 5 minutes, the sections were incubated with 0.5% secondary biotinylated antibody for 30 minutes. Then, after rinsing with TBS for 5 minutes, the sections were incubated with 2% ABC-HRP (avidin-biotin-complex horse radish peroxidase) for 30 minutes at RT, which was freshly made at least 30 minutes prior to its usage (Fadul, 2016).

2.2.3.1 Visualisation of ABC-HRP complex

The sections were washed with TBS for 5 minutes at RT and then incubated with the peroxidase enzyme substrate 3,3′-diaminobenzidine tetrahydrochloride (DAB) (Vector Laboratories, Peterborough, UK). 100 µl of DAB was added to each section and incubated at RT for 5 minutes. The reaction was observed under the microscope and once developed; sections were washed with dH_2O to quench the HRP enzyme activity. The sections were counterstained with haematoxylin (Leica Biosystems) for 30 seconds and blued in Scott's tap water. Following this step, slides were dehydrated using a graded series of ethanol in ascending concentration: 70%, 95%, 100%, and 100% for 1 minute each, then cleared in xylene before mounting in DPX (Leica Biosystems) and dried in an oven overnight (Fadul, 2016).

Table 2-3 Preparation of Vectastain Solutions

Reagent name	Composition
Blocking Solution	3 drops (150µl) of normal horse serum blocking solution in 10 ml TBS
Secondary Biotinylated Antibody	1 drop (50µl) of biotinylated anti-mouse IgG antibody in 10 ml TBS
Avidin-biotin-complex (ABC) horse radish peroxidase complex	2 drops of A solution (100µl) and 2 drops (100µl) of B in 10 ml TBS
DAB	2 drops (100µl) of the buffer, 2 drops (100µl) of H_2O_2 and 4 drops (200µl) of DAB in 5 ml of distilled water (dH_2O)

TBS: Tris Buffered Saline, DAB: 3,3′-diaminobenzidine tetrahydrochloride.

Table 2-4 Antibodies source and dilution

Table of markers used to characterise microglial phenotype of confluent lesions.

Antibody	Dilution	Isotype	Source
MHC-II (HLA-DR)	1:20	Mouse, IgG	Dako, UK TAL 1B5
CD-68 (PG-M1)	1:100	Mouse, $IgG_{3\kappa}$	Dako, UK

2.2.4 Analysis of the microglial immunoreactive profile of confluent lesions

2.2.4.1 Semi-quantitative Analysis

The immunoreactive profiles of MHC II and CD68 within the periventricular and deep subcortical regions of radiologically identified confluent lesions were assessed semi-quantitatively by two independent observers (J.S) and (M.F). The immunoreactive profile of MHC II$^+$ and CD68$^+$ microglia were observed across the entire WM, starting from the ventricular region and scanning across to the subcortical area using bright-field microscopy. Each observer classified the staining based on the localisation of both, MHC-II$^+$ and CD68$^+$ microglial cells in the periventricular and deep subcortical regions: occasional immunopositive cell (+); moderate expression (++); high levels of expression (+++). Agreement for the scores was assessed using Cohen's Kappa. If the independent observers disagreed on the score for cases, the stained sections were reviewed together to reach consensus on the rating. Representative images were captured using Nikon Eclipse 80i microscope (20x objective) and analysed using the NIS-Elements Imaging Software (Nikon UK, Kingston Upon Thames).

2.2.4.2 Quantitative analysis

Stained sections were scanned under a 20x objective lens using NanoZoomer-XR scanner and viewed using NDP view software version 2.3 (Hamamatsu, Photonics Ltd, Hertfordshire, UK). Assessment of the immunoreactive profile of CD68 and MHC-II was performed by starting from the area next to the ventricular region to capture 3 images in the periventricular region (PV), followed by capturing 3 images in the deep subcortical region (DSC), and a randomly selected region in between

(MID) where 3 images were captured. This process was done for each case in the study (Figure 2.1). The area of the selected field dimensions: 2834 x 1665 pixels; size 0.436 mm^2 (436000 μm^2) using x20 magnification. The images were analysed using Analysis^D software (Nikon UK, Kingston Upon Thames). The total immunoreactive area of both CD68 and MHC-II within the captured images was determined per total area studied. The average % area immunoreactivity of both CD68 and MHC-II within the PV, MID and DSC regions was calculated for statistical analysis.

2.2.5 Statistics

Agreement for semi-quantitative scores was assessed using Cohen's Kappa (unweighted) using SPSS software version 26 (Chicago, IL, USA). Statistical comparisons to assess the variation of CD68 and MHC-II mean % area immunoreactivity across the white matter regions (PV, MID and DSC) were carried out using Friedman's analysis of variance (ANOVA) for non-parametric data using SPSS. A P-value < 0.05 was considered statistically significant.

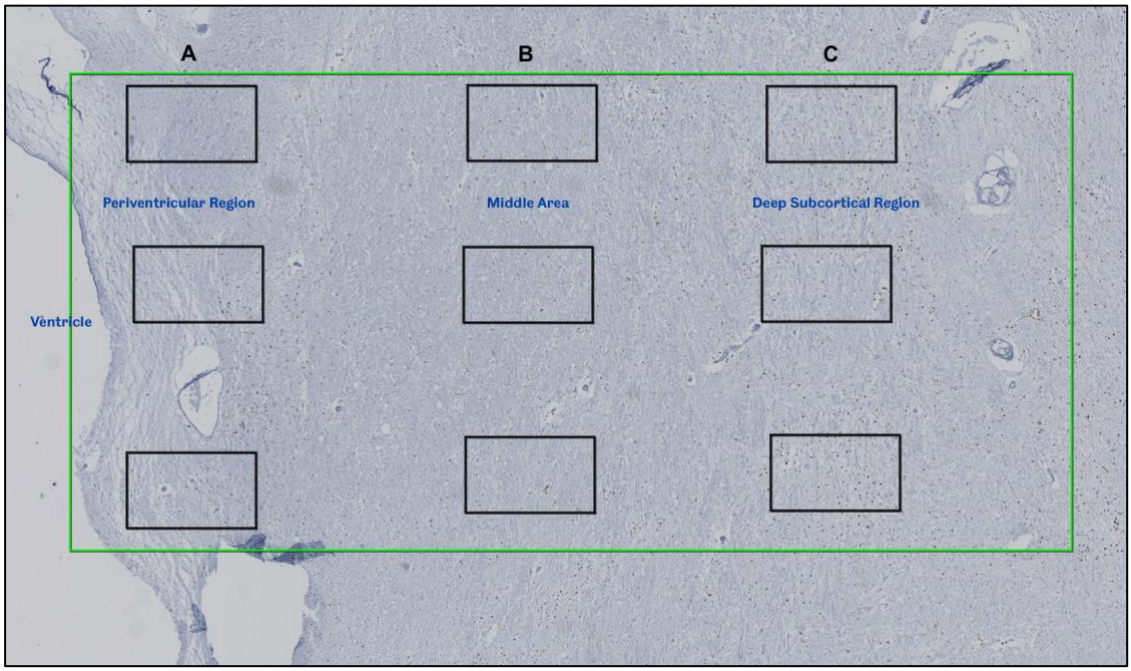

Figure 2.1 Approach used in quantitative analysis of WM confluent lesions

Selection of analysis region was made by capturing three images from each of the three different white matter regions: periventricular [PV] (A),) mid-region [MID] (B) and deep subcortical [DSC] (C) at x20 magnification. Images were imported into Analysis^D software to quantitatively analyse the % area immunoreactivity of both CD68 and MHC-II in the three different white matter regions.

2.3 Results

2.3.1 Characterising microglial pathology in confluent lesions

The confluent lesion cohort displayed a spectrum of MHC II$^+$ and CD68$^+$ microglial morphologies and phenotypes in both the deep subcortical and periventricular regions. MHC-II$^+$ microglial mainly displayed a ramified morphology with extending processes from the cell body. CD68$^+$ microglia mainly showed retracted processes with swollen and enlarged cellular bodies, reflecting an amoeboid microglial phenotype as shown in Figure 2.2.

2.3.2 Quantitative assessment of MHC-II and CD68 immunoreactivity in confluent lesions

Quantitative assessment of MHC-II and CD68 immunoreactivity was performed using analysis ^D software. The immunoreactive profile of CD68 and MHC-II (mean % area ± Standard Deviation (SD)) varied across the three regions of all confluent lesions. CD68+ microglia were a feature of the deep subcortical (DSC) region (0.343 ±0.303), compared to middle (MID) (0.308 ±0.200) and periventricular regions [0.201 ±0.162). In contrast, MHC-II+ microglia were a feature of the periventricular region (0.231 ±0.221), compared to both middle (0.183 ±0.127) and deep subcortical regions (0.150 ±0.148), as shown in Figure 2.3.

Friedman's test demonstrated a significant variation between CD68 χ^2 (N = 18, df = 2) =12.197, p = 0.002 and MHC-II χ^2 (N = 18, df = 2) =8.444, p = 0.015 across the confluent lesions in the ageing white matter.

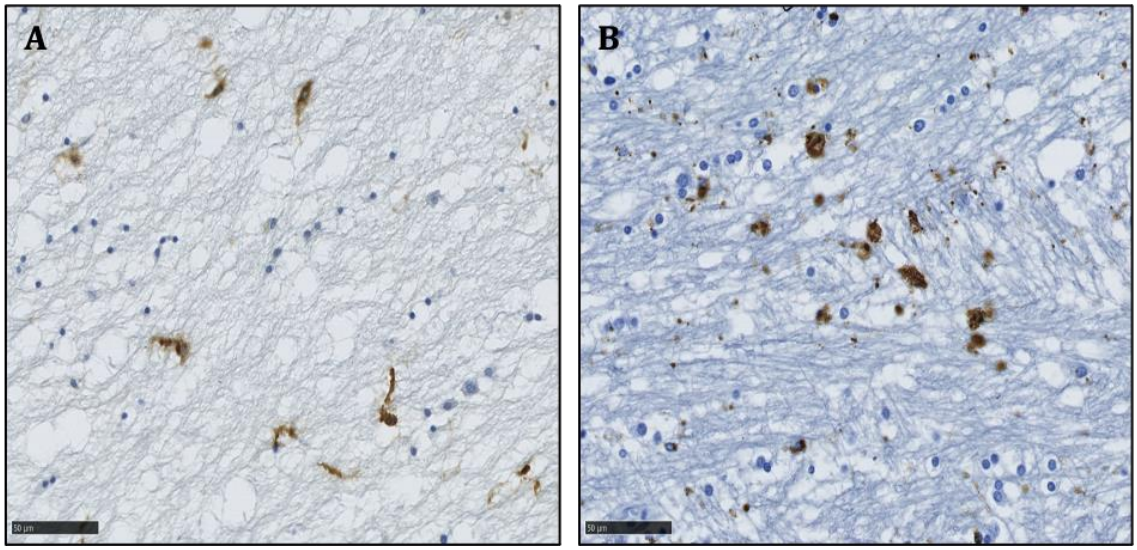

Figure 2.2 Microglial phenotypes in confluent lesions

MHC-II^{+} microglial mainly displayed a ramified morphology with extending processes from the cell body (A). While CD68^{+} microglia mainly showed retracted processes with swollen and enlarged cellular bodies, reflecting an amoeboid microglial phenotype (B). *Scale bar represents 50 µm*.

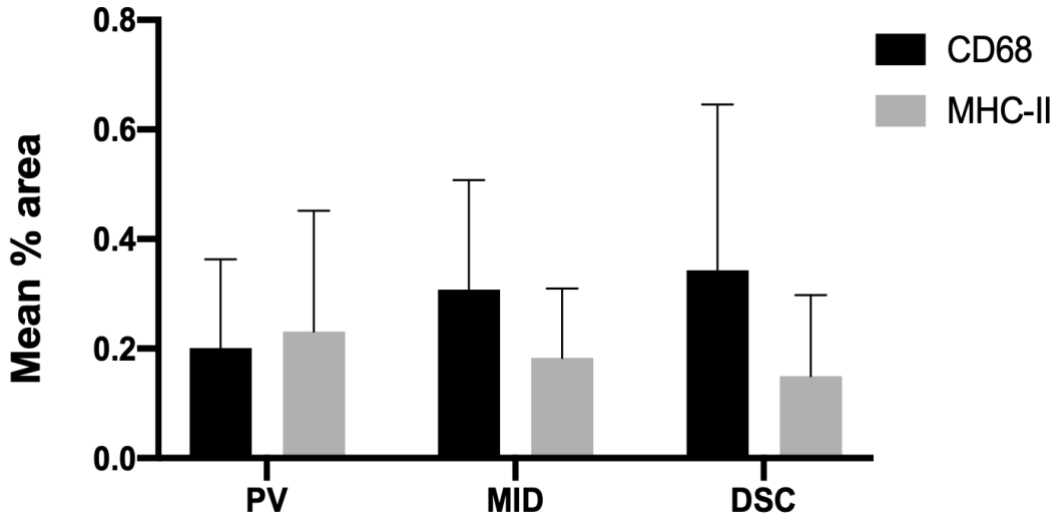

Figure 2.3 Mean %area immunoreactivity of CD68 and MHC-II in PV, MID and DSC white matter region of confluent lesions

Mean percentage (%) area of CD68 in the periventricular region (PV) [mean ± Standard Deviation (SD)= 0.201 ±0.162], MID region (0.308 ±0.200) and for deep subcortical region (DSC) (0.343 ±0.303). For MHC-II, the mean % area in the PV region was (0.231 ±0.221), MID region (0.183 ±0.127), and for DSC region (0.150 ±0.148). (Data represent mean ± SD).

2.3.3 Qualitative assessment of the immunoreactive profile of confluent lesions

Qualitatively, four distinct staining patterns were observed. Immunostaining revealed that ramified MHC II$^+$ microglia were present primarily in the periventricular region but not the deep subcortical region (Figure 2.4. A) and that amoeboid CD68$^+$ microglia were primarily a feature of the deep subcortical region (Figure 2.4. D), this pattern was classified as Type 1, and observed in 2/18 confluent lesions. In Type 2 lesions, immunostaining revealed a prominent MHC II$^+$ microglia with a ramified morphology present throughout the confluent lesion, at similar levels in both the periventricular and deep subcortical regions (Figure 2.5. A, B), this pattern was observed in 4/18 confluent lesions. Whereas in Type 3 lesions, immunostaining revealed prominent CD68$^+$ microglia with an amoeboid morphology were present throughout the confluent lesion, at similar levels in both periventricular and deep subcortical regions (Figure 2.6 C, D), this pattern was observed in 2/18 confluent lesions. Immunostaining in Type 4 lesions, displayed a mixed pattern of staining, where all regions of the confluent lesion contained both CD68$^+$ and MHC II$^+$ microglia (Figure 2.7), this pattern was observed in 10/18 confluent lesions.

In summary, the immunoreactive profile of microglia within confluent lesions could be classified into four lesion types with distinct staining patterns:

1. MHC II$^+$ and CD68$^+$ microglia primarily associated with the periventricular region and deep subcortical region, respectively (Figure 2.4).
2. MHC II$^+$ microglia predominantly throughout all regions (Figure 2.5).
3. CD68$^+$ microglia predominantly throughout all regions (Figure 2.6).

4. A mix of both $CD68^+$ and MHC II^+ microglia were present throughout the confluent lesion (Figure 2.7).

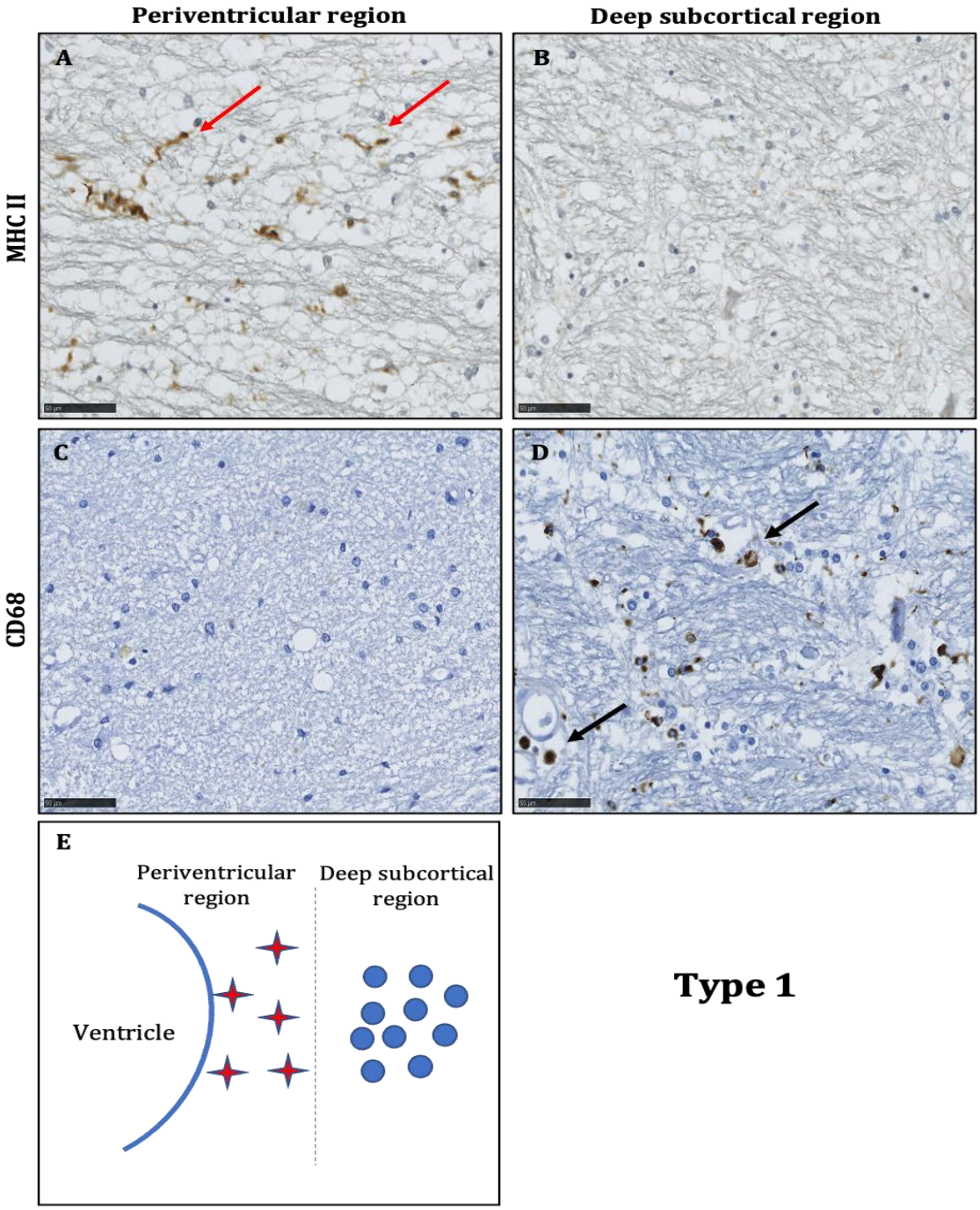

Figure 2.4 Microglial staining of confluent lesions: type 1 lesion

MHC II⁺ (A and B) and CD68⁺ (C and D) microglia are discrete to the periventricular and deep subcortical region, respectively. Diagrammatic representation of the staining pattern (E), where MHC II⁺ ramified microglia are illustrated by the red star-shape, while CD68⁺ amoeboid phagocytic microglia (D) are indicated by the blue round circles (E). *Scale bar represents 50 µm.*

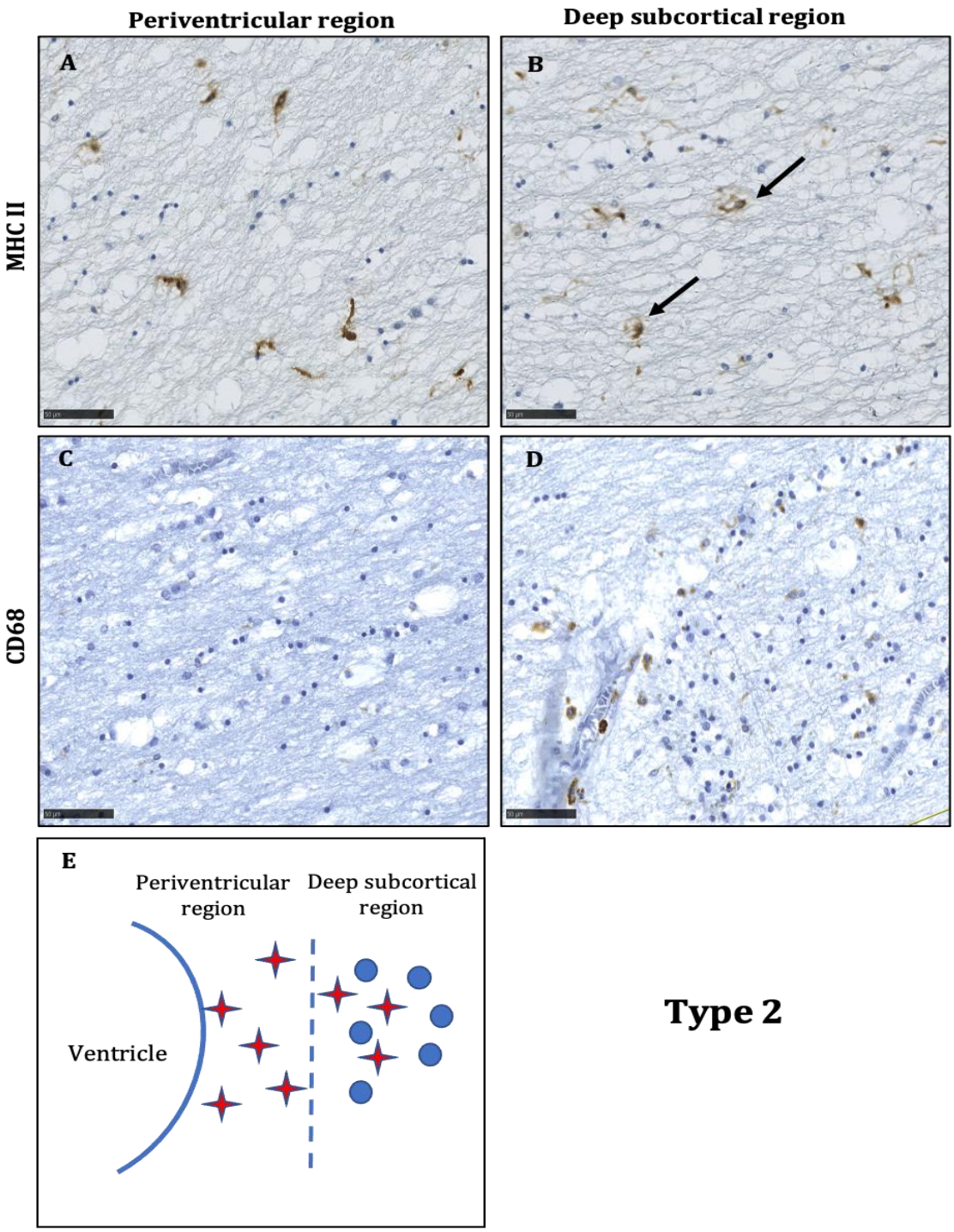

Figure 2.5 Type 2 lesion pattern

In type 2 confluent lesions ramified MHC II+ microglia were present in both, the periventricular (A) and the deep subcortical region (B), as indicated in the diagrammatic representation (E). MHC II+ microglia are indicated by the red star, while CD68+ microglia are indicated by the blue circles. *Scale bar represents 50 µm*.

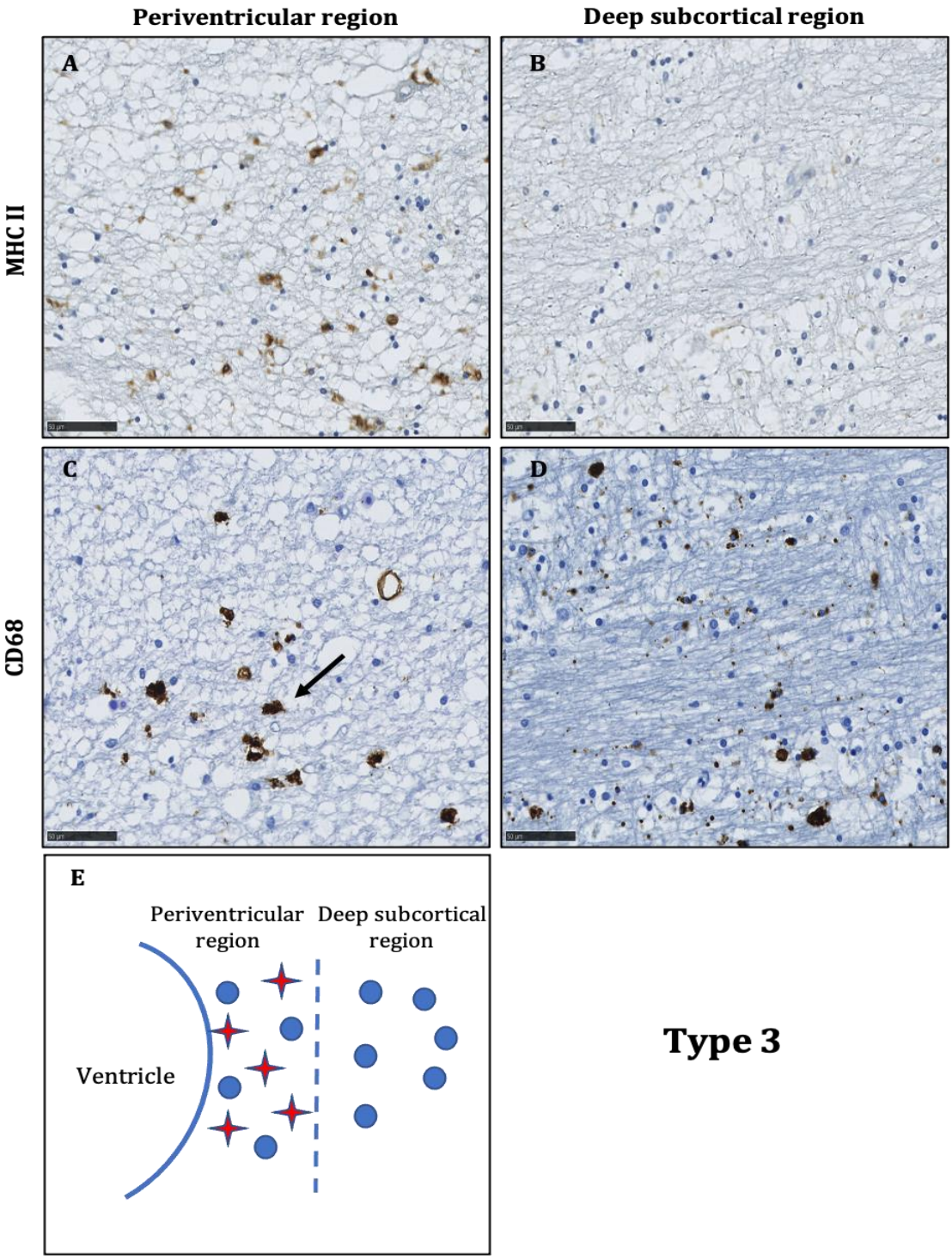

Figure 2.6 Microglial staining of confluent lesions: type 3 lesion

In type 3 confluent lesions, amoeboid CD68⁺ microglial were present in both the periventricular (C) and deep subcortical region (D), as indicated in the diagrammatic representation (E). MHC II⁺ microglia are indicated by the red star, while CD68⁺ microglia are indicated by the blue circles. *Scale bar represents 50 µm.*

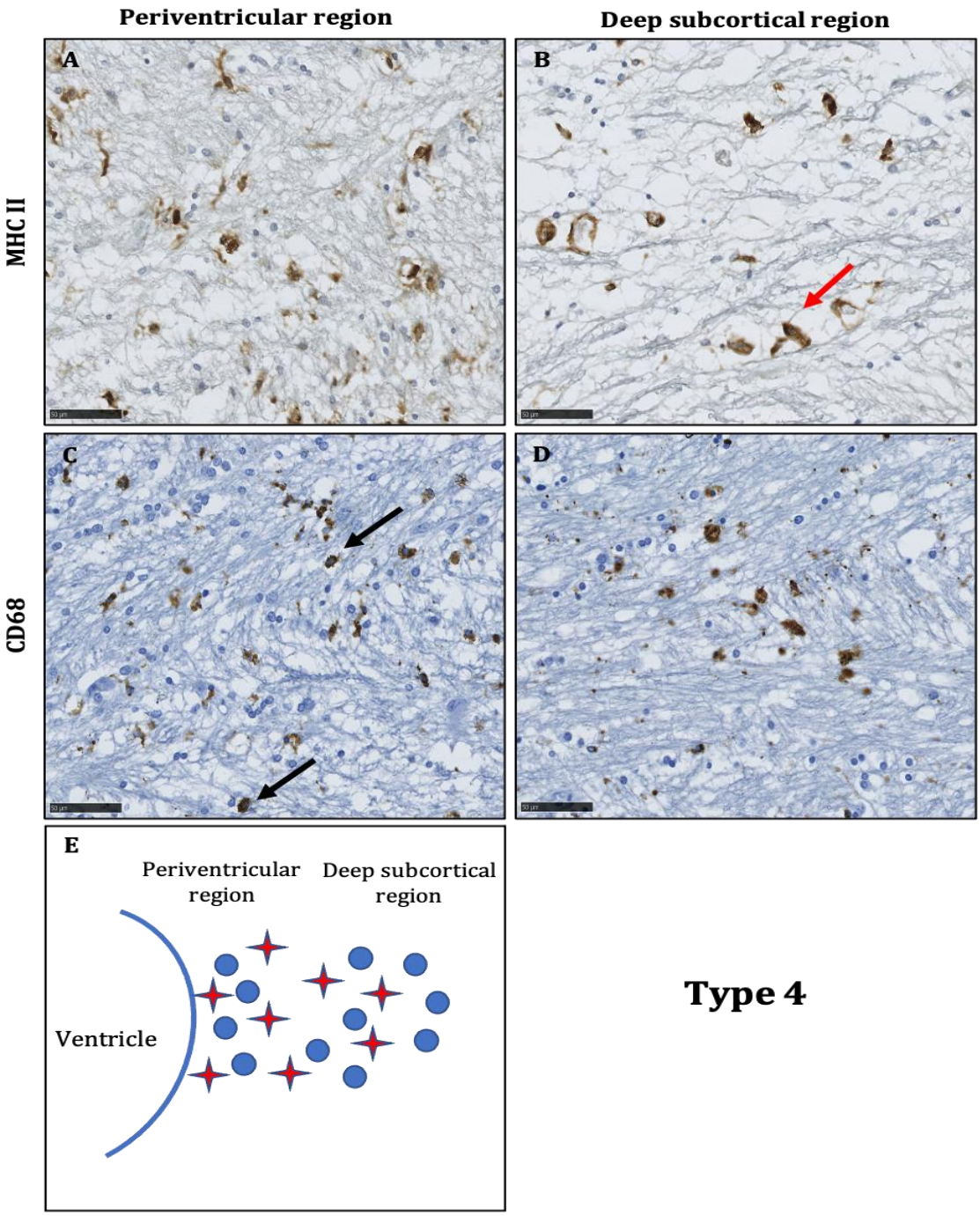

Figure 2.7 Type 4 Confluent Lesion Pattern

The figure illustrates a mixed pattern of staining, where all regions of the confluent lesion contained both CD68⁺ and MHC II⁺ microglia (E). MHC II⁺ ramified microglia were present in the deep subcortical region, indicated by red arrows (B), while CD68⁺ amoeboid microglia found in the periventricular region, indicated by black arrows (C). MHC II⁺ microglia are indicated by the red star, while CD68⁺ microglia are indicated by the blue circles (E). *Scale bar represents 50 µm*.

2.3.4 Analysis of staining patterns (semi-quantitative & quantitative)

The microglial staining patterns were semi-quantitatively assessed by two independent observers, who agreed on the staining pattern of 10/18 confluent lesions with a moderate agreement (κ = 0.4) (Table 2-5). Where the observers disagreed on the staining pattern of cases, they re-evaluated the staining pattern together and agreed to a consensus staining pattern.

In type 1 lesions, the mean of percentage (%) area of CD68 in the PV region was (mean ± SD= 0.066 ±0.049), MID region (0.119 ± 0.115) and DSC region (0.096 ±0.091). The mean of MHC-II % area in the PV region was (0.089 ±0.052), MID region (0.094 ±0.061) and for the DSC region (0.045 ±0.035). For type 2 lesions, the mean of % area of CD68 in the PV region was [(mean ±SD) 0.025 ±0.007], MID region (0.090 ±0.099) and for the DSC region (0.102 ±0.021). The mean of MHC-II area in the PV region was (mean ± SD= 0.108 ±0.035), MID region (0.1435 ±0.007) and DSC region (0.083 ±0.085). For type 3 lesions, the mean of % area of CD68 in the PV region was (0.234 ±0.176), MID (0.364 ±0.224), DSC (0.402 ±0.297). The mean of MHC-II % area in the PV region was (0.142 ±0.116), MID (0.101 ±0.055), and DSC (0.070 ±0.059). For type 4 lesions, the mean % area of CD68 in the PV region was (0.281 ±0.142), MID region (0.402 ±0.141), and for the DSC region (0.468 ±0.338). The mean of MHC-II % area in the PV region was (0.402 ±0.261), MID (0.303 ±0.118), and DSC (0.283 ±0.152) as shown in Table 2-6. The variation of CD68 and MHC-II immunoreactivity across white matter regions for different confluent lesion subtypes is shown in Figure 2.8, statistical analysis was not performed due to the small number of cases in each confluent lesion subtype.

Table 2-5 Inter-observer agreement of confluent lesion type

Independent scores of 2 observers assessing the microglial pathology and lesion type in a cohort of confluent lesions, showing moderate agreement (Kappa (κ) = 0.4) for assignment of staining type.

		Second Observer (J.S)				
		Type 1	**Type 2**	**Type 3**	**Type 4**	**Total**
First observer (M.F)	**Type 1**	2	1	0	0	3
	Type 2	2	1	1	0	4
	Type 3	0	0	1	2	3
	Type 4	1	0	1	6	8
	Total	5	2	3	8	18

Table 2-6 AnalySIS ^D quantitative analysis of % area immunoreactivity of microglial staining

This table represents the % area immunoreactivity of microglial staining for both MHC-II and CD68 in PV, MID and DSC regions.

Lesion type	Case	CD68			MHC-II		
		PV	MID	DSC	PV	MID	DSC
Type 1	**Case 6**	0.011	0.007	0.001	0.150	0.160	0.083
	Case 7 Block 1	0.097	0.113	0.110	0.057	0.080	0.043
	Case 14	0.090	0.237	0.177	0.060	0.041	0.008
	Mean	**0.066**	**0.119**	**0.096**	**0.089**	**0.094**	**0.045**
Type 2	**Case 13**	0.033	0.157	0.117	0.133	0.150	0.143
	Case 15	0.017	0.023	0.087	0.083	0.137	0.023
	Mean	**0.025**	**0.09**	**0.102**	**0.108**	**0.1435**	**0.083**
Type 3	**Case 5**	0.517	0.350	0.447	0.293	0.060	0.097
	Case 8 Block 1	0.163	0.287	0.240	0.060	0.083	0.057
	Case 9	0.210	0.770	0.367	0.057	0.123	0.012
	Case 10	0.103	0.170	0.193	0.137	0.087	0.060
	Case 11	0.050	0.173	0.193	0.030	0.050	0.023
	Case 12	0.360	0.433	0.970	0.277	0.203	0.170
	Mean	**0.234**	**0.364**	**0.402**	**0.142**	**0.101**	**0.070**
Type 4	**Case 1**	0.523	0.440	0.897	0.723	0.340	0.553
	Case 2	0.120	0.220	0.230	0.437	0.380	0.173
	Case 3	0.137	0.263	0.263	0.610	0.380	0.343
	Case 4	0.300	0.303	0.173	0.333	0.393	0.397
	Case 7 Block 2	0.260	0.507	0.370	0.583	0.223	0.163
	Case 8 Block 2	0.397	0.567	0.997	0.050	0.070	0.197
	Case 16	0.227	0.517	0.343	0.077	0.337	0.157
	Mean	**0.281**	**0.402**	**0.468**	**0.402**	**0.303**	**0.283**

PV, periventricular region; MID, middle region; DSC, deep subcortical region; SD, standard deviation.

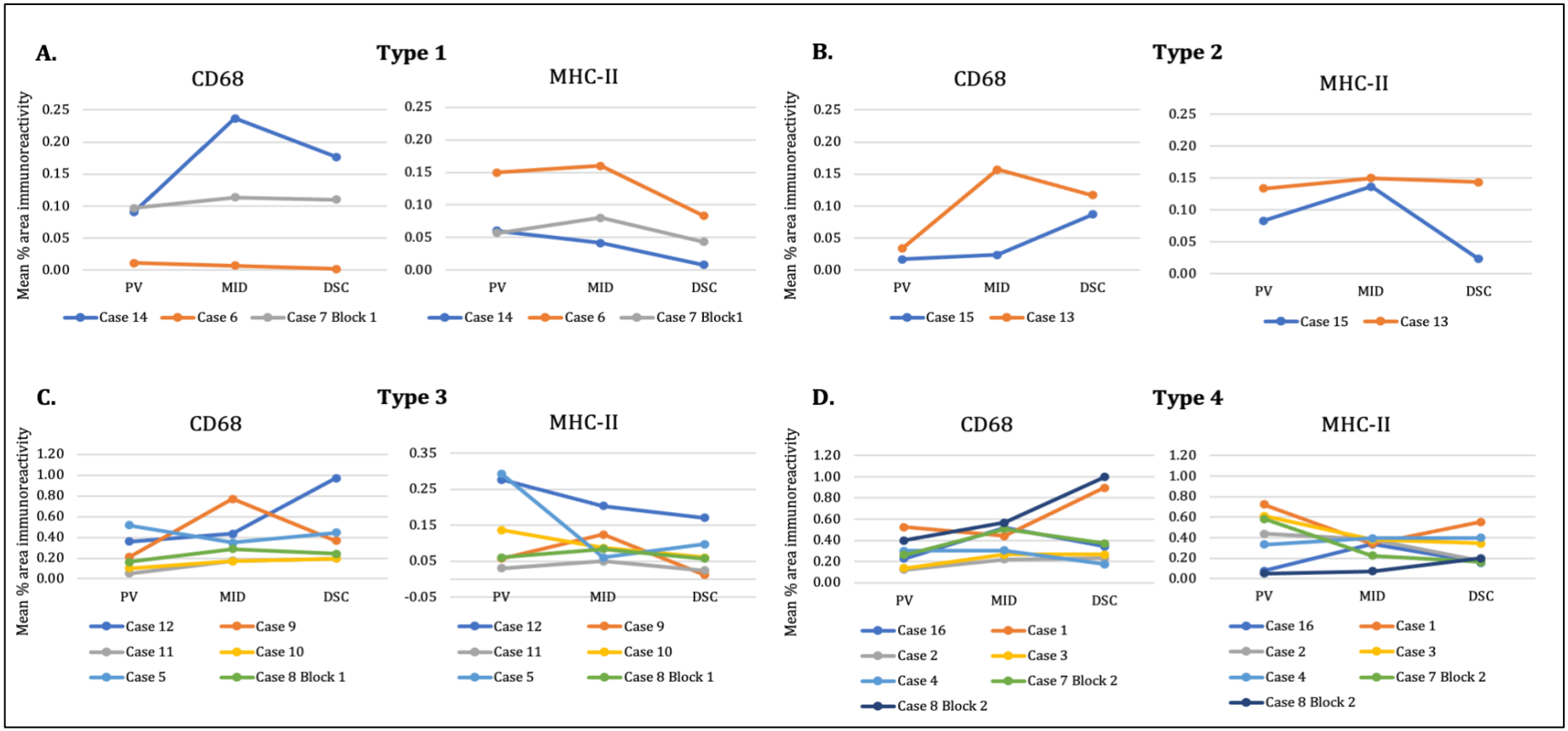

Figure 2.8 Immunoreactive profile of CD68 and MHC-II across the 4 confluent lesion subtypes

This figure illustrates the variation in the immunoreactive profile of CD68 and MHC-II across the periventricular, mid and deep subcortical regions of the 4 confluent lesion subtypes.

2.4 Discussion

Large confluent lesions, which encompass both the periventricular and deep subcortical regions (Barkhof & Scheltens, 2006), are clinically relevant and are associated with a greater risk of developing dementia (Schmidt *et al.*, 2002; Ovbiagele & Saver, 2006). Multiple radiological studies have mainly focussed on the growth and progression of these lesions in patient cohorts but, to date, histological studies have been limited. Detailed characterisation of PVL and DSCL have shown that these types of WML are predominantly associated with differing microglial profiles: PVL contains higher levels of immune activated MHC-II$^+$ microglia while DSCL contains higher levels of CD68$^+$ microglia with a phagocytic phenotype (Simpson *et al.*, 2007a, 2007b; Murray *et al.*, 2012). Studies characterising the microglial profile of confluent white matter lesions are limited. The current study characterised the expression of CD68$^+$ and MHC-II$^+$ microglia of confluent lesions in the CFAS ageing population-representative neuropathology cohort, demonstrating that confluent lesions are not characterised by one predominant microglial phenotype, instead 4 distinct lesion types were identified.

Longitudinal radiological studies of an ageing community-dwelling cohort to assess white matter hyperintensities have shown that early confluent and confluent lesions progress during ageing (Schmidt *et al.*, 2003). Patients with lacunes are at greater risk of developing confluent WMH and deep WMH (Ghaznawi *et al.*, 2019). While some radiological studies suggest that WML likely represent a continuum of pathology (Fazekas, 2014), other studies suggest distinct differences (Valdés

Hernández *et al.*, 2014; Kim *et al.*, 2008; Gouw *et al.*, 2011; Iordanishvili *et al.*, 2019). In patients with a history of stroke, WML have a propensity to extend from the periventricular region to the deep white matter, becoming more confluent (Valdés Hernández *et al.*, 2014). In contrast, studies suggest that DSCL have a tendency to become more confluent by extending to the periventricular region (Hase *et al.*, 2018).

Histological characterisation of PVL and DSCL has demonstrated that while these lesions share some similarities, including myelin loss and astrogliosis, their microglial phenotype differs (Simpson *et al.*, 2007a, 2007b; Schmidt *et al.*, 2011). Based on these differences, the current study assessed the microglial profile of confluent lesions to determine whether they represent distinct PVL and DSCL pathologies (MHC-II$^+$ in the periventricular region and CD68$^+$ in the deep subcortical region; type 1 lesion), the spread of pathology from the periventricular lesion (MHC-II$^+$ phenotype; type 2 lesion), the spread of pathology from the deep subcortical region (CD68$^+$ phenotype; type 3 lesion), or a mix of both pathologies (MHC-II$^+$ and CD68$^+$ throughout; type 4 lesion). Our findings demonstrate that confluent lesions are not characterised by one distinct microglial profile, rather they contain 4 profiles which suggests these lesions can arise as a spread of PVL, DSCL or both. While the small number of cases examined do not have enough power to perform robust statistical analysis of the frequency of these lesion types, this initial study suggests that most age-associated confluent lesions arise as a result of the spread of both PVL and DSCL: type 1 (5/18) and type 4 (8/18). This finding highlights that detection of confluent WML in patients by MRI does not enable the lesion type to be identified

and given that different mechanisms may underlie lesion pathogenesis, a potential treatment of patients may require different therapeutic strategies.

Previous histological characterisation studies have demonstrated that DSCL are associated with cerebral hypoperfusion giving rise to a hypoxic environment (Fernando *et al.*, 2006) and are characterised by the presence of increased numbers of CD68^{+} microglia with a phagocytic phenotype (Simpson *et al.*, 2007b). In contrast, PVL are associated with increased markers of BBB dysfunction and contain high levels of immune activated MHC II^{+} microglia with a ramified morphology (Simpson *et al.*, 2007a; Murray *et al.*, 2012). The current study demonstrates a range of confluent lesion subtypes which may reflect a spread of DSCL pathology, PVL lesion pathology or both, suggesting that a variety of mechanisms may be associated with the pathogenesis of confluent lesions.

2.5 Conclusion

In summary, the current study provides evidence that a proportion of confluent lesions display the microglial profile associated with PVL, containing MHC II^{+} microglia with a ramified morphology that extends into deep subcortical regions, suggesting confluent lesions arise as a spread of PVL. A proportion of confluent lesions display the microglial profile associated with DSCL, containing CD68^{+} microglia with an amoeboid morphology that extends into periventricular regions, suggesting confluent lesions arise as a spread of DSCL. A proportion of confluent lesions display a microglial profile suggesting a spread of pathology from both PVL

and DSCL: the periventricular region containing high levels of MHC-II$^+$ microglia and the deep subcortical region containing CD68$^+$ microglia. And a final proportion of cases contain a mix of both MHC II$^+$ and CD68$^+$ microglia throughout periventricular and deep subcortical regions.

Understanding how WML arise, particularly the role of microglia in the pathogenesis of WM pathology, may identify novel therapeutic treatments designed to modulate the microglial phenotype. Currently, much more is known about the microglial phenotype and transcriptomic profile of DSCL than PVL; therefore, the next chapter aims to interrogate the profile of PVL.

CHAPTER 3: CHARACTERISING THE TRANSCRIPTOMIC PROFILE OF PVL

3.1 Introduction

White matter lesions appear as hyperintensities on T2 weighted magnetic resonance images (MRI) (de Leeuw, 2001) and are classified anatomically into PVL and DSCL (Fazekas *et al.*, 1987; Wharton *et al.*, 2015). Using the radiological assessment of white matter hyperintensities by fluid-attenuated inversion recovery (FLAIR) MRI, Fazekas proposed the following rating system for periventricular white hyperintensities: absent (0); caps or pencil-thin lining (1); smooth halo (2); irregular periventricular hyperintensity extending into the deep white matter (3); and for deep white matter hyperintensities: absent (0); punctate (1); early confluent (2); and confluent (3) (Fazekas *et al.*, 1987). This scale was subsequently modified by Scheltens, and was designed based on the brain regions and divided into four areas: periventricular white matter hyperintensities (WMH), deep subcortical WMH, infratentorial WMH and basal ganglia WMH (Scheltens *et al.*, 1993), as shown in section 2.2.1.

WML have a propensity to extend to become more confluent, as discussed in the previous chapter. Several mechanisms underlying lesion formation have been proposed, including cerebral hypoperfusion, dysfunction of the BBB and neurodegeneration due to overlying cortical pathologies (Huang *et al.*, 2007; Wharton *et al.*, 2015; Li *et al.*, 2017; Moscoso *et al.*, 2020). However, the exact mechanism(s) underlying the formation of WML remain unknown.

Transcriptome profiling provides comprehensive information on all genome transcribed RNAs in a particular type of tissue or cell, under both physiological and

pathological conditions to identify the genes expressed in the selected tissue or cell (Casamassimi *et al.*, 2017). This technology also helps in identifying the alterations of the biological and genetic variations, which may underlie human diseases (Casamassimi *et al.*, 2017). Microarray and Ribonucleic acid-Sequencing (RNA-Seq) are the major techniques used for transcriptomic profiling (Nelson, 2001; Wang *et al.*, 2009). RNA-Seq refers to the quantification and detection of RNA. Initially, RNA is converted into cDNA fragments to build a cDNA library. These short transcripts are sequenced and are then analysed to recreate reads for a specific gene (Wang *et al.*, 2009; Ozsolak & Milos, 2011).

Microarray analysis, and in particular the Affymetrix GeneChip Human Genome U133 Plus 2.0 microarray used in the current study, measures the expression levels of an extensive number of genes, interrogating more than 47,000 transcripts representing over 20,000 genes (Zwemer *et al.*, 2014). Microarray technology can be used for the determination of crucial molecular pathways to elucidate the changes in gene expression underlying pathological conditions (Ding & Cantor, 2004) and can cover the whole genome or be specifically designed to identify the expression of a selected panel of genes (Cuccaro *et al.*, 2018). The basis of this technology involves a synthesis of complementary DNA from RNA by reverse transcription. This is followed by complementary cDNA fragmentation and labelling, which is then hybridised to the microarray chip for scanning (Lonergan *et al.*, 2007). The amount of labelled cDNA is reflected by the presence of signal intensity spots bound to the microarray chip. The intensity of these signals, reflecting mRNA expression, is measured and used for statistical comparisons between the selected

samples. Microarrays can be used to assess the transcriptomic profile of samples and identify differentially expressed genes.

Advancement in these gene expression technologies has enabled the identification of changes in gene expression and biological processes associated with multiple pathologies, including astrocytic transcriptomic profiling in the ageing brain (Simpson *et al.*, 2011) and multiple sclerosis (Waller *et al.*, 2016), in addition to the identification of blood-brain barrier changes in ageing populations (Goodall *et al.*, 2019).

Laser capture microdissection (LCM) is a robust method which enables precise extraction of a specific region of interest or cellular type from a tissue section under microscopic visualisation (Decarlo *et al.*, 2011). This technology has been used in conjunction with microarray to characterise gene expression changes in human post-mortem tissue and animal models to identify the transcriptomic gene expression changes in multiple neurological diseases and provide an insight into the mechanisms and the pathogenesis of these diseases.

Histological characterisation of deep subcortical white matter lesions in human post-mortem studies has shown they are associated with an increased expression of multiple hypoxia-related molecules, suggesting an increase in vascular insufficiency together with hypoperfusion are the primary underlying mechanism for the formation of these lesions (Fernando *et al.*, 2006). Transcriptomic profiling of these lesions using a combined LCM and microarray approach confirms the association of

these lesions with an increased expression of hypoxia-related genes together with the dysregulation of immune-regulatory genes, including those associated with antigen processing and presentation, phagocytosis and signalling pathways associated with pro-inflammatory cytokines (Simpson *et al.*, 2009).

3.1.1 Transcriptomic profiling of PVL

While transcriptomic profiling of LCM-ed DSCL has been employed to determine their gene expression signature, to date, no comparable studies have characterised the transcriptome of established PVL. Therefore, the work in this chapter will test the hypothesis that microglia within PVL adapt a neurotoxic M1 phenotype.

Specifically, this chapter aims to

1. Characterise the gene expression profile of age-associated PVL and identify significant changes in biologically relevant functional groups and pathways using DAVID.
2. Perform bioinformatics analysis using EnrichR to focus on the microglial-associated gene expression changes
3. Perform computational microglial deconvolution of the bioinformatics datasets to identify microglial-specific transcriptomic changes.

3.2 Materials and methods

3.2.1 Identification of PVL and control periventricular white matter

MRI analysis of formalin-fixed post-mortem tissue obtained from the CFAS neuropathology cohort was employed to identify PVL and scored by consultant radiologists using a modified Schelten's rating (refer to section 2.2.1). PVL were scored between 0 to 3: where 0 represents an absence of white matter hyperintensities; 1 represents a PVL ≤ 5mm; 2 represents smooth halo PVL between 6-10 mm with regular margins; and 3 represents an irregular periventricular halo of ≥ 10mm. All PVL used in the current project were scored 3 on the Schelten's rating scale (Scheltens *et al.*, 1993).

Frozen periventricular white matter was obtained from the CFAS neuropathology cohort (Table 3-1), following ethical approval (Appendix I). Using MRI of the formalin-fixed hemisphere to guide sampling of the contralateral snap-frozen hemisphere, all periventricular sampled blocks were initially stained with haematoxylin and eosin (H&E) and luxol fast blue (LFB) to assess their basic histology.

Briefly, 10 μm sections were warmed to room temperature (RT) for 5 min, fixed in ice-cold acetone at 4°C for 10min, and air-dried before staining with either H&E or LFB. For H&E, sections were immersed in Harris haematoxylin (CellPath Ltd, Powys, UK) for 2 minutes, washed briefly in tap water, differentiated in 1% acid alcohol,

Table 3-1 Cohort demographics

	Case number	PV MRI Rating	DSC MRI Rating	Age (y)	Gender	PMD (h)	pH
Control	**Control 1**	0	0	89	F	24	7.07
	Control 2	0	0	73	M	23	6.85
	Control 3	0	0	89	F	12	6.00
	Control 4	0	0	84	F	6	6.68
	Control 5	0	0	85	F	N/A	7.02
	Control 6	0	0	71	F	8	6.46
	Control 7	0	0	89	F	6	6.82
	Control 8	0	0	95	M	N/A	6.68
	Control 9	0	0	74	F	5	6.30
	Control 10	0	0	71	M	16	6.38
	Control 11	0	0	78	F	17	6.84
	Control12	0	0	98	M	37	6.76
Pre-lesion	**Prelesion 1**	0	0	70	F	42	6.80
	Prelesion 2	0	0	84	M	10	N/A
	Prelesion 3	0	0	76	M	7	7.05
	Prelesion 4	0	0	80	M	16	6.56
PVL	**Lesion 1**	3	0	90	M	N/A	5.30
	Lesion 2	3	3	95	F	24	6.29
	Lesion 3	3	3	88	F	18	6.09
	Lesion 4	3	5	89	F	7	6.48
	Lesion 5	3	0	85	F	32	6.56
	Lesion 6	3	0	90	M	32	6.36
	Lesion 7	3	3	85	M	72	6.57

PV: Periventricular; DSC: Deep Subcortical; PVL: Periventricular Lesion; PMD: Post-Mortem Delay; M: male; F: female.

before being rinsed in tap water. Sections were immersed in Scott's tap water to blue for 2 min before further rinsing in tap water. After that, sections were immersed in 1% eosin (CellPath Ltd, Powys, UK) for 5 minutes before washing briefly in tap water and dehydrated through a graded series of alcohols (70%, 95%, absolute [x2]), cleared in xylene, permanently mounted in distyrene plasticizer xylene (DPX) (Leica Biosystems), and dried in an oven overnight.

For LFB, sections were fixed in acetone as detailed above and immersed in luxol fast blue (0.1% of LFB – 0.5g Luxol fast blue powder (Fischer, UK) and 2.5 ml of acetic acid in 500 ml of 95% ethanol) pre-heated to 60°C for two hours. Sections were washed in 70% alcohol for 15 seconds before washing in tap water. Differentiation was performed by using freshly prepared 0.5% lithium carbonate (0.25g lithium carbonate was dissolved in 500ml of dH_2O) for 30 seconds which was then continued in 95% alcohol. Afterwards, sections were rinsed in tap water followed by dehydration through a graded series of alcohols, before being cleared in xylene and permanently mounted in DPX.

3.2.2 Immunohistochemistry (IHC)

3.2.2.1 Immunostaining of MHC-II and PLP

Frozen sections (10 µm) were prepared on a cryostat (Leica, UK) and collected onto charged glass slides. Sections were warmed to room temperature for 5 min before fixing them in ice-cold acetone for 10 minutes prior to IHC using the ABC-HRP technique and Vectastain Elite kit (Vector Laboratories, UK) with DAB (Vector

Laboratories, UK) as substrate (refer to section 2.2.3 for full details). Antibody details are shown in Table 3-2.

3.2.3 Analysis of frozen PVL samples

Immunostaining enabled the histological characterisation of the periventricular region of interest identified by the MRI scans, thereby confirming whether a PVL was present or absent. The histologically stained frozen sections from each sampled case were assessed by an experienced clinical neuropathologist (SBW) blind to any data or MRI score using a light microscope to locate the periventricular region which was then classified as either lesional or non-lesional. H&E and LFB stained samples were analysed to locate the periventricular region within the tissue sections and for myelin attenuation, respectively. Immunostaining for PLP was used in addition to LFB to assess myelin integrity. In addition, MHC II used to visualise and assess the presence of immune activated microglia within the periventricular white matter. While four cases were radiologically classified as control (rated 0 in the PV and DSC regions on MRI scans), these samples were histologically characterised by intact myelin (LFB staining) but contained high levels of immune activated microglia (MHC-II) and were classified as “pre-lesional”.

Table 3-2 Antibody source and dilutions

Antibody	Dilution	Isotype	Source
MHC II (HLA-DR)	1:20	Mouse, IgG	Dako, UK
PLP	1:800	Mouse, IgG	Bio-Rad, UK

PLP: Proteolipid lipoprotein.

3.2.4 RNA extraction

3.2.4.1 Trizol RNA isolation prior to LCM

RNA analysis pre-LCM was performed in all cases. Five frozen sections (20µm) were prepared using a cryostat (CM3050S, Leica Microsystems, Milton Keynes, UK) and placed into a sterile 1.5 ml Eppendorf tube. Sections were lysed in 1000 µl of Trizol (Life Technologies Inc, UK) and homogenised using a handheld homogeniser (Argos Technologies, London, UK). 200 µl of chloroform (Fisher Scientific, UK) was added and vigorously vortexed for 5 seconds before incubation for 3 minutes at RT. The samples were centrifuged (Sigma centrifuges, UK) at 12000g for 15 minutes at 4°C. The upper aqueous phase was transferred into a new sterile 1.5 ml Eppendorf tube before the addition of 500 µl of isopropanol (Fisher Scientific, Loughborough, UK) and incubated at RT for 10 minutes. The sample was centrifuged at 12000g for 10 minutes at 4°C. The supernatant was discarded before the RNA pellet was re-suspended in 1000 µl of 75% EtOH and vortexed for 5 seconds before further centrifugation at 7500g for 5 minutes at 4°C. The supernatant was removed, and pellet air-dried for 10 minutes at RT. The pellet was re-suspended in 15 µl RNase-free water and incubated for 10 minutes at 55°C. The sample was stored at -80°C until required.

3.2.4.2 Assessing the quality and integrity of RNA

Extracted RNA was assessed for quantity using the Nanodrop 1000 Spectrophotometer (Labtech International, Uckfield, UK). Both the RNA integrity (RIN) and the RNA quality were determined using a PicoChip in an Agilent 2100

Bioanalyser (Agilent, UK). The RIN number is a range from 1 to 10 where a RIN of 10 indicates fully intact RNA, and a RIN of 1 indicates severely degraded RNA.

3.2.4.3 Laser capture microdissection (LCM) of periventricular white matter

Five periventricular white matter frozen sections (10μm) were freshly prepared and collected onto uncharged sterile glass slides (Leica, UK). Sections were warmed to RT, fixed in ice-cold acetone (Fisher Scientific, UK) for 3 minutes, and stained with Toluidine blue for 30 seconds. Sections were rinsed in diethylpyrocarbonate (DEPC) water and dehydrated using a graded series of ethanol (70%, 95%, and 100%) for ~30s each. Sections were cleared in xylene for 3 min before being placed in an air-flow hood for at least one hour prior to LCM. The periventricular areas were identified on histologically stained sections (obtained in section 3.2.3) and mapped onto the Toluidine Blue stained slides to guide LCM.

The periventricular region was isolated using a PixCell II laser-capture microdissection system (LCM) (Arcturus BioScience, Mountain View, CA, USA) and CapSure Macro Caps (Arcturus Engineering, Mountain View, CA, USA) (Figure 3.1). A 30 μm laser spot size was used to capture the periventricular area, using a pulse power of 65-90 mW. Following isolation of periventricular region with several laser pulses, the film was carefully removed from the cap using sterile forceps and placed in a sterile 0.2 ml Eppendorf tube, covered with 50 μl of extraction buffer and stored at -80°C.

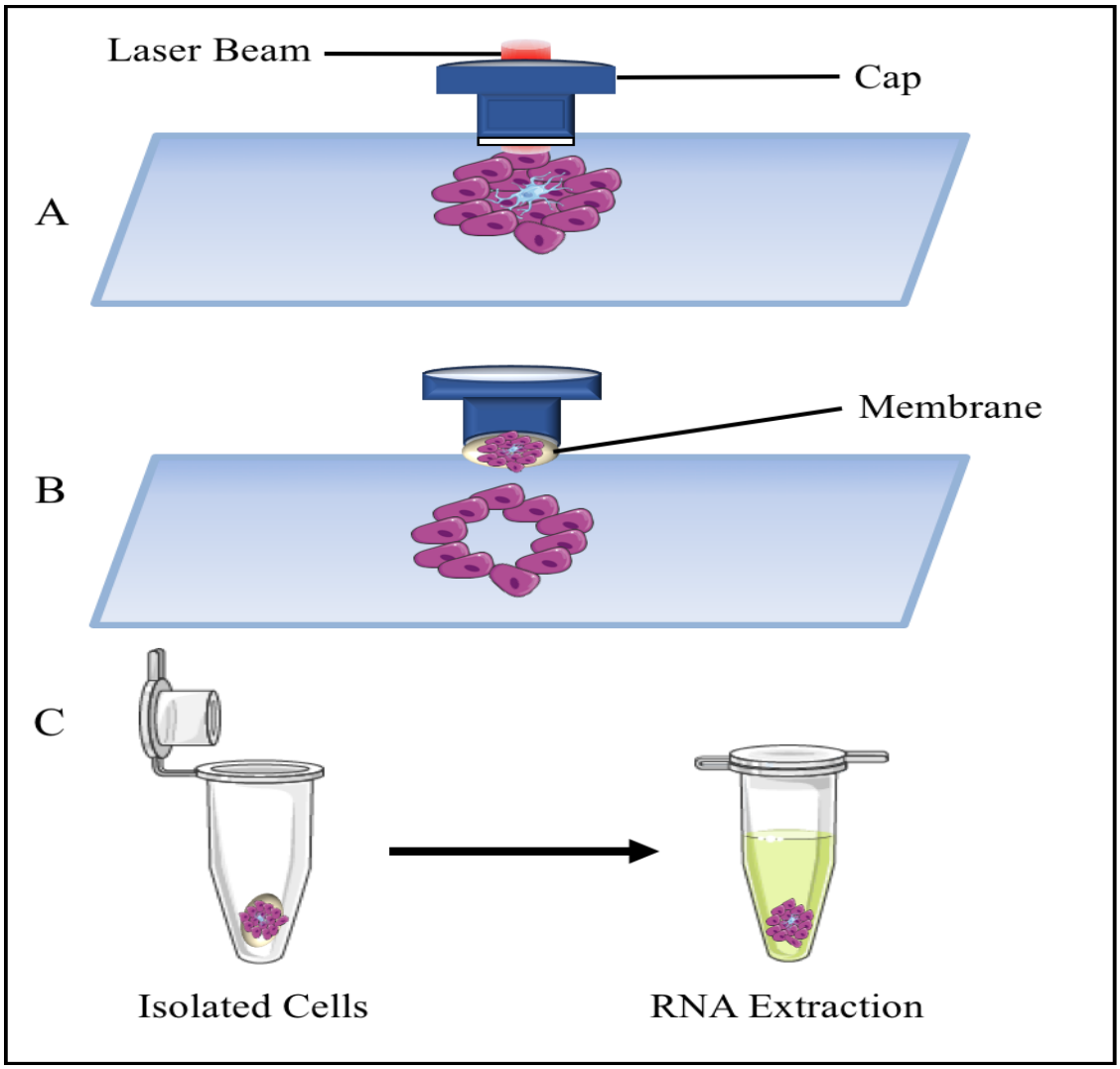

Figure 3.1 Laser Capture Microdissection

The mechanism of laser capture microdissection in isolating a region of interest from a tissue section. (A) The laser beam is targeted to the periventricular region. (B) The region of interest is micro-dissected from the tissue. (C) The film from the cap containing the isolated region of interest is transferred to a sterile Eppendorf for RNA extraction.

3.2.5 RNA extraction of LCM-ed material

RNA isolation was performed using the Arcturus Pico Pure RNA isolation kit (Life Technologies, (Arcturus, Applied Biosystems, USA). The film containing the LCM-ed tissue in 50 µl of extraction buffer was incubated at 42°C for 30 minutes in a thermal cycler. In the meantime, a column was prepared by adding 250 µl of conditioning buffer and incubated at RT for 5 minutes before being centrifuged at 13300g for 1 minute. The sample was mixed with 50 µl of 70% EtOH by pipetting and carefully added to the pre-conditioned column before centrifugation at 100g for 2 minutes, followed by 1 minute at 13300g. 100 µl of wash buffer 1 was added into the column and centrifuged at 8000g for 1 minute. 100 µl Wash buffer 2 was added and centrifuged at 8000g for 1 minute. This step was repeated with the centrifugation speed increased to 13300g for 1 minute. The column was transferred to a sterile 1.5 ml Eppendorf, and 11 µl of elution buffer was added to the membrane of the column and incubated at RT for 1 minute. The tube was centrifuged at 1000g and then 13300g for 1 minute each to elute the RNA. Extracted RNA samples were stored at -80 °C until required.

3.2.5.1 Assessing the quality and integrity of RNA

Extracted RNA was assessed for quantity using the Nanodrop 1000 Spectrophotometer (Labtech International, Uckfield, UK), and quality using the Agilent 2100 Bioanalyser (Agilent, UK), as detailed in Section 3.2.4.2.

3.2.6 Affymetrix GeneChip cDNA Microarray Hybridization

3.2.6.1 Poly-A RNA control preparation

Extracted RNA from the periventricular white matter samples were processed and amplified with the 3' IVT Pico Reagent kit (ThermoFisher Scientific, MA, USA), to prepare low input RNA samples for gene expression profiling. In summary, 50ng of total RNA per periventricular sample was mixed with 5µl of poly-A RNA control. This step was performed to monitor the process and contains probe sets from *B. subtilis* that are absent in eukaryotic samples. These 'spike-in' controls were set at different concentrations to enable monitoring of the labelling process efficiency.

3.2.6.2 First-strand cDNA synthesis

In order to make cDNA, RNA was converted to single-stranded cDNA (ss-cDNA) with a T7 promoter sequence at the 5' end by reverse transcription. The first-strand master mix was prepared by adding 40 µl of First-strand buffer to 10 µl of the first-strand enzyme in a nuclease-free tube and mixed thoroughly by gentle vortexing and centrifuging. Then on ice, 5 µl of the first-strand master mix was added to each sample and mixed thoroughly by gentle vortexing before incubation for 1 hr at 25 °C, followed by 1 hr at 42 °C, and finally 2 min at 4 °C in a thermal cycler. For clean-up, 2 µl of 3' IVT pico clean-up reagent was added to each sample and mixed thoroughly before incubation for 30 min at 37 °C, 10 min at 70 °C, and 2 min at 4 °C.

3.2.6.3 3' adaptor cDNA synthesis

3' adaptor was added to the ss-cDNA which acted as a template for ds-cDNA synthesis in the pre-IVT amplification reaction. The reaction uses DNA polymerase

and RNase H to break down the RNA strand and synthesise ss-cDNA with a 3' adaptor. On ice, the 3' adaptor master mix was made by adding 70 µl of 3' adaptor buffer to 10 µl of 3' adaptor enzyme in a nuclease-free tube, vortexed and centrifuged before adding 8 µl of the 3' master mix to each of the first strand cDNA samples. Afterwards, samples were vortexed and centrifuged before incubation in a thermal cycler for 15 minutes at 15 °C, then 15 minutes at 35 °C, 10 minutes at 70 °C and for 2 minutes at 4 °C. Tubes were centrifuged briefly to collect the samples at the bottom of the tube.

3.2.6.4 Double-strand cDNA synthesis

In this step, ss-cDNA is converted to ds-cDNA which acts as a template for *in vitro* transcription (IVT). This reaction uses Taq DNA polymerase and adaptor-specific primers to synthesise and pre-amplify ds-cDNA. The pre-IVT master mix was prepared by adding 290 µl of IVT Pico PCR buffer with 10 µl of IVT Pico PCR enzyme to the sample in a nuclease-free tube and mixed thoroughly by vortexing, followed by centrifugation. Then 30 µl of the mix was added to each 3' adaptor cDNA samples, vortexed and centrifuged before incubating for 2 minutes at 4 °C, for 9 cycles of 30 seconds at 94 °C and 5 minutes at 70 °C. Samples were centrifuged to collect ds-cDNA at the bottom of the tube.

3.2.6.5 Preparation of complementary RNA by in vitro transcription

In vitro transcription (IVT) of the ds-cDNA template using a T7 RNA polymerase was performed to synthesise antisense RNA (complementary RNA, cRNA). The IVT master mix was made by adding 240 µl of IVT buffer to 60 µl of IVT enzyme, mixed

thoroughly and centrifuged briefly at room temperature. 30 µl of the mix was added to each sample of ds-cDNA before incubation in a thermal cycler for 14 hours at 40 °C and kept at 4 °C.

Purification was performed to remove enzymes, salt, unincorporated nucleotides and inorganic phosphates. In a well of a round bottom plate, 80 µl of each cRNA sample was mixed with 140 µl of magnetic purification beads and gently pipetted up and down 10 times before being incubated for 10-minutes. The plate was moved to a magnetic stand to capture the purification beads for 5 minutes. The supernatant was carefully removed without disturbing the purification beads. Washing of the purification beads was carried out using 200 µl of freshly prepared 80% ethanol and repeated three times to enhance purification of cRNA, before air-drying. Next, cRNA was eluted by adding 27 µl of pre-heated nuclease free-water (65 °C) and incubated for 1 minute before pipetting up and down 10 times. The plate was moved to a magnetic stand for approximately 5 minutes and the supernatant, which contains the eluted cRNA, was transferred to a nuclease-free tube. The quantity of cRNA was assessed on the Nanodrop™ 1000 Spectrophotometer (ThermoFisher Scientific, MA, USA).

3.2.6.6 Second cycle single-stranded cDNA synthesis

Purified cRNA was reverse transcribed to synthesise sense-strand cDNA using 2nd-cycle primers. On ice, 16 µl of cRNA was added to 4 µl of 2nd cycle primers which were mixed before incubating for 5 minutes at 70 °C, followed by 5 minutes at 25 °C and 2 minutes at 4 °C. A 2nd cycle master mix was made by adding 8 µl of 2nd cycle

ss-cDNA buffer and 4 µl of 2nd cycle ss-cDNA enzyme. Both components were mixed thoroughly before centrifuging and incubated for 10 minutes at 25 °C for 90 minutes, followed by 70 °C for 10 minutes and 2 minutes at 4 °C.

3.2.6.7 Hydrolysis of RNA using RNase H

In this step, RNase H hydrolyses the cRNA template to be removed from the ss-cDNA. On ice, 4 µl of RNase H was added to each 2nd-cycle ss-cDNA sample and mixed thoroughly by vortexing and briefly centrifuged to collect the reaction at the bottom of the tube. The samples were incubated for 25 minutes at 37 °C, followed by 5 minutes at 95 °C and finally for 2 minutes at 4 °C. Following this, 11 µl of nuclease-free water was added to each sample for a final reaction volume of 55 µl.

3.2.6.8 Purification of ds-cDNA

Following hydrolysis, 2nd cycle ss-cDNA is purified to remove salts, enzymes and unincorporated dNTPs. In a well of a round bottom plate, 100 µl of purification beads were added to bind to ss-cDNA. The plate was moved to a magnetic stand to capture the purification beads for 5 minutes. The supernatant was removed carefully without disturbing the purification beads. Washing of the purification beads was carried out using 200 µl of 80% ethanol and repeated three times to enhance purification of ss-cDNA before air-drying. Next, ss-cDNA was eluted by adding 27 µl of pre-heated nuclease free-water (65 °C) and incubated for 1 minute before pipetting up and down 10 times. The plate was moved to a magnetic stand for approximately 5 minutes and the supernatant, which contains the eluted cRNA, was transferred to a nuclease-free tube.

3.2.6.9 ds-cDNA fragmentation and labelling

Purified ds-cDNA was fragmented using uracil-DNA glycosylase (UDG) and apurinic/apyrimidinic endonuclease 1 (APE1) enzymes. The fragmented cDNA was labelled by terminal deoxynucleotidyl transferase (TdT) using DNA labelling reagent provided with the kit, which was covalently linked to biotin. In this procedure, 5.5 µg of ds-cDNA was added to 0.2ml RNase free tube, and RNase free dH2O was added to make a final volume of 46µl. Fragmentation and Labelling Master Mix was prepared in a nuclease-free tube by adding 12µl of the 3' IVT Pico Fragmentation and Labelling Buffer with 2µl of the 3' IVT Pico Fragmentation and Labelling Enzyme per reaction and mixed thoroughly before adding the master mix to each (46µl) purified ds-cDNA sample and incubated for 1 hour at 37 °C, for 2 minutes at 93 °C and finally 2 minutes at 4 °C. The Agilent 2100 Bioanalyzer (Agilent, UK) was used to ensure that fragmentation was successful (Figure 3.2).

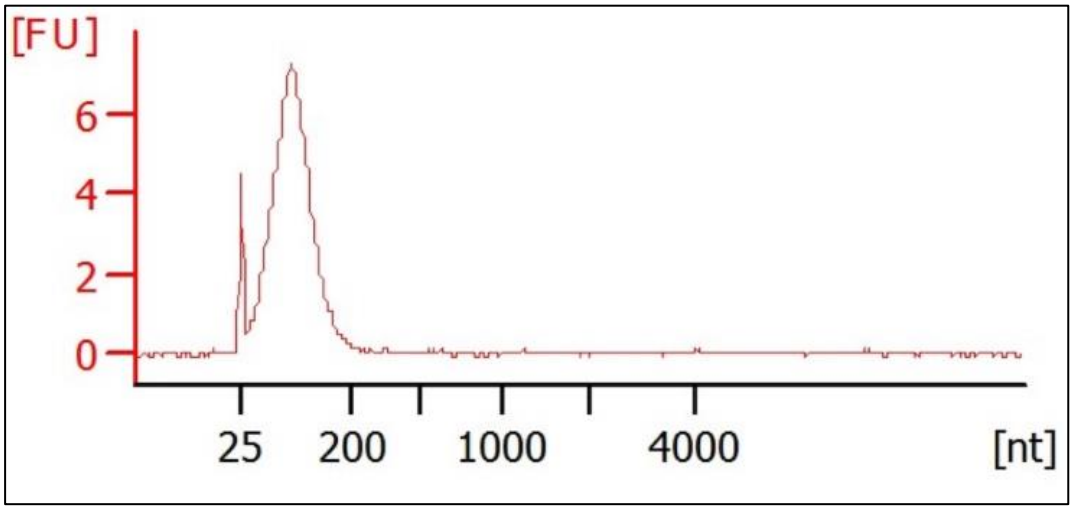

Figure 3.2 Assessment of fragmented ds-cDNA

The Agilent 2100 Bioanalyser was used to assess fragmentation of ds-cDNA. The fragmentation band lies with the size of 40 and 70 nucleotides, with a slight peak shift to the larger number of nucleotides, which is indicative of successful fragmentation. (FU: fluorescence unit).

3.2.6.10 Array Hybridisation

In this procedure, fragmented and labelled ss-cDNA was hybridised to GeneChip® Human Genome U133 Plus 2 Arrays (ThermoFisher Scientific, MA, USA) using a GeneChip® Hybridisation wash and stain kit. Initially, the hybridisation master mix was prepared in a nuclease-free tube by combining pre-heated 20x hybridisation controls (BioB, BioC, BioD, Cre heated at 65 °C) with control Oligo B2, DMSO, 2x hybridisation mix and nuclease-free water (160 µl). The contents of the tubes were mixed thoroughly by gentle vortexing and centrifuged before adding 60 µl of ds-cDNA samples. The mix was incubated for 5 minutes at 99 °C, followed by 5 minutes at 45 °C, and centrifuged briefly. Samples were injected and hybridised to GeneChip® probe array cartridges and incubated in a hybridisation oven for 16 hours at 45 °C and 60 rpm. Next, the hybridisation cocktail mix was removed, and the arrays washed with wash buffer A and left to equilibrate at room temperature before staining with Affymetrix GeneChip® Command Console Fluidics Control (ThermoFisher Scientific, MA, USA). Scanning of the arrays was performed using a GeneChip® Scanner 3000, and the Affymetrix Expression Console generated the raw signal intensity values (CEL files).

3.2.7 Analysis of transcriptomic data

3.2.7.1 Analysis using transcriptome analysis console (TAC)

Microarray data were analysed using the Transcriptome Analysis Console (TAC) software version 4.1.1 (Affymetrix®, UK). TAC was also used to compare the gene expression profile of the 3 groups (control, “pre-lesion” and lesion). Genes were considered significantly differentially expressed if they showed a minimum fold

change ≥ +/-1.2 and p≤0.05. Qlucore Omics Explorer (version 3.0) software (Qlucore, Lund, Sweden) was used to visualise the distribution of the samples using Principal Component Analysis (PCA).

3.2.7.2 Analysis using DAVID

Transcriptomic datasets were analysed using the Database for Annotation Visualisation and Integrated Discovery (DAVID) version 6.8 (Huang *et al.*, 2009) which recognises the main changes in the gene expression associated with specific pathways and functional groups. Each functional cluster provided an enrichment score, where the higher the enrichment score, the more significant the finding. DAVID was employed to filter the annotated genes using the highest stringency setting to obtain high specificity and to minimise the rate of false-positive results.

3.2.7.3 Analysis using EnrichR

To elucidate microglial functions, we focussed on the top 1000 differentially expressed genes from each comparison group (lesion versus control, "pre-lesion" versus control and "pre-lesion" versus lesion). Genes were analysed using EnrichR, which aids clustering of the genes based on their similar functions (Chen *et al.*, 2013), mainly focussing on the top 10 enrichment score obtained from the top 1000 based on the following groups; KEGG, Panther and Gene Ontology (GO) biological process, which provides a detailed interpretation of functions and pathways for a large list of genes.

3.2.8 Computational deconvolution analysis of the data

Computational deconvolution of transcriptomic data was used to interrogate microglial functions within the periventricular white matter region (Avila Cobos *et al.*, 2018). Specific cell-type markers for activated and inactivated microglia were used based on single-cell mass cytometry of the Experimental Allergic Encephalomyelitis (EAE) mouse model (Ajami *et al.*, 2018). Here, a similar technique was used to identify (A) inactivated and (B) activated microglia to characterise microglial phenotypes in the non-lesional control, "pre-lesion" and lesional white matter groups. *BST2 (CD317)* was selected to assess the inactivated microglia, while *CD39 (ENTPD1), HLA-DRA, CD86, CD80, TIMD4, ITGAX, TREM2, CCR5, MRC1* and *CD274* were selected as activated microglial-representative genes as shown in Table 3-3.

GeneMania web interface was used to build an interaction network of the co-expressed genes to construct and generate a network of genes of interest. These data were mainly collected from the Gene Expression Omnibus (GEO) (Warde-Farley *et al.*, 2010; Barrett *et al.*, 2013). In GeneMania, a co-expression network category with default weighting methods was selected (20 maximum resultant genes and 10 maximum resultant attributes) to reduce undesirable data and to identify relevant pathways and co-localisation of gene networks which were then analysed using a dataset tool. As a final validation, co-expression networks were interrogated, which

Table 3-3 Microglial genes: Group A (inactivated) and Group B (activated)

	Gene symbol	Gene name
Group A	*CD317 (BST2)*	Bone marrow stromal cell antigen 2
Group B	*CD39 (ENTPD1)*	Ectonucleoside Triphosphate Diphosphohydrolase 1
	HLA-DRA	Major Histocompatibility Complex, Class II, DR Alpha
	CD86	Cluster of differentiation 86
	CD80	Cluster of differentiation 80
	CD274	Cluster of differentiation 274
	TIMD4	T Cell Immunoglobulin and Mucin Domain Containing 4
	CD11C (ITGAX)	Integrin Subunit Alpha X
	TREM2	Triggering Receptor Expressed on Myeloid Cells 2
	CCR5	C-C chemokine receptor type 5
	MRC1	Mannose Receptor C-Type 1

focused on microglial subtypes associated with human CNS cell-types using an independent dataset (http://www.brainrnaseq.org/) (Zhang *et al.*, 2016).

Candidate genes were interrogated in the raw microarray data to detect the expression of each gene in non-lesional control, "pre-lesion" and PVL. However, some genes were referenced by multiple probesets, so we aimed to combine probesets into a single value to be compared between the three categories. To achieve this, the mean of all probesets referenced by a single gene was calculated. Next, the standard deviation (SD) of each probeset mean value was calculated, as shown in Figure 3.3. However, for genes with two probesets, the lowest variability between both probesets, and the probeset with lower value of mean expression was selected. Once values generated for each gene in all three categories (Control, "Pre-lesion" and Lesion), the data were normalised to the non-lesional control category.

Candidate genes were analysed using DAVID to identify the changes in pathways and functional groups. Similarly, confirmation for the involvement of candidate genes in microglia was performed using EnrichR, mainly focussing on wikipathways and Jensen Tissue expression data, which uses four human transcriptomic datasets to cluster the gene-tissue association.

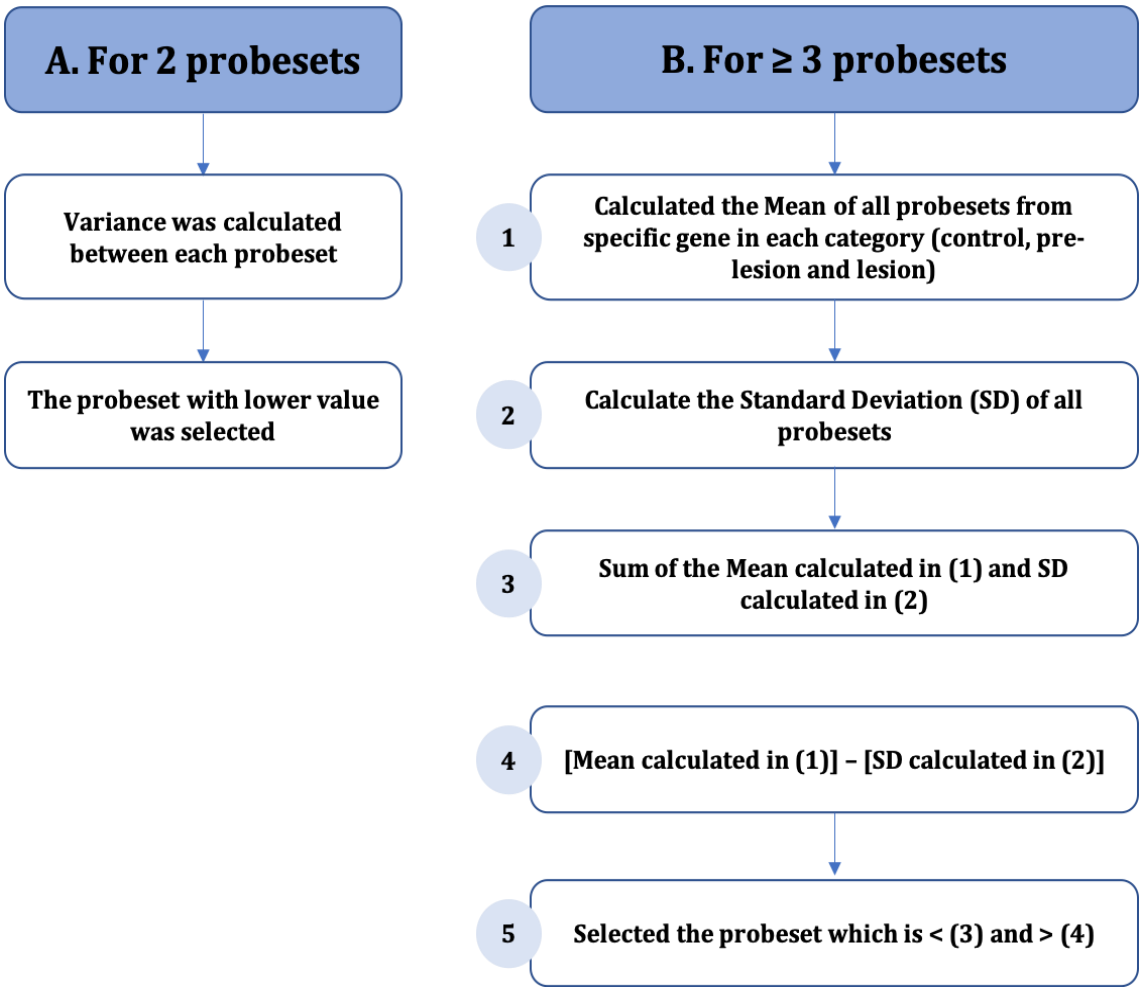

Figure 3.3 Multiple probesets calculation

Probesets were combined into a single value to be compared between the three categories for the genes referenced by multiple probesets. For genes with 2 probesets (A), the variance between both probesets was calculated and the lower value of mean expression was selected for comparison. However, in the case of 3 or more probesets referenced by a single gene (B), the mean for all probesets was calculated (1), followed by the calculation of SD (2). Next, the sum of both values was calculated (3). In order to identify the highest value of these probesets, the calculated SD was subtracted (2) from the mean calculated in (1). The probeset selected for comparison is the value less than < (3) and more than (>) (4).

3.3 Results

3.3.1 Histological characterisation of control WM, "pre-lesional" & PVL

3.3.1.1 Histological assessment of sampled periventricular WM

MRI of the formalin-fixed brain hemisphere was used to guide sampling of the contralateral frozen periventricular region, and histological characterisation performed to confirm the classification of the tissue as non-lesional control or PVL. In total, 28 frozen tissue blocks were sampled from 23 cases for histological characterisation and were classified into two major groups: non-lesional control and PVL. Non-lesional control cases showed an intact ependymal lining (Figure 3.4. A) with regular staining of myelin throughout the periventricular region (Figure 3.4. B). In contrast, PVL cases were characterised by the presence of pale H&E staining (Figure 3.4. D) and a reduction in LFB staining in the periventricular region, indicating myelin attenuation (Figure 3.4. E). In addition, variable histopathological changes of ependymal lining were noted: 5 PVL cases showed fully intact ependymal lining, whereas 4 cases revealed a partially denuded ependyma.

3.3.1.2 Demyelination in the periventricular region of the ageing brain

In addition to LFB staining, myelin attenuation was also confirmed by immunohistochemistry using a specific antibody against myelin proteolipid protein. All PLP-immunostained non-lesional control cases showed preserved myelin throughout the periventricular region (Figure 3.4. C). In contrast, demyelination, as identified by reduced staining for PLP, was a feature of all PVL cases.

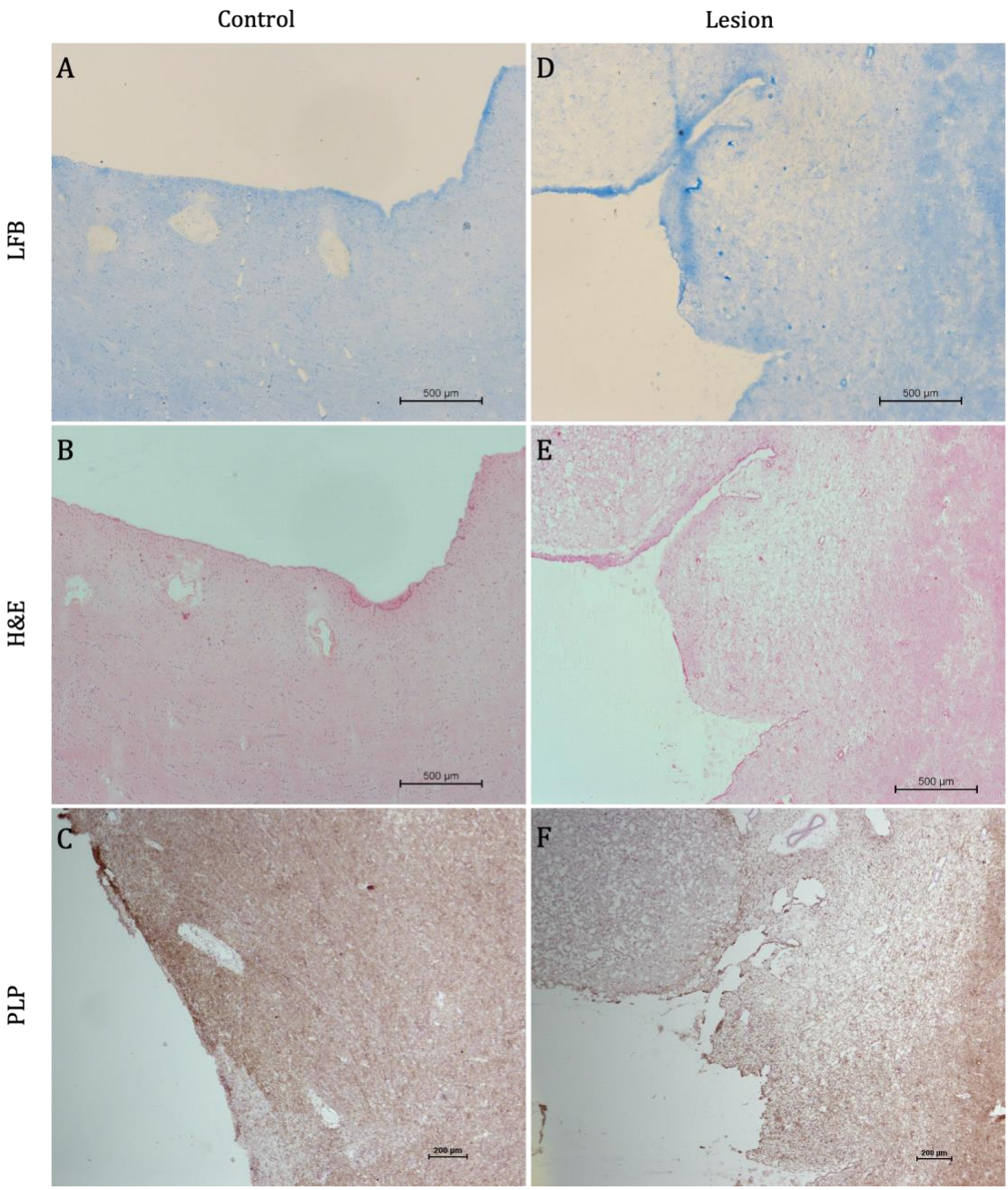

Figure 3.4 Histological characterisation of periventricular white matter

Luxol fast blue (LFB, A) and H&E staining (B) of radiologically normal-appearing white matter demonstrated a regular pattern of myelin staining across the periventricular region. In contrast, LFB (D) and H&E staining (E) of radiologically identified lesional cases displayed a band of periventricular demyelination. Proteolipid protein of non-lesional control samples showed a regular pattern of myelin staining across the periventricular region (C) In contrast, PVL samples showed severe demyelination (F). *Scale bar represents 500µm (A, B, D, E), and 200µm (C, F).*

Immunohistochemistry for PLP identified variation in the extent of demyelination within PVL ranging from a discrete band of demyelination beneath the ependymal layer to a larger extended region of periventricular demyelination (Figure 3.4. F).

3.3.1.3 MHC II

Activated microglia within the periventricular region were visualised using antibodies to MHC-II, which immunolabelled the microglial cell body and proximal processes. A range of microglial morphologies was observed in both lesional and non-lesional groups (Figure 3.5). These cells are sensitive to changes in the surrounding environment and react to disturbances in the homeostatic state by changing their phenotype (Nimmerjahn *et al.*, 2005; Chagas *et al.*, 2020). Microglia in non-lesional controls mainly displayed a ramified morphology with long processes extending from the cell body (Figure 3.5. A). However, the presence of microglial cells with an amoeboid morphology was also noted, where their processes were retracted, and the cell body enlarged. 16 cases of MRI-rated non-lesional control WM contained low levels of MHC II immunoreactive microglia throughout the PV region; however, 4 cases of MRI-rated non-lesional control WM contained high levels of MHC II expression. While the MRI and histological characterisation of this group indicated that there was no demyelination (Figure 3.6. C), the immunoreactive profile of MHC II suggested immune activation of microglia (Figure 3.5. B). Therefore, the control group was subsequently subdivided into non-lesional control (MRI rated control; low levels of MHC II immunoreactivity) and "pre-lesional" (MRI rated control; high levels of MHC II). 5 cases of MRI-rated PVL

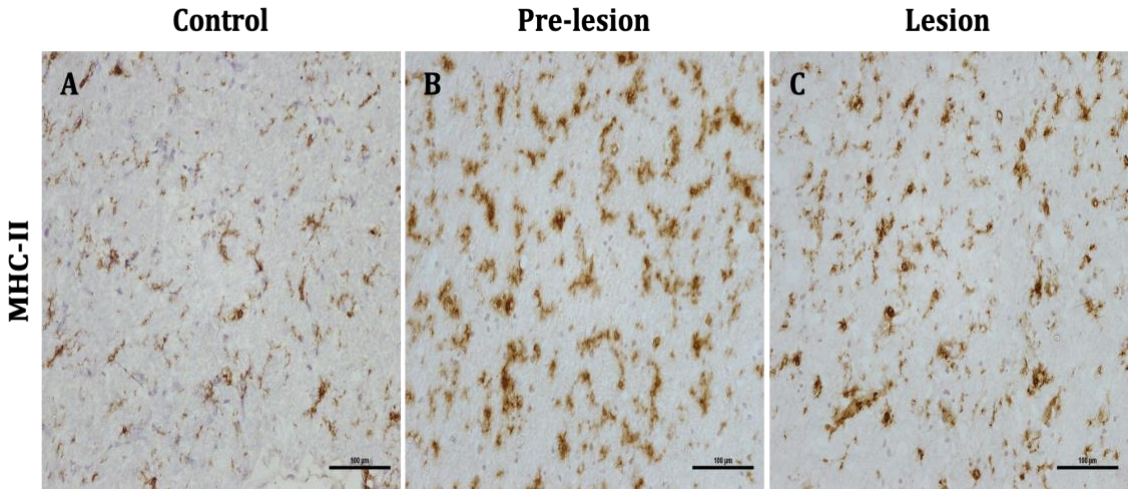

Figure 3.5 Patterns of MHC-II immunoreactivity detected in the periventricular region

A range of different microglial immune-profiles and morphologies were observed in the periventricular white matter samples. MHC II immunostaining of radiologically normal-appearing white matter identified low levels of ramified MHC-II^{+} microglia (A). However, "pre-lesion" (B) and PVL (C) samples were associated with high levels of MHC-II^{+} microglia. *Scale bar represents 100µm*.

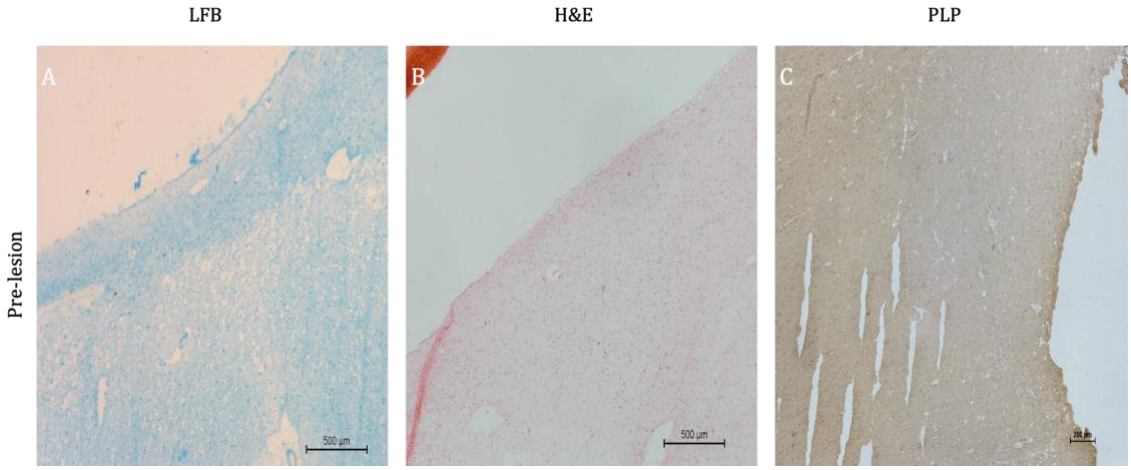

Figure 3.6 Histological characterisation of pre-lesional samples

Luxol fast blue (LFB, A) and H&E staining (B) of "pre-lesional" samples revealed similarity to the radiologically normal-appearing white matter, displaying a regular pattern of myelin staining across the periventricular region. Proteolipid protein of "pre-lesional" control samples showed a regular pattern of myelin staining across the periventricular region (C). *Scale bar represents 500µm (A, B) and 200µm (C).*

contained high levels of MHC II immunoreactive microglia, as shown in Figure 3.5.C.

Histological characterisation of "pre-lesional" samples revealed a similar pattern of staining for myelin compared to radiologically normal-appearing white matter, displaying preserved myelin throughout the periventricular region (Figure 3.6 A, C) with an intact ependymal lining (Figure 3.6 B).

3.3.2 Characterisation and isolation of periventricular white matter for gene expression analysis

3.3.2.1 RNA integrity from frozen post-mortem periventricular samples

Twenty-three cases were identified from the CFAS cohort to study the transcriptomic profile of the periventricular region. These samples were classified into lesional (7 cases) and non-lesional control groups (16 cases of which 12 were classified as non-lesional controls & 4 were classified as "pre-lesional" controls). RNA was extracted from all the samples, before and after LCM to assess the impact of the LCM procedure on the quality of the RNA obtained from the periventricular region. The RNA quality of the samples pre- and post-LCM is indicated in Table 3-4. Pre-LCM, the samples had an average RIN value of 2.764 (range 1.2 - 6.4) in controls, 3.1 (2.6 – 3.7) in "pre-lesion" and 3.68 (2.4 – 6) in PVL. A representative electropherogram of the pre-LCM profile is shown in Figure 3.7.

After assessing the pre-LCM RIN value, the entire periventricular region was isolated from the frozen post-mortem samples using LCM, and the RNA quantity and quality were assessed. On average, 6.062 ng/µl RNA was extracted from the

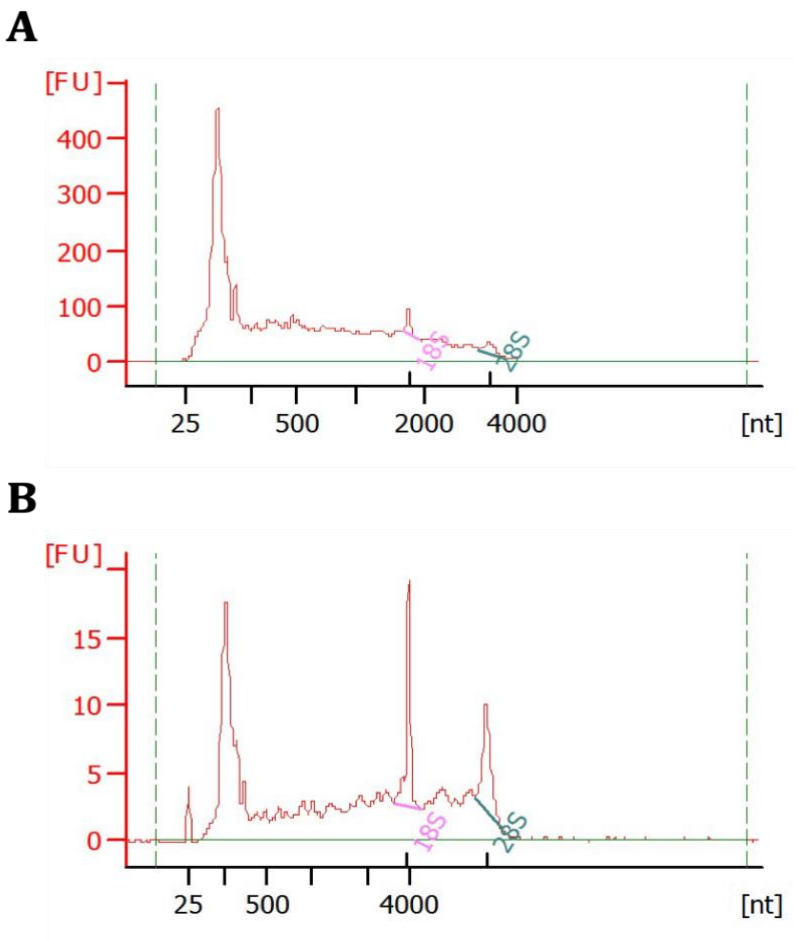

Figure 3.7 RNA integrity of Pre-LCMed RNA profile

Example of electropherogram profiles obtained from two different frozen post-mortem tissue prior to LCM with low (2.3) and (B) high (5.6) RIN values. Both peaks illustrated in the figures represent 18S and 28S ribosomal RNA. (*FU: fluorescence unit).*

Table 3-4 Initial concentrations of RNA in frozen post-mortem samples

Prior to LCM, RNA was extracted from the frozen post-mortem brain samples using TRIzol and the RNA quality assessed by Agilent 2100 Bioanalyser. Both the RNA quantity and quality were assessed post-LCM. Cases selected for downstream transcriptomic profiling are highlighted in green.

WM group	Case	Pre-LCM RIN	Post-LCM RIN	RNA concentration (ng/µl)
Control	**Control 1**	1.6	N/A	12.564
	Control 2	5.6	N/A	5.723
	Control 3	2.4	N/A	6.465
	Control 4	2.3	2.9	15.923
	Control 5	6.4	N/A	10.063
	Control 6	1.8	2.3	4.504
	Control 7	2.3	2.9	5.688
	Control 8	N/A	N/A	6.096
	Control 9	2.1	2.8	1.98
	Control 10	2.4	2.1	1.366
	Control 11	2.3	2	1.835
	Control 12	1.2	2.3	0.537
	Mean (range)	**2.764 (1.2 – 6.4)**	**2.471 (2 – 2.9)**	**6.062 (0.537 – 15.923)**
Lesion	**Lesion 1**	N/A	N/A	11.283
	Lesion 2	4.5	2.5	4.019
	Lesion 3	3	N/A	9.273
	Lesion 4	6	2.5	3.139
	Lesion 5	3.1	N/A	4.754
	Lesion 6	2.4	2.3	1.252
	Lesion 7	3.1	N/A	7.543
	Mean (range)	**3.683 (2.4 – 6)**	**2.433 (2.3 – 2.5)**	**5.895 (1.252 – 11.283)**
Pre-lesion	**Prelesion 1**	3.3	3	3.569
	Prelesion 2	3.7	1.4	15
	Prelesion 3	2.8	N/A	5.157
	Prelesion 4	2.6	N/A	6.834
	Mean (range)	**3.1 (2.6 – 3.7)**	**2.2 (1.4 – 3)**	**7.64 (3.569 – 15)**

periventricular region (range 0.54 – 15.9 ng/µl). Post-LCM, the RIN decreased in almost all cases to an average of 2.47 (2 – 2.9) in controls, 2.2 (1.4 – 3) in "pre-lesion" and 2.43 (2.3 – 2.5) in PVL. In 11 cases, no RIN was detectable (Table 3-4). However, while the RIN is a good indicator of RNA integrity, the RNA profile should also be considered, and in all cases (even those where a RIN was not available) the RNA profile indicated that the RNA extracted from the cases was indeed comparable and of suitable quality for downstream transcriptomic profiling. A representative electropherogram post-LCM profile is shown in Figure 3.8.

3.3.2.2 RNA preparation for microarray analysis

The gene expression profile of 7 non-lesional controls, 4 "pre-lesional" cases and 7 PVL was assessed (Table 3-4). Approximately 50ng of RNA per sample was used, and the yield of cRNA was measured with a NanoDrop 1000 after the purification of ss-cDNA, as shown in Table 3-5. Next, 16 µl of cRNA was reverse transcribed for the synthesis of ss-cDNA, and the yield measured using spectrophotometry, as shown in Table 3-6.

3.3.3 Microarray quality control measures

3.3.3.1 Labelling controls

Poly-A RNA spikes were used for labelling controls. These Spikes which derived from *Bacillus Subtilis* (*Dap, Thr, Phe, Lys*) are added to the RNA samples at different concentrations in the following order: *Lys*, *Phe*, *Thr* and *Dap* (1:100,000, 1:50,000, 1:25,000 and 1:6,667, respectively) in all samples. In our arrays, we had different

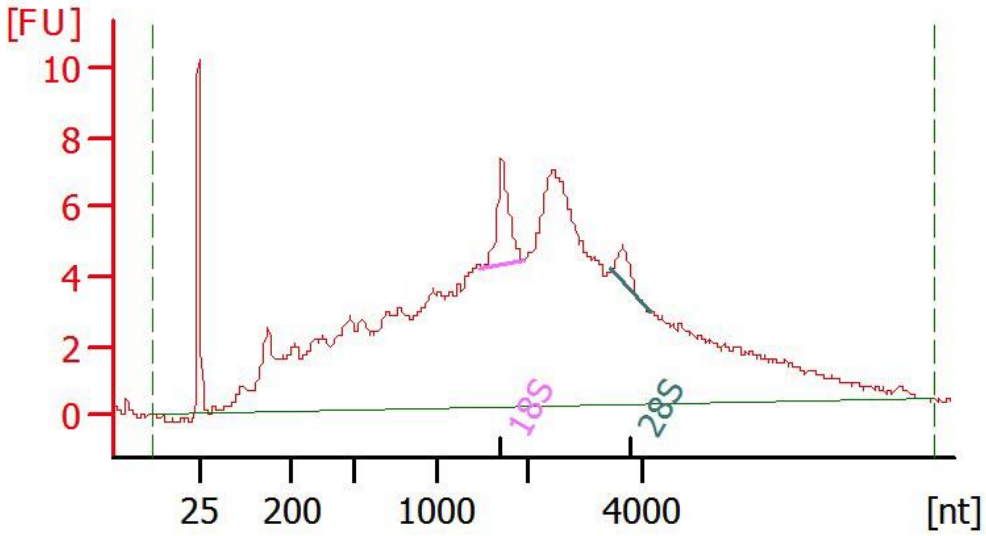

Figure 3.8 Post-LCM RNA

Representation of the electropherogram profile from LCM-ed periventricular white matter. (*FU: fluorescence unit).*

Table 3-5 Concentration of cRNA after ss-cDNA synthesis

Condition	Case	cRNA concentration (ng/µl)
Control	Control 1	3776
	Control 2	3820
	Control 3	3812
	Control 4	3073
	Control 5	3801
	Control 6	3357
	Control 7	3864
Lesion	Lesion 1	3926
	Lesion 2	3447
	Lesion 3	3875
	Lesion 4	3921
	Lesion 5	3938
	Lesion 6	4007
	Lesion 7	3725
Pre-lesion	Prelesion 1	3934
	Prelesion 2	3776
	Prelesion 3	3874
	Prelesion 4	3733
	Mean ± SD	**3758.83 ± 237.17**

Table 3-6 Concentration of ss-cDNA obtained after the second amplification cycle

Condition	Case	ss-cDNA concentration (ng/µl)
Control	Control 1	414
	Control 2	408
	Control 3	370
	Control 4	380
	Control 5	389
	Control 6	392
	Control 7	400
Lesion	Lesion 1	375
	Lesion 2	353
	Lesion 3	387
	Lesion 4	408
	Lesion 5	373
	Lesion 6	390
	Lesion 7	378
Pre-lesion	Prelesion 1	457
	Prelesion 2	392
	Prelesion 3	384
	Prelesion 4	350
	Mean ± SD	**388.8 ± 24.2**

patterns in the labelling efficiency for the Poly-A RNA controls. However, almost all of the samples showed an increasing pattern across our samples (Figure 3.9).

3.3.3.2 Hybridisation and signal quality

In this assessment, the eukaryotic hybridisation controls were added into the hybridisation mix, which composed of biotin-labelled cRNA transcripts from *E.Coli* (*BioB*, *bioC*, *bioD*) and the P1 bacteriophage (*Cre*) in a concentration of 1.5 pM, 5 pM, 25 pM and 100 pM, respectively. Analysed microarray signals for all hybridisation revealed an appropriate increasing of signal intensities in all samples from *BioB* to *Cre*, suggesting a good hybridisation efficiency across all samples, as shown in Figure 3.10.

3.3.3.3 Signal intensities across the arrays

Affymetrix Expression Console Software enables the assessment of signal intensities generated from arrays which can be plotted as a histogram. In our data, the signals from the arrays were comparable across all the samples, with some discrepancies between some samples, as shown in Figure 3.11.

Relative Log Expression (RLE) is a calculation method generated by MicroArray Suite (MAS) 5.0 software and is used for the comparison of signal intensity detected for each probeset in the arrays against the median signal value across all arrays. These data are represented as a plot to assess the spread of data across the samples. Our samples showed a similar spread of RLE in most of the arrays, as shown in Figure 3.12.

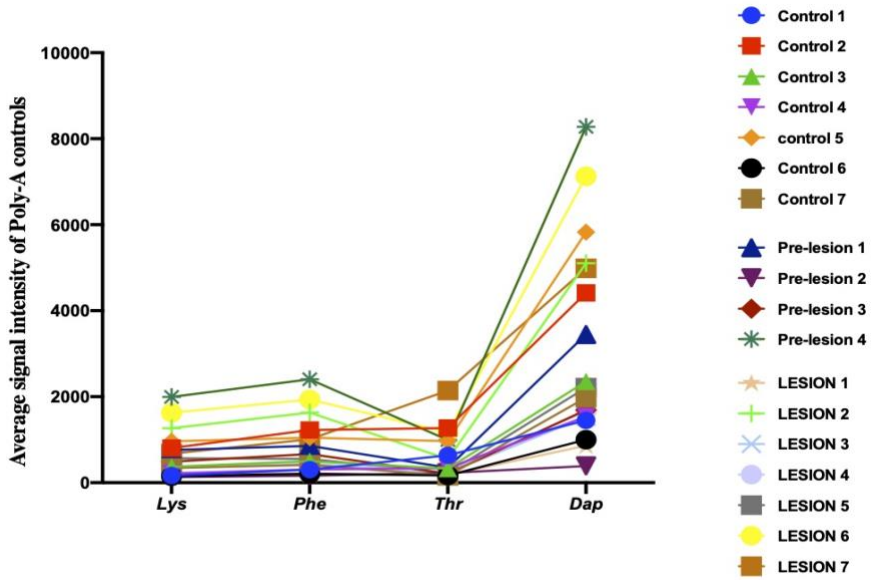

Figure 3.9 Poly-A RNA spike-in controls

Signal intensities plot depicting the mean of signal intensities of Poly-A controls (*Lys*, *Phe*, *Thr* and *Dap*) which were added to the 18 samples.

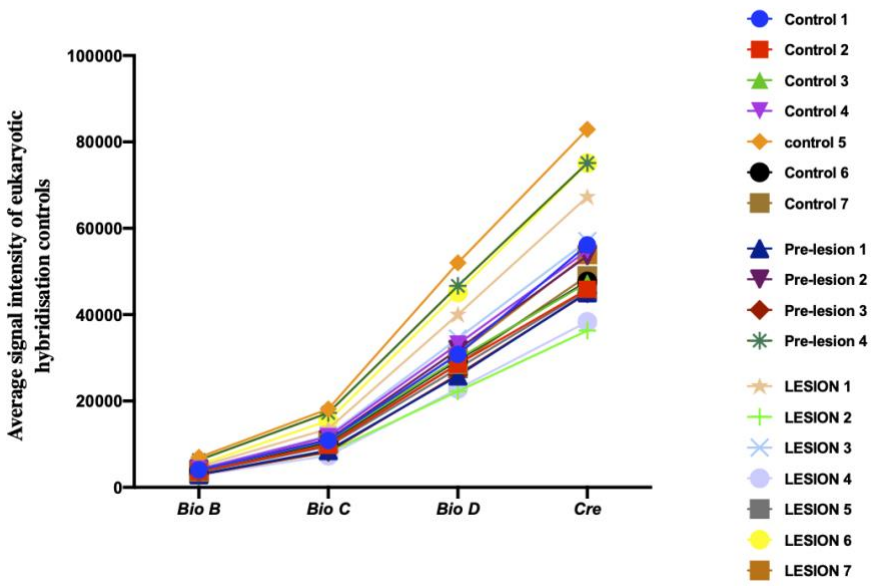

Figure 3.10 Eukaryotic hybridisation controls for control, pre-lesion and periventricular white matter lesion

This graph illustrated the mean signal intensity of hybridisation controls (*BioB*, *BioC*, *BioD*, and *Cre*), showing an appropriate increasing of signal intensities in control, "pre-lesion" and lesional samples.

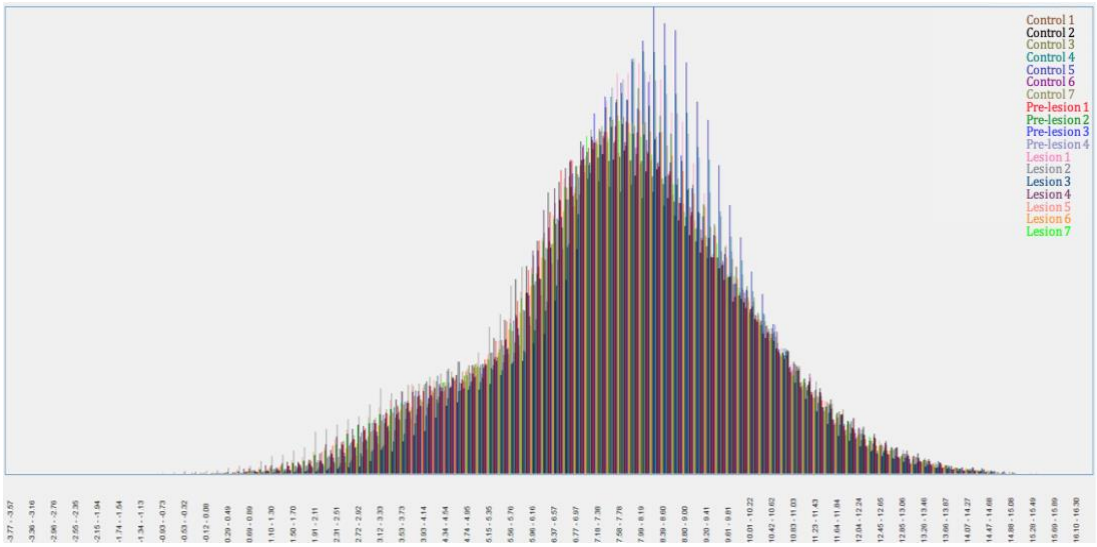

Figure 3.11 Signal intensities histogram for the periventricular arrays

Signal histogram illustrating the signal intensities of the probesets in the selected 18 samples. While 14 signals from the arrays were the same across all the samples, four samples showed higher signals.

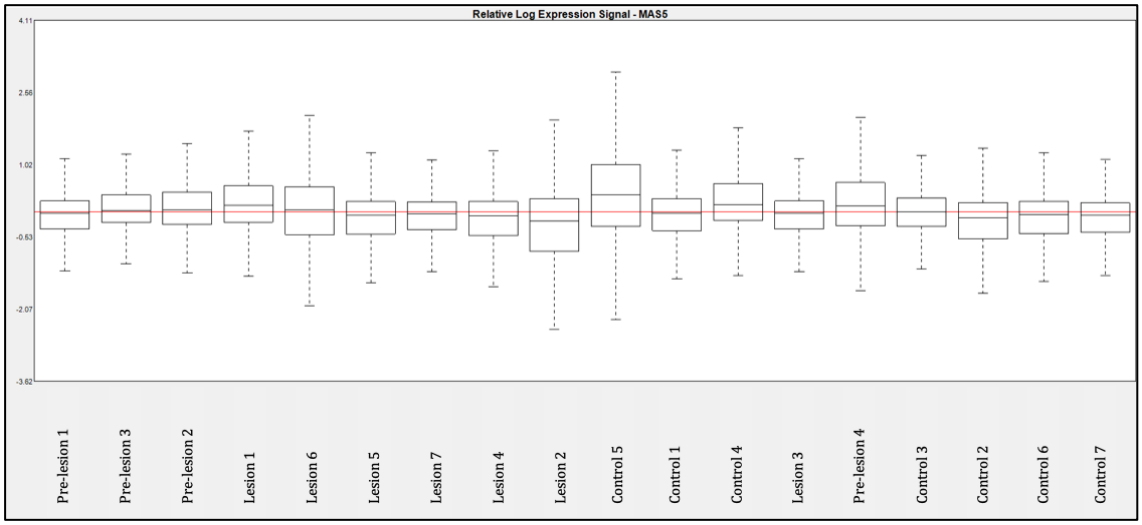

Figure 3.12 Relative log expression (RLE) box plots for the periventricular white matter arrays

Box plot representation of the median gene expression in all 18 arrays. The Y-axis represents the relative log expression signal for all the 18 samples (X-axis).

3.3.4 Microarray analysis

3.3.4.1 Transcriptomic analysis and comparison of the gene expression

Transcriptomic analysis of periventricular white matter was conducted using Human Genome U133 Plus 2.0 Arrays, which contain at least one probe for each gene and recognize more than 39,000 genes. Genes were considered significantly differentially expressed if they had a minimum fold change (FC) of ≥ 1.2 and a p-value ≤ 0.05. 2,256 genes were differentially expressed in PVL compared to non-lesional control (1,378 upregulated and 878 down-regulated) (Figure 3.13A); 2,398 genes significantly differentially expressed in "pre-lesional" control versus non-lesional control (1,527 upregulated and 871 down-regulated) (Figure 3.13B) and 2,649 genes were significantly differentially expressed in "pre-lesional" control compared to PVL (1,390 upregulated and 1,259 down-regulated) (Figure 3.13C). The microarray datasets are freely available at the Gene Expression Omnibus (GEO) public database (accession code GSE157363).

Qlucore Omics Explorer (version 3.0) software (Qlucore, Lund, Sweden) was used to identify the distribution of the samples and differences in the transcriptome of the periventricular cases. The principal component analysis plot confirmed that there were no sample outliers, and a distinct separation between the groups was observed (Figure 3.14).

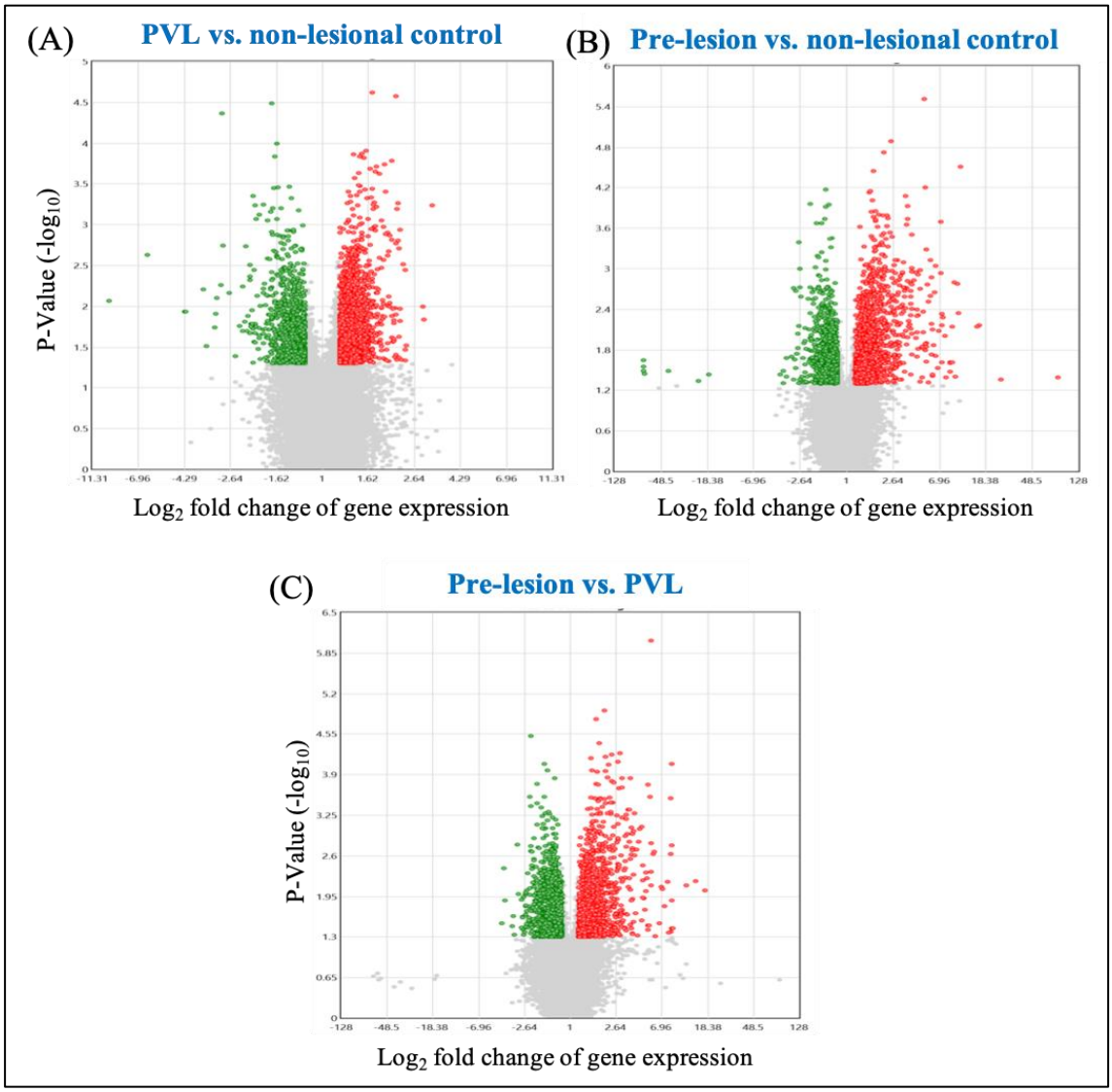

Figure 3.13 Volcano plot of differential gene expression

(A) Volcano plot representing the differentially expressed genes in PVL compared to non-lesional controls. A total of 2,256 genes were identified with 1,378 genes upregulated (red), whilst 878 genes were down-regulated (green). (B) In "pre-lesion" compared to non-lesional control, a total of 2,398 genes were identified with 1527 upregulated and 871 genes down-regulated. (C) In "pre-lesion" compared to PVL, a total of 2,649 genes were differentially expressed, with 1390 upregulated and 1259 down-regulated genes. The volcano plot was plotted using $\log_2$ (fold change) and the negative $\log_{10}$ p-value in the x and y-axes respectively. Each gene locus is represented by a dot (•). A fold change of ≤ 1.2 and a p-value ≤ 0.05 were set to identify the differentially expressed genes. Upregulated genes are indicated by a red dot, while down-regulated genes are indicated by a green dot.

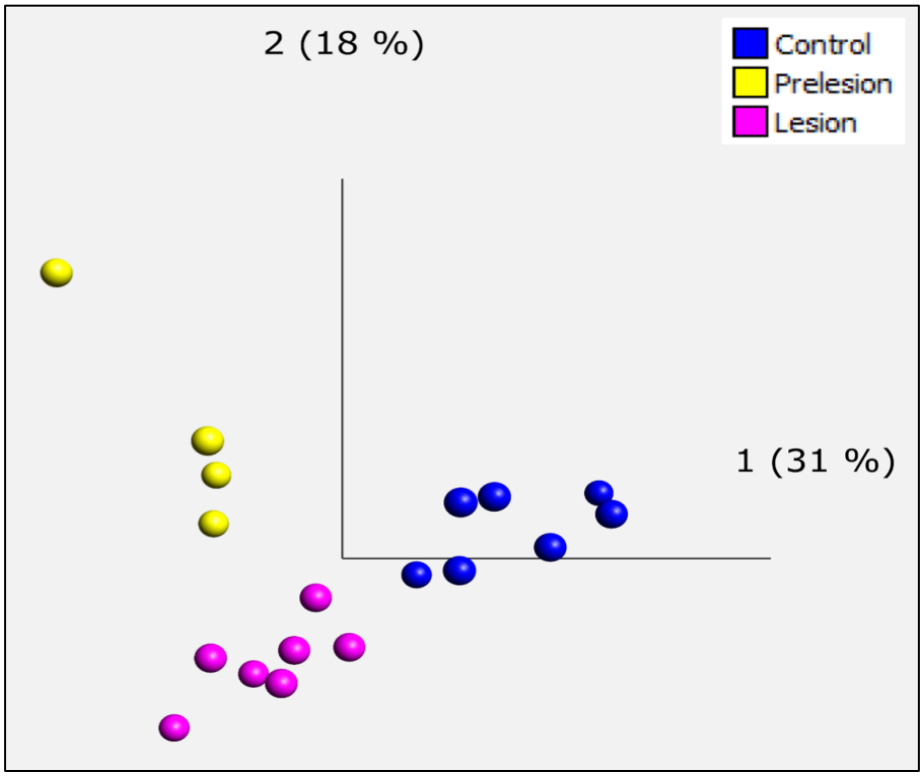

Figure 3.14 PCA Plot

The principal component analysis (PCA) plot of control (blue), "pre-lesion" (yellow) and PVL (pink) demonstrating a clear separation of differentially expressed genes between the three groups (control, "pre-lesion" and lesion).

3.3.4.2 Transcriptomic analysis of PVL reveals dysregulation of the immune response

Initially, the full list of probeset IDs of the significantly, differentially expressed genes was analysed by TAC software and imported into DAVID to identify altered functional groups and pathways. In addition, the list of up-and down-regulated genes was imported independently into DAVID for separate analysis. Using the highest stringency setting for functional clustering, the transcriptomic profile of the PVL was compared to the non-lesional control group (LvC). Functional annotation grouping analysis identified dysregulation of genes that were primarily associated with MHC class II receptor activity and antigen processing and presentation (enrichment score: 3.26), together with collagen IV (enrichment score: 1.52). Kyoto encyclopedia of genes and genomes (KEGG) pathway analysis in DAVID identified 53 significantly dysregulated pathways (see Appendix II for the full list of dysregulated pathways), including immune response-associated pathways (Table 3-7). In PVL, significant upregulation of multiple genes associated with phosphatidylinositol 3-kinase PI3K/AKT signalling were detected, including v-akt murine thymoma viral oncogene homolog 3 (*AKT3*) (probeset 219393_S_AT, FC= 1.33, p= 0.002), and retinoid X receptor alpha (*RXRA*) (probeset 202449_S_AT, FC= 1.34, p= 0.0035) and upregulation of genes associated with mitogen-activated protein kinase (MAPK) signalling, including mitogen-activated protein kinase 10 (*MAPK10*) (probeset 214376_AT, FC= 1.38, p= 0.0278) as shown in Table 3-8. In addition, significant upregulation of heat shock proteins was identified, including heat shock protein 90 alpha family class A member 1 (HSP90AA1) (probeset

Table 3-7 KEGG pathway analysis and functional annotations of ageing periventricular white matter transcriptomic datasets (lesion vs. control)

Dysregulation of genes associated with immune response-associated pathways were identified in PVL compared to control using DAVID analysis.

Compared Groups	**Functional group**		**DEG**	***p*-value**	**FDR value**
Lesion vs Control	MHC-II		8	1.06E-04	0.1518
	Antigen processing and presentation		8	1.56E-04	0.2904
	Collagen IV		4	0.0065	11.3855
	Pathway Name	**Pathway Source**	**DEG**	***P*-Value**	**FDR Value**
	hsa04612: Antigen processing and presentation	KEGG	20	9.17E-06	0.0121
	hsa04145: Phagosome	KEGG	24	0.0028	3.6410
	hsa04672: Intestinal immune network for IgA production	KEGG	11	0.0045	5.7265
	hsa04662: B cell receptor signaling pathway	KEGG	12	0.0256	29.0463

DEG: Differentially expressed genes; FDR: False discovery rate; KEGG: Kyoto Encyclopedia of Genes and Genomes

Table 3-8 DAVID functional and pathway enrichment analysis of up-regulated genes (lesion vs control)

Compared Group	Functional group		DEG	*p*-value	FDR value
Lesion vs Control (1378 genes)	Metabolic processes (NADP Oxidoreductase)		4	0.0035	5.4026
	Aldo keto reductase		4	0.0117	11.7111
	Pathway Name	**Pathway Source**	**DEG**	***P*-Value**	**FDR Value**
	AMPK Signalling pathway	KEGG	16	6.40E-04	8.30E-01
	MAPK signalling pathway	KEGG	22	8.20E-03	1.00E+01
	Neurotrophin signalling pathway	KEGG	13	1.10E-02	1.30E+01
	HIF-1 Signalling pathway	KEGG	11	1.50E-02	1.80E+01
	cAMP signalling pathway	KEGG	15	8.50E-02	6.80E+01
	PI3K-Akt signaling pathway	KEGG	26	0.020976	24.0868

DEG: Differentially expressed genes; FDR: False discovery rate; KEGG: Kyoto Encyclopedia of Genes and Genomes

211968_s_at, FC= 2.02, p= 0.0075) and heat shock protein family A (Hsp70) member 1 like (HSPA1L) (probeset 210189_at, FC= 1.48, p= 0.0015).

In contrast, significant down-regulation of the genes associated with antigen processing and presentation were detected in PVL versus non-lesional control white matter (Table 3-9), including *HLA-DRA* (probeset 210982_s_at, FC= -1.71, p= 0.0038) and CD74 HLA class II histocompatibility antigen gamma chain (*CD74*) (probeset 1567627_at, FC= -2.67, p= 0.0068). Significant down-regulation of genes associated with the phagosome were also detected, including Fc fragment of immunoglobulin gamma Fc receptor 1A (*FCGR1A*) (probeset 216951_at, FC= -2.12, p= 0.0164) (Table 3-9). See Appendix III for the full list of up-and down-regulated genes.

Functional grouping analysis of the significantly differentially expressed genes in "pre-lesional" compared to non-lesional control white matter (PvC), identified dysregulation of glutamate receptor activity (enrichment score: 2.73), MHC II (enrichment score: 2.61), and GABA (enrichment score: 2.60). KEGG pathway analysis identified 79 dysregulated pathways (see Appendix II for the full list of dysregulated pathways), including immune-associated pathways and signalling pathways (including calcium, cAMP and MAPK) and synaptic pathways (including GABAergic, glutamatergic, dopaminergic and cholinergic synapses) (Table 3-10).

In "pre-lesional" versus non-lesional control white matter samples, analysis of the datasets identified upregulation of multiple genes associated with GABAergic

Table 3-9 DAVID functional and pathway enrichment analysis of down-regulated genes (lesion vs. control)

Significant down-regulation of genes associated with the antigen presentation and phagosome were identified in PVL compared to control using DAVID analysis.

Compared group	Functional group		DEG	*p*-value	FDR value
Lesion vs Control (878 genes)	MHC-II receptor activity		9	2.86E-09	4.36E-06
	Antigen processing and presentation		8	2.64E-07	4.65E-04
	Cyclooxygenase pathway		4	0.0025	4.4053
	Collagen type IV		4	4.14E-04	0.5825
	Toll/interleukin-1 receptor (TIR)		5	0.0056	8.5508
	Pathway Name	**Pathway Source**	**DEG**	***P*-Value**	**FDR Value**
	Staphylococcus aureus infection	KEGG	14	3.40E-08	4.40E-05
	Antigen processing and presentation	KEGG	14	2.30E-06	3.00E-03
	Phagosome	KEGG	19	5.70E-06	7.40E-03
	Focal Adhesion	KEGG	16	6.80E-03	8.50E+00

DEG: Differentially expressed genes; FDR: False discovery rate; KEGG: Kyoto Encyclopedia of Genes and Genomes

Table 3-10 KEGG pathway analysis and functional annotations of ageing periventricular white matter transcriptomic datasets (pre-lesion vs. control)

Compared group	Functional group		DEG	*p*-value	FDR value
Pre-lesion vs Control	GABA-A receptor activity		8	3.78E-04	0.6161
	Glutamate receptor, L-glutamate/glycine-binding		7	0.0016	2.7003
	MHC classes I/II-like antigen recognition protein		11	0.0017	2.8750
	Pathway Name	**Pathway Source**	**DEG**	***P*-Value**	**FDR Value**
	hsa04020: Calcium signaling pathway	KEGG	42	3.38E-09	4.44E-06
	hsa04728: Dopaminergic synapse	KEGG	34	5.29E-09	6.96E-06
	hsa04724: Glutamatergic synapse	KEGG	30	6.28E-08	8.26E-05
	hsa04725: Cholinergic synapse	KEGG	29	1.29E-07	1.70E-04
	hsa04727: GABAergic synapse	KEGG	23	1.82E-06	0.0024
	hsa04612: Antigen processing and presentation	KEGG	20	1.58E-05	0.021
	hsa04024: cAMP signaling pathway	KEGG	34	1.54E-04	0.203
	hsa04010: MAPK signaling pathway	KEGG	40	2.23E-04	0.292
	hsa04145: Phagosome	KEGG	25	0.002	2.750
	hsa04660: T cell receptor signaling pathway	KEGG	17	0.011	13.578

DEG: Differentially expressed genes; **FDR**: False discovery rate; **KEGG**: Kyoto Encyclopedia of Genes and Genomes

synaptic signalling, including gamma-aminobutyric acid (GABA) A receptor, alpha 5 (*GABRA5*) (probeset 206456_at, FC= 7.1, p= 0.0002; probeset 215531_S_AT, FC= 3.89, p= 0.001; probeset 217280_X_AT, FC= 1.6, p= 0.0095) and gamma-aminobutyric acid (GABA) A receptor alpha 4 (*GABRA4*) (probeset 233437_AT, FC= 1.91, p= 0.0027) and upregulation of calcium signalling, including calcium voltage-gated channel subunit alpha 1E (*CACNA1E)* (probeset 236013_at, FC= 4.46, p= 0.001; probeset 244256_at, FC= 4.11, p= 0.001; probeset 240650_at, FC= 1.31, p= 0.016; probeset 208432_s_at, FC= 1.62, p= 0.012). Also, an upregulation of genes associated with heat shock proteins was identified, including heat shock protein 90 alpha family class A member 1 (HSP90AA1) (probeset 214328_s_at, FC= 1.34, p= 0.0028) and heat shock protein family A (Hsp70) member 8 (HSPA8) (probeset 208687_x_at, FC= 1.28, p= 0.0424). Interrogation of the datasets also identified significant upregulation of glutamatergic synaptic signalling, including glutamate receptor, metabotropic 5 (*GRM5*) (probeset 1565389_S_AT, FC= 5.37, p= 0.0017; probeset 214217_AT, FC= 1.78, p= 0.0004) as shown in Table 3-11. Multiple genes associated with phagosome and antigen processing and presentation were significantly down-regulated (Table 3-12), including major histocompatibility complex, class II, DP alpha 1 (*HLA-DPA1*) (probeset 213537_at, FC= -2.72, p= 0.0004; probeset 211991_S_AT, FC= -1.93, p= 0.0228; probeset 211990_AT, FC= -3.77, p= 0.0324) and *HLA-DQB1* (probeset 211654_x_at, FC= -1.76, p= 0.0046). See Appendix III for the full list of up-and down-regulated genes.

Table 3-11 DAVID functional and pathway enrichment analysis of up-regulated genes (pre-lesion vs. control)

Multiple signalling pathways were upregulated in "pre-lesion" compared to control samples, including calcium and glutamatergic synaptic signalling.

Compared group	**Functional group**		**DEG**	***p*-value**	**FDR value**
Pre-lesion vs Control (1527 genes)	GABA receptor activity		8	7.55E-06	0.0108
	Glutamate receptor activity		7	8.88E-05	0.1443
	Neurotransmitter-gated ion channels		9	8.57E-04	1.3848
	Pathway Name	**Pathway Source**	**DEG**	***P*-Value**	**FDR Value**
	Retrograde endocannabinoid signalling	KEGG	32	4.50E-18	1.00E-15
	Calcium signalling pathway	KEGG	36	1.50E-13	1.10E-11
	Glutamatergic synapse	KEGG	28	8.70E-13	4.80E-11
	Dopaminergic synapse	KEGG	29	2.60E-12	1.20E-10
	GABAergic synapse	KEGG	23	1.84E-11	2.35E-08
	cAMP signalling pathway	KEGG	28	3.30E-07	5.60E-06
	MAPK signalling pathway	KEGG	31	1.60E-06	2.30E-05
	Alzheimer's Disease	KEGG	14	4.70E-02	1.70E-01

DEG: Differentially expressed genes; **FDR**: False discovery rate; **KEGG**: Kyoto Encyclopedia of Genes and Genomes

Table 3-12 DAVID functional and pathway enrichment analysis of down-regulated genes ("pre-lesion" vs. control)

Down-regulation of antigen processing and presentation and phagosome were identified in "pre-lesional" cases compared to controls.

Compared group	Functional group		DEG	*p*-value	FDR value
Pre-lesion vs Control (871 genes)	MHC-II receptor activity		11	1.14E-06	0.0018
	Metallothionein		5	7.85E-04	1.2488
	Pathway Name	**Pathway Source**	**DEG**	***P*-Value**	**FDR Value**
	Staphylococcus aureus infection	KEGG	18	1.40E-11	1.80E-08
	Phagosome	KEGG	22	4.60E-07	6.00E-04
	Antigen processing and presentation	KEGG	15	1.50E-06	1.90E-03

DEG: Differentially expressed genes; **FDR**: False discovery rate; **KEGG**: Kyoto Encyclopedia of Genes and Genomes

The significant differentially expressed genes in "pre-lesional" compared to PVL cases (PvL) were analysed, where functional annotation analysis identified an enrichment of genes associated with GABA receptor activity (enrichment score: 2.71), neurotransmitter gated ion channels (enrichment score: 1.8), adenylate cyclase activity (enrichment score: 2.4), and metallothionein (enrichment score: 2.36). KEGG pathway analysis in DAVID identified 38 significantly dysregulated pathways (see Appendix II for the full list of dysregulated pathways), including signalling pathways (including, cAMP, cGMP, MAPK and calcium) and synaptic pathways (glutamatergic, GABAergic and dopaminergic synapses) (Table 3-13). Multiple genes encoding the calcium signalling pathway were significantly upregulated in the pre-lesional periventricular white matter (Table 3-14), including calcium/calmodulin-dependent protein kinase II alpha (*CAMK2A*) (probeset 213108_at, FC= 1.67, p= 0.043; probeset 207613_s_at, FC= 7.06, p= 0.008) and upregulation of multiple genes associated with glutamatergic signalling pathways, including glutamate receptor, ionotropic, N-methyl D-aspartate 1 (*GRIN1*) (probeset 205915_X_AT, FC= 1.45, p= 0.011; probeset 211125_X_AT, FC= 1.65, p= 0.0409; probeset 210781_X_AT, FC= 1.82, p= 0.0182), glutamate receptor, ionotropic, AMPA 2 (*GRIA2*) (probeset 241172_at, FC= 1.55, p= 0.015). In contrast, down-regulation of genes associated with WNT signalling pathways were identified in the pre-lesional white matter (Table 3-15), including casein kinase 1, alpha 1 (*CSNK1A1*) (probeset 1556006_S_AT, FC= -1.64, p= 0.023; probeset 208867_S_AT, FC= -1.24, p= 0.045; probeset 208866_AT, FC= -1.21, p= 0.0218). See Appendix III for the full list of up- and down-regulated genes.

Table 3-13 KEGG pathway analysis and functional annotations of ageing periventricular white matter transcriptomic datasets ("pre-lesion" vs. lesion)

Compared group	Functional group		DEG	*p*-value	FDR value
Pre-lesion vs Lesion	GABA-A receptor activity		8	6.99E-04	1.148
	Adenylate cyclase activity		7	0.004	6.637
	Metallothionein domain		6	0.004	7.460
	Neurotransmitter-gated ion-channel		10	0.017	26.53
	Pathway Name	**Pathway Source**	**DEG**	***P*-Value**	**FDR Value**
	hsa04020: Calcium signaling pathway	KEGG	46	4.71E-11	6.22E-08
	hsa04723: Retrograde endocannabinoid signaling	KEGG	27	3.86E-07	5.09E-04
	hsa04724: Glutamatergic synapse	KEGG	29	3.97E-07	5.24E-04
	hsa04921: Oxytocin signaling pathway	KEGG	34	5.84E-07	7.71E-04
	hsa04727: GABAergic synapse	KEGG	21	3.58E-05	0.0472
	hsa04024: cAMP signaling pathway	KEGG	33	5.36E-04	0.705
	hsa04022: cGMP-PKG signaling pathway	KEGG	28	5.96E-04	0.783
	hsa04010: MAPK signaling pathway	KEGG	34	0.01433	17.353
	hsa04728: Dopaminergic synapse	KEGG	22	0.0038	4.997

DEG: Differentially expressed genes; FDR: False discovery rate; KEGG: Kyoto Encyclopedia of Genes and Genomes

Table 3-14 DAVID functional and pathway enrichment analysis of up-regulated genes ("pre-lesion" vs. lesion)

Multiple signalling pathways were upregulated in pre-lesion compared to PVL samples, including calcium and glutamatergic synaptic signalling.

Compared group	**Functional group**		**DEG**	***p*-value**	**FDR value**
Pre-lesion vs Lesion (1390 genes)	GABA receptor activity		8	3.20E-06	4.50E-03
	Neurotransmitter-gated ion channel		10	5.70E-05	9.30E-02
	Glutamate activity		6	4.90E-04	7.80E-01
	Pathway Name	**Pathway Source**	**DEG**	***P*-Value**	**FDR Value**
	Retrograde endocannabinoid signalling	KEGG	25	1.60E-12	2.05E-09
	Calcium Signalling Pathway	KEGG	32	6.70E-12	8.58E-09
	Glutamatergic synapse	KEGG	25	2.59E-11	3.31E-08
	cAMP signalling pathway	KEGG	26	5.49E-07	7.02E-04
	Alzheimer's Disease	KEGG	14	0.0223	25.1583

DEG: Differentially expressed genes; **FDR**: False discovery rate; **KEGG**: Kyoto Encyclopedia of Genes and Genomes

Table 3-15 DAVID functional and pathway enrichment analysis of down-regulated genes (pre-lesion vs. lesion)

Compared group	Functional group		DEG	*p*-value	FDR value
Pre-lesion vs Lesion (1259 genes)	Metallothionein		6	2.81E-04	0.4642
	Cadmium ion		5	4.09E-04	0.5780
	Mitochondrial carrier		7	0.0332	42.9437
	Transforming growth factor beta		3	0.0204	27.8330
	Pathway Name	**Pathway Source**	**DEG**	***P*-Value**	**FDR Value**
	WNT signalling pathway	KEGG	15	0.005	6.3480
	Focal Adhesion	KEGG	17	0.031	34.2352
	Metabolic pathways	KEGG	71	0.034	36.1588

DEG: Differentially expressed genes; **FDR**: False discovery rate; **KEGG**: Kyoto Encyclopedia of Genes and Genomes

3.3.5 EnrichR analysis result:

The top 1000 differentially expressed genes were imported into EnrichR to identify their relationship with KEGG pathways, biological processes, Panther pathways and the human gene atlas. Out of these 1000, the top 10 significant involved pathways and cell types such as antigen processing and presentation (KEGG pathway, p = 6.77E-06), inflammation (Panther, p = 1.20E-04), MHC II (Cellular Component p = 1.24E-04) and CD14 monocytes (Gene Atlas, p= 0. 4.22E-04. The top 10 pathway and functional groups identified by EnrichR are shown in Table 3-16.

3.3.6 Activated vs inactivated microglia

BST2 was appointed to identify the co-expressed genes associated with inactivated microglia (group A), while for activated microglia (group B), multiple genes were selected (*TREM2, HLA-DRA, ENTPD1, CD80, CD86, CCR5, CD274, ITGAX, TIMD4,* and *MRC1).* In both groups, 17 genes were co-expressed with the genes selected (Table 3-17). These genes showed a different pattern between the three groups: PVL, "pre-lesion" and non-lesional control in the microarray datasets (Figure 3.15). Analysis of the co-expressed genes revealed similarity of activated and inactivated microglia levels within PVL compared to the control group, with the exception of *CD80*, which showed a reduced expression. Similarly, "pre-lesional" cases showed inconsistency in the directional change of the expression of a number of genes associated with activated and inactivated microglia. Co- expressed genes associated with activated microglia (group B) were imported into DAVID to identify their enrichment score, function and pathways where these genes are involved.

Table 3-16 Top 10 pathway and functional groups identified by EnrichR

The PVL versus control non-lesional white matter transcriptomic dataset was imported into EnrichR to check the relationship with KEGG pathways, biological processes, Panther pathways and the human gene atlas. The top 10 pathways/functional groups identified by the analysis are shown below. Selected functions and pathways are highlighted in green.

Category	*Term*	*P-value*	*Adjusted P-value*
KEGG Pathway	Antigen processing and presentation	6.77E−06	0.0020
	Epstein-Barr virus	1.06E−04	0.0156
	Prostate cancer	1.49E−04	0.0145
	Leishmaniasis	4.58E−04	0.0336
	Herpes simplex infection	8.04E−04	0.0471
	Graft-versus-host disease	8.61E−04	0.0421
	Type I diabetes mellitus	0.0012	0.0483
	Estrogen signaling pathway	0.0015	0.0532
	Allograft rejection	0.0030	0.0989
	Influenza A	0.0031	0.0920
Panther Pathway	Inflammation mediated by chemokine and cytokine signaling pathway	1.20E−04	0.0134
	T cell activation	0.0068	0.3801
	N-acetylglucosamine metabolism	0.0199	0.7440
	Serine glycine biosynthesis	0.0199	0.5580
	B cell activation	0.0217	0.4853
	Axon guidance mediated by semaphorins	0.0257	0.4789
	Parkinson disease	0.0359	0.5748
	Toll receptor signaling pathway	0.0391	0.5476
	Apoptosis signaling pathway	0.0426	0.5297
	Histamine H2 receptor mediated signaling pathway	0.0443	0.4963
HUMAN GENE ATLAS	Whole Blood	2.00E-04	0.0168
	CD14+_Monocytes	4.22E-04	0.0177
	Retina	0.0019	0.0545
	CD33+_Myeloid	0.0050	0.1052
	CD4+_Tcells	0.0087	0.1465
	Smooth Muscle	0.0134	0.1878
	Cerebellum Peduncles	0.0166	0.1995
	Adipocyte	0.0227	0.2385
	Uterus	0.0234	0.2188
	CD56+_NKCells	0.0356	0.2994
GO cellular component (ontologies)	MHC class II protein complex	1.24E-04	0.1008
	nuclear speck	3.02E-04	0.1231
	membrane raft	4.73E-04	0.1286
	ER to Golgi transport vesicle membrane	5.67E-04	0.1157
	clathrin-coated phagocytic vesicle membrane	9.54E-04	0.1557
	LYSP100-associated nuclear domain	0.0022	0.2961
	nuclear dicing body	0.0022	0.2538
	sphere organelle	0.0022	0.2221
	nuclear body	0.0022	0.1974
	histone locus body	0.0023	0.1859

Table 3-17 Microglial deconvolution

In inactive microglia (group A), *BST2 (CD317)* was used to identify the co-expressed genes, while for activated microglia (group B) *CD39 (ENTPD1), HLA-DRA, CD86, CD80, TIMD4, ITGAX, TREM2, CCR5, MRC1* and *CD274* were selected to build co-expression network of genes associated with the selected candidate microglial markers using GeneMania.

Group A (Inactivated Microglia)	**Group B (Activated Microglia)**
ISG15	*HLA-DPB1*
MX1	*HLA-DQB1*
IFI44L	*HLA-DMB*
OAS2	*HLA-DPA1*
IFI35	*LCP2*
OAS1	*FCER1G*
LY6E	*GBP5*
IFIT1	*CYBB*
IFI44	*SAMSN1*
UBE2L6	*SLAMF8*
IFIT3	*MS4A6A*
IRF7	*IGSF6*
XAF1	*HAVCR2*
RSAD2	*TFEC*
OAS3	*CD163*
IRF9	*FCGR2A*
USP18	*MSR1*

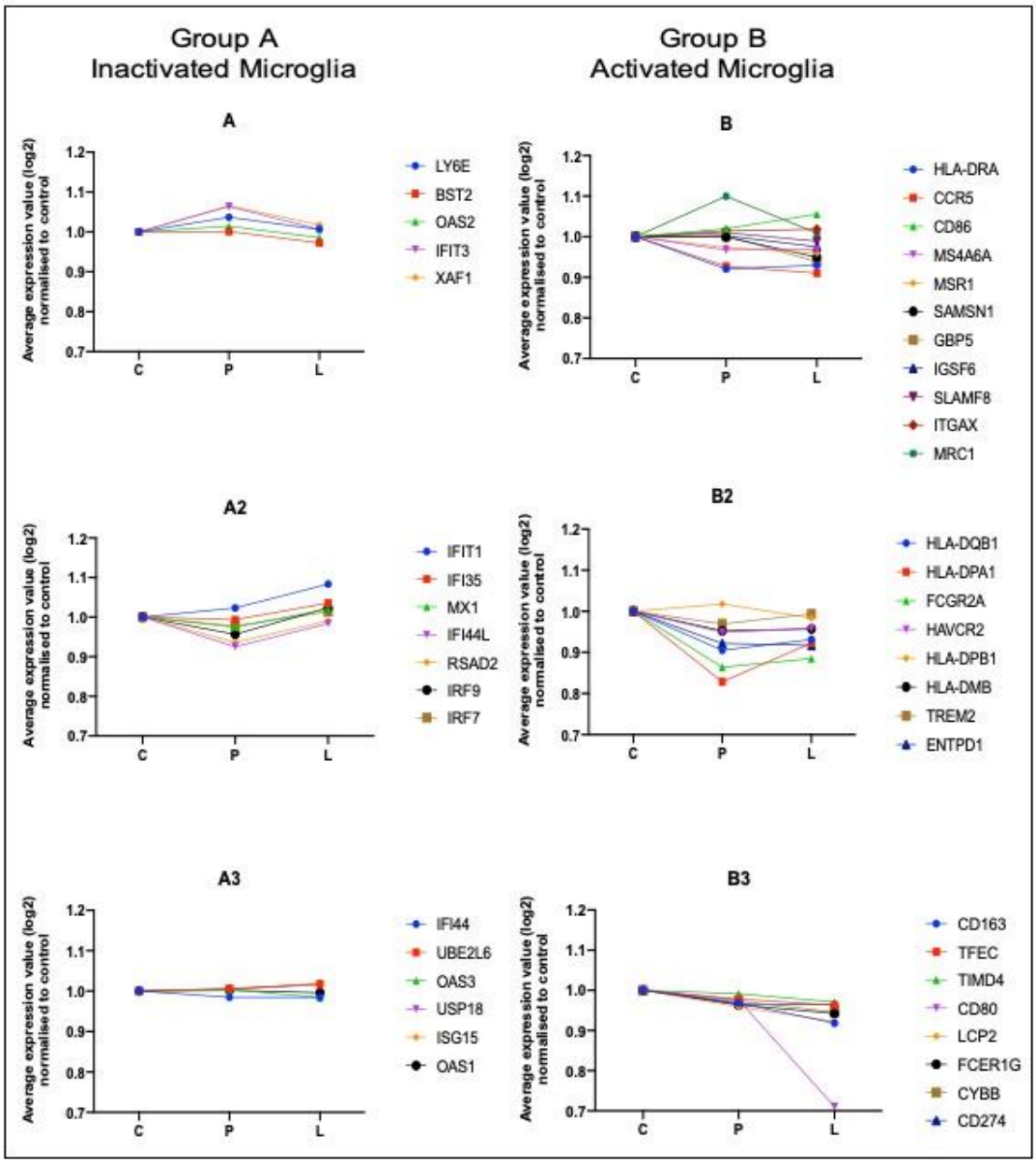

Figure 3.15 Graphical representation of gene annotations in both, activated and inactivated microglia in ageing periventricular white matter

This figure illustrates the annotations of microglial genes in inactivated (group A) microglia and activated microglia (group B) in non-lesional controls, "pre-lesion" and periventricular lesional samples. *BST2* gene was used to identify the co-expressed genes associated with inactivated microglia (A1, A2 and A3). While for the activated group, *TREM2*, *HLA-DRA*, *ENTPD1*, *CD80*, *CD86*, *CCR5*, *CD274*, *ITGAX*, *TIMD4* and *MRC1* (group B) were selected (B1, B2 and B3).

Immunoglobulin domain had the highest enrichment of 9.14 (14 genes, p-value: 6.27E-12 and FDR: 6.23E-09), followed by: the involvement of transmembrane functions with an enrichment of 8.6 (23 genes, p-value: 3.27E-10, FDR: 3.68E-07); immune response with an enrichment of 5.8 (10 genes, p-value: 2.15E-09, FDR: 2.71E-06); MHC-II (5 genes, p-value: 4.71E-09, FDR: 5.01E-06) and antigen processing and presentation (5 genes, p-value: 6.29E-09, FDR: 7.93E-06) which had an enrichment score of 5.8. In contrast, KEGG pathway revealed the involvement of 8 genes associated with the phagosome (p-value: 3.30E-08, FDR: 3.00E-05), and 5 genes associated with antigen processing and presentation (p-value: 2.94E-05, FDR: 0.02670242) (Table 3-18). *CD86*, *ITGAX* and *TREM2* genes were highly enriched in microglia in Jensen Tissues Database (Table 3-19).

Similarly, the inactivated microglia group showed that innate immunity, together with the type 1 interferon signalling pathway had the highest enrichment score of 14.4, followed by interferon-gamma mediated signalling pathways with an enrichment score of 2.9. KEGG pathway analysis identified the involvement of these genes in infectious diseases such as Influenza A, Herpes Simplex Infection and Measles (Table 3-20). EnrichR showed a significant expression of multiple genes associated with monocytes using Jensen Tissue database (Table 3-21).

Table 3-18 DAVID analysis of activated microglial genes

KEGG pathway analysis of activated microglial genes reveals an involvement of multiple genes associated with the phagosome and antigen processing and presentation.

Functional group		**DEG**	***P*-value**	**FDR value**
Immunoglobulin-like domain		14	6.27E-12	6.23E-09
Transmembrane region		23	3.27E-10	3.68E-07
Immune response		10	2.15E-09	2.71E-06
MHC-II		5	4.71E-09	5.01E-06
Antigen processing and presentation		5	6.29E-09	7.93E-06
Pathway Name	**Pathway Source**	**DEG**	***P*-Value**	**FDR Value**
hsa05330: Allograft rejection	KEGG	7	1.88E-10	1.71E-07
hsa04940: Type I diabetes mellitus	KEGG	7	4.21E-10	3.83E-07
hsa04145: Phagosome	KEGG	8	3.30E-08	3.00E-05
hsa04612: Antigen processing and presentation	KEGG	5	2.94E-05	0.02670

DEG: Differentially expressed genes; **FDR**: False discovery rate; **KEGG**: Kyoto Encyclopedia of Genes and Genomes

Table 3-19 EnrichR - Activated microglia

EnrichR showed a significant gene expression of multiple genes associated with monocytes and microglia (highlighted in green).

Category	Term	Overlap	P-value	Adjusted P-value
Wikipathways	Allograft Rejection WP2328	6/89	3.57E-09	1.68E-06
	Ebola Virus Pathway on Host WP4217	6/129	3.35E-08	7.90E-06
	PI3K/AKT/mTOR - VitD3 Signalling WP4141	3/22	4.60E-06	7.24E-04
	Microglia Pathogen Phagocytosis Pathway WP3937	3/40	2.90E-05	0.0034
	Macrophage markers WP4146	2/9	7.78E-05	0.0073
	TYROBP Causal Network WP3945	3/61	1.03E-04	0.0081
Jensen Tissue - Human	Immune system	12/1046	1.42E-08	2.61E-05
	Microglia	3/9	2.54E-07	2.34E-04
	Peritoneal macrophage	2/8	6.06E-05	0.0372
	Alveolar macrophage	2/10	9.71E-05	0.0447
	Monocyte	18/7640	0.0126	1

Table 3-20 DAVID analysis of inactivated microglial genes

Functional group		**DEG**	***p*-value**	**FDR value**
Type I interferon signaling pathway		13	1.91E-26	2.10E-23
Interferon-gamma-mediated signaling pathway		5	6.70E-07	7.33E-04
Innate immunity		10	1.64E-13	1.67E-10
Pathway Name	**Pathway Source**	**DEG**	***P*-Value**	**FDR Value**
hsa05164: Influenza A	KEGG	7	1.90E-08	1.26E-05
hsa05160: Hepatitis C	KEGG	6	2.97E-07	1.96E-04
hsa05162: Measles	KEGG	6	2.97E-07	1.96E-04
hsa05168: Herpes simplex infection	KEGG	6	1.46E-06	9.65E-04

DEG: Differentially expressed genes; **FDR**: False discovery rate; **KEGG**: Kyoto Encyclopedia of Genes and Genomes

Table 3-21 EnrichR - inactivated microglia

EnrichR analysis showed a significant expression of genes associated with monocytes in Jensen Tissue (highlighted in green).

Category	Term	Overlap	P-value	Adjusted P-value
Wikipathways	The human immune response to tuberculosis WP4197	6/23	2.09E-14	9.87E-12
	Non-genomic actions of 1,25 dihydroxyvitamin D3 WP4341	4/71	4.30E-07	1.01E-04
	Type II interferon signaling (IFNG) WP619	3/37	4.67E-06	7.34E-04
	RIG-I-like Receptor Signaling WP3865	2/60	0.0013	0.154
Jensen Tissue - Human	B-lymphoblastoid cell	15/5983	2.59E-04	0.12
	Immune system	6/1046	2.17E-04	0.133
	Monocyte	14/7640	7.42E-04	0.195

3.4 Discussion

WMLs are a feature of ageing and are associated with multiple neurological diseases such as vascular dementia and Alzheimer's disease, giving rise to clinical manifestations including cognitive impairment (Prins *et al.*, 2005) and depression (O'Brien *et al.*, 1996). In addition, WMLs are an independent risk factor for the development of dementia (Fernando & Ince, 2004; Matthews *et al.*, 2009; Kim *et al.*, 2015b).

WMLs are classified into PVL and DSCL based on their neuroanatomical locations. To date, the majority of research has focussed on DSCL, with fewer studies conducted on PVL. Histological characterisation of DSCL has demonstrated that they are associated with axonal loss, demyelination, and gliosis (Gouw *et al.*, 2011). In addition, it has been demonstrated through histological characterisation and transcriptomic profiling that hypoxia and hypoperfusion within the deep subcortical region are a prominent feature of DSCL, likely contributing to their pathogenesis (Fernando *et al.*, 2006; Schmidt *et al.*, 2011).

PVL are present in approximately 95% of the ageing population (de Leeuw, 2001), and are associated with cognitive impairment (Kim *et al.*, 2011; Bolandzadeh *et al.*, 2012; Griffanti *et al.*, 2018), BBB dysfunction (Freeze *et al.*, 2020) and significant levels of immune activated MHC-II^{+} microglia (Simpson *et al.*, 2007b, 2010), suggesting a failure in the cerebrovascular integrity results in microglial activation and underlies their pathogenesis. The current study aimed to extend these findings and, using a non-hypothesis driven transcriptomic analysis approach, to identify the

mechanisms underlying the pathogenesis of PVL. We demonstrate that established, demyelinated PVL is associated with dysregulation of the immune response and are part of a spectrum of white matter injury, whilst increased signalling is a feature of "pre-lesional" periventricular white matter and may represent attempts to prevent lesion formation.

3.4.1 Histological characterisation of radiologically control post-mortem periventricular white matter reveals "pre-lesional" pathology

In the current study, MRI of the formalin-fixed hemisphere was used to guide sampling of frozen brain slices from the contralateral hemisphere. This approach is routinely used to identify white matter lesions, where MRI hyperintensities histologically correlate with myelin loss (Fazekas *et al.*, 1991; Fernando & Ince, 2004). While myelin changes are part of the normal ageing process (Marner *et al.*, 2003), extensive periventricular demyelination is associated with an increased risk of dementia (Barber *et al.*, 1999; Prins *et al.*, 2004). In the current study, radiologically non-lesional control samples were histologically characterised by preservation of myelin staining. In contrast, demyelination was a prominent feature of PVL, which was found to vary from sharply demarcated areas of reduced myelin staining to larger extended areas of demyelination in the periventricular region. This supports the findings of other studies which identified severe loss of myelin basic protein (MBP) in PVL (Simpson *et al.*, 2007a; Murray *et al.*, 2012).

The microglial phenotype can be investigated using a variety of markers, including CD68, Iba-1, and MHC-II. CD68 is a lysosomal marker for microglia which was has been shown to label amoeboid phagocytic microglia within DSCL, while MHC-II is highly associated with ramified microglia in PVL (Simpson *et al.*, 2007a, 2007b). Iba-1 is a cytoplasmic protein that generally considered a pan-microglial marker that immunolabels all of microglia in both DSCL and PVL (Korzhevskii & Kirik, 2016). However, a recent study revealed that not all microglial cells are Iba-1$^+$ (Waller *et al.*, 2019). In the current study, MHC II$^+$ microglia were detected in both lesional and non-lesional periventricular white matter. Based on MHC II staining, variable microglial morphologies were observed in the periventricular white matter. Some cells displayed a ramified morphology with long processes extending from the cell body, while others showed retracted thick processes and an enlarged cell body.

High levels of MHC II expression in PVL support previous observations (Simpson *et al.*, 2007b) and suggest an immune response, as microglia are known to be involved in antigen presentation in the CNS (Almolda *et al.*, 2011). While low levels of MHC II$^+$ microglia are a feature of most non-lesional control white matter cases, a subgroup of radiologically normal periventricular white matter samples was identified, which were characterised by preserved myelin, but which contained high levels of MHC-II$^+$ microglia and were re-classified as "pre-lesional". Previous studies have identified an increase in levels of activated microglia in radiologically normal-appearing white matter from lesional cases, suggesting immune activation may precede demyelination (Simpson *et al.*, 2007b). However, it should be acknowledged that whether the cases used in this study would have gone on to

develop PVL is unknown, and further extensive characterisation of these cases is required.

Homeostatic imbalance and pathological insult within the CNS are one of the major causes of microglial activation, which is reflected by changes in microglial morphology and function (Sastre *et al.*, 2011; Perry & Holmes, 2014). The high levels of immune activated microglia in the periventricular region of the ageing brain could be due to a variety of factors, including microglial priming, BBB dysfunction and/or back diffusion of CSF.

Innate immune activation occurs during brain ageing and is associated with cognitive decline (Cribbs *et al.*, 2012). Microglia become primed during neurodegeneration, neuroinflammation and also as part of the normal ageing process (Li *et al.*, 2018). Primed microglia have a reduced threshold for activation and when stimulated produce an augmented exaggerated inflammatory response (DiBona *et al.*, 2019), which may contribute to both cognitive impairment and neurodegeneration. Primed microglia express high levels of MHC-II, in addition to an increased inflammatory response (Frank *et al.*, 2006; Perry & Holmes, 2014). It is likely that primed microglia shift to an M1 neurotoxic phenotype (Hu *et al.*, 2012) which results in the increased production of pro-inflammatory cytokines, proteases and reactive oxygen species (Cunningham *et al.*, 2009). Our findings revealed an increased expression of MHC-II^{+} microglia in both PVL and "pre-lesional" periventricular white matter, which may reflect age-associated microglial priming in the ageing brain and which requires further investigation.

The production of pro-inflammatory mediators such as NO and TNF-α by M1 activated microglia in the ageing brain has been proposed to have a neurotoxic effect which impacts myelin attenuation (Merrill *et al.*, 1993; Tarkowski *et al.*, 2003; Jana & Pahan, 2013). In addition, degeneration of oligodendrocytes, the myelin-producing cells, may occur as part of normal ageing, resulting in myelin loss (Kohama *et al.*, 2012; Peters, 2002).

Disruption of the BBB may result in the accumulation of plasma proteins which are normally excluded from the CNS, resulting in the activation of microglia. Several studies provide evidence to support this theory, demonstrating BBB dysfunction is a feature of PVL in the ageing brain (Simpson *et al.*, 2007b; Lu *et al.*, 2001). Breakdown of the ependymal lining may lead to loss of integrity and the abnormal back-diffusion of CSF into the periventricular area (Scheltens *et al.*, 1995; Simpson *et al.*, 2007a). A significant correlation between ependymal loss and increased volume of WML has been reported (Shim *et al.*, 2015) and supports the findings of the current project which demonstrated denudation of ependymal lining as a feature of PVL. The microgliosis observed in the periventricular white matter region may represent a neuroprotective or detrimental effect.

The role of microglia and their contribution to neurodegeneration has been undervalued, but recent research has focussed on these glial cells, which play a significant role within the CNS, including homeostasis and surveillance mechanisms (Koellhoffer *et al.*, 2017). Therefore, in the current project, we assessed the transcriptomic profile of PVL and "pre-lesional" white matter compared to control

non-lesional periventricular white matter, with the aim of identifying microglial-mediated mechanisms underlying lesion pathogenesis.

3.4.2 Transcriptomic profiling of post-mortem tissue

Having histologically identified PVL, "pre-lesional" and non-lesional control periventricular white matter cases, LCM has been employed to isolate the periventricular region, using a similar approach used by Blalock, which selectively LCM-ed CA1 hippocampal grey matter from post-mortem tissue (Blalock *et al.*, 2011).

Gene expression changes in each of the three groups were interrogated to identify potential pathways and mechanisms underlying lesion pathogenesis. The RIN value of each case was assessed pre-and post-LCM, identifying a decrease in the RIN associated with the LCM protocol. Genomic studies can be hindered by difficulties in obtaining high-quality RNA from post-mortem tissue due to multiple factors such as tissue pH, post-mortem delay, and the agonal state of the patient prior to death (Tomita *et al.*, 2004; Chevyreva *et al.*, 2008). However, the functional data obtained in these post-mortem human tissue studies may be more relevant than cell or animal disease models, which do not entirely recapitulate all aspects of the disease process. While the RNA extracted from the PVL was undoubtedly of low quality, it remains of comparable quality to our previously published array studies (Simpson *et al.*, 2009, 2011) and enabled changes in the gene expression profile to be detected and identified those gene changes which are associated with lesion pathology, thereby

increasing our understanding of potential mechanisms associated with lesion evolution.

3.4.3 Microarray data analysis

Transcriptomic profiling of PVL and "pre-lesional" white matter identified dysregulation of functions and pathways associated with immune response, while "pre-lesions" were also associated with significantly increased expression of genes related to signalling and synaptic pathways.

3.4.3.1 "Pre-lesional" periventricular white matter and PVL are associated with dysregulation of the immune response

Functional annotation grouping analysis of the "pre-lesional" and PVL datasets identified dysregulation of genes associated with immune-response, including MHC-II receptor activity and antigen processing and presentation. PVL and "pre-lesion" compared to non-lesional control were mainly associated with significant down-regulation of *HLA-DOB*, *HLA-DRA* and *CD74*. This conflicts with our immunohistochemical finding, which showed increased detection of MHC-II in our cohort, and also conflicts with other studies investigating the immune response in ageing populations which show that with increasing age, the expression of HLA-DR/MHC-II^{+} microglia increase in the white matter (Sheffield & Berman, 1998). Also, a microarray study conducted on post mortem tissue showed an upregulation of genes associated with MHC-II in DSCL (Simpson *et al.*, 2009). Differentially expressed transcripts have significantly higher correlations between mRNA and protein levels (Koussounadis *et al.*, 2015). However, this is not always the case, as

mRNA expression changes do not always correlate with protein levels for the specific gene and may give conflicting results as shown with MHC-II in this project. This may reflect the decoupling in time of both mRNA and protein expression (Fournier *et al.*, 2010; Koussounadis *et al.*, 2015).

In the current study, the histological evaluation was done using a single marker (MHC-II). Using a single microglial marker does not take into account the wide range of markers which are expressed by the diverse population of microglia, which require an extensive panel of markers to capture the full spectrum of microglial phenotypes in the white matter.

3.4.3.2 Periventricular white matter contains similar levels of both activated and inactivated microglia

To elucidate microglial-associated genes, we performed a computational deconvolution to interrogate changes in the gene expression and build a specific microglial signature to identify both activated and inactivated microglia within control, "pre-lesions" and PVL.

BST2 (*CD317*) was selected to identify the co-expressed genes associated with inactivated microglia, as this gene is associated with reducing the expression of inflammatory associated genes and pro-inflammatory cytokines (Ajami *et al.*, 2018). Microglia express the BST2 receptor immunoglobulin-like transcript 7 (ILT7), and binding to this receptor results in the down-regulation of pro-inflammatory immune modulators, including TNF-α, and IL1β (Polyak *et al.*, 2013).

The transformation of microglia from a homeostatic to reactive phenotype in dementia pathologies is associated with multiple genes, including Triggering Receptor Expressed on Myeloid cells 2 (*TREM2*) (Rodríguez-Gómez *et al.*, 2020), *HLA-DRA* (Yin *et al.*, 2017), *ITGAX* (CD11c) (Keren-Shaul *et al.*, 2017), *CCR5* (Li & Zhu, 2019), *CD274* (Schachtele *et al.*, 2014), *CD80* (B7-1) (Busse *et al.*, 2015), *CD86* (B7-2) (Simpson *et al.*, 2007b), *ENTPD1* (CD39) (Baron *et al.*, 2014), *MRC1* (Friedman *et al.*, 2018) and *TIMD4* (Askew & Gomez-Nicola, 2018). *TREM2* is highly expressed by microglia (Jay *et al.*, 2017) and interacts with tyrosine kinase-binding protein (TYROBP) to promote microglial activation (Yeh *et al.*, 2017; Ulland & Colonna, 2018) and induce phagocytosis (Wang *et al.*, 2015). Similarly, *FCER1G* and *FCGR2A*, which are members of immunoglobulin Fc receptor family mediate microglial phagocytosis (Quan *et al.*, 2009). *ITGAX* is highly expressed in the white matter of aged mouse brains (Raj *et al.*, 2017), and CD11c^{+} microglia have been shown to accumulate around amyloid plaques in a mouse model of AD where they initiate the phagocytic process (Kamphuis *et al.*, 2016). Similarly, *CD163* is expressed by activated microglia (Borda *et al.*, 2008), and CD163^{+} microglia have been shown to accumulate around Aβ plaques in AD (Pey *et al.*, 2014).

To further validate the involvement of selected candidate microglial activation-associated genes, KEGG pathway analysis was performed and confirmed a role for the selected genes in phagosome and antigen processing and presentation. Additional confirmation was performed using the EnrichR tool and the Jensen Tissues Database (Palasca *et al.*, 2018), which showed a high enrichment of *CD86*,

ITGAX, and *TREM2* in microglia, while multiple genes associated with the immune response were also highly enriched, including *CD274*, *MSR1*, *ENTPD1*, *CD163*, *FCER1G*, *FCGR2A*, *MRC1*, *HLA-DPB1*, *CYBB*, *HLA-DRA*, *LCP2* and *CCR5*. Therefore, these genes were selected to identify the co-expressed genes associated with activated microglia in the current study. Our data revealed a similar pattern of expression of both active and inactive microglial transcripts are present in control, "pre-lesions" and PVL except for CD80, which is markedly decreased in PVL.

Post-mortem tissue analyses are fundamentally constrained in that they represent a single time point and disease stage. Human tissue single-cell RNA sequencing can be used to interrogate microglial phenotypes; however, these findings then need to be validated at the protein level to confirm their relevance (Swanson *et al.*, 2020). Multiple studies have investigated microglial changes over the course of neurodegeneration, showing specific differences in microglia isolated in early and late stages of neurodegeneration in mouse models (Mathys *et al.*, 2017), so-called disease-associated microglia (DAM) (Keren-Shaul *et al.*, 2017).

Microglial heterogeneity is extensive (Mathys *et al.*, 2017; Sankowski *et al.*, 2019), and our findings demonstrate that microglia within the periventricular white matter in the ageing brain reflects a highly heterogeneous population and highlights the need to use a comprehensive and extensive panel of microglial markers to capture the full spectrum of microglial cell states and to assess the microglia phenotype associated with neuropathologies.

3.4.3.3 "Pre-lesional" periventricular white matter and PVL are associated with increased expression of heat shock proteins

While antigen processing and presentation genes are down-regulated in both PVL and "pre-lesions" compared to non-lesional controls, gene expression analysis identified significant upregulation of heat shock proteins (HSP) associated genes, including the HSP70-associated genes *HSPA1A*, *HSPA4*, and *HSPA8*, and the HSP90-associated genes *HSP90AA1* and *HSP90AB1*.

The 70-kDa heat shock protein (Hsp70) is a member of a family of chaperone proteins which play a major role in preventing protein aggregation (Liberek *et al.*, 2008; Griffith & Holmes, 2019), and are highly inducible following brain ischemia (Planas *et al.*, 1997; Kim *et al.*, 2020). In addition, Hsp70 is involved in anti-inflammatory processes including inhibiting neuroinflammatory pathways in cultured astrocytes from mice (Kim *et al.*, 2015a); reducing the expression of prostaglandin-endoperoxide synthase 2, COX-2 (PTGS2) and nitric oxide (NO) in a mouse model by preventing nuclear factor kappa B (NFκB) activation (Kim *et al.*, 2015a); anti-apoptosis (Lanneau *et al.*, 2007); and protecting against cell death induced by ischemia (Giffard *et al.*, 2004). Post mortem analysis of heat shock protein expression in MS demonstrates significant upregulation of HSP70 in CNS lesions (Stadelmann *et al.*, 2005) and in myelin isolated from MS lesions (Aquino *et al.*, 1997; Pinar *et al.*, 2017).

HSP90, which is another member of the chaperone protein family, has been shown to induce microglial activation and clearance of Aβ peptides (Kakimura *et al.*, 2002;

Polanski *et al.*, 2010). In addition to these functions, HSP90 is involved in the regulation of signal transduction and acts to maintain signalling kinases (Li & Buchner, 2013), including mitogen-activated protein kinase (MAPK) (Lei *et al.*, 2017).

These data suggest that the upregulation of HSP in both "pre-lesional" and PVL may reflect attempts to protect against demyelination in "pre-lesional" cases and prevent further demyelination in PVL.

3.4.3.4 Upregulation of calcium and glutamate signalling in "pre-lesional" white matter may reflect a neuroprotective response

Analysis of the "pre-lesional" microarray datasets revealed the significant upregulation of several signalling pathways, including calcium and glutamate signalling, which may reflect a neuroprotective response to prevent lesion formation.

Calcium signalling is essential to maintain homeostasis in the CNS and plays a major role in regulating multiple cellular processes, including cellular excitability, apoptosis, the release of neurotransmitters and signal transduction (Clapham, 1995; Horigane *et al.*, 2019). Calcium dyshomeostasis strongly correlates with ageing and neurodegenerative disorders (Bezprozvanny, 2009; Gant *et al.*, 2018). Dysregulation of calcium is strongly associated with the loss of white matter integrity following an ischaemic stroke in aged mice, which ultimately induces oligodendrocytes damage and axonal dysfunction (Baltan, 2009). Also, abnormality

in calcium exchange, influx and buffering results in calcium imbalance, which ultimately leads to neuronal dysfunction and cell death (Kurnellas *et al.*, 2007; Calvo-Rodriguez *et al.*, 2020).

Disruption of the BBB is a common feature of normal ageing and neurodegenerative diseases, and multiple studies have demonstrated an association between BBB dysfunction and WM pathologies (Tomimoto *et al.*, 1996; Akiguchi *et al.*, 1998; Li *et al.*, 2017). BBB dysfunction leads to an increase in intracellular calcium which in turn impacts the modification of tight junctions (Brown & Davis, 2002; Chen *et al.*, 2016b). In a mouse model, activation of calmodulin/calcium-dependent protein kinase plays a role in the repair of the BBB after stroke, which in turn prevents pro-inflammatory factor infiltration (Sun *et al.*, 2019). In the current study, we demonstrate the significant upregulation of genes associated with calcium/calmodulin dependent protein kinase genes, including, *CAMK4* and *CAMK2B*. CAMK4 inhibits excitotoxicity via the activation of the anti-apoptotic pathway PI3K/AKT3 (Bell *et al.*, 2013). CAMK2B is a member of the calcium/calmodulin-dependant protein kinase family and mediates calcium signalling in the brain (Swulius & Waxham, 2008; Ghosh & Giese, 2015), and is involved in multiple signalling pathways and plays a role in oligodendrocyte maturation and CNS myelination (Waggener *et al.*, 2013).

Mature oligodendrocytes are responsible for axonal myelination (Sherman & Brophy, 2005), and express a wide range of receptors for neurotransmitters, including glutamate and GABA. Vesicular release of glutamate from axons increases

myelin production in a mechanism known as adaptive myelination (Douglas Fields, 2015; Habermacher *et al.*, 2019). Glutamate released from the axons binds to α-Amino-3-hydroxy-5-methyl-4-isoxazole propionic acid (AMPA) receptors, which mediate synaptic transmission in the CNS (Scheefhals & MacGillavry, 2018). The present study identified significant upregulation of glutamatergic synapse-associated genes in "pre-lesional" white matter, including *GRIA2* and *GRIA3* which encode the AMPA receptors, glutamate ionotropic receptor (GLUR2) and GLUR3, respectively, and are involved in mediating fast synaptic transmission in the CNS (Meng *et al.*, 2003). A study conducted on a post-mortem vascular dementia cohort revealed an upregulation of AMPA GLUR2 immunoreactivity and mRNA in subcortical ischemic vascular dementia (Mohamed *et al.*, 2011).

γ-aminobutyric acid (GABA) is the primary inhibitory neurotransmitter in the CNS and is converted from glutamate. Glutamate together with GABA and ATP is essential for modulating the proliferation of oligodendrocyte precursor cells (OPC) and the survival of oligodendrocytes and axonal myelination (Gudz *et al.*, 2006; Zonouzi *et al.*, 2015). $GABA_A$, an ionotropic receptor, is expressed by OPC (Zonouzi *et al.*, 2015), once activated it enables GABA to depolarise OPC, which facilitates calcium entry into these cells. Thus an increase in calcium levels within OPC may help in the regulation of proliferation, migration and maturation of OPC which may eventually help in the myelination process by oligodendrocytes (Baraban *et al.*, 2018; Paez & Lyons, 2020). Our data reveal a significant upregulation of GABAergic synaptic signalling in "pre-lesions", associated with *GABRA1*, *GABRA4* and *GABRA5*, encoding $GABA_A$ receptor genes. Upregulation of these genes might reflect

activation of this receptor, which help in facilitating the myelination process by OPC and oligodendrocytes in “pre-lesions”.

Taken together, the upregulation of calcium and glutamate signalling pathways in “pre-lesional” periventricular white matter may reflect a neuroprotective response to prevent the formation of PVL.

3.5 Conclusion

Age-associated PVL are highly associated with cognitive decline in the ageing population, but the mechanisms underlying their pathogenesis are unknown. The current study interrogated the transcriptomic profile of PVL and radiologically normal-appearing control periventricular white matter cases to identify novel mechanisms underlying their formation. Histological characterisation of control white matter samples identified a group which characterised by the presence of high levels of MHC-II immunoreactive microglia and was classified as “pre-lesional”. Although histological assessment of a single marker (MHC-II) includes immune activated microglia in lesion pathology, transcriptomic analysis implies a substantial down-regulation of a number of activated microglial markers and suggests that established PVLs are part of a continuous process of white matter injury. Overall, the data presented here lead us to reject the original hypothesis that microglia within established PVL adapt a neurotoxic M1 phenotype. Interestingly, the gene expression profile of "pre-lesional" periventricular white matter indicates

upregulation of many signalling pathways, including calcium and glutamate, which may reflect a neuroprotective response to prevent the pathogenesis of PVL.

CHAPTER 4: VALIDATION OF THE TRANSCRIPTOMIC PROFILE OF AGE-ASSOCIATED PVL

4.1 Introduction

Gene expression analysis is a widely used method to identify potential mechanisms and changes in key pathways associated with the pathogenesis of a range of diseases, and may lead to the discovery of novel therapeutic targets. In the previous chapter, transcriptomic profiling using a microarray analysis approach was employed to identify relevant gene expression changes associated with PVL in the ageing brain. The data indicated established that PVL displays significant downregulation of several genes associated with an immune response, including genes associated with activated microglial markers and cytokines/chemokines. Furthermore, the gene expression profile of "pre-lesional" periventricular white matter was associated with the significant upregulation of several signalling pathways. To increase confidence in these results, additional validation experiments to confirm the differential expression of a panel of candidate genes were carried out. This chapter reports two independent validation approaches, namely NanoString and immunohistochemistry, to validate changes in gene expression and the proteins they encode, respectively.

Post-mortem tissue is frequently associated with RNA degradation due to multiple factors, including pH and post-mortem delay (PMD), which can affect RNA integrity and are generally considered as one of the significant challenges associated with transcriptomic profiling. The NanoString nCounter system is a novel technology which allows interrogation of the expression of more than 800 genes using a single sample with fluorescently tagged mRNA molecules (Geiss *et al.*, 2008). This assay can detect the expression of specific mRNAs using nCounter Reporter Probes

"barcodes" with high sensitivity and is fully automated without the need to amplify mRNA (Figure 4.1). Another significant advantage of this technology is the accuracy of quantification of low quality and quantity mRNA within the sample.

mRNA gene expression changes are not always expressed at the protein level for every selected gene. However, a recent experiment revealed a strong correlation between mRNA and protein levels in differentially expressed transcripts, which have far stronger associations between mRNA and protein levels than transcripts that are not differentially expressed (Koussounadis *et al.*, 2015). Therefore, techniques such as immunohistochemistry can be employed to assess the expression of the proteins encoded by candidate genes identified in transcriptomic studies. In addition to enabling changes in protein expression to be assessed, this approach also provides additional information to be obtained by enabling the cellular localisation of the protein to be determined.

4.1.1 Hypothesis:

Microarray analysis of ageing periventricular white matter characterised the transcriptomic profile associated with "pre-lesions" and established PVL (chapter 3). The current chapter will extend these findings and further test the hypothesis that the mechanisms underlying the pathogenesis of PVL are different to DSCL, specifically that "pre-lesions" and PVL are associated with the significant down-regulation of an immune response.

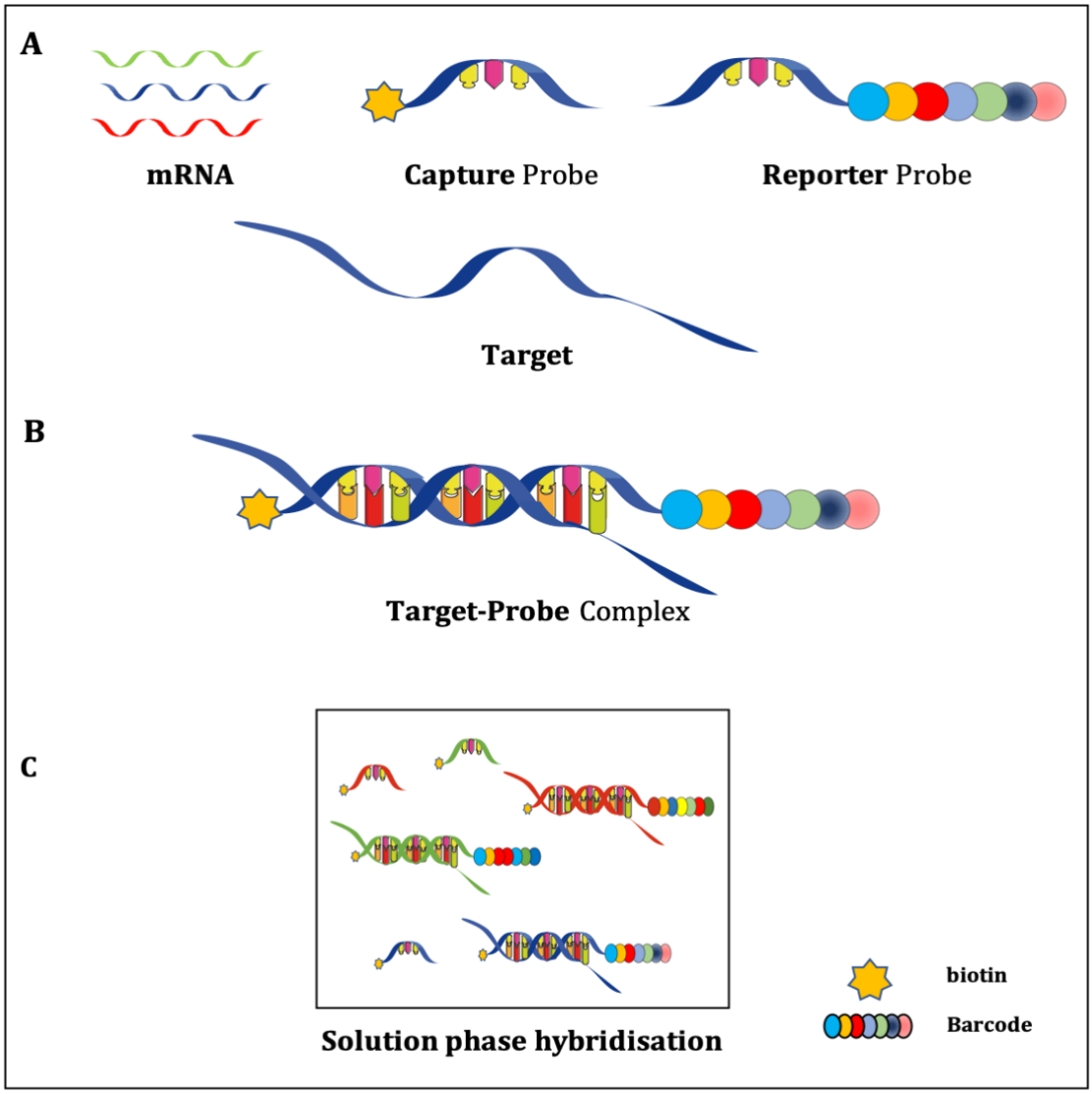

Figure 4.1 Schematic representation of NanoString nCounter protocol

Total RNA was extracted from the periventricular region using LCM and mixed with the probe set provided by NanoString containing both capture and reporter probes (A). These probes bind specifically to their RNA targets and create the target-probe complex (B). The excess probes are removed after hybridisation (C), and the fluorescent colour sequences are counted. Each colour-coded barcode represents a single gene. Adapted from (Grahl *et al.*, 2018).

4.1.2 Aims:

- To validate a key panel of candidate gene expression identified by microarray using NanoString nCounter.
- To confirm the differential expression of the proteins encoded by a panel of key gene changes using IHC.

4.2 Materials and methods

4.2.1 NanoString

Messenger RNA (mRNA) was isolated from the periventricular white matter of control, lesional and "pre-lesional" cases using LCM, as described in detail in section 3.2.4.3. In the current study, 12 samples from the previous microarray study were analysed, and included 4 non-lesional controls, 3 "pre-lesional" and 5 PVL, as shown in Table 4-1. A customised nCounter codeset human gene panel was designed, consisting of 29 inflammation, antigen processing and presentation-related genes. In addition, 3 housekeeping genes were included for normalisation (*ACTB*, *GAPDH* and *RPLP0*) (NanoString Technologies, Seattle, WA), as shown in Table 4-2.

4.2.1.1 NanoString Sample Hybridisation

A master mix was prepared by adding 70 µl of hybridisation buffer to the tube containing the Reporter Codeset, followed by brief centrifugation. Following this, 8 µl of the master mix was added to 12 pre-labelled tubes of the hybridisation strip before adding 100 ng of sample RNA. To complete the hybridisation reaction, 2 µl of Capture ProbeSet was added to each tube followed by brief centrifugation, to make a final volume of 15 µl (Table 4-3). The tubes were placed in a PTC 200 thermal cycler (MJ Research, Quebec, Canada) and incubated at 65˚C for 22 hours. Following this incubation, the samples were placed on ice before adding 15 µl of hybridisation buffer to make a total of 30 µl. In accordance with the manufacturer's instructions, each sample was loaded into the nCounter SPRINT cartridge by placing the tip of the pipette vertically into cartridge loading port, followed by pressing the pipette

Table 4-1 NanoString samples

	Sample no.	Case number
Control	Sample 1	Control 1
	Sample 2	Control 3
	Sample 3	Control 4
	Sample 4	Control 5
Lesion	Sample 5	Lesion 1
	Sample 6	Lesion 2
	Sample 7	Lesion 3
	Sample 8	Lesion 5
	Sample 9	Lesion 7
Pre-lesion	Sample 10	Prelesion 1
	Sample 11	Prelesion 3
	Sample 12	Prelesion 4

Table 4-2 NanoString validation candidates

This table shows the highly annotated candidate genes generated from microarray data analysis and EnrichR dataset focussing on genes associated with both inflammation and antigen processing and presentation.

Function	Gene symbol	Accession Number	Gene name
Inflammation	*AKT3*	NM_005465.4	V-akt murine thymoma viral oncogene homolog 3/RAC-gamma serine/threonine-protein kinase
	CCL2	NM_002982.3	C-C motif chemokine ligand 2
	CCL3	NM_002983.2	C-C motif chemokine ligand 3
	CCL4	NM_002984.2	C-C motif chemokine ligand 4
	CCR5	NM_000579.1	C-C motif chemokine receptor 5 (gene/pseudogene)
	COL6A3	NM_004369.3	Collagen type VI alpha 3 chain
	CX3CR1	NM_001337.3	C-X3-C motif chemokine receptor 1
	IFNAR1	NM_000629.2	Interferon alpha and beta receptor subunit 1
	IKBKB	NM_001556.1	Inhibitor of nuclear factor kappa B kinase subunit beta
	IL1A	NM_000575.3	Interleukin 1 alpha
	IL1B	NM_000576.2	Interleukin 1 beta
	JUN	NM_002228.3	Jun proto-oncogene, AP-1 transcription factor subunit
	PTGS2	NM_000963.1	Prostaglandin-endoperoxide synthase 2
Antigen processing and presentation	*CD74*	NM_001025159.1	CD74 molecule, HLA class II histocompatibility antigen gamma chain
	HLA-DRA	NM_019111.3	Major histocompatibility complex, class II, DR alpha
	CD8A	NM_001768.5	CD8a molecule, T-cell surface glycoprotein CD8 alpha chain
	CD163	NM_004244.4	CD163 molecule, Scavenger Receptor Cysteine-Rich Type 1 Protein M130
CD14 Monocytes	*EPSTI1*	NM_001002264.2	Epithelial stromal interaction protein 1
	FGL2	NM_006682.2	Fibrinogen like 2
	FPR1	NM_002029.3	Formyl peptide receptor 1
	IGSF6	NM_005849.2	Immunoglobulin superfamily member 6
	PHF21A	NM_016621.3	PHD finger protein 21A
Inactivated Microglia	*IRF7*	NM_001572.3	Interferon regulatory factor 7
	OAS1	NM_001032409.1	2'-5'-oligoadenylate synthetase 1
	RSAD2	NM_080657.4	Radical S-adenosyl methionine domain containing 2
Activated Microglia	*FCER1G*	NM_004106.1	Fc fragment of IgE receptor Ig
	MSR1	NM_002445.3	Macrophage scavenger receptor 1
	SLAMF8	NM_020125.2	SLAM family member 8
	CYBB	NM_000397.3	Cytochrome b-245, beta polypeptide
Housekeeping Genes	*ACTB*	NM_001101.2	Actin cytoplasmic 1
	GAPDH	NM_001256799.1	Glyceraldehyde-3-phosphate dehydrogenase
	RPLP0	NM_001002.3	60S acidic ribosomal protein P0

Table 4-3 nCounter sample preparation

Component	**Volume (µl)**
Master Mix (Hybridisation + Reporter CodeSet)	8
RNA	5
Capture Probeset	2
Total	**15**

plunger to the second stop, creating an air bubble and removing the pipette before releasing the plunger to prevent sucking the sample out. The top of the cartridge was wiped, coated with a seal and placed into the nCounter SPRINT instrument for mRNA transcript counting (NanoString Technologies Inc., Seattle, WA).

4.2.1.2 Validation of gene expression changes - NanoString

The reporter library file (RLF), generated by NanoString, contained the unique custom CodeSet information and was imported to nSolver Analysis Software (v4.0.70) (NanoString Technologies). Raw data (RCC files) were analysed to ensure all samples passed the quality parameters, including imaging and binding density quality control (QC) metrics, positive control linearity and limit of detection.

NanoString cartridge images were taken in small divided sections or lanes referred to as a field of view (FOV), which enabled the counting of the barcodes in 194 FOV. The percentage of FOV containing barcodes divided by the total number of FOV that the instrument attempted to scan was assessed for each sample, with greater than 75% considered as a successful run.

The binding density, a measure of the number of fluorescent spots per μm^2, was calculated to determine the level of image saturation in each lane and, according to the manufacturer, should lie between 0.1 – 1.8.

Positive control linearity was automatically checked using nSolver software, which assessed the linearity of six positive controls (range 128 fM to 0.125 fM). The

software calculated the linear regression between the known concentration of each of the positive controls and their actual counts using log2-transformed values, where the correlation coefficient (R^2) values should be greater than 0.95.

Data were normalised using two methods by nSolver software. Initially, the data were normalised to the geometric mean of housekeeping genes in the designed codeset. The second normalisation method used the pre-mixed positive controls with the reporter probes to normalise the gene expression data.

Each sample was annotated to the comparison group using the nSolver experiment option. Once analysed, ratio data was selected to identify both fold change (FC) and p-value for each gene of interest. Additional analysis was performed using the Advanced Analysis package on nSolver. Genes which showed an FC of ≥ +/- 2 and also a p-value ≤ 0.05 were considered significantly differentially expressed between the comparison groups.

4.2.1.3 Comparison of the NanoString findings with the microarray datasets

The datasets generated were compared between NanoString and Affymetrix to assess the correlation of gene expression and fold change directionality for the selected targets. As nCounter software uses a single probeset ID for selected genes (Chen *et al.*, 2016c), but multiple probesets are employed in the microarray analysis, we selected the probeset with the lowest p-value in the Affymetrix microarray datasets.

4.2.2 Validation of gene expression changes - Immunohistochemistry

To further validate the gene expression changes identified by microarray analysis, the expression of the proteins encoded by a panel of candidate genes was assessed by IHC using ABC-HRP method (Section 2.2.3), the antibody details are shown in Table 4-4. The stained sections were assessed using a Nikon Eclipse 80i microscope and NIS-Elements Imaging Software (Nikon UK, Kingston Upon Thames). Quantification of specific immunoreactivity was performed in 3 different white matter regions of the periventricular region for each case. The images were analysed using Analysis^D software (Nikon UK, Kingston Upon Thames) to assess the % area immunoreactivity.

4.2.3 Statistical analysis

Immunohistochemical data were not normally distributed using the Shapiro-Wilk test and did not show equality of variances between groups; thus, analyses were conducted using non-parametric methods. Statistical comparisons of quantitative data between groups were carried out using the Kruskal-Wallis test using SPSS software version 26.0 (SPSS Inc., Chicago, IL, USA). P-values were adjusted for multiple testing using the Bonferroni correction method and considered significant if $p < 0.05$.

Table 4-4 Antibody source and conditions

Antibody	Isotype	Dilution (time [h], temperature)	Supplier
CD163	Monoclonal Mouse IgG	1:100 (1h RT)	Bio-Rad, UK
CD74	Polyclonal Rabbit IgG	1:200 (1h RT)	Sigma, UK
CD80/B7-1	Monoclonal Mouse IgG_1	1:20 (overnight 4°C)	R&D Systems, UK
CD86/B7-2	Polyclonal goat IgG	1:20 (overnight 4°C)	R&D Systems, UK
CX3CR1	Monoclonal Mouse IgG_1	1:25 (overnight 4°C)	Biolegend, UK
IL-1β	Polyclonal Rabbit IgG	1:200 (1h RT)	Proteintech, UK

Key. RT: room temperature; IL-1β: interleukin 1 beta; κ: Kappa

4.3 Results

4.3.1 NanoString validation of microarray-identified candidate gene expression changes

NanoString is a hybridisation-multiplex digital technology which uses capture probes and unique colour-coded barcode reporter probes to measure almost 800 mRNA in a single reaction. This technology does not require reverse transcription of mRNA or amplification of cDNA.

NanoString was employed to validate gene expression changes identified by microarray transcriptomic profiling. A panel of highly annotated candidate gene expression changes from microarray data analysis and EnrichR dataset focussing on genes associated with both inflammation and antigen presentation was interrogated in PVL versus non-lesional control (LvC), "pre-lesion" versus non-lesional control (PvC) and "pre-lesional" white matter versus PVL (PvL). All analysed samples passed all quality control measures: imaging 99-100% FOV; binding density of 0.14-0.17; and for the positive control linearity, the linear regression R^2 of the samples was 0.99.

4.3.1.1 Nanostring validation of gene expression changes in periventricular lesions compared to non-lesional control white matter.

In PVL versus non-lesional control (LvC), NanoString analysis confirmed the significant differential expression of 7 genes with similar directional change compared to microarray findings. Furthermore, while the expression of 19 genes

was not significantly different between groups, they showed a similar directional change to the microarray findings. Only three genes showed a different, but non-significant, directional change between both platforms Table 4-5.

Upregulation of multiple genes involved in signalling pathways were detected in PVL compared to non-lesional controls, including the significant upregulation of *JUN* (FC= 1.98, p=0.008). In contrast, inflammation-associated genes were significantly downregulated in PVL, including the significant downregulation of *CCL3* (FC= -16.11, p=0.008), *CCR5* (FC= -2.17, p=0.0003), *CX3CR1* (FC= -1.64, p=0.01), *IL-1β* (FC= -4.72, p=0.007), and *PTGS2* (FC= -2.59, p=0.007). The antigen processing and presentation gene *CD74* was also significantly down-regulated in PVL (FC= -1.54, p=0.013).

4.3.1.2 Nanostring validation of gene expression changes in "pre-lesions" compared to non-lesional control white matter

In "pre-lesions" compared to non-lesional control periventricular white matter (PvC), 4 genes displayed a significant differential expression with a similar directional change to the microarray dataset, while 14 genes showed the same directional change but did not reach statistical significance. 11 genes showed a non-significant and different directional change between both platforms, as shown in Table 4-6.

Significant downregulation of genes associated with inflammation were identified, including *PTGS2* (FC= -2.56, p=0.04), *IL-1β* (FC= -4.17, p=0.013), the chemokine ligand *CCL3* (FC= -6.64, p=0.04) and its receptor *CX3CR1* (FC= -1.55, p=0.04).

Table 4-5 Validation of selected candidate genes expression by NanoString nCounter in Lesion compared to non-lesional control

The table shows the comparison between microarray and NanoString using the fold change and P-value.

Lesion compared to Control				
	Microarray		NanoString	
Gene	**FC**	**P-Value**	**FC**	**P-Value**
JUN	1.33	0.008 **	1.98	0.008 **
IKBKB	1.38	0.839	1.88	0.097
AKT3	1.33	0.002 **	1.52	0.128
PHF21A	1.36	0.008 **	1.5	0.121
IFNAR1	1.79	0.004 **	1.25	0.190
OAS1	-1.12	0.829	1.14	0.644
RSAD2	-1.2	0.066	1.09	0.758
IRF7	1.04	0.674	-1.04	0.847
MSR1	-1.95	0.023 *	-1.06	0.878
CD163	-3.27	0.315	-1.07	0.928
IGSF6	-1.27	0.258	-1.12	0.585
CYBB	-1.62	0.013 *	-1.17	0.578
CD8A	-1.28	0.016 *	-1.23	0.568
FCER1G	-1.52	0.077	-1.28	0.265
FGL2	-1.77	0.012 *	-1.29	0.191
EPSTI1	-1.31	0.839	-1.39	0.102
SLAMF8	-1.03	0.680	-1.48	0.327
HLA-DRA	-1.71	0.004 **	-1.51	0.072
CD74	-2.67	0.006 **	-1.54	0.013 *
CX3CR1	-1.5	0.005 **	-1.64	0.010 *
IL1A	-1.06	0.207	-1.71	0.062
COL6A3	-1.62	0.010 *	-1.72	0.075
CCL2	-1.7	0.051 *	-1.88	0.290
CCR5	-1.49	0.016 *	-2.17	0.0003 ***
PTGS2	-1.3	0.011 *	-2.59	0.007 **
FPR1	-2.39	0.017 *	-2.82	0.067
IL1B	-1.34	0.010 *	-4.72	0.007 **
CCL4	-1.16	0.060	-5.14	0.098
CCL3	-1.31	0.052 *	-16.11	0.008 **
ACTB	1.01	0.341	-1.1	0.233
GAPDH	1.08	0.067	1.17	0.067
RPLP0	-1.22	0.565	-1.06	0.584

* $p \leq 0.05$, ** $p \leq 0.01$, ***$p \leq 0.001$, pink represents down-regulated transcripts, green represents up-regulated transcripts

Table 4-6 Validation of selected candidate genes expression by NanoString nCounter in "Pre-lesion" compared to non-lesional control

The table show the comparison between microarray and NanoString using the fold change and P-value.

Pre-lesion compared to Control				
	Microarray		NanoString	
Gene	**FC**	**P-Value**	**FC**	**P-Value**
AKT3	1.34	0.005 **	1.65	0.222
IKBKB	-1.01	0.619	1.63	0.359
PHF21A	-1.05	0.516	1.52	0.397
OAS1	-1.31	0.567	1.24	0.644
IFNAR1	-1.09	0.063	1.16	0.394
IRF7	-1.08	0.564	1.13	0.740
MSR1	-3.13	0.02 *	1.04	0.933
JUN	-1.45	0.599	1.03	0.895
IGSF6	-1.38	0.233	1.02	0.953
FGL2	-1.5	0.03 *	1	0.995
EPSTI1	-1.88	0.030 *	-1.01	0.981
COL6A3	-2.01	0.003 **	-1.06	0.824
FCER1G	-1.59	0.336	-1.3	0.516
CCR5	-1.47	0.082	-1.38	0.540
CX3CR1	-1.39	0.253	-1.55	0.04 *
CD8A	1.05	0.469	-1.62	0.459
IL1A	-1.2	0.071	-1.62	0.461
HLA-DRA	-1.54	0.022 *	-1.63	0.228
CYBB	-1.28	0.048 *	-1.67	0.256
CD74	-1.57	0.018 *	-1.69	0.123
RSAD2	-1.2	0.071	-1.74	0.131
SLAMF8	-1.57	0.044 *	-2.16	0.152
CCL4	1.07	0.959	-2.24	0.360
CCL2	-2.12	0.010 *	-2.38	0.074
PTGS2	-1.15	0.134	-2.56	0.04 *
CD163	-1.97	0.727	-2.8	0.372
FPR1	-1.83	0.044 *	-3.45	0.101
IL1B	-1.26	0.042 *	-4.17	0.013 *
CCL3	-1.2	0.133	-6.64	0.04 *
ACTB	1.09	0.406	-1.18	0.327
GAPDH	-1.1	0.915	1.25	0.308
RPLP0	-1.12	0.249	-1.16	0.541

* $p \leq 0.05$, ** $p \leq 0.01$, ***$p \leq 0.001$, pink represents down-regulated transcripts, green represents up-regulated transcripts

4.3.2 Validation of microarray candidate gene expression by immunohistochemistry

To further validate candidate gene expression, the expression of the proteins encoded by four relevant genes from pathways highlighted by both microarray and NanoString datasets (*CD74*, *IL-1β*, *CD163*, *CD86*) were investigated by immunohistochemistry (Figure 4.2), and the immunoreactive area quantified, as shown in Table 4-7.

CD74 immunoreactivity was a prominent feature of the non-lesional control periventricular white matter and immunolabelled microglia, which displayed a ramified morphology with long processes extending from the cell body Figure 4.2 (A-C). Quantification of the expression of CD74 revealed a significant difference across the three groups (p=0.003), with non-lesional control periventricular white matter containing significantly higher levels of CD74 compared to both "pre-lesions" (p=0.033) and PVL (p=0.003), as shown in Figure 4.3A.

IL-1β, CD163 and CD86 immunoreactivity was positively associated with the cell bodies and extending processes of cells morphologically resembling microglia, as shown in Figure 4.2. Expression of IL-1β (p=0.7), CD163 (p=0.38) and CD86 (p=0.63) immunoreactivity did not significantly vary across the three groups, as shown in Figure 4.3.

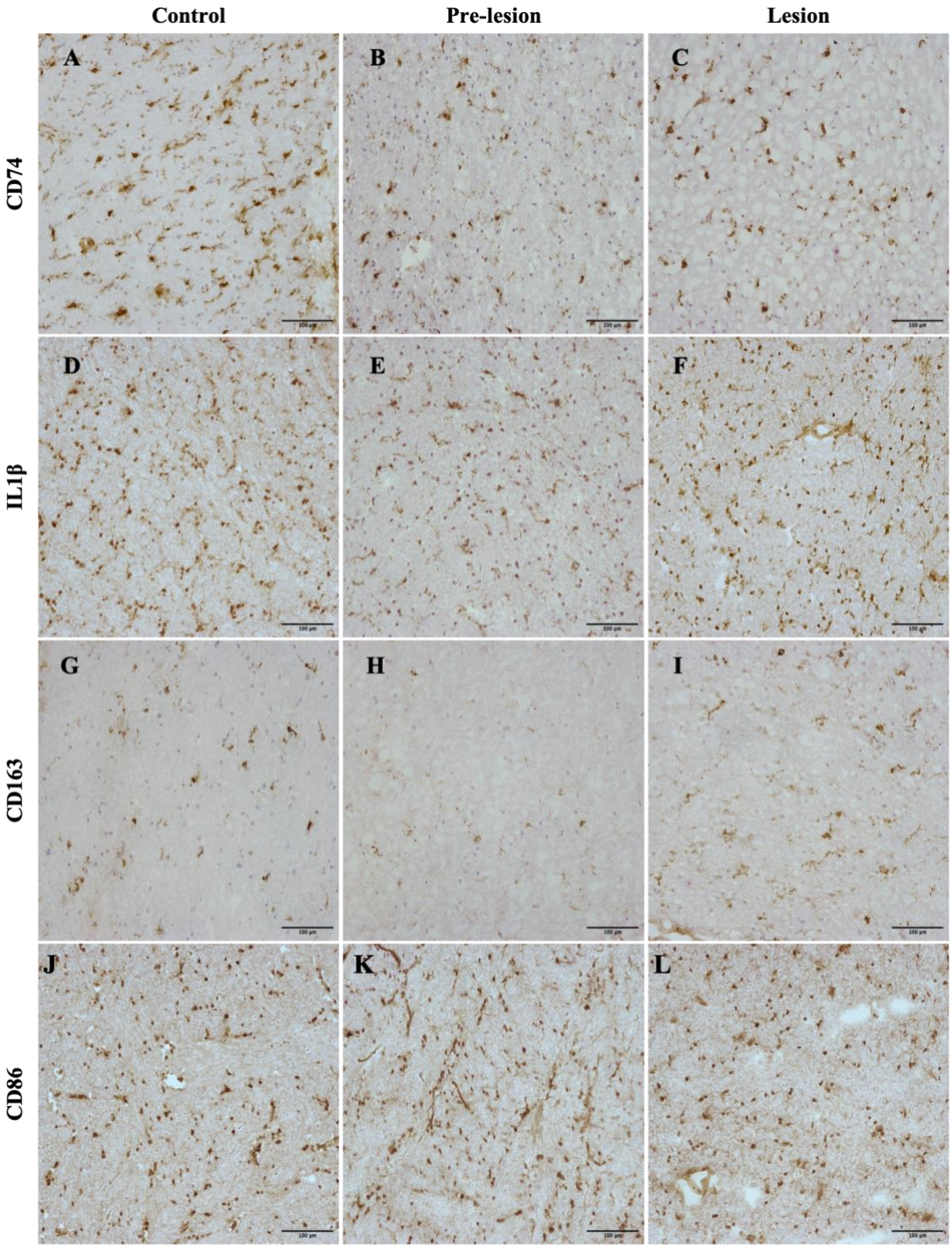

Figure 4.2 Histological validation of candidate gene expression changes

Expression of proteins encoded by candidate genes highlighted by both microarray and NanoString datasets was assessed. (A-C) CD74, (D-F) IL-1β, (G-I) CD163 and (J-L) CD86 positively immunolabelled the cell body and processes of microglial cells in all periventricular white matter groups (control, "pre-lesion" and PVL). *Scale bar represents 100μm*.

Table 4-7 Expression of CD74, IL-1β, CD163 and CD86 in ageing periventricular white matter

The % area of immunoreactivity of each of the markers is shown, median (IQR).

WM group	Control	Pre-lesional	PVL
CD74	3.47 (3.08-4.15)	1.66 (0.9-2.14)	1.3 (1.13-1.66)
IL-1β	3.87 (1.91-4.86)	2.76 (1.91-4.07)	3.43 (2.48-4.22)
CD163	0.93 (0.75-1.21)	0.39 (0.29-1.08)	0.95 (0.59-1.32)
CD86	4.55 (4.52-5.66)	5.34 (3.98-6.23)	5.04 (3.35-6.03)

IQR: inter-quartile range

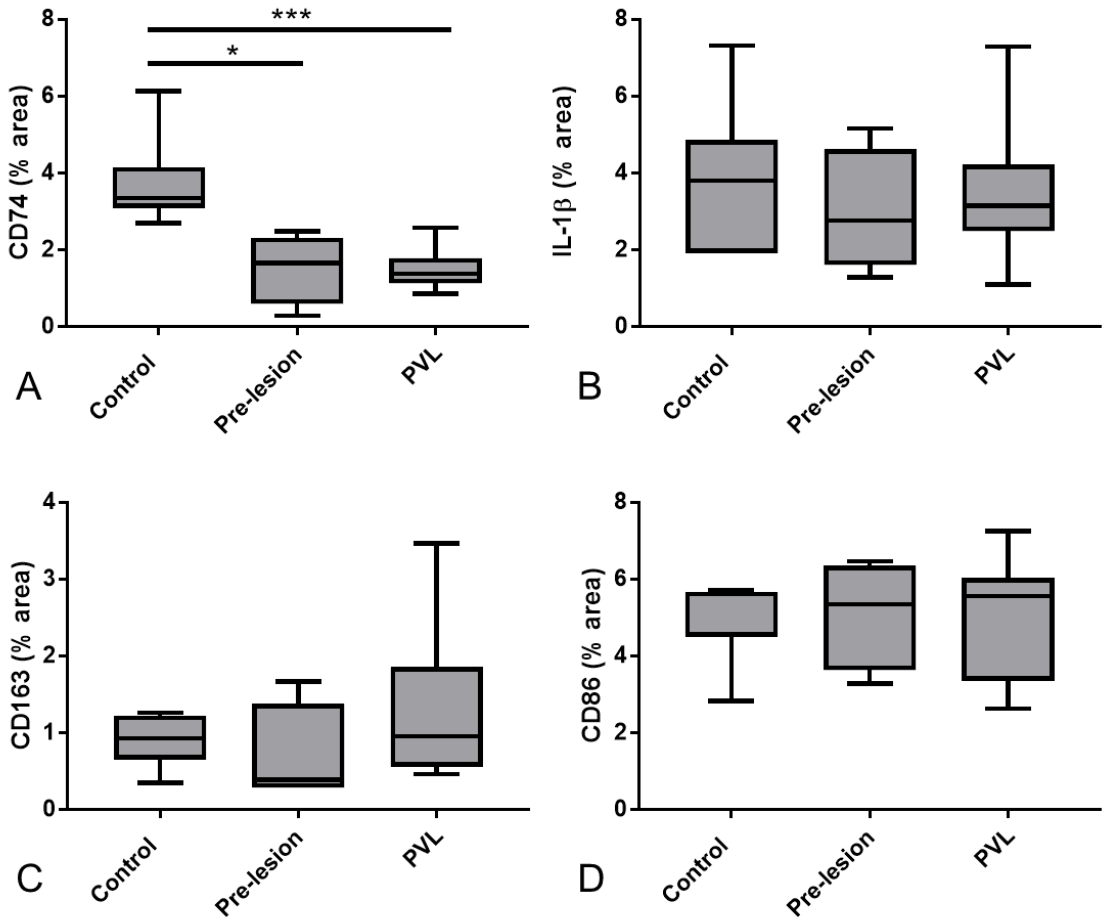

Figure 4.3 Quantitation of the expression of candidates in periventricular white matter

The % area immunoreactivity of the protein encoded by a panel of candidate genes was assessed in the three periventricular white matter groups. (A) CD74 expression was significantly higher in non-lesional control periventricular white matter compared to both "pre-lesional" ($p=0.033$) and PVL ($p=0.003$). The immunoreactive profile of (B) IL-1β, (C) CD163 and (D) CD86 did not significantly differ across the three groups. *$p<0.05$, ***$p<0.005$

4.4 Discussion:

Characterisation of the transcriptomic profile of PVL and "pre-lesions" using microarrays revealed a gene expression signature associated with the significant down-regulation of the immune response, therefore the research presented in this chapter aimed to validate these findings using two independent approaches, namely Nanostring and immunohistochemistry.

The reproducibility between Affymetrix microarray and NanoString technologies is high, as demonstrated by a recent study which revealed a moderate correlation, where 70-80% of genes between both platforms displayed similar gene expression changes (Delmonico *et al.*, 2019). NanoString technology can measure the expression of multiple genes in a single reaction with small amounts of starting material, which is particularly advantageous when analysing LCM-ed post-mortem tissue, where often a limited amount of highly degraded RNA is obtained. Therefore, the current study employed NanoString to validate the expression of a panel of candidate gene expression findings identified by the previous microarray study, examining the expression of 29 selected candidate genes related to inflammation and antigen processing and presentation.

For the NanoString analysis, we selected highly annotated genes generated from microarray data analysis and EnrichR dataset focussing on genes associated with both inflammation and antigen processing and presentation. The majority of selected genes identified by the microarray analysis showed the same directional change with the NanoString, validating the findings from the microarray study. In

PVL compared to non-lesional controls, 24% of the genes revealed a significant differential expression with a similar directional change between NanoString and microarray platforms, and 65% of the genes selected displayed a non-significant but similar directional change. Similarly, in "pre-lesions" compared to non-lesional controls, 13% of the genes revealed a significant differential expression with the same directional change between NanoString and microarray platforms, and 48% of the genes selected displayed a non-significant but similar directional change. Recently, a study using frozen samples revealed a moderate concordance between experiments conducted using both Affymetrix microarrays and NanoString (Chen *et al.*, 2016c). Similarly, a recent study comparing the correlation between next generation sequencing and NanoString examined the expression of 750 genes, and found similar gene expression changes in 734 genes (Bondar *et al.*, 2020). These studies demonstrate moderate concordance and high correlation between both platforms support our findings. Overall, the gene expression changes identified in the NanoString analysis, support the findings of the microarray data analysis, as well as confirming the need to validate transcriptomic datasets using an independent approach.

4.4.1 Both "pre-lesions" and PVL are associated with a significant decrease in the expression of chemokines and their receptors

Nanostring analysis confirmed the significant downregulation of multiple chemokine-related genes in both "pre-lesional" and PVL versus non-lesional controls. One of the essential functions of immune cells is to continuously survey the

brain for any insult, which requires rapid recruitment and migration of cells to the lesion site or to initiate an inflammatory mechanism to help in the damage repairing process. Chemoattractant cytokines, or chemokines, play an important role in the activation and directional migration of cells along a chemotactic gradient (Sorce *et al.*, 2011; Hughes & Nibbs, 2018). Depending on their structure they are subclassified as CXC, CC or CX_3C chemokines, and exert their effect via interacting with their complementary receptors to modulate cellular responses and signal transduction (Hughes & Nibbs, 2018).

Increased chemokine expression is a feature of a number of neurological diseases, including AD, multiple sclerosis (MS), Parkinson's Disease (PD), Motor Neuron Diseases (MND) (Azizi *et al.*, 2014; Liu *et al.*, 2019a; Perner *et al.*, 2018; Cui *et al.*, 2020). However, in contrast to these diseases, both "pre-lesions" and established PVL are associated with a significant decrease in chemokine and chemokine receptor expression, suggesting dysregulation of the immune response and a change in microglial function may contribute to the pathogenesis of age-associated PVL.

CCL3 and CCL4 are members of the β-family of chemokines and act as ligands for the C-C chemokine receptor type 5 (CCR5) (Gu *et al.*, 2016). Binding to CCR5 plays a role in the neuroinflammatory response, including microglial activation (Bokhari *et al.*, 2009; Cui *et al.*, 2020), and recruitment (Hahn *et al.*, 2010). A significant increase in CCR5 expression by microglia has been demonstrated in a mouse model of stroke (Joy *et al.*, 2019), and actively demyelinating lesions in both MS (Simpson *et al.*, 1998; Sørensen *et al.*, 1999) and an animal model of MS (Gu *et al.*, 2016). In

contrast to these studies, significant downregulation of *CCR5* and *CCL3* were detected in established PVL.

Fractalkine or CX3CL1 is a member of the chemokine CX3C that is primarily secreted by neurons. CX3CL1 binds to and activates its receptor CX3CR1, which is mainly expressed and produced by myeloid cells, specifically microglia (Harrison *et al.*, 1998; Garcia *et al.*, 2013), and together they mediate microglia-neuron interactions (Arnoux & Audinat, 2015; Mecca *et al.*, 2018). Activation of CX3CR1 plays a role in regulating the recruitment of microglia to the site of injury (Tang *et al.*, 2014; Ahn *et al.*, 2019), promoting and regulating glial activation (Cardona *et al.*, 2006) and stimulating the secretion of pro-inflammatory cytokines (Blauth *et al.*, 2015; Stuart *et al.*, 2015).

Expression of cytokines, chemokines and their receptors are altered during ageing (Castro-Sánchez *et al.*, 2019). Large-scale transcriptomic profiling of human prefrontal cortex, reveals a significant age-associated downregulation of *CX3CR1* (Primiani *et al.*, 2014), and a similar significant has been demonstrated in the hippocampus of ageing rats (Bachstetter *et al.*, 2011). Furthermore, transcriptomic profiling of a murine model of CX3CR1-deficient microglia found that loss of CX3CR1 impacts antigen presentation and chemokine-chemokine receptor signalling (Gyoneva *et al.*, 2019). For example, CX3CR1 deficient mouse microglia demonstrate impaired phagocytosis and migratory function (Castro-Sánchez *et al.*, 2019).

There is a strong relationship between CX3CR1 and the pro-inflammatory cytokine IL-1β. IL-1β is a pro-inflammatory cytokine which, while playing a major role in tissue repair and cellular defence, is also implicated in a range of pathogenic processes (Hewett *et al.*, 2012). Activation of CX3CR1 triggers the secretion of IL-1β by microglia (Eyo *et al.*, 2017) via the mitogen-activated protein kinase (MAPK) pathway (Clark *et al.*, 2006). The current study revealed the significant downregulation of *CX3CR1* and *IL1B* in both "pre-lesions" and PVL compared to non-lesional control periventricular white matter. While the decreased expression of *CX3CR1* may represent an age-associated disruption of signalling pathways (Norden & Godbout, 2013), it may also indicate the dysregulation or malfunction of microglia in both "pre-lesions" and established PVL.

4.4.2 Down-regulation of antigen processing and presentation is a feature of established PVL

Microarray analysis in the previous chapter indicated that the transcriptomic profile of PVL was associated with significant dysregulation of genes associated with immune function. Downregulation of major histocompatibility complex, class II, DR alpha (*HLA-DRA*), *CD74* and *CD163* in PVL was validated by NanoString technology, but it should be noted that except for *CD74* these changes were non-significant.

CD74 is an MHC-II chaperone that regulates antigen processing and presentation and is highly expressed by microglia in AD patients (Yoshiyama *et al.*, 2000; Bryan *et al.*, 2008). In addition, CD74 interacts with the pro-inflammatory cytokine, macrophage migratory inhibitory factor (MIF) with a high affinity (Leng *et al.*, 2003;

Meza-Romero *et al.*, 2019). MIF is an essential activator for inflammatory processes, promoting the production of cytokines and chemokines (Koda *et al.*, 2004; Zhou *et al.*, 2018). Binding of MIF to CD74 induces multiple signalling pathways, including MAPK, which has been shown to regulate cell survival and proliferation (Bucala & Shachar, 2016) and promote leukocyte migration (Fan *et al.*, 2011).

Our data revealed downregulation of *CD74*, which may result in an inability to bind to MIF, leading to dysregulation of immune response and reduction of migratory chemotactic function. These findings are in line with previous studies which found blocking CD74 results in a reduction of cytokine levels (Trifone *et al.*, 2018), and reduces the migratory response of monocytes to chemokines both *in vivo* and *in vitro* using $MIF^{-/-}$ and $CD74^{-/-}$ mice (Fan *et al.*, 2011).

4.4.3 "Pre-lesions" and PVL are associated with decreased expression of CD74

Further validation of the transcriptomic findings was carried out by selecting four biologically relevant genes from both microarray and NanoString to identify the expression of proteins encoded by the selected candidate genes *CD74, CD163*, *CD86* and *IL1B*.

As discussed previously, CD74 is an MHC-II chaperone that regulates antigen processing and presentation (Yoshiyama *et al.*, 2000; Bryan *et al.*, 2008), and IL-1β is a pro-inflammatory cytokine which plays a major role in regulating the neuroimmune response (Song *et al.*, 2013; Mantovani *et al.*, 2019). The cluster of

differentiation 163 (CD163) is a scavenger receptor mainly expressed by macrophage and monocyte cells (Pey *et al.*, 2014), and is widely regarded as a marker for M2 anti-inflammatory microglia (Wattananit *et al.*, 2016; Kanazawa *et al.*, 2017). CD86 (or B7-2) is expressed by antigen-presenting cells and is associated with M1 pro-inflammatory microglia (Erkenstam *et al.*, 2016).

The immunoreactive profile of these candidates supports other studies demonstrating that microglia are primarily associated with CD74 (Swanson *et al.*, 2020), CD163 (Holfelder *et al.*, 2011; Tippett *et al.*, 2011; Pey *et al.*, 2014; Jing *et al.*, 2018), CD86 (de Haas *et al.*, 2008) and IL-1β (An *et al.*, 2011; Liu & Quan, 2018). mRNA and protein expression can be decoupled in time (Fournier *et al.*, 2010; Koussounadis *et al.*, 2015); however, it has been shown that differentially-expressed transcripts have significantly higher correlations between mRNA and protein levels (Koussounadis *et al.*, 2015). Indeed, the current study confirmed that CD74 is significantly down-regulated in both "pre-lesion" and PVL, at both the mRNA and protein levels.

4.4.4 The mechanisms underlying the pathogenesis of PVL are different to DSCL

Interestingly, the transcriptomic profile identified in the current study of age-associated periventricular pathology is markedly different from the gene expression profile of age-associated deep subcortical white matter pathology. Similar to the PVL profile observed in the current study, microarray analysis of DSCL demonstrates these lesions are associated with the significant differential

expression of immune-regulatory genes (Simpson *et al.*, 2009). However, in contrast to the down-regulation of immune-associated genes observed in established PVL, DSCL are associated with the upregulation of genes involved in antigen presentation (including up-regulation of MHC class II), complement, lymphocyte activation, pro-inflammatory cytokine signalling and phagocytosis (Simpson *et al.*, 2009). These findings highlight the major differences between these WML subtypes and the need to investigate them independently. Their opposing transcriptomic profile suggests that the cellular mechanisms underlying their pathogenesis is different and requires further investigation to fully elucidate these mechanisms and to identify potential novel therapeutic targets.

4.5 Conclusion:

NanoString is a robust profiling technology which enables quantification of mRNA without the use of reverse transcription or amplification of cDNA. The current study employed this technology to validate the transcriptomic profile identified in the microarray analysis, confirming both "pre-lesions" and established PVL are associated with the significant down-regulation of immune-associated genes compared to non-lesional periventricular white matter. We demonstrate that the transcriptomic signature of PVL is distinct from other white matter pathologies and suggest that dysfunction of the immune response plays a role in their pathogenesis.

CHAPTER 5: MAJOR FINDINGS, STUDY LIMITATIONS & FUTURE WORK

5.1 Confluent lesions display a range of microglial profiles

Age-associated white matter lesions, including PVL, DSCL and confluent lesions, which encompass both the periventricular and deep subcortical WM regions, are a common feature of the ageing brain and are significantly associated with cognitive decline (Alber *et al.*, 2019; Kloppenborg *et al.*, 2014). Previous histological studies characterising the microglial profile associated with these lesions demonstrated that PVL are predominantly characterised by MHC-II$^+$ microglia with an immune activated phenotype, while DSCL contains significantly higher levels of CD68$^+$ microglia with a phagocytic phenotype (Simpson *et al.*, 2007a, 2007b; Murray *et al.*, 2012; Waller *et al.*, 2019); however, the microglial phenotype associated with confluent lesions is currently unknown. Therefore, the current study examined the MHC-II and CD68 immunostaining patterns associated with confluent lesions to determine if the immunoreactive profile indicates if these lesions arise as a spread of PVL, DSCL or both. The findings presented in this thesis partially support the original hypothesis that confluent lesions arise as a result of combined PVL and DSCL spread. Four distinct immunoreactive profiles were identified which associate with confluent lesions: (i) MHC II$^+$ and CD68$^+$ microglia primarily associated with the periventricular and deep subcortical regions, respectively; (ii) MHC II$^+$ microglia predominantly throughout the lesion; (iii) CD68$^+$ microglia predominantly throughout the lesion; (iv) a mix of both CD68$^+$ and MHC II$^+$ microglia present throughout the confluent lesion. These microglial profiles demonstrate a range of confluent lesion subtypes which may reflect a spread of DSCL pathology, PVL lesion

pathology or both, suggesting that a variety of mechanisms may be associated with the pathogenesis of confluent lesions.

5.1.1 Study Limitations & Future Work

Several limitations of this study should be acknowledged. The histological characterisation of the microglial phenotype associated with confluent lesions was conducted on 18 cases; however, the 4 profiles identified meant small numbers of cases in each of the 4 groups. Future studies are required to extend the study to include a greater number of cases to enable robust statistical analyses to be performed. While the inter-observer qualitative scoring of confluent lesions showed a moderate agreement, qualitative analysis is subjective to individual interpretation of the staining patterns observed. By extending the number of cases examined, the study would have sufficient power to robustly analyse the quantitative data.

Furthermore, the study examined the expression of just two microglial markers, namely MHC-II and CD68. A comprehensive panel of microglial markers should be employed to fully elucidate the phenotype of age-associated confluent lesions. M1 microglia express the distinctive markers CD74, CD40, CD86, CCR7 (Peferoen *et al.*, 2015), whereas M2 microglia are associated with the expression of mannose receptor and CCL22 (Peferoen *et al.*, 2015; Liu *et al.*, 2018). Extending the study to interrogate the immunoreactive profile of these markers will enable the M1/M2 profile of confluent lesions to be characterised in detail. Additionally, the study should also be extended to assess markers of cerebral hypoxia and BBB dysfunction, thereby investigating potential mechanisms of confluent lesion pathogenesis, as

well as investigating the relevance of these lesions to the risk of depression, stroke and mortality. Understanding how WML arise, particularly the role of microglia in the pathogenesis of WM pathology, may identify novel therapeutic treatments designed to modulate the microglial phenotype.

5.2 Histological characterisation of radiologically normal periventricular white matter detects "Pre-lesional" cases

Radiologically identified normal and PVL cases were sampled and underwent histological characterisation. In support of the literature, the current study demonstrated that demyelination is a prominent feature of PVL as evidenced by the loss of myelin basic protein (Simpson *et al.*, 2007a; Murray *et al.*, 2012). Denudation of ependymal lining is also a feature of PVL (Simpson *et al.*, 2007a), where the loss of ependymal lining, which acts as a barrier between brain parenchyma and cerebral spinal fluid, may lead to back diffusion of CSF into the periventricular region and exacerbate lesion pathogenesis (Shim *et al.*, 2015). Established PVL were also shown to be associated with increased expression of MHC-II^{+} microglia (Simpson *et al.*, 2007b).

Interestingly, four cases of the radiological control samples in the current study, which were rated 0 by consultant radiologists using the Schelten's rating (Scheltens *et al.*, 1993), displayed an increased immunoreactive profile for MHC-II, and were subsequently classified as "pre-lesional".

5.2.1 Study limitations & Future Work

The initial study design was to compare the gene expression profile of PVL compared to non-lesional control periventricular WM. The histological characterisation of control WM identified a subgroup of cases which displayed no evidence of demyelination but contained high levels of MHC-II$^+$ microglia. These cases were subsequently termed "pre-lesional", but it should be acknowledged that it cannot be known whether these cases would have gone on to develop PVL. Future work is required to perform a comprehensive and detailed histological characterisation of these cases and to extend the study to include a larger number of "pre-lesions", as a minimum of 12 samples per group is required for the identification of the significantly differentially expressed genes (Schurch *et al.*, 2016).

5.3 Transcriptomic profiling of PVL and "pre-lesions" identifies dysregulation of the immune response

PVL, control and "pre-lesional" periventricular WM regions were isolated from post-mortem tissue by LCM and their transcriptomic profile assessed by microarray analysis. Surprisingly, despite the increased immunohistochemical detection of MHC-II$^+$ microglia in both the "pre-lesions" and PVL, there was a substantial down-regulation of both antigen processing and presentation, and immune response-related genes. Therefore, subsequent validation experiments were performed to confirm these findings, using NanoString and IHC to validate the candidate genes

and proteins encoded by the selected genes, respectively. A major advantage of Nanostring is that it does not require purification or reverse transcription of RNA (Geiss *et al.*, 2008). The majority of the selected candidate genes were validated using this approach, confirming the dysregulation of immune response pathways in both "pre-lesions" and established PVL.

The transcriptomic profile of the PVL was found to be distinct from DSCL. In contrast to the PVL gene expression profile identified in the current study, microarray analysis of DSCL has demonstrated that these lesions are associated with a significant increase of immune-regulatory genes, including upregulation of antigen presentation, pro-inflammatory cytokine signalling and phagocytosis (Simpson *et al.*, 2009). The significant differences in the transcriptomic profile of PVL compared to DSCL support the original hypothesis that the mechanisms underlying the pathogenesis of PVL are different to DSCL and highlight the need for future studies to assess these WML subgroups independently.

Computational deconvolution analysis in the current study enabled gene expression associated with microglial phenotype to be identified. Inactivated and activated microglia were assessed by identifying a co-expression network of genes associated with the selected candidate microglial markers using GeneMania (Warde-Farley *et al.*, 2010). Our data indicate heterogeneity of the microglial population in the periventricular white matter. Furthermore, the current study reports similarity in expression levels of the co-expressed genes across the control, "pre-lesion" and PVL

samples, with the exception of CD80, leading us to reject the original hypothesis that microglia within PVL adapt a neurotoxic M1 phenotype.

5.3.1 Study limitations & Future Work

The current project assessed the transcriptomic profile associated with microglia in age-associated periventricular white matter. Gene expression studies are sensitive to RNA quality which can be impacted by several factors, including PMD and brain pH (Mexal *et al.*, 2006; Ferreira *et al.*, 2018). Furthermore, the LCM technique itself can affect RNA integrity, as demonstrated by the decline in RNA integrity number following LCM in our samples. This finding supports other studies which demonstrate a decline in RNA integrity following LCM (Waller *et al.*, 2012; Mazurek *et al.*, 2013). However, while there are clearly limitations to using this approach, it should also be acknowledged that microarray analysis of post-mortem tissue is a valuable tool to identify novel mechanisms potentially underlying specific pathologies.

It should also be acknowledged that the approach used in the current study isolated the entire periventricular region using LCM and will therefore have isolated RNA from a heterogeneous population of cells, including astrocytes. Astrocytes share several functional similarities with microglia, including contributing to the immune response (Fakhoury, 2018; Vainchtein & Molofsky, 2020). Future studies should be employed to perform single-cell transcriptomic analysis, specifically examining the gene expression profile of microglia within the periventricular region using an immuno-LCM methodology. This method enables the isolation of immunolabelled

microglia from frozen post-mortem tissue (Waller *et al.*, 2012; Simpson *et al.*, 2018). Transcriptomic analysis using microarray or RNA-Seq would then enable microglial gene expression changes to be confirmed, validating their role in age-associated periventricular white matter pathology. Alternatively, a comprehensive panel of significantly differentially expressed genes should be validated at the protein level by immunohistochemistry to enable the association of candidate gene expression changes with microglia to be confirmed.

5.4 Upregulation of calcium and glutamate signalling pathways in "pre-lesions" may be a neuroprotective response to prevent the pathogenesis of PVL.

Microglia respond to a number of extracellular stimuli, leading to an increase in their intracellular calcium, which provides energy and induces the release of adenosine triphosphate (ATP). Increased levels of ATP regulate multiple signalling pathways which may promote physiological and protective mechanisms (Butt *et al.*, 2014), as well as promoting microglial migration to sites of injuries (Sieger *et al.*, 2012).

Transcriptomic profiling of "pre-lesions" identified the significant upregulation of genes associated with signalling pathways, including calcium and glutamate. Calcium signalling is essential in maintaining homeostasis in the CNS (Zündorf & Reiser, 2011). A reduction in calcium signalling induces multiple physiological changes, including loss of white matter integrity, by inducing oligodendrocyte damage and axonal dysfunction (Baltan, 2009); thus, significant upregulation of

calcium signalling in "pre-lesional" periventricular white matter may reflect a neuroprotective effect to prevent the pathogenesis of PVL.

Glutamate released from axons promotes myelination by binding to AMPA receptors to mediate synaptic transmissions (Scheefhals & MacGillavry, 2018). The current study revealed a significant upregulation of glutamatergic synaptic genes in "pre-lesional" white matter, suggesting a potential mechanism to maintain myelin integrity and prevent lesion pathogenesis.

5.4.1 Study Limitations & Future work

Although recent advances in technologies enable gene expression changes in post-mortem tissue to be identified, the profiling of this tissue (frequently with low RNA quality and at end-stage of disease) does not enable researchers to assess potentially relevant changes at all stages of disease progression. Therefore, the use of an appropriate animal model could be used to interrogate and confirm the gene expression profile at different stages of PVL formation. The C57BL/6J mouse model is highly vulnerable to cerebral ischemia and displays WM pathology. Small focal periventricular white matter lesions have been induced in this model by injecting the vasoconstrictor endothelin-1, which result in gliosis and microglial activation at the site of injury (Ahmad *et al.*, 2015). Interrogation of this model at various stages of PVL formation would enable changes in signalling pathways to be confirmed at "pre-lesional" stages. Furthermore, studies to manipulate the microglial phenotype should be conducted with the aim of delaying or preventing lesion formation.

5.5 Summary of the major findings

While transcriptomic profiling of DSCL has previously been performed to identify the underlying mechanisms associated with the formation of these lesions (Simpson *et al.*, 2009), the current study is the first in the field to employ this approach and identify gene expression changes which may underlie the formation of PVL. The research presented in this thesis suggests that established PVL are part of a continuous spectrum of white matter injury and that increased signalling pathways in "pre-lesions", including calcium and glutamate signalling, may play a neuroprotective role to prevent the formation of PVL.

REFERENCES

Ahmad, A.S., Satriotomo, I., Fazal, J.A., Nadeau, S.E., Doré, S., et al. (2015). Optimization of a Clinically Relevant Model of White Matter Stroke in Mice: Histological and Functional Evidences. *Journal of neurology and neurosurgery*. 2 (2): 114.

Ahn, J.H., Kim, D.W., Park, J.H., Lee, T.K., Lee, H.A., et al. (2019). Expression changes of CX3CL1 and CX3CR1 proteins in the hippocampal CA1 field of the gerbil following transient global cerebral ischemia. *International Journal of Molecular Medicine*. 44 (3): 939–948.

Ajami, B., Samusik, N., Wieghofer, P., Ho, P.P., Crotti, A., et al. (2018). Single-cell mass cytometry reveals distinct populations of brain myeloid cells in mouse neuroinflammation and neurodegeneration models. *Nature Neuroscience*. 21: 541–551.

Akashi, T., Takahashi, S., Mugikura, S., Sato, S., Murata, T., et al. (2017). Ischemic White Matter Lesions Associated With Medullary Arteries: Classification of MRI Findings Based on the Anatomic Arterial Distributions. *American Journal of Roentgenology*. 209 (3): W160–W168.

Akiguchi, I., Tomimoto, H., Suenaga, T., Wakita, H. & Budka, H. (1998). Blood-brain barrier dysfunction in Binswanger's disease; An immunohistochemical study. *Acta Neuropathologica*. 95 (1): 78–84.

Al-Mashhadi, S., Simpson, J.E., Heath, P.R., Dickman, M., Forster, G., et al. (2015). Oxidative glial cell damage associated with white matter lesions in the aging human brain. *Brain Pathology*. 25 (5): 565–574.

Alber, J., Alladi, S., Bae, H.J., Barton, D.A., Beckett, L.A., et al. (2019). White matter hyperintensities in vascular contributions to cognitive impairment and dementia (VCID): Knowledge gaps and opportunities. *Alzheimer's and Dementia: Translational Research and Clinical Interventions*. 5: 107–117.

Almolda, B., Gonzalez, B. & Castellano, B. (2011). Antigen presentation in EAE: Role of microglia, macrophages and dendritic cells. *Frontiers in Bioscience*. 16 (3): 1157–1171.

An, Y., Chen, Q. & Quan, N. (2011). Interleukin-1 exerts distinct actions on different

cell types of the brain in vitro. *Journal of Inflammation Research*. 4 (1): 11–20.

Angelova, D.M. & Brown, D.R. (2019). Microglia and the aging brain: are senescent microglia the key to neurodegeneration? *Journal of Neurochemistry*. 151 (6): 676–688.

Aquino, D.A., Capello, E., Weisstein, J., Sanders, V., Lopez, C., et al. (1997). Multiple sclerosis: Altered expression of 70- and 27-kDa heat shock proteins in lesions and myelin. *Journal of Neuropathology and Experimental Neurology*. 56 (6): 664–672.

Arnoux, I. & Audinat, E. (2015). Fractalkine Signaling and Microglia Functions in the Developing Brain. *Neural Plasticity*. 2015: 689404.

Askew, K. & Gomez-Nicola, D. (2018). A story of birth and death: Insights into the formation and dynamics of the microglial population. *Brain, Behavior, and Immunity*. 69: 9–17.

Auriel, E., Csiba, L., Berenyi, E., Varkonyi, I., Mehes, G., et al. (2012). Leukoaraiosis is associated with arterial wall thickness: a quantitative analysis. *Neuropathology : official journal of the Japanese Society of Neuropathology*. 32 (3): 227–33.

Avila Cobos, F., Vandesompele, J., Mestdagh, P. & De Preter, K. (2018). Computational deconvolution of transcriptomics data from mixed cell populations. *Bioinformatics*. 34 (11): 1969–1979.

Azizi, G., Khannazer, N. & Mirshafiey, A. (2014). The potential role of chemokines in alzheimer's disease pathogenesis. *American Journal of Alzheimer's Disease and other Dementias*. 29 (5): 415–425.

Bachstetter, A.D., Morganti, J.M., Jernberg, J., Schlunk, A., Mitchell, S.H., et al. (2011). Fractalkine and CX3CR1 regulate hippocampal neurogenesis in adult and aged rats. *Neurobiology of Aging*. 32 (11): 2030–2044.

Baezner, H., Blahak, C., Poggesi, A., Pantoni, L., Inzitari, D., et al. (2008). Association of gait and balance disorders with age-related white matter changes: The LADIS Study. *Neurology*. 70 (12): 935–942.

Baltan, S. (2009). Ischemic injury to white matter: An age-dependent process. *Neuroscientist*. 15 (2): 126–133.

Baraban, M., Koudelka, S. & Lyons, D.A. (2018). Ca 2+ activity signatures of myelin

sheath formation and growth in vivo. *Nature Neuroscience*. 21 (1): 19–25.

Barber, R., Scheltens, P., Gholkar, A., Ballard, C., McKeith, I., et al. (1999). White matter lesions on magnetic resonance imaging in dementia with Lewy bodies, Alzheimer's disease, vascular dementia, and normal aging. *Journal of Neurology Neurosurgery and Psychiatry*. 67 (1): 66–72.

Barkhof, F. & Scheltens, P. (2006). Is the whole brain periventricular? *Journal of Neurology, Neurosurgery & Psychiatry*. 77 (2): 143–144.

Baron, R., Babcock, A.A., Nemirovsky, A., Finsen, B. & Monsonego, A. (2014). Accelerated microglial pathology is associated with Aβ plaques in mouse models of Alzheimer's disease. *Aging Cell*. 13 (4): 584–595.

Barrett, T., Wilhite, S.E., Ledoux, P., Evangelista, C., Kim, I.F., et al. (2013). NCBI GEO: Archive for functional genomics data sets - Update. *Nucleic Acids Research*. 41 (D1): D991–D995.

Bartzokis, G. (2011). Alzheimer's disease as homeostatic responses to age-related myelin breakdown. *Neurobiology of Aging*. 32 (8) p.1341–1371.

Basile, A.M., Pantoni, L., Pracucci, G., Asplund, K., Chabriat, H., et al. (2006). Age, hypertension, and lacunar stroke are the major determinants of the severity of age-related white matter changes: The LADIS (Leukoaraiosis and Disability in the Elderly) study. *Cerebrovascular Diseases*. 21 (5–6): 315–322.

Bell, K.F.S., Bent, R.J., Meese-Tamuri, S., Ali, A., Forder, J.P. & Aarts, M.M. (2013). Calmodulin kinase IV-dependent CREB activation is required for neuroprotection via NMDA receptor-PSD95 disruption. *Journal of Neurochemistry*. 126 (2): 274–287.

Van Den Bergh, R. (1969). Centrifugal elements in the vascular pattern of the deep intracerebral blood supply. *Angiology*. 20 (2): 88–94.

von Bernhardi, R. (2007). Glial cell dysregulation: A new perspective on Alzheimer disease. *Neurotoxicity Research*. 12 (4): 215–232.

Bezprozvanny, I. (2009). Calcium signaling and neurodegenerative diseases. *Trends in Molecular Medicine*. 15 (3): 89–100.

Biffi, A. & Greenberg, S.M. (2011). Cerebral amyloid angiopathy: A systematic review. *Journal of Clinical Neurology*. 7 (1): 1–9.

Black, S., Gao, F. & Bilbao, J. (2009). Understanding white matter disease: Imaging-

pathological correlations in vascular cognitive impairment. In: *Stroke*. 2009, S48–S52.

Blalock, E.M., Buechel, H.M., Popovic, J., Geddes, J.W. & Landfield, P.W. (2011). Microarray analyses of laser-captured hippocampus reveal distinct gray and white matter signatures associated with incipient Alzheimer's disease. *Journal of Chemical Neuroanatomy*. 42 (2): 118–126.

Blauth, K., Zhang, X., Chopra, M., Rogan, S. & Markovic-Plese, S. (2015). The role of fractalkine (CX3CL1) in regulation of CD4+ cell migration to the central nervous system in patients with relapsing-remitting multiple sclerosis. *Clinical Immunology*. 157 (2): 121–132.

Block, M.L., Zecca, L. & Hong, J.S. (2007). Microglia-mediated neurotoxicity: Uncovering the molecular mechanisms. *Nature Reviews Neuroscience*. 8 (1): 57–69.

Boche, D., Perry, V.H. & Nicoll, J.A.R. (2013). Review: Activation patterns of microglia and their identification in the human brain. *Neuropathology and Applied Neurobiology*. 39 (1): 3–18.

Bokhari, S.M., Yao, H., Bethel-Brown, C., Fuwang, P., Williams, R., et al. (2009). Morphine enhances Tat-induced activation in murine microglia. *Journal of NeuroVirology*. 15 (3): 219–228.

Bolandzadeh, N., Davis, J.C., Tam, R., Handy, T.C. & Liu-Ambrose, T. (2012). The association between cognitive function and white matter lesion location in older adults: a systematic review. *BMC Neurology*. 12 (1): 126.

Bondar, G., Xu, W., Elashoff, D., Li, X., Faure-Kumar, E., et al. (2020). Comparing NGS and NanoString platforms in peripheral blood mononuclear cell transcriptome profiling for advanced heart failure biomarker development. *Journal of Biological Methods*. 7 (1): e123.

Borda, J.T., Alvarez, X., Mohan, M., Hasegawa, A., Bernardino, A., et al. (2008). CD163, a marker of perivascular macrophages, is up-regulated by microglia in simian immunodeficiency virus encephalitis after haptoglobin-hemoglobin complex stimulation and is suggestive of breakdown of the blood-brain barrier. *American Journal of Pathology*. 172 (3): 725–737.

Böttcher, C., Schlickeiser, S., Sneeboer, M., Kunkel, D., Knop, A., et al. (2019). Human

microglia regional heterogeneity and phenotypes determined by multiplexed single-cell mass cytometry. *Nature Neuroscience*. 22 (1): 78–90.

Boyle, P.A., Yu, L., Nag, S., Leurgans, S., Wilson, R.S., et al. (2015). Cerebral amyloid angiopathy and cognitive outcomes in community-based older persons. *Neurology*. 85 (22): 1930–1936.

Braak, H. & Braak, E. (1991). Neuropathological stageing of Alzheimer-related changes. *Acta Neuropathologica*. 82 (4): 239–259.

Brayne, C., McCracken, C. & Matthews, F.E. (2006). Cohort profile: The medical research council cognitive function and ageing study (CFAS). *International Journal of Epidemiology*. 35 (5): 1140–1145.

Brickman, A.M. (2013). Contemplating Alzheimer's Disease and the Contribution of White Matter Hyperintensities. *Current Neurology and Neuroscience Reports*. 13 (12): 415.

Brown, R.C. & Davis, T.P. (2002). Calcium modulation of adherens and tight junction function: A potential mechanism for blood-brain barrier disruption after stroke. *Stroke*. 33 (6): 1706–1711.

Bryan, K.J., Zhu, X., Harris, P.L., Perry, G., Castellani, R.J., et al. (2008). Expression of CD74 is increased in neurofibrillary tangles in Alzheimer's disease. *Molecular Neurodegeneration*. 3 (1).

Bucala, R. & Shachar, I. (2016). The Integral Role of CD74 in Antigen Presentation, MIF Signal Transduction, and B Cell Survival and Homeostasis. *Mini-Reviews in Medicinal Chemistry*. 14 (14): 1132–1138.

Burns, J.M., Church, J. a, Johnson, D.K., Xiong, C., Marcus, D., et al. (2005). White matter lesions are prevalent but differentially related with cognition in aging and early Alzheimer disease. *Archives of neurology*. 62: 1870–1876.

Busse, S., Steiner, J., Alter, J., Dobrowolny, H., Mawrin, C., et al. (2015). Expression of HLA-DR, CD80, and CD86 in Healthy Aging and Alzheimer's Disease. *Journal of Alzheimer's Disease*. 47 (1): 177–184.

Butt, A.M., Fern, R.F. & Matute, C. (2014). Neurotransmitter signaling in white matter. *Glia*. 62 (11): 1762–1779.

Caceres, J.A. & Goldstein, J.N. (2012). Intracranial Hemorrhage. *Emergency Medicine Clinics of North America*. 30 (3): 771–794.

Callisaya, M.L., Beare, R., Phan, T., Blizzard, L., Thrift, A.G., et al. (2015). Progression of white matter hyperintensities of presumed vascular origin increases the risk of falls in older people. *Journals of Gerontology - Series A Biological Sciences and Medical Sciences*. 70 (3): 360–366.

Calvo-Rodriguez, M., Hou, S.S., Snyder, A.C., Kharitonova, E.K., Russ, A.N., et al. (2020). Increased mitochondrial calcium levels associated with neuronal death in a mouse model of Alzheimer's disease. *Nature Communications*. 11 (1): 2146.

Cardona, A.E., Pioro, E.P., Sasse, M.E., Kostenko, V., Cardona, S.M., et al. (2006). Control of microglial neurotoxicity by the fractalkine receptor. *Nature Neuroscience*. 9 (7): 917–924.

Casamassimi, A., Federico, A., Rienzo, M., Esposito, S. & Ciccodicola, A. (2017). Transcriptome profiling in human diseases: New advances and perspectives. *International Journal of Molecular Sciences*. 18 (8): 1652.

Case, N.F., Charlton, A., Zwiers, A., Batool, S., McCreary, C.R., et al. (2016). Cerebral Amyloid Angiopathy is Associated with Executive Dysfunction and Mild Cognitive Impairment. *Stroke*. 47 (8): 2010–2016.

Castro-Sánchez, S., García-Yagüe, Á.J., Kügler, S. & Lastres-Becker, I. (2019). CX3CR1-deficient microglia shows impaired signalling of the transcription factor NRF2: Implications in tauopathies. *Redox Biology*. 22: 101118.

Chagas, L. da S., Sandre, P.C., Ribeiro, N.C.A.R.E., Marcondes, H., Silva, P.O., et al. (2020). Environmental signals on microglial function during brain development, neuroplasticity, and disease. *International Journal of Molecular Sciences*. 21 (6).

Chen, A., Akinyemi, R.O., Hase, Y., Firbank, M.J., Ndung'u, M.N., et al. (2016a). Frontal White matter hyperintensities, clasmatodendrosis and gliovascular abnormalities in ageing and post-stroke dementia. *Brain*. 139 (1): 242–258.

Chen, J.T., Lin, Y.L., Chen, T.L., Tai, Y.T., Chen, C.Y. & Chen, R.M. (2016b). Ketamine alleviates bradykinin-induced disruption of the mouse cerebrovascular endothelial cell-constructed tight junction barrier via a calcium-mediated redistribution of occludin polymerization. *Toxicology*. 368–369: 142–151.

Chen, P.S., McQuoid, D.R., Payne, M.E. & Steffens, D.C. (2006). White matter and subcortical gray matter lesion volume changes and late-life depression

outcome: a 4-year magnetic resonance imaging study. *International Psychogeriatrics / IPA*. 18 (3): 445–56.

Chen, X., Deane, N.G., Lewis, K.B., Li, J., Zhu, J., et al. (2016c). Comparison of Nanostring nCounter® Data on FFPE Colon Cancer Samples and Affymetrix Microarray Data on Matched Frozen Tissues. *PLOS ONE*. 11 (5): e0153784.

Chen, X.X., Chen, Y., Xu, M., Yu, T. & Li, J. (2018). The impact of intracerebral hemorrhage on the progression of white matter hyperintensity. *Frontiers in Human Neuroscience*. 12: 471.

Chevyreva, I., Faull, R.L.M., Green, C.R. & Nicholson, L.F.B. (2008). Assessing RNA quality in postmortem human brain tissue. *Experimental and Molecular Pathology*. 84 (1): 71–77.

Cipolla, M.J. (2009). *The Cerebral Circulation*. San Rafael, CA: Morgan & Claypool Life Sciences.

Clapham, D.E. (1995). Calcium signaling. *Cell*. 80 (2): 259–268.

Clark, A.K., D'Aquisto, F., Gentry, C., Marchand, F., McMahon, S.B. & Malcangio, M. (2006). Rapid co-release of interleukin 1β and caspase 1 in spinal cord inflammation. *Journal of Neurochemistry*. 99 (3): 868–880.

Combrinck, M.I., Perry, V.H. & Cunningham, C. (2002). Peripheral infection evokes exaggerated sickness behaviour in pre-clinical murine prion disease. *Neuroscience*. 112 (1): 7–11.

Corraini, P., Henderson, V.W., Ording, A.G., Pedersen, L., Horváth-Puhó, E. & Sørensen, H.T. (2017). Long-term risk of dementia among survivors of ischemic or hemorrhagic stroke. *Stroke*. 48 (1): 180–186.

Cribbs, D.H., Berchtold, N.C., Perreau, V., Coleman, P.D., Rogers, J., et al. (2012). Extensive innate immune gene activation accompanies brain aging, increasing vulnerability to cognitive decline and neurodegeneration: a microarray study. *Journal of Neuroinflammation*. 9 (1): 179.

Cuccaro, D., Guarnaccia, M., Iemmolo, R., D`Agata, V. & Cavallaro, S. (2018). NeuroArray, A Custom CGH Microarray to Decipher Copy Number Variants in Alzheimer's Disease. *Current Genomics*. 19 (6): 499–504.

Cui, L.-Y.Y., Chu, S.-F.F. & Chen, N.-H.H. (2020). The role of chemokines and chemokine receptors in multiple sclerosis. *International Immunopharmacology*.

83: 106314.

Cunningham, C., Campion, S., Lunnon, K., Murray, C.L., Woods, J.F.C., et al. (2009). Systemic Inflammation Induces Acute Behavioral and Cognitive Changes and Accelerates Neurodegenerative Disease. *Biological Psychiatry*. 65 (4): 304–312.

Damani, M.R., Zhao, L., Fontainhas, A.M., Amaral, J., Fariss, R.N. & Wong, W.T. (2011). Age-related alterations in the dynamic behavior of microglia. *Aging Cell*. 10 (2): 263–276.

Davies, D.S., Ma, J., Jegathees, T. & Goldsbury, C. (2017). Microglia show altered morphology and reduced arborization in human brain during aging and Alzheimer's disease. *Brain Pathology*. 27 (6): 795–808.

Debette, S. & Markus, H.S. (2010). The clinical importance of white matter hyperintensities on brain magnetic resonance imaging: Systematic review and meta-analysis. *BMJ*. 341: c3666.

Decarlo, K., Emley, A., Dadzie, O.E. & Mahalingam, M. (2011). Laser capture microdissection: Methods and applications. In: G. I. Murray (ed.). *Methods in Molecular Biology*. Totowa, NJ: Humana Press, 1–15.

Delmonico, L., Attiya, S., Chen, J.W., Obenauer, J.C., Goodwin, E.C. & Fournier, M. V. (2019). Expression Concordance of 325 Novel RNA Biomarkers between Data Generated by NanoString nCounter and Affymetrix GeneChip. *Disease Markers*. 2019: 1940347.

DeTure, M.A. & Dickson, D.W. (2019). The neuropathological diagnosis of Alzheimer's disease. *Molecular Neurodegeneration*. 14 (1): 32.

DiBona, V.L., Zhu, W., Shah, M.K., Rafalia, A., Ben Cheikh, H., et al. (2019). Loss of Par1b/MARK2 primes microglia during brain development and enhances their sensitivity to injury. *Journal of Neuroinflammation*. 16 (1): 11.

Van Dijk, E.J., Breteler, M.M.B., Schmidt, R., Berger, K., Nilsson, L.G., et al. (2004). The association between blood pressure, hypertension, and cerebral white matter lesions: Cardiovascular determinants of dementia study. *Hypertension*. 44 (5): 625–630.

Van Dijk, E.J., Prins, N.D., Vrooman, H.A., Hofman, A., Koudstaal, P.J. & Breteler, M.M.B. (2008). Progression of cerebral small vessel disease in relation to risk factors and cognitive consequences: Rotterdam scan study. *Stroke*. 39 (10): 2712–

2719.

Ding, C. & Cantor, C.R. (2004). Quantitative Analysis of Nucleic Acids - the Last Few Years of Progress. *Journal of Biochemistry and Molecular Biology*. 37 (1): 1–10.

Douglas Fields, R. (2015). A new mechanism of nervous system plasticity: activity-dependent myelination. *Nature Reviews Neuroscience*. 16 (12): 756–767.

Dufouil, C., de Kersaint-Gilly, A., Besançon, V., Levy, C., Auffray, E., et al. (2001). Longitudinal study of blood pressure and white matter hyperintensities: the EVA MRI Cohort. *Neurology*. 56 (7): 921–6.

Duncombe, J., Kitamura, A., Hase, Y., Ihara, M., Kalaria, R.N. & Horsburgh, K. (2017). Chronic cerebral hypoperfusion: A key mechanism leading to vascular cognitive impairment and dementia. Closing the translational gap between rodent models and human vascular cognitive impairment and dementia. *Clinical Science*. 131 (19): 2451–2468.

Engelhardt, B. & Sorokin, L. (2009). The blood-brain and the blood-cerebrospinal fluid barriers: Function and dysfunction. *Seminars in Immunopathology*. 31 (4): 497–511.

Erkenstam, N.H., Smith, P.L.P., Fleiss, B., Nair, S., Svedin, P., et al. (2016). Temporal characterization of microglia/macrophage phenotypes in a mouse model of neonatal hypoxic-ischemic brain injury. *Frontiers in Cellular Neuroscience*. 10: 286.

Eyo, U.B., Peng, J., Murugan, M., Mo, M., Lalani, A., et al. (2017). Regulation of Physical Microglia-Neuron Interactions by Fractalkine Signaling after Status Epilepticus. *eNeuro*. 3 (6): ENEURO.0209-16.2016.

Fadul, M. (2016). *Characterising NDRG2 expression and defining transcriptomic profile of NDRG2+ astrocytes in the aging brain*. Master's Thesis. University of Sheffield.

Fakhoury, M. (2018). Microglia and Astrocytes in Alzheimer's Disease: Implications for Therapy. *Current neuropharmacology*. 16 (5): 508–518.

Fan, H., Hall, P., Santos, L.L., Gregory, J.L., Fingerle-Rowson, G., et al. (2011). Macrophage Migration Inhibitory Factor and CD74 Regulate Macrophage Chemotactic Responses via MAPK and Rho GTPase. *The Journal of Immunology*. 186 (8): 4915–4924.

Farkas, E., Donka, G., de Vos, R.A.I., Mihály, A., Bari, F. & Luiten, P.G.M. (2004). Experimental cerebral hypoperfusion induces white matter injury and microglial activation in the rat brain. *Acta Neuropathologica*. 108 (1): 57–64.

Fazekas, F. (2014). Incidental periventricular white matter hyperintensities revisited: What detailed morphologic image analyses can tell us. *American Journal of Neuroradiology*. 35 (1): 63–64.

Fazekas, F., Chawluk, J.B. & Alavi, A. (1987). MR signal abnormalities at 1.5 T in Alzheimer's dementia and normal aging. *American Journal of Neuroradiology*. 8 (3) p.421–426.

Fazekas, F., Kleinert, R., Offenbacher, H., Payer, F., Schmidt, R., et al. (1991). The morphologic correlate of incidental punctate white matter hyperintensities on MR images. *American Journal of Roentgenology*. 157 (6): 1317–1323.

Fazekas, F., Niederkorn, K., Schmidt, R., Offenbacher, H., Homer, S., et al. (1988). White matter signal abnormalities in normal individuals: Correlation with carotid ultrasonography, cerebral blood flow measurements, and cerebrovascular factors. *Stroke*. 19 (10): 1285–1288.

Fernando, M.S. & Ince, P.G. (2004). Vascular pathologies and cognition in a population-based cohort of elderly people. *Journal of the Neurological Sciences*. 226 (1-2 SPEC.ISS.): 13–17.

Fernando, M.S., O'Brien, J.T., Perry, R.H., English, P., Forster, G., et al. (2004). Comparison of the pathology of cerebral white matter with post-mortem magnetic resonance imaging (MRI) in the elderly brain. *Neuropathology and Applied Neurobiology*. 30 (4): 385–395.

Fernando, M.S., Simpson, J.E., Matthews, F., Brayne, C., Lewis, C.E., et al. (2006). White matter lesions in an unselected cohort of the elderly: Molecular pathology suggests origin from chronic hypoperfusion injury. *Stroke*. 37 (6): 1391–1398.

Ferreira, P.G., Muñoz-Aguirre, M., Reverter, F., Sá Godinho, C.P., Sousa, A., et al. (2018). The effects of death and post-mortem cold ischemia on human tissue transcriptomes. *Nature Communications*. 9 (1): 490.

Filley, C.M. & Fields, R.D. (2016). White matter and cognition: Making the connection. *Journal of Neurophysiology*. 116 (5): 2093–2104.

Floden, A.M. & Combs, C.K. (2011). Microglia demonstrate age-dependent interaction with amyloid-beta fibrils. *Journal of Alzheimer's Disease*. 25 (2): 279–293.

Fournier, M.L., Paulson, A., Pavelka, N., Mosley, A.L., Gaudenz, K., et al. (2010). Delayed correlation of mRNA and protein expression in rapamycin-treated cells and a role for Ggc1 in cellular sensitivity to rapamycin. *Molecular and Cellular Proteomics*. 9 (2): 271–284.

Frank, M.G., Barrientos, R.M., Biedenkapp, J.C., Rudy, J.W., Watkins, L.R. & Maier, S.F. (2006). mRNA up-regulation of MHC II and pivotal pro-inflammatory genes in normal brain aging. *Neurobiology of Aging*. 27 (5): 717–722.

Freeze, W.M., Jacobs, H.I.L., de Jong, J.J., Verheggen, I.C.M., Gronenschild, E.H.B.M., et al. (2020). White matter hyperintensities mediate the association between blood-brain barrier leakage and information processing speed. *Neurobiology of Aging*. 85: 113–122.

French, H.M., Reid, M., Mamontov, P., Simmons, R.A. & Grinspan, J.B. (2009). Oxidative stress disrupts oligodendrocyte maturation. *Journal of Neuroscience Research*. 87 (14): 3076–3087.

Friedman, B.A., Srinivasan, K., Ayalon, G., Meilandt, W.J., Lin, H., et al. (2018). Diverse Brain Myeloid Expression Profiles Reveal Distinct Microglial Activation States and Aspects of Alzheimer's Disease Not Evident in Mouse Models. *Cell Reports*. 22 (3): 832–847.

Funaki, T. & Miyamoto, S. (2021). Periventricular Anastomosis. In: *Moyamoya Disease: Current Knowledge and Future Perspectives*. Springer Singapore, 155–166.

Furuse, M., Hirase, T., Itoh, M., Nagafuchi, A., Yonemura, S., et al. (1993). Occludin: A novel integral membrane protein localizing at tight junctions. *Journal of Cell Biology*. 123 (6 II): 1777–1788.

Galatro, T.F., Holtman, I.R., Lerario, A.M., Vainchtein, I.D., Brouwer, N., et al. (2017). Transcriptomic analysis of purified human cortical microglia reveals age-associated changes. *Nature Neuroscience*. 20 (8): 1162–1171.

Gant, J.C., Kadish, I., Chen, K.C., Thibault, O., Blalock, E.M., et al. (2018). Aging-Related Calcium Dysregulation in Rat Entorhinal Neurons Homologous with the Human

Entorhinal Neurons in which Alzheimer's Disease Neurofibrillary Tangles First Appear. *Journal of Alzheimer's Disease*. 66 (4): 1371–1378.

Garcia, J.A., Pino, P.A., Mizutani, M., Cardona, S.M., Charo, I.F., et al. (2013). Regulation of Adaptive Immunity by the Fractalkine Receptor during Autoimmune Inflammation. *The Journal of Immunology*. 191 (3): 1063–1072.

Garnier-Crussard, A., Bougacha, S., Wirth, M., André, C., Delarue, M., et al. (2020). White matter hyperintensities across the adult lifespan: relation to age, Aβ load, and cognition. *Alzheimer's Research & Therapy*. 12 (1): 127.

Geiss, G.K., Bumgarner, R.E., Birditt, B., Dahl, T., Dowidar, N., et al. (2008). Direct multiplexed measurement of gene expression with color-coded probe pairs. *Nature Biotechnology*. 26 (3): 317–325.

Ghaznawi, R., Geerlings, M.I., Jaarsma-Coes, M.G., Zwartbol, M.H.T., Kuijf, H.J., et al. (2019). The association between lacunes and white matter hyperintensity features on MRI: The SMART-MR study. *Journal of Cerebral Blood Flow and Metabolism*. 39 (12): 2486–2496.

Ghosh, A. & Giese, K.P. (2015). Calcium/calmodulin-dependent kinase II and Alzheimer's disease. *Molecular Brain*. 8 (1): 78.

Giacci, M.K., Bartlett, C.A., Smith, N.M., Iyer, K.S., Toomey, L.M., et al. (2018). Oligodendroglia Are Particularly Vulnerable to Oxidative Damage After Neurotrauma In Vivo. *The Journal of Neuroscience*. 38 (29): 6491 LP – 6504.

Giffard, R.G., Xu, L., Zhao, H., Carrico, W., Ouyang, Y., et al. (2004). Chaperones, protein aggregation, and brain protection from hypoxic/ischemic injury. *Journal of Experimental Biology*. 207 (18): 3213–3220.

Giwa, M.O., Williams, J., Elderfield, K., Jiwa, N.S., Bridges, L.R., et al. (2012). Neuropathologic evidence of endothelial changes in cerebral small vessel disease. *Neurology*. 78 (3): 167–174.

Godbout, J.P., Chen, J., Abraham, J., Richwine, a F., Berg, B.M., et al. (2005). Exaggerated neuroinflammation and sickness behavior in aged mice following activation of the peripheral innate immune system. *The FASEB journal : official publication of the Federation of American Societies for Experimental Biology*. 19 (10): 1329–1331.

Goodall, E.F., Leach, V., Wang, C., Cooper-Knock, J., Heath, P.R., et al. (2019). Age-

associated mRNA and miRNA expression changes in the blood-brain barrier. *International Journal of Molecular Sciences*. 20 (12): 3097.

Gouw, A.A., Seewann, A., Van Der Flier, W.M., Barkhof, F., Rozemuller, A.M., et al. (2011). Heterogeneity of small vessel disease: A systematic review of MRI and histopathology correlations. *Journal of Neurology, Neurosurgery and Psychiatry*. 82 (2): 126–135.

Grahl, N., Dolben, E.L., Filkins, L.M., Crocker, A.W., Willger, S.D., et al. (2018). Profiling of Bacterial and Fungal Microbial Communities in Cystic Fibrosis Sputum Using RNA. *mSphere*. 3 (4): e00292-18.

Graves, S.I. & Baker, D.J. (2020). Implicating endothelial cell senescence to dysfunction in the ageing and diseased brain. *Basic & Clinical Pharmacology & Toxicology*. 127 (2): 102–110.

Griffanti, L., Jenkinson, M., Suri, S., Zsoldos, E., Mahmood, A., et al. (2018). Classification and characterization of periventricular and deep white matter hyperintensities on MRI: A study in older adults. *NeuroImage*. 170: 174–181.

Griffin, R., Nally, R., Nolan, Y., McCartney, Y., Linden, J. & Lynch, M.A. (2006). The age-related attenuation in long-term potentiation is associated with microglial activation. *Journal of Neurochemistry*. 99 (4): 1263–1272.

Griffith, A.A. & Holmes, W. (2019). Fine tuning: Effects of post-translational modification on Hsp70 chaperones. *International Journal of Molecular Sciences*. 20 (17): 4207.

de Groot, J.C., de Leeuw, F.-E., Oudkerk, M., Hofman, A., Jolles, J. & Breteler, M.M.B. (2000). Cerebral White Matter Lesions and Depressive Symptoms in Elderly Adults. *Archives of General Psychiatry*. 57 (11): 1071.

De Groot, J.C., De Leeuw, F.E., Oudkerk, M., Van Gijn, J., Hofman, A., et al. (2002). Periventricular cerebral white matter lesions predict rate of cognitive decline. *Annals of Neurology*. 52 (3): 335–341.

Gu, S.M., Park, M.H., Yun, H.M., Han, S.B., Oh, K.W., et al. (2016). CCR5 knockout suppresses experimental autoimmune encephalomyelitis in C57BL/6 mice. *Oncotarget*. 7 (13): 15382–15393.

Gudz, T.I., Komuro, H. & Macklin, W.B. (2006). Glutamate stimulates oligodendrocyte progenitor migration mediated via an αv integrin/myelin proteolipid protein

complex. *Journal of Neuroscience*. 26 (9): 2458–2466.

Gyoneva, S., Hosur, R., Gosselin, D., Zhang, B., Ouyang, Z., et al. (2019). Cx3cr1-deficient microglia exhibit a premature aging transcriptome. *Life Science Alliance*. 2 (6): e201900453.

de Haas, A.H., Boddeke, H.W.G.M. & Biber, K. (2008). Region-specific expression of immunoregulatory proteins on microglia in the healthy CNS. *Glia*. 56 (8): 888–894.

Habermacher, C., Angulo, M.C. & Benamer, N. (2019). Glutamate versus GABA in neuron–oligodendroglia communication. *Glia*. 67 (11): 2092–2106.

Hachinski, V.C., Potter, P. & Merskey, H. (1986). Leuko-araiosis: an ancient term for a new problem. *The Canadian Journal of Neurological Sciences.* 13 (4 Suppl): 533–534.

Hahn, Y.K., Vo, P., Fitting, S., Block, M.L., Hauser, K.F. & Knapp, P.E. (2010). β-Chemokine production by neural and glial progenitor cells is enhanced by HIV-1 Tat: Effects on microglial migration. *Journal of Neurochemistry*. 114 (1): 97–109.

Hainsworth, A.H., Minett, T., Andoh, J., Forster, G., Bhide, I., et al. (2017). Neuropathology of White Matter Lesions, Blood-Brain Barrier Dysfunction, and Dementia. *Stroke*. 48 (10): 2799–2804.

Halliday, M.R., Rege, S. V., Ma, Q., Zhao, Z., Miller, C.A., et al. (2016). Accelerated pericyte degeneration and blood-brain barrier breakdown in apolipoprotein E4 carriers with Alzheimer's disease. *Journal of Cerebral Blood Flow and Metabolism*. 36 (1): 216–227.

Hardy, J. & Selkoe, D.J. (2002). The amyloid hypothesis of Alzheimer's disease: Progress and problems on the road to therapeutics. *Science*. 297 (5580) p.353–356.

Harrison, J.K., Jiang, Y., Chen, S., Xia, Y., Maciejewski, D., et al. (1998). Role for neuronally derived fractalkine in mediating interactions between neurons and CX3CR1-expressing microglia. *Proceedings of the National Academy of Sciences of the United States of America*. 95 (18): 10896–10901.

Hase, Y., Horsburgh, K., Ihara, M. & Kalaria, R.N. (2018). White matter degeneration in vascular and other ageing-related dementias. *Journal of Neurochemistry*. 144

(5): 617–633.

Hashemiaghdam, A. & Mroczek, M. (2020). Microglia heterogeneity and neurodegeneration: The emerging paradigm of the role of immunity in Alzheimer's disease. *Journal of Neuroimmunology*. 341: 577185.

Hefendehl, J.K., Neher, J.J., Sühs, R.B., Kohsaka, S., Skodras, A. & Jucker, M. (2014). Homeostatic and injury-induced microglia behavior in the aging brain. *Aging Cell*. 13 (1): 60–69.

Henry, C.J., Huang, Y., Wynne, A.M. & Godbout, J.P. (2009). Peripheral lipopolysaccharide (LPS) challenge promotes microglial hyperactivity in aged mice that is associated with exaggerated induction of both pro-inflammatory IL-1β and anti-inflammatory IL-10 cytokines. *Brain, Behavior, and Immunity*. 23 (3): 309–317.

van den Heuvel, D.M.J., ten Dam, V.H., de Craen, a J.M., Admiraal-Behloul, F., Olofsen, H., et al. (2006). Increase in periventricular white matter hyperintensities parallels decline in mental processing speed in a non-demented elderly population. *Journal of Neurology, Neurosurgery, and Psychiatry*. 77 (2): 149–53.

Hewett, S.J., Jackman, N.A. & Claycomb, R.J. (2012). Interleukin-1β in Central Nervous System Injury and Repair. *European journal of neurodegenerative disease*. 1 (2): 195–211.

Holfelder, K., Schittenhelm, J., Trautmann, K., Haybaeck, J., Meyermann, R. & Beschorner, R. (2011). De novo expression of the hemoglobin scavenger receptor CD163 by activated microglia is not associated with hemorrhages in human brain lesions. *Histology and Histopathology*. 26 (8): 1007–1017.

Honig, L.S., Vellas, B., Woodward, M., Boada, M., Bullock, R., et al. (2018). Trial of solanezumab for mild dementia due to Alzheimer's disease. *New England Journal of Medicine*. 378 (4): 321–330.

Horigane, S.I., Ozawa, Y., Yamada, H. & Takemoto-Kimura, S. (2019). Calcium signalling: A key regulator of neuronal migration. *Journal of Biochemistry*. 165 (5): 401–409.

Hu, H.-Y., Ou, Y.-N., Shen, X.-N., Qu, Y., Ma, Y.-H., et al. (2021). White matter hyperintensities and risks of cognitive impairment and dementia: A systematic review and meta-analysis of 36 prospective studies. *Neuroscience &*

Biobehavioral Reviews. 120: 16–27.

Hu, X., Leak, R.K., Shi, Y., Suenaga, J., Gao, Y., et al. (2015). Microglial and macrophage polarization—new prospects for brain repair. *Nature reviews. Neurology*. 11 (1): 56–64.

Hu, X., Li, P., Guo, Y., Wang, H., Leak, R.K., et al. (2012). Microglia/macrophage polarization dynamics reveal novel mechanism of injury expansion after focal cerebral ischemia. *Stroke*. 43 (11): 3063–3070.

Huang, D.W., Sherman, B.T. & Lempicki, R.A. (2009). Systematic and integrative analysis of large gene lists using DAVID bioinformatics resources. *Nature Protocols*. 4 (1): 44–57.

Huang, J., Friedland, R.P. & Auchus, A.P. (2007). Diffusion tensor imaging of normal-appearing white matter in mild cognitive impairment and early Alzheimer disease: Preliminary evidence of axonal degeneration in the temporal lobe. *American Journal of Neuroradiology*. 28 (10): 1943–1948.

Hughes, C.E. & Nibbs, R.J.B. (2018). A guide to chemokines and their receptors. *FEBS Journal*. 285 (16): 2944–2971.

Iadecola, C. (2013). The Pathobiology of Vascular Dementia. *Neuron*. 80 (4): 844–866.

Ince, P.G. (2001). Pathological correlates of late-onset dementia in a multicentre, community-based population in England and Wales. *Lancet*. 357 (9251): 169–175.

Iordanishvili, E., Schall, M., Loução, R., Zimmermann, M., Kotetishvili, K., et al. (2019). Quantitative MRI of cerebral white matter hyperintensities: A new approach towards understanding the underlying pathology. *NeuroImage*. 202.

Jana, M. & Pahan, K. (2013). Down-regulation of Myelin Gene Expression in Human Oligodendrocytes by Nitric Oxide: Implications for Demyelination in Multiple Sclerosis. *Journal of clinical & cellular immunology*. 4 (312).

Jay, T.R., Von Saucken, V.E. & Landreth, G.E. (2017). TREM2 in Neurodegenerative Diseases. *Molecular Neurodegeneration*. 12 (1): 56.

Jiao, C., Gao, F., Ou, L., Yu, J., Li, M., et al. (2018). Tetrahydroxystilbene glycoside antagonizes β-amyloid-induced inflammatory injury in microglia cells by regulating PU.1 expression. *NeuroReport*. 29 (10): 787–793.

Jing, C., Zhang, H., Shishido, H., Keep, R.F. & Hua, Y. (2018). Association of Brain CD163 Expression and Brain Injury/Hydrocephalus Development in a Rat Model of Subarachnoid Hemorrhage. *Frontiers in Neuroscience*. 12: 313.

Joy, M.T., Ben Assayag, E., Shabashov-Stone, D., Liraz-Zaltsman, S., Mazzitelli, J., et al. (2019). CCR5 Is a Therapeutic Target for Recovery after Stroke and Traumatic Brain Injury. *Cell*. 176 (5): 1143-1157.e13.

Kadry, H., Noorani, B. & Cucullo, L. (2020). A blood–brain barrier overview on structure, function, impairment, and biomarkers of integrity. *Fluids and Barriers of the CNS*. 17 (1): 69.

Kakimura, J.-I., Kitamura, Y., Takata, K., Umeki, M., Suzuki, S., et al. (2002). Microglial activation and amyloid-β clearance induced by exogenous heat-shock proteins. *The FASEB Journal*. 16 (6): 601–603.

Kalaria, R.N. (2018). The pathology and pathophysiology of vascular dementia. *Neuropharmacology*. 134: 226–239.

Kamphuis, W., Kooijman, L., Schetters, S., Orre, M. & Hol, E.M. (2016). Transcriptional profiling of CD11c-positive microglia accumulating around amyloid plaques in a mouse model for Alzheimer's disease. *Biochimica et Biophysica Acta - Molecular Basis of Disease*. 1862 (10): 1847–1860.

Kanazawa, M., Ninomiya, I., Hatakeyama, M., Takahashi, T. & Shimohata, T. (2017). Microglia and monocytes/macrophages polarization reveal novel therapeutic mechanism against stroke. *International Journal of Molecular Sciences*. 18 (10): 2135.

Keith, J., Gao, F.Q., Noor, R., Kiss, A., Balasubramaniam, G., et al. (2017). Collagenosis of the Deep Medullary Veins: An Underrecognized Pathologic Correlate of White Matter Hyperintensities and Periventricular Infarction? *Journal of neuropathology and experimental neurology*. 76 (4): 299–312.

Keren-Shaul, H., Spinrad, A., Weiner, A., Matcovitch-Natan, O., Dvir-Szternfeld, R., et al. (2017). A Unique Microglia Type Associated with Restricting Development of Alzheimer's Disease. *Cell*. 169 (7): 1276-1290.e17.

Kim, J.H., Hwang, K.J., Kim, J.-H., Lee, Y.H., Rhee, H.Y. & Park, K.-C. (2011). Regional white matter hyperintensities in normal aging, single domain amnestic mild cognitive impairment, and mild Alzheimer's disease. *Journal of Clinical*

Neuroscience. 18 (8): 1101–1106.

Kim, J.Y., Kim, J.W. & Yenari, M.A. (2020). Heat shock protein signaling in brain ischemia and injury. *Neuroscience Letters*. 715: 134642.

Kim, J.Y., Yenari, M.A. & Lee, J.E. (2015a). Regulation of inflammatory transcription factors by heat shock protein 70 in primary cultured astrocytes exposed to oxygen-glucose deprivation. *Neuroscience*. 286: 272–280.

Kim, K.W., MacFall, J.R. & Payne, M.E. (2008). Classification of White Matter Lesions on Magnetic Resonance Imaging in Elderly Persons. *Biological Psychiatry*. 64 (4): 273–280.

Kim, S., Choi, S.H., Lee, Y.M., Kim, M.J., Kim, Y.D., et al. (2015b). Periventricular white matter hyperintensities and the risk of dementia: a CREDOS study. *International Psychogeriatrics*. 27 (12): 2069–2077.

Kloppenborg, R.P., Nederkoorn, P.J., Geerlings, M.I. & Van Den Berg, E. (2014). Presence and progression of white matter hyperintensities and cognition: A meta-analysis. *Neurology*. 82 (23): 2127–2138.

Koda, M., Nishio, Y., Hashimoto, M., Kamada, T., Koshizuka, S., et al. (2004). Up-regulation of macrophage migration-inhibitory factor expression after compression-induced spinal cord injury in rats. *Acta Neuropathologica*. 108 (1): 31–36.

Koellhoffer, E.C., McCullough, L.D. & Ritzel, R.M. (2017). Old maids: Aging and its impact on microglia function. *International Journal of Molecular Sciences*. 18 (4): 769.

Kohama, S.G., Rosene, D.L. & Sherman, L.S. (2012). Age-related changes in human and non-human primate white matter: From myelination disturbances to cognitive decline. *Age*. 34 (5): 1093–1110.

Korzhevskii, D.E. & Kirik, O. V. (2016). Brain Microglia and Microglial Markers. *Neuroscience and Behavioral Physiology*. 46 (3): 284–290.

Koussounadis, A., Langdon, S.P., Um, I.H., Harrison, D.J. & Smith, V.A. (2015). Relationship between differentially expressed mRNA and mRNA-protein correlations in a xenograft model system. *Scientific Reports*. 5 (1): 10775.

Kurnellas, M.P., Donahue, K.C. & Elkabes, S. (2007). Mechanisms of neuronal damage in multiple sclerosis and its animal models: Role of calcium pumps and

exchangers. *Biochemical Society Transactions*. 35 (5): 923–926.

De Laat, K.F., Tuladhar, A.M., Van Norden, A.G.W., Norris, D.G., Zwiers, M.P. & De Leeuw, F.E. (2011). Loss of white matter integrity is associated with gait disorders in cerebral small vessel disease. *Brain*. 134 (1): 73–83.

Lanneau, D., de Thonel, A., Maurel, S., Didelot, C. & Garrido, C. (2007). Apoptosis versus cell differentiation: role of heat shock proteins HSP90, HSP70 and HSP27. *Prion*. 1 (1): 53–60.

Lee, E.-S., Yoon, J.-H., Choi, J., Andika, F.R., Lee, T. & Jeong, Y. (2017). A mouse model of subcortical vascular dementia reflecting degeneration of cerebral white matter and microcirculation. *Journal of Cerebral Blood Flow & Metabolism*. 39 (1): 44–57.

Lee, J.J., Lee, E.Y., Lee, S.B., Park, J.H., Kim, T.H., et al. (2015). Impact of white matter lesions on depression in the patients with alzheimer's disease. *Psychiatry Investigation*. 12 (4): 516–522.

Lee, S., Viqar, F., Zimmerman, M.E., Narkhede, A., Tosto, G., et al. (2016). White matter hyperintensities are a core feature of Alzheimer's disease: Evidence from the dominantly inherited Alzheimer network. *Annals of Neurology*. 79 (6): 929–939.

de Leeuw, F.-E. (2001). Prevalence of cerebral white matter lesions in elderly people: a population based magnetic resonance imaging study. The Rotterdam Scan Study. *Journal of Neurology, Neurosurgery and Psychiatry*. 70 (1): 9–14.

de Leeuw, F.-E., de Groot, J.C., Oudkerk, M., Witteman, J.C.M., Hofman, A., et al. (2002). Hypertension and cerebral white matter lesions in a prospective cohort study. *Brain*. 125 (4): 765–772.

Lei, W., Mullen, N., McCarthy, S., Brann, C., Richard, P., et al. (2017). Heat-shock protein 90 (Hsp90) promotes opioid-induced anti-nociception by an ERK mitogen-activated protein kinase (MAPK) mechanism in mouse brain. *Journal of Biological Chemistry*. 292 (25): 10414–10428.

Leng, L., Metz, C.N., Fang, Y., Xu, J., Donnelly, S., et al. (2003). MIF signal transduction initiated by binding to CD74. *Journal of Experimental Medicine*. 197 (11): 1467–1476.

Leys, D., Pruvo, J.P., Parent, M., Vermersch, P., Soetaert, G., et al. (1991). Could

Wallerian degeneration contribute to 'leuko-araiosis' in subjects free of any vascular disorder? *Journal of neurology, neurosurgery, and psychiatry*. 54 (1): 46–50.

Li, J.-W., Zong, Y., Cao, X.-P., Tan, L. & Tan, L. (2018). Microglial priming in Alzheimer's disease. *Annals of Translational Medicine*. 6 (10): 176–176.

Li, J. & Buchner, J. (2013). Structure, function and regulation of the Hsp90 machinery. *Biomedical Journal*. 36 (3): 106–117.

Li, T. & Zhu, J. (2019). Entanglement of CCR5 and Alzheimer's Disease. *Frontiers in Aging Neuroscience*. 11: 209.

Li, Y., Li, M., Zhang, X., Shi, Q., Yang, S., et al. (2017). Higher blood–brain barrier permeability is associated with higher white matter hyperintensities burden. *Journal of Neurology*. 264 (7): 1474–1481.

Liberek, K., Lewandowska, A. & Ziętkiewicz, S. (2008). Chaperones in control of protein disaggregation. *EMBO Journal*. 27 (2) p.328–335.

Lin, J., Wang, D., Lan, L. & Fan, Y. (2017). Multiple Factors Involved in the Pathogenesis of White Matter Lesions. *BioMed Research International*. 2017: 9372050.

Liu, J.Q., Chu, S.F., Zhou, X., Zhang, D.Y. & Chen, N.H. (2019a). Role of chemokines in Parkinson's disease. *Brain Research Bulletin*. 152 (2): 11–18.

Liu, Q., Zhang, Y., Liu, S., Liu, Y., Yang, X., et al. (2019b). Cathepsin C promotes microglia M1 polarization and aggravates neuroinflammation via activation of Ca2+-dependent PKC/p38MAPK/NF-κB pathway. *Journal of Neuroinflammation*. 16 (1): 1–18.

Liu, X. & Quan, N. (2018). Microglia and CNS interleukin-1: Beyond immunological concepts. *Frontiers in Neurology*. 9: 8.

Liu, X., Wen, S., Yan, F., Liu, K., Liu, L., et al. (2018). Salidroside provides neuroprotection by modulating microglial polarization after cerebral ischemia. *Journal of Neuroinflammation*. 15 (1): 1–11.

Lonergan, W., Whistler, T. & Vernon, S.D. (2007). Comparison of target labeling methods for use with Affymetrix GeneChips. *BMC Biotechnology*. 7 (1): 24.

Lu, J., Moochhala, S., Kaur, C. & Ling, E.A. a (2001). Cellular inflammatory response associated with breakdown of the blood-brain barrier after closed head injury

in rats. *Journal of Neurotrauma*. 18 (4): 399–408.

Luo, X.-G., Ding, J.-Q. & Chen, S.-D. (2010). Microglia in the aging brain: relevance to neurodegeneration. *Molecular Neurodegeneration*. 5 (1): 12.

Lynch, A.M., Murphy, K.J., Deighan, B.F., O'Reilly, J.-A., Gun'ko, Y.K., et al. (2010). The impact of glial activation in the aging brain. *Aging and Disease*. 1 (3): 262–278.

Makedonov, I., Black, S.E. & Macintosh, B.J. (2013). Cerebral small vessel disease in aging and Alzheimer's disease: A comparative study using MRI and SPECT. *European Journal of Neurology*. 20 (2): 243–250.

Mantovani, A., Dinarello, C.A., Molgora, M. & Garlanda, C. (2019). Interleukin-1 and Related Cytokines in the Regulation of Inflammation and Immunity. *Immunity*. 50 (4): 778–795.

Marnane, M., Al-Jawadi, O.O., Mortazavi, S., Pogorzelec, K.J., Wang, B.W., et al. (2016). Periventricular hyperintensities are associated with elevated cerebral amyloid. *Neurology*. 86 (6): 535–543.

Marner, L., Nyengaard, J.R., Tang, Y. & Pakkenberg, B. (2003). Marked loss of myelinated nerve fibers in the human brain with age. *Journal of Comparative Neurology*. 462 (2): 144–152.

Marstrand, J.R., Garde, E., Rostrup, E., Ring, P., Rosenbaum, S., et al. (2002). Cerebral perfusion and cerebrovascular reactivity are reduced in white matter hyperintensities. *Stroke*. 33 (4): 972–976.

Mathys, H., Adaikkan, C., Gao, F., Young, J.Z., Manet, E., et al. (2017). Temporal Tracking of Microglia Activation in Neurodegeneration at Single-Cell Resolution. *Cell Reports*. 21 (2): 366–380.

Matthews, F.E., Brayne, C., Lowe, J., McKeith, I., Wharton, S.B. & Ince, P. (2009). Epidemiological pathology of dementia: Attributable-risks at death in the medical research council cognitive function and ageing study. *PLoS Medicine*. 6 (11): e1000180.

Mazurek, N., Frisk, A.L., Beekman, J.M., Hartwig, A. & Meyer, K. (2013). Comparison of progestin transcriptional profiles in rat mammary gland using Laser Capture Microdissection and whole tissue-sampling. *Experimental and Toxicologic Pathology*. 65 (7–8): 949–960.

McAleese, K.E., Firbank, M., Dey, M., Colloby, S.J., Walker, L., et al. (2015). Cortical tau

load is associated with white matter hyperintensities. *Acta Neuropathologica Communications*. 3 (1): 60.

McAleese, K.E., Walker, L., Graham, S., Moya, E.L.J., Johnson, M., et al. (2017). Parietal white matter lesions in Alzheimer's disease are associated with cortical neurodegenerative pathology, but not with small vessel disease. *Acta Neuropathologica*. 1–15.

Mecca, C., Giambanco, I., Donato, R. & Arcuri, C. (2018). Microglia and aging: The role of the TREM2–DAP12 and CX3CL1-CX3CR1 Axes. *International Journal of Molecular Sciences*. 19 (1): 318.

Medrano Martorell, S., Cuadrado Blázquez, M., García Figueredo, D., González Ortiz, S. & Capellades Font, J. (2012). Hyperintense punctiform images in the white matter: A diagnostic approach. *Radiología (English Edition)*. 54 (4): 321–335.

Meng, Y., Zhang, Y. & Jia, Z. (2003). Synaptic transmission and plasticity in the absence of AMPA glutamate receptor GluR2 and GluR3. *Neuron*. 39 (1): 163–176.

Merrill, J.E., Ignarro, L.J., Sherman, M.P., Melinek, J. & Lane, T.E. (1993). Microglial cell cytotoxicity of oligodendrocytes is mediated through nitric oxide. *Journal of immunology (Baltimore, Md. : 1950)*. 151 (4): 2132–2141.

Mexal, S., Berger, R., Adams, C.E., Ross, R.G., Freedman, R. & Leonard, S. (2006). Brain pH has a significant impact on human postmortem hippocampal gene expression profiles. *Brain Research*. 1106 (1): 1–11.

Meza-Romero, R., Benedek, G., Gerstner, G., Kent, G., Nguyen, H., et al. (2019). Increased CD74 binding and EAE treatment efficacy of a modified DRα1 molecular construct. *Metabolic Brain Disease*. 34 (1): 153–164.

Mills, C.D., Kincaid, K., Alt, J.M., Heilman, M.J. & Hill, A.M. (2000). M-1/M-2 Macrophages and the Th1/Th2 Paradigm. *The Journal of Immunology*. 164 (12): 6166–6173.

Miron, V.E., Boyd, A., Zhao, J.W., Yuen, T.J., Ruckh, J.M., et al. (2013). M2 microglia and macrophages drive oligodendrocyte differentiation during CNS remyelination. *Nature Neuroscience*. 16 (9): 1211–1218.

Mohamed, N.E., Zhao, Y., Lee, J.H., Tan, M.G., Esiri, M.M., et al. (2011). Upregulation of AMPA receptor GluR2 (GluA2) subunits in subcortical ischemic vascular

dementia is repressed in the presence of Alzheimer's disease. *Neurochemistry International*. 58 (7): 820–825.

Montagne, A., Barnes, S.R., Sweeney, M.D., Halliday, M.R., Sagare, A.P., et al. (2015). Blood-Brain barrier breakdown in the aging human hippocampus. *Neuron*. 85 (2): 296–302.

Moody, D.M., Brown, W.R., Challa, V.R. & Anderson, R.L. (1995). Periventricular venous collagenosis: association with leukoaraiosis. *Radiology*. 194 (2): 469–476.

Moreno-García, A., Kun, A., Calero, O., Medina, M. & Calero, M. (2018). An Overview of the Role of Lipofuscin in Age-Related Neurodegeneration. *Frontiers in neuroscience*. 12: 464.

Moscoso, A., Rey-bretal, D., Silva-Rodríguez, J., Aldrey, J.M., Cort, J., et al. (2020). White matter hyperintensities are associated with subthreshold amyloid accumulation. *NeuroImage*. 218: 116944.

Murray, M.E., Vemuri, P., Preboske, G.M., Murphy, M.C., Schweitzer, K.J., et al. (2012). A quantitative postmortem MRI design sensitive to white matter hyperintensity differences and their relationship with underlying pathology. *Journal of neuropathology and experimental neurology*. 71 (12): 1113–1122.

Nakagawa, Y. & Chiba, K. (2014). Role of microglial M1/M2 polarization in relapse and remission of psychiatric disorders and diseases. *Pharmaceuticals*. 7 (12): 1028–1048.

Nelson, N.J. (2001). Microarrays have arrived: Gene expression tool matures. *Journal of the National Cancer Institute*. 93 (7): 492–493.

Nimmerjahn, A., Kirchhoff, F. & Helmchen, F. (2005). Resting microglial cells are highly dynamic surveillants of brain parenchyma in vivo. *Science*. 308 (5726): 1314–1318.

Norden, D.M. & Godbout, J.P. (2013). Review: Microglia of the aged brain: Primed to be activated and resistant to regulation. *Neuropathology and Applied Neurobiology*. 39 (1): 19–34.

O'Brien, J., Desmond, P., Ames, D., Schweitzer, I., Harrigan, S. & Tress, B. (1996). A magnetic resonance imaging study of white matter lesions in depression and Alzheimer's disease. *The British journal of psychiatry : the journal of mental*

science. 168 (4): 477–485.

Ohsawa, K., Imai, Y., Sasaki, Y. & Kohsaka, S. (2004). Microglia/macrophage-specific protein Iba1 binds to fimbrin and enhances its actin-bundling activity. *Journal of Neurochemistry*. 88 (4): 844–856.

Ovbiagele, B. & Saver, J.L. (2006). Cerebral white matter hyperintensities on MRI: Current concepts and therapeutic implications. *Cerebrovascular Diseases*. 22 (2–3): 83–90.

Ozsolak, F. & Milos, P.M. (2011). RNA sequencing: Advances, challenges and opportunities. *Nature Reviews Genetics*. 12 (2): 87–98.

Paez, P.M. & Lyons, D.A. (2020). Calcium Signaling in the Oligodendrocyte Lineage: Regulators and Consequences. *Annual Review of Neuroscience*. 43 (1): 163–186.

Palasca, O., Santos, A., Stolte, C., Gorodkin, J. & Jensen, L.J. (2018). TISSUES 2.0: An integrative web resource on mammalian tissue expression. *Database*. 2018 (2018).

Pantoni, L. (2010). Cerebral small vessel disease: from pathogenesis and clinical characteristics to therapeutic challenges. *The Lancet Neurology*. 9 (7): 689–701.

Pantoni, L. & Garcia, J.H. (1997). Pathogenesis of Leukoaraiosis A Review. *Stroke*. 28 (3): 652–659.

Pantoni, L. & Garcia, J.H. (1995). The significance of cerebral white matter abnormalities 100 years after Binswanger's report. A review. *Stroke*. 26 (7): 1293–1301.

Park, S.Y., Lee, H., Hur, J., Kim, S.Y., Kim, H., et al. (2002). Hypoxia induces nitric oxide production in mouse microglia via p38 mitogen-activated protein kinase pathway. *Brain research. Molecular brain research*. 107 (1): 9–16.

Peferoen, L.A.N., Vogel, D.Y.S., Ummenthum, K., Breur, M., Heijnen, P.D.A.M., et al. (2015). Activation status of human microglia is dependent on lesion formation stage and remyelination in multiple sclerosis. *Journal of Neuropathology and Experimental Neurology*. 74 (1): 48–63.

Perner, C., Perner, F., Stubendorff, B., Förster, M., Witte, O.W., et al. (2018). Dysregulation of chemokine receptor expression and function in leukocytes from ALS patients. *Journal of Neuroinflammation*. 15 (1): 10–14.

Perry, V.H. & Holmes, C. (2014). Microglial priming in neurodegenerative disease.

Nature Reviews Neurology. 10 (4): 217–224.

Peters, A. (2002). The effects of normal aging on myelin and nerve fibers: A review. *Journal of Neurocytology*. 31 (8–9): 581–93.

Pey, P., Pearce, R.K.B., Kalaitzakis, M.E., Griffin, W.S.T. & Gentleman, S.M. (2014). Phenotypic profile of alternative activation marker CD163 is different in Alzheimer's and Parkinson's disease. *Acta Neuropathologica Communications*. 2 (1): 21.

Pinar, O., Ozden, Y.A., Omur, E. & Muhtesem, G. (2017). Heat shock proteins in multiple sclerosis. *Advances in Experimental Medicine and Biology*. 958: 29–42.

Planas, A.M., Soriano, M.A., Estrada, A., Sanz, O., Martin, F. & Ferrer, I. (1997). The heat shock stress response after brain lesions: Induction of 72 kDa heat shock protein (cell types involved, axonal transport, transcriptional regulation) and protein synthesis inhibition. *Progress in Neurobiology*. 51 (6): 607–636.

Polanski, W., Enzensperger, C., Reichmann, H. & Gille, G. (2010). The exceptional properties of 9-methyl-β-carboline: Stimulation, protection and regeneration of dopaminergic neurons coupled with anti-inflammatory effects. *Journal of Neurochemistry*. 113 (6): 1659–1675.

Polyak, M.J., Vivithanaporn, P., Maingat, F.G., Walsh, J.G., Branton, W., et al. (2013). Differential type 1 interferon-regulated gene expression in the brain during AIDS: Interactions with viral diversity and neurovirulence. *FASEB Journal*. 27 (7): 2829–2844.

Primiani, C.T., Ryan, V.H., Rao, J.S., Cam, M.C., Ahn, K., et al. (2014). Coordinated Gene Expression of Neuroinflammatory and Cell Signaling Markers in Dorsolateral Prefrontal Cortex during Human Brain Development and Aging. *PLoS ONE*. 9 (10): e110972.

Prins, N.D., Van Dijk, E.J., Den Heijer, T., Vermeer, S.E., Jolles, J., et al. (2005). Cerebral small-vessel disease and decline in information processing speed, executive function and memory. *Brain*. 128 (9): 2034–2041.

Prins, N.D., van Dijk, E.J., Den Heijer, T., Vermeer, S.E., Koudstaal, P.J., et al. (2004). Cerebral white matter lesions and the risk of dementia. *Archives of Neurology*. 61 (10): 1531–1534.

Prins, N.D. & Scheltens, P. (2015). White matter hyperintensities, cognitive

impairment and dementia: an update. *Nature reviews. Neurology*. 11 (3): 157–165.

Quan, Y., Möller, T. & Weinstein, J.R. (2009). Regulation of Fcγ receptors and immunoglobulin G-mediated phagocytosis in mouse microglia. *Neuroscience Letters*. 464 (1): 29–33.

Raj, D., Yin, Z., Breur, M., Doorduin, J., Holtman, I.R., et al. (2017). Increased white matter inflammation in aging- and alzheimer's disease brain. *Frontiers in Molecular Neuroscience*. 10.

Ramprasad, M.P., Terpstra, V., Kondratenko, N., Quehenberger, O. & Steinberg, D. (1996). Cell surface expression of mouse macrosialin and human CD68 and their role as macrophage receptors for oxidized low density lipoprotein. *Proceedings of the National Academy of Sciences of the United States of America*. 93 (25): 14833–14838.

Ransohoff, R.M. (2016). A polarizing question: do M1 and M2 microglia exist? *Nature Neuroscience*. 19 (8): 987–991.

Rio-Hortega, D. & P (1919). El tercer elemento de los centros nerviosos. I. La microglia en estados normal. II. Intervencio de la microglia en los processos patologicas. III. Naturaleza probable de la microglia. *Bol Soc Espanola Biol*. 9: 69–120.

Rodríguez-Gómez, J.A., Kavanagh, E., Engskog-Vlachos, P., Engskog, M.K.R., Herrera, A.J., et al. (2020). Microglia: Agents of the CNS Pro-Inflammatory Response. *Cells*. 9 (7): 1717.

Román, G.C., Erkinjuntti, T., Wallin, A., Pantoni, L. & Chui, H.C. (2002). Subcortical ischaemic vascular dementia. *Lancet Neurology*. 1 (7): 426–436.

Rosario, B.L., Rosso, A.L., Aizenstein, H.J., Harris, T., Newman, A.B., et al. (2016). Cerebral white matter and slow gait: Contribution of hyperintensities and normal-appearing parenchyma. *Journals of Gerontology - Series A Biological Sciences and Medical Sciences*. 71 (7): 968–973.

Rosenberg, G.A. (2009). Inflammation and white matter damage in vascular cognitive impairment. *Stroke*. 40 (3 SUPPL. 1): 20–24.

Rowbotham, G.F. & Little, E. (1965). Circulations of the cerebral hemispheres. *British Journal of Surgery*. 52 (1): 8–21.

Sachdev, P.S., Brodaty, H., Valenzuela, M.J., Lorentz, L., Looi, J.C.L., et al. (2004). The neuropsychological profile of vascular cognitive impairment in stroke and TIA patients. *Neurology*. 62 (6): 912–919.

Safaiyan, S., Kannaiyan, N., Snaidero, N., Brioschi, S., Biber, K., et al. (2016). Age-related myelin degradation burdens the clearance function of microglia during aging. *Nature Neuroscience*. 19 (8): 995–998.

Sankowski, R., Böttcher, C., Masuda, T., Geirsdottir, L., Sagar, et al. (2019). Mapping microglia states in the human brain through the integration of high-dimensional techniques. *Nature Neuroscience*. 22 (12): 2098–2110.

Sastre, M., Richardson, J.C., Gentleman, S.M. & Brooks, D.J. (2011). Inflammatory risk factors and pathologies associated with Alzheimer's disease. *Current Alzheimer Research*. 8 (2): 132–141.

Satoh, J.I. (2018). Gene expression profiles of M1 and M2 microglia characterized by comparative analysis of public datasets. *Clinical and Experimental Neuroimmunology*. 9 (2): 124–138.

Saunders, N.R., Daneman, R., Dziegielewska, K.M. & Liddelow, S.A. (2013). Transporters of the blood-brain and blood-CSF interfaces in development and in the adult. *Molecular Aspects of Medicine*. 34 (2–3): 742–752.

Saunders, N.R., Habgood, M.D., Møllgård, K. & Dziegielewska, K.M. (2016). The biological significance of brain barrier mechanisms: help or hindrance in drug delivery to the central nervous system? *F1000Research*. 5: F1000 Faculty Rev-313.

Schachtele, S.J., Hu, S., Sheng, W.S., Mutnal, M.B. & Lokensgard, J.R. (2014). Glial cells suppress postencephalitic CD8+ T lymphocytes through PD-L1. *Glia*. 62 (10): 1582–1594.

Scheefhals, N. & MacGillavry, H.D. (2018). Functional organization of postsynaptic glutamate receptors. *Molecular and Cellular Neuroscience*. 91: 82–94.

Scheltens, P., Barkhof, F., Leys, D., Pruvo, J.P., Nauta, J.J.P., et al. (1993). A semiquantative rating scale for the assessment of signal hyperintensities on magnetic resonance imaging. *Journal of the Neurological Sciences*. 114 (1): 7–12.

Scheltens, P., Barkhof, F., Leys, D., Wolters, E.C., Ravid, R. & Kamphorst, W. (1995).

Histopathologic correlates of white matter changes on MRI in Alzheimer's disease and normal aging. *Neurology*. 45 (5): 883–888.

Schmidt, R., Enzinger, C., Ropele, S., Schmidt, H. & Fazekas, F. (2003). Progression of cerebral white matter lesions: 6-Year results of the Austrian Stroke Prevention Study. *Lancet*. 361 (9374): 2046–2048.

Schmidt, R., Fazekas, F., Kleinert, G., Offenbacher, H., Gindl, K., et al. (1992). Magnetic Resonance Imaging Signal Hyperintensities in the Deep and Subcortical White Matter: A Comparative Studyc Between Stroke Patients and Normal Volunteers. *Archives of Neurology*. 49 (8) p.825–827.

Schmidt, R., Schmidt, H., Haybaeck, J., Loitfelder, M., Weis, S., et al. (2011). Heterogeneity in age-related white matter changes. *Acta Neuropathologica*. 122 (2): 171–185.

Schmidt, R., Schmidt, H., Kapeller, P., Enzinger, C., Ropele, S., et al. (2002). The natural course of MRI white matter hyperintensities. In: *Journal of the Neurological Sciences*. 2002, 253–257.

Schurch, N.J., Schofield, P., Gierliński, M., Cole, C., Sherstnev, A., et al. (2016). How many biological replicates are needed in an RNA-seq experiment and which differential expression tool should you use? *RNA*. 22 (6): 839–851.

Segarra, M., Aburto, M.R. & Acker-Palmer, A. (2021). Blood–Brain Barrier Dynamics to Maintain Brain Homeostasis. *Trends in Neurosciences*. 44 (5): 393–405.

Selkoe, D.J. (2001). Alzheimer's disease: Genes, proteins, and therapy. *Physiological Reviews*. 81 (2) p.741–766.

Sheffield, L.G. & Berman, N.E.J. (1998). Microglial Expression of MHC Class II Increases in Normal Aging of Nonhuman Primates. *Neurobiology of Aging*. 19 (1): 47–55.

Sherman, D.L. & Brophy, P.J. (2005). Mechanisms of axon ensheathment and myelin growth. *Nature Reviews Neuroscience*. 6 (9) p.683–690.

Shigemoto-Mogami, Y., Hoshikawa, K. & Sato, K. (2018). Activated Microglia Disrupt the Blood-Brain Barrier and Induce Chemokines and Cytokines in a Rat in vitro Model . *Frontiers in Cellular Neuroscience* . 12: 494.

Shim, Y.S., Yang, D.-W., Roe, C.M., Coats, M.A., Benzinger, T.L., et al. (2015). Pathological correlates of white matter hyperintensities on magnetic

resonance imaging. *Dementia and Geriatric Cognitive Disorders*. 39 (1–2): 92–104.

Sieger, D., Moritz, C., Ziegenhals, T., Prykhozhij, S. & Peri, F. (2012). Long-Range Ca2+ Waves Transmit Brain-Damage Signals to Microglia. *Developmental Cell*. 22 (6): 1138–1148.

Simpson, J.E., Fernando, M.S., Clark, L., Ince, P.G., Matthews, F., et al. (2007a). White matter lesions in an unselected cohort of the elderly: Astrocytic, microglial and oligodendrocyte precursor cell responses. *Neuropathology and Applied Neurobiology*. 33 (4): 410–419.

Simpson, J.E., Hosny, O., Wharton, S.B., Heath, P.R., Holden, H., et al. (2009). Microarray RNA expression analysis of cerebral white matter lesions reveals changes in multiple functional pathways. *Stroke*. 40 (2): 369–375.

Simpson, J.E., Ince, P.G., Higham, C.E., Gelsthorpe, C.H., Fernando, M.S., et al. (2007b). Microglial activation in white matter lesions and nonlesional white matter of ageing brains. *Neuropathology and Applied Neurobiology*. 33 (6): 670–683.

Simpson, J.E., Ince, P.G., Shaw, P.J., Heath, P.R., Raman, R., et al. (2011). Microarray analysis of the astrocyte transcriptome in the aging brain: Relationship to Alzheimer's pathology and APOE genotype. *Neurobiology of Aging*. 32 (10): 1795–1807.

Simpson, J.E., Newcombe, J., Cuzner, M.L. & Woodroofe, M.N. (1998). Expression of monocyte chemoattractant protein-1 and other β- chemokines by resident glia and inflammatory cells in multiple sclerosis lesions. *Journal of Neuroimmunology*. 84 (2): 238–249.

Simpson, J.E., Wharton, S.B., Cooper, J., Gelsthorpe, C., Baxter, L., et al. (2010). Alterations of the blood-brain barrier in cerebral white matter lesions in the ageing brain. *Neuroscience Letters*. 486 (3): 246–251.

Simpson, J.E., Wharton, S.B. & Heath, P.R. (2018). Immuno-laser-capture microdissection for the isolation of enriched glial populations from frozen post-mortem human brain. In: G. I. Murray (ed.). *Methods in Molecular Biology*. New York, NY: Springer New York, 273–284.

Singh Kushwaha, S., Patro, N. & Kumar Patro, I. (2018). A Sequential Study of Age-Related Lipofuscin Accumulation in Hippocampus and Striate Cortex of Rats.

Annals of Neurosciences. 25 (4): 223–233.

Solár, P., Zamani, A., Kubíčková, L., Dubový, P. & Joukal, M. (2020). Choroid plexus and the blood–cerebrospinal fluid barrier in disease. *Fluids and Barriers of the CNS*. 17 (1): 35.

Song, C., Zhang, Y. & Dong, Y. (2013). Acute and subacute IL-1β administrations differentially modulate neuroimmune and neurotrophic systems: Possible implications for neuroprotection and neurodegeneration. *Journal of Neuroinflammation*. 10 (1): 826.

Sonohara, K., Kozaki, K., Akishita, M., Nagai, K., Hasegawa, H., et al. (2008). White matter lesions as a feature of cognitive impairment, low vitality and other symptoms of geriatric syndrome in the elderly. *Geriatrics and Gerontology International*. 8 (2): 93–100.

Sorce, S., Myburgh, R. & Krause, K.H. (2011). The chemokine receptor CCR5 in the central nervous system. *Progress in Neurobiology*. 93 (2): 297–311.

Sørensen, T.L., Tani, M., Jensen, J., Pierce, V., Lucchinetti, C., et al. (1999). Expression of specific chemokines and chemokine receptors in the central nervous system of multiple sclerosis patients. *Journal of Clinical Investigation*. 103 (6): 807–815.

Srikanth, V., Phan, T.G., Chen, J., Beare, R., Stapleton, J.M. & Reutens, D.C. (2010). The location of white matter lesions and gait-A voxel-based study. *Annals of Neurology*. 67 (2): 265–269.

Stadelmann, C., Ludwin, S., Tabira, T., Guseo, A., Lucchinetti, C.F., et al. (2005). Tissue preconditioning may explain concentric lesions in Baló's type of multiple sclerosis. *Brain*. 128 (5): 979–987.

Stevenson, B.R., Siliciano, J.D., Mooseker, M.S. & Goodenough, D.A. (1986). Identification of ZO-1: A high molecular weight polypeptide associated with the tight junction (Zonula Occludens) in a variety of epithelia. *Journal of Cell Biology*. 103 (3): 755–766.

Streit, W.J., Sammons, N.W., Kuhns, A.J. & Sparks, D.L. (2004). Dystrophic Microglia in the Aging Human Brain. *GLIA*. 45 (2): 208–212.

Stuart, M.J., Singhal, G. & Baune, B.T. (2015). Systematic Review of the Neurobiological Relevance of Chemokines to Psychiatric Disorders. *Frontiers in Cellular Neuroscience*. 9: 357.

Suemoto, C.K., Nitrini, R., Grinberg, L.T., Ferretti, R.E.L., Farfel, J.M., et al. (2011). Atherosclerosis and dementia: A cross-sectional study with pathological analysis of the carotid arteries. *Stroke*. 42 (12): 3614–3615.

Sun, A. & Benet, L.Z. (2020). Late-Stage Failures of Monoclonal Antibody Drugs: A Retrospective Case Study Analysis. *Pharmacology*. 105 (3–4): 145–163.

Sun, P., Bu, F., Min, J.W., Munshi, Y., Howe, M.D., et al. (2019). Inhibition of calcium/calmodulin-dependent protein kinase kinase (CaMKK) exacerbates impairment of endothelial cell and blood–brain barrier after stroke. *European Journal of Neuroscience*. 49 (1): 27–39.

Swanson, M.E.V., Murray, H.C., Ryan, B., Faull, R.L.M., Dragunow, M. & Curtis, M.A. (2020). Quantitative immunohistochemical analysis of myeloid cell marker expression in human cortex captures microglia heterogeneity with anatomical context. *Scientific Reports*. 10 (1): 11693.

Swulius, M.T. & Waxham, M.N. (2008). Ca2+/calmodulin-dependent protein kinases. *Cellular and Molecular Life Sciences*. 65 (17) p.2637–2657.

Tang, Y. & Le, W. (2016). Differential Roles of M1 and M2 Microglia in Neurodegenerative Diseases. *Molecular Neurobiology*. 53 (2): 1181–1194.

Tang, Z., Gan, Y., Liu, Q., Yin, J.X., Liu, Q., et al. (2014). CX3CR1 deficiency suppresses activation and neurotoxicity of microglia/macrophage in experimental ischemic stroke. *Journal of Neuroinflammation*. 11 (1): 26.

Tarkowski, E., Tullberg, M., Fredman, P. & Wikkelsö, C. (2003). Normal pressure hydrocephalus triggers intrathecal production of TNF-α. *Neurobiology of Aging*. 24 (5): 707–714.

Teeling, J.L. & Perry, V.H. (2009). Systemic infection and inflammation in acute CNS injury and chronic neurodegeneration: Underlying mechanisms. *Neuroscience*. 158 (3): 1062–1073.

Tippett, E., Cheng, W.J., Westhorpe, C., Cameron, P.U., Brew, B.J., et al. (2011). Differential Expression of CD163 on Monocyte Subsets in Healthy and HIV-1 Infected Individuals. *PLoS ONE*. 6 (5): e19968.

Tomimoto, H., Akiguchi, I., Suenaga, T., Nishimura, M., Wakita, H., et al. (1996). Alterations of the blood-brain barrier and glial cells in white-matter lesions in cerebrovascular and Alzheimer's disease patients. *Stroke; a journal of cerebral*

circulation. 27 (11): 2069–74.

Tomimoto, H., Akiguchi, I., Wakita, H., Suenaga, T., Nakamura, S. & Kimura, J. (1997). Regressive changes of astroglia in white matter lesions in cerebrovascular disease and Alzheimer's disease patients. *Acta Neuropathologica*. 94 (2): 146–152.

Tomimoto, H., Ihara, M., Wakita, H., Ohtani, R., Lin, J.X., et al. (2003). Chronic cerebral hypoperfusion induces white matter lesions and loss of oligodendroglia with DNA fragmentation in the rat. *Acta Neuropathologica*. 106 (6): 527–534.

Tomita, H., Vawter, M.P., Walsh, D.M., Evans, S.J., Choudary, P. V., et al. (2004). Effect of agonal and postmortem factors on gene expression profile: Quality control in microarray analyses of postmortem human brain. *Biological Psychiatry*. 55 (4): 346–352.

Trifone, C., Salido, J., Ruiz, M.J., Leng, L., Quiroga, M.F., et al. (2018). Interaction Between Macrophage Migration Inhibitory Factor and CD74 in Human Immunodeficiency Virus Type I Infected Primary Monocyte-Derived Macrophages Triggers the Production of Proinflammatory Mediators and Enhances Infection of Unactivated CD4+ T Cell. *Frontiers in Immunology*. 9: 1494.

Ueno, M., Tomimoto, H., Akiguchi, I., Wakita, H. & Sakamoto, H. (2002). Blood-brain barrier disruption in white matter lesions in a rat model of chronic cerebral hypoperfusion. *Journal of Cerebral Blood Flow and Metabolism*. 22 (1): 97–104.

Ulland, T.K. & Colonna, M. (2018). TREM2 — a key player in microglial biology and Alzheimer disease. *Nature Reviews Neurology*. 14 (11): 667–675.

Vainchtein, I.D. & Molofsky, A. V. (2020). Astrocytes and Microglia: In Sickness and in Health. *Trends in Neurosciences*. 43 (3): 144–154.

Valdés Hernández, M.C., Piper, R.J., Bastin, M.E., Royle, N.A., Muñoz Maniega, S., et al. (2014). Morphologic, distributional, volumetric,and intensity characterization of periventricular hyperintensities. *American Journal of Neuroradiology*. 35 (1): 55–62.

Vangberg, T.R., Eikenes, L. & Håberg, A.K. (2019). The effect of white matter hyperintensities on regional brain volumes and white matter microstructure, a population-based study in HUNT. *NeuroImage*. 203: 116158.

Verhaaren, B.F.J., Vernooij, M.W., De Boer, R., Hofman, A., Niessen, W.J., et al. (2013). High blood pressure and cerebral white matter lesion progression in the general population. *Hypertension*. 61 (6): 1354–1359.

Vermeer, S.E., Prins, N.D., den Heijer, T., Hofman, A., Koudstaal, P.J. & Breteler, M.M. (2003). Silent brain infarcts and the risk of dementia and cognitive decline. *The New England Journal of Medicine*. 348 (13): 1215–1222.

Veselý, B., Antonini, A. & Rektor, I. (2016). The contribution of white matter lesions to Parkinson's disease motor and gait symptoms: a critical review of the literature. *Journal of Neural Transmission*. 123 (3): 241–250.

Vickers, J., Mitew, S., Woodhouse, A., M. Fernandez-Martos, C., T. Kirkcaldie, M., et al. (2015). Defining the earliest pathological changes of Alzheimer's disease. *Current Alzheimer Research*. 13 (3): 281–287.

Vinters, H. V, Ellis, W.G., Zarow, C., Zaias, B.W., Jagust, W.J., et al. (2000). Neuropathologic Substrates of Ischemic Vascular Dementia. *Journal of neuropathology and experimental neurology*. 59 (11): 931–945.

Waggener, C.T., Dupree, J.L., Elgersma, Y. & Fuss, B. (2013). CaMKIIβ regulates oligodendrocyte maturation and CNS myelination. *Journal of Neuroscience*. 33 (25): 10453–10458.

Wahlund, L.-O. & Bronge, L. (2000). Contrast-enhanced MRI of White Matter Lesions in Patients with Blood-Brain Barrier Dysfunction. *Annals of the New York Academy of Sciences*. 903 (1): 477–481.

Wahlund, L.O., Almkvist, O., Basun, H. & Julin, P. (1996). MRI in successful aging, a 5-year follow-up study from the eighth to ninth decade of life. *Magnetic Resonance Imaging*. 14 (6): 601–608.

Walker, D.G. & Lue, L. (2015). Immune phenotypes of microglia in human neurodegenerative disease: challenges to detecting microglial polarization in human brains. *Alzheimer's Research & Therapy*. 7 (1): 56.

Waller, R., Baxter, L., Fillingham, D.J., Coelho, S., Pozo, J.M., et al. (2019). Iba-1 - /CD68 + microglia are a prominent feature of age-associated deep subcortical white matter lesions. *PLoS ONE*. 14 (1): 1–18.

Waller, R., Woodroofe, M.N., Francese, S., Heath, P.R., Wharton, S.B., et al. (2012). Isolation of enriched glial populations from post-mortem human CNS material

by immuno-laser capture microdissection. *Journal of Neuroscience Methods*. 208 (2): 108–113.

Waller, R., Woodroofe, M.N., Wharton, S.B., Ince, P.G., Francese, S., et al. (2016). Gene expression profiling of the astrocyte transcriptome in multiple sclerosis normal appearing white matter reveals a neuroprotective role. *Journal of Neuroimmunology*. 299: 139–146.

Wang, Z., Gerstein, M. & Snyder, M. (2009). RNA-Seq: A revolutionary tool for transcriptomics. *Nature Reviews Genetics*. 10 (1): 57–63.

Warde-Farley, D., Donaldson, S.L., Comes, O., Zuberi, K., Badrawi, R., et al. (2010). The GeneMANIA prediction server: Biological network integration for gene prioritization and predicting gene function. *Nucleic Acids Research*. 38 (SUPPL. 2): W214–W220.

Wardlaw, J.M., Smith, C. & Dichgans, M. (2013). Mechanisms of sporadic cerebral small vessel disease: Insights from neuroimaging. *The Lancet Neurology*. 12 (5): 483–497.

Wardlaw, J.M., Valdés Hernández, M.C. & Muñoz-Maniega, S. (2015). What are white matter hyperintensities made of? Relevance to vascular cognitive impairment. *Journal of the American Heart Association*. 4 (6): 001140.

Washida, K., Hattori, Y. & Ihara, M. (2019). Animal models of chronic cerebral hypoperfusion: From mouse to primate. *International Journal of Molecular Sciences*. 20 (24): 6176.

Wattananit, S., Tornero, D., Graubardt, N., Memanishvili, T., Monni, E., et al. (2016). Monocyte-derived macrophages contribute to spontaneous long-term functional recovery after stroke in mice. *Journal of Neuroscience*. 36 (15): 4182–4195.

Weller, R.O., Hawkes, C.A., Kalaria, R.N., Werring, D.J. & Carare, R.O. (2015). White matter changes in dementia: Role of impaired drainage of interstitial fluid. *Brain Pathology*. 25 (1): 63–78.

Wharton, S.B., Brayne, C., Savva, G.M., Matthews, F.E., Forster, G., et al. (2011). Epidemiological Neuropathology: The MRC Cognitive Function and Aging Study Experience. *Journal of Alzheimers Disease*. 25 (2): 359–372.

Wharton, S.B., Simpson, J.E., Brayne, C. & Ince, P.G. (2015). Age-Associated white

matter lesions: The MRC cognitive function and ageing study. *Brain Pathology*. 25 (1): 35–43.

Winkler, E.A., Sagare, A.P. & Zlokovic, B. V. (2014). The pericyte: A forgotten cell type with important implications for alzheimer's disease? *Brain Pathology*. 24 (4): 371–386.

Wong, S.M., Jansen, J.F.A., Zhang, C.E., Hoff, E.I., Staals, J., et al. (2019). Blood-brain barrier impairment and hypoperfusion are linked in cerebral small vessel disease. *Neurology*. 92 (15): e1669–e1677.

Xiong, Y.Y. & Mok, V. (2011). Age-Related White Matter Changes L. Pantoni (ed.). *Journal of Aging Research*. 2011: 1–13.

Yang, J., Ding, S., Huang, W., Hu, J., Huang, S., et al. (2016). Interleukin-4 ameliorates the functional recovery of intracerebral hemorrhage through the alternative activation of microglia/macrophage. *Frontiers in Neuroscience*. 10: 61.

Yeh, F.L., Hansen, D. V. & Sheng, M. (2017). TREM2, Microglia, and Neurodegenerative Diseases. *Trends in Molecular Medicine*. 23 (6): 512–533.

Yin, Z., Raj, D., Saiepour, N., Van Dam, D., Brouwer, N., et al. (2017). Immune hyperreactivity of Aβ plaque-associated microglia in Alzheimer's disease. *Neurobiology of Aging*. 55: 115–122.

Ylikoski, R., Ylikoski, A., Erkinjuntti, T., Sulkava, R., Raininko, R. & Tilvis, R. (1993). White Matter Changes in Healthy Elderly Persons Correlate with Attention and Speed of Mental Processing. *Archives of Neurology*. 50 (8): 818–824.

Yoshiyama, Y., Arai, K., Oki, T. & Hattori, T. (2000). Expression of invariant chain and pro-cathepsin L in Alzheimer's brain. *Neuroscience Letters*. 290 (2): 125–128.

Zhang, Y., Sloan, S.A., Clarke, L.E., Caneda, C., Plaza, C.A., et al. (2016). Purification and Characterization of Progenitor and Mature Human Astrocytes Reveals Transcriptional and Functional Differences with Mouse. *Neuron*. 89 (1): 37–53.

Zhao, Y., Ke, Z., He, W. & Cai, Z. (2019). Volume of white matter hyperintensities increases with blood pressure in patients with hypertension. *Journal of International Medical Research*. 47 (8): 3681–3689.

Zhao, Z., Nelson, A.R., Betsholtz, C. & Zlokovic, B. V. (2015). Establishment and Dysfunction of the Blood-Brain Barrier. *Cell*. 163 (5): 1064–1078.

Zhou, Y., Guo, W., Zhu, Z., Hu, Y., Wang, Y., et al. (2018). Macrophage migration

inhibitory factor facilitates production of CCL5 in astrocytes following rat spinal cord injury. *Journal of Neuroinflammation*. 15 (1): 253.

Zhuang, F.J., Chen, Y., He, W.B. & Cai, Z.Y. (2018). Prevalence of white matter hyperintensities increases with age. *Neural Regeneration Research*. 13 (12): 2141–2146.

Zonouzi, M., Scafidi, J., Li, P., McEllin, B., Edwards, J., et al. (2015). GABAergic regulation of cerebellar NG2 cell development is altered in perinatal white matter injury. *Nature Neuroscience*. 18 (5): 674–682.

Zotova, E., Holmes, C., Johnston, D., Neal, J.W., Nicoll, J.A.R. & Boche, D. (2011). Microglial alterations in human Alzheimer's disease following Aβ42 immunization. *Neuropathology and Applied Neurobiology*. 37 (5): 513–524.

Zündorf, G. & Reiser, G. (2011). Calcium dysregulation and homeostasis of neural calcium in the molecular mechanisms of neurodegenerative diseases provide multiple targets for neuroprotection. *Antioxidants and Redox Signaling*. 14 (7): 1275–1288.

Zwemer, L.M., Hui, L., Wick, H.C. & Bianchi, D.W. (2014). RNA-Seq and expression microarray highlight different aspects of the fetal amniotic fluid transcriptome. *Prenatal Diagnosis*. 34 (10): 1006–1014.

APPENDICES

Appendix I

Research Ethical Committee (REC) approval (REC Reference number: 15/SW/0246, approved on 10th August 2015). "CFAS Epidemiological Neuropathology: Integrated Studies of the Cellular and Molecular Pathology of Cognitive Impairment and Frailty in the Ageing Brain". IRAS No: 184134

Appendix II

Full list of dysregulated KEGG pathways

These tables represent the dysregulated KEGG pathways identified in the periventricular white matter. These pathways were identified in the isolated periventricular white matter using DAVID analysis.

KEGG pathways (PVL compared to controls)

Pathway Name	DEG	P-Value	FDR
hsa05215: Prostate cancer	23	1.81E-06	0.002
hsa04510: Focal adhesion	38	4.74E-06	0.006
hsa04612: Antigen processing and presentation	20	9.17E-06	0.012
hsa05416: Viral myocarditis	15	1.69E-04	0.223
hsa05332: Graft-versus-host disease	11	2.29E-04	0.303
hsa05150: Staphylococcus aureus infection	14	3.56E-04	0.469
hsa04940: Type I diabetes mellitus	12	4.63E-04	0.609
hsa05200: Pathways in cancer	51	0.001	1.730
hsa05152: Tuberculosis	28	0.001	1.777
hsa05145: Toxoplasmosis	20	0.002	2.090
hsa05140: Leishmaniasis	15	0.002	2.340
hsa05212: Pancreatic cancer	14	0.002	2.945
hsa04151: PI3K-Akt signaling pathway	45	0.002	3.159
hsa05330: Allograft rejection	10	0.003	3.431
hsa04145: Phagosome	24	0.003	3.641
hsa05213: Endometrial cancer	12	0.003	3.956
hsa05166: HTLV-I infection	35	0.003	4.415
hsa05222: Small cell lung cancer	16	0.004	5.016
hsa04672: Intestinal immune network for IgA production	11	0.004	5.727

hsa05168: Herpes simplex infection	27	0.005	5.786
hsa04520: Adherens junction	14	0.005	6.471
hsa05169: Epstein-Barr virus infection	20	0.005	6.796
hsa04380: Osteoclast differentiation	21	0.005	6.908
hsa04974: Protein digestion and absorption	16	0.005	6.957
hsa05321: Inflammatory bowel disease (IBD)	13	0.006	7.279
hsa04152: AMPK signaling pathway	20	0.006	7.413
hsa04514: Cell adhesion molecules (CAMs)	22	0.006	8.164
hsa04068: FoxO signaling pathway	21	0.007	8.828
hsa04015: Rap1 signaling pathway	29	0.008	9.980
hsa05310: Asthma	8	0.010	12.266
hsa04611: Platelet activation	20	0.010	13.005
hsa04512: ECM-receptor interaction	15	0.012	14.491
hsa05210: Colorectal cancer	12	0.012	14.821
hsa05323: Rheumatoid arthritis	15	0.013	15.852
hsa05223: Non-small cell lung cancer	11	0.016	18.785
hsa04915: Estrogen signaling pathway	16	0.016	19.054
hsa04913: Ovarian steroidogenesis	10	0.018	21.224
hsa05231: Choline metabolism in cancer	16	0.019	22.199
hsa05211: Renal cell carcinoma	12	0.019	22.276
hsa05142: Chagas disease (American trypanosomiasis)	16	0.024	27.455
hsa04662: B cell receptor signaling pathway	12	0.026	29.046
hsa05320: Autoimmune thyroid disease	10	0.026	29.109
hsa05160: Hepatitis C	19	0.026	29.294
hsa04064: NF-kappa B signaling pathway	14	0.026	29.750
hsa04012: ErbB signaling pathway	14	0.026	29.750
hsa05322: Systemic lupus erythematosus	19	0.028	31.003
hsa05146: Amoebiasis	16	0.028	31.290
hsa05164: Influenza A	23	0.030	33.182
hsa04014: Ras signaling pathway	28	0.034	36.390

hsa04923: Regulation of lipolysis in adipocytes	10	0.040	41.282
hsa04010: MAPK signaling pathway	30	0.045	45.923
hsa00910: Nitrogen metabolism	5	0.047	46.933
hsa04150: mTOR signaling pathway	10	0.048	47.782

KEGG pathway (Pre-lesion compared to control)

Pathway Name	**DEG**	**P-Value**	**FDR**
hsa04723: Retrograde endocannabinoid signaling	32	1.39E-10	1.83E-07
hsa04020: Calcium signaling pathway	42	3.38E-09	4.44E-06
hsa04728: Dopaminergic synapse	34	5.29E-09	6.96E-06
hsa04713: Circadian entrainment	28	1.41E-08	1.86E-05
hsa04921: Oxytocin signaling pathway	36	2.98E-08	3.92E-05
hsa04724: Glutamatergic synapse	30	6.28E-08	8.26E-05
hsa05033: Nicotine addiction	17	6.74E-08	8.86E-05
hsa04725: Cholinergic synapse	29	1.29E-07	1.70E-04
hsa05031: Amphetamine addiction	21	3.45E-07	4.54E-04
hsa05150: Staphylococcus aureus infection	18	1.45E-06	0.002
hsa04720: Long-term potentiation	20	1.63E-06	0.002
hsa05032: Morphine addiction	24	1.66E-06	0.002
hsa04727: GABAergic synapse	23	1.82E-06	0.002
hsa05140: Leishmaniasis	20	5.40E-06	0.007
hsa05169: Epstein-Barr virus infection	27	1.08E-05	0.014
hsa05014: Amyotrophic lateral sclerosis (ALS)	16	1.17E-05	0.015
hsa04612: Antigen processing and presentation	20	1.58E-05	0.021
hsa04940: Type I diabetes mellitus	14	3.11E-05	0.041
hsa05332: Graft-versus-host disease	12	5.92E-05	0.078
hsa04261: Adrenergic signaling in cardiomyocytes	27	1.02E-04	0.133

hsa04024: cAMP signaling pathway	34	1.54E-04	0.203
hsa04010: MAPK signaling pathway	40	2.23E-04	0.293
hsa05152: Tuberculosis	31	2.26E-04	0.297
hsa04726: Serotonergic synapse	22	4.37E-04	0.573
hsa04730: Long-term depression	15	4.46E-04	0.585
hsa05166: HTLV-I infection	39	4.92E-04	0.645
hsa04915: Estrogen signaling pathway	20	6.73E-04	0.881
hsa05310: Asthma	10	6.78E-04	0.888
hsa05030: Cocaine addiction	13	7.10E-04	0.930
hsa04911: Insulin secretion	18	7.82E-04	1.024
hsa05330: Allograft rejection	11	8.58E-04	1.123
hsa05416: Viral myocarditis	14	8.92E-04	1.167
hsa05168: Herpes simplex infection	30	8.94E-04	1.170
hsa05145: Toxoplasmosis	21	0.001	1.312
hsa04971: Gastric acid secretion	16	0.001	1.534
hsa04380: Osteoclast differentiation	23	0.002	2.218
hsa04014: Ras signaling pathway	34	0.002	2.246
hsa04672: Intestinal immune network for IgA production	12	0.002	2.278
hsa04022: cGMP-PKG signaling pathway	26	0.002	2.628
hsa05162: Measles	23	0.002	2.701
hsa04145: Phagosome	25	0.002	2.750
hsa04514: Cell adhesion molecules (CAMs)	24	0.002	2.866
hsa04970: Salivary secretion	17	0.002	3.167
hsa04924: Renin secretion	14	0.003	3.538
hsa04925: Aldosterone synthesis and secretion	16	0.003	4.450
hsa05164: Influenza A	27	0.004	4.818
hsa04922: Glucagon signaling pathway	18	0.004	5.573
hsa04062: Chemokine signaling pathway	28	0.005	6.082
hsa05414: Dilated cardiomyopathy	16	0.005	6.304
hsa04151: PI3K-Akt signaling pathway	45	0.005	6.404

hsa04360: Axon guidance	21	0.006	7.329
hsa04721: Synaptic vesicle cycle	13	0.007	8.526
hsa04012: ErbB signaling pathway	16	0.007	8.706
hsa04310: Wnt signaling pathway	22	0.007	8.910
hsa04015: Rap1 signaling pathway	30	0.007	9.026
hsa04540: Gap junction	16	0.008	9.642
hsa04080: Neuroactive ligand-receptor interaction	37	0.008	9.989
hsa05214: Glioma	13	0.009	10.862
hsa04750: Inflammatory mediator regulation of TRP channels	17	0.009	11.355
hsa04919: Thyroid hormone signaling pathway	19	0.009	11.361
hsa04660: T cell receptor signaling pathway	17	0.011	13.578
hsa05412: Arrhythmogenic right ventricular cardiomyopathy (ARVC)	13	0.011	13.620
hsa05320: Autoimmune thyroid disease	11	0.012	14.751
hsa05205: Proteoglycans in cancer	28	0.012	15.119
hsa04662: B cell receptor signaling pathway	13	0.014	16.818
hsa05410: Hypertrophic cardiomyopathy (HCM)	14	0.015	18.141
hsa04611: Platelet activation	20	0.015	18.324
hsa05323: Rheumatoid arthritis	15	0.018	20.837
hsa05146: Amoebiasis	17	0.019	21.994
hsa04916: Melanogenesis	16	0.024	26.913
hsa04260: Cardiac muscle contraction	13	0.026	29.038
hsa05200: Pathways in cancer	46	0.029	31.684
hsa04914: Progesterone-mediated oocyte maturation	14	0.035	37.006
hsa04068: FoxO signaling pathway	19	0.038	40.197
hsa04144: Endocytosis	30	0.040	41.719
hsa05321: Inflammatory bowel disease (IBD)	11	0.046	46.018
hsa05203: Viral carcinogenesis	26	0.047	47.138

hsa04923: Regulation of lipolysis in adipocytes	10	0.048	47.959
hsa04621: NOD-like receptor signaling pathway	10	0.048	47.959

KEGG Pathway (Pre-lesion compared to PVL)

Pathway Name	DEG	P-Value	FDR
hsa04020: Calcium signaling pathway	46	4.71E-11	6.22E-08
hsa04723: Retrograde endocannabinoid signaling	27	3.86E-07	5.09E-04
hsa04724: Glutamatergic synapse	29	3.97E-07	5.24E-04
hsa04713: Circadian entrainment	26	4.11E-07	5.42E-04
hsa04921: Oxytocin signaling pathway	34	5.84E-07	7.71E-04
hsa05033: Nicotine addiction	16	6.56E-07	8.66E-04
hsa05032: Morphine addiction	23	9.23E-06	0.012
hsa04727: GABAergic synapse	21	3.58E-05	0.047
hsa05031: Amphetamine addiction	18	4.00E-05	0.053
hsa05014: Amyotrophic lateral sclerosis (ALS)	15	7.12E-05	0.094
hsa04720: Long-term potentiation	17	1.47E-04	0.194
hsa05412: Arrhythmogenic right ventricular cardiomyopathy (ARVC)	17	1.78E-04	0.234
hsa04725: Cholinergic synapse	23	2.30E-04	0.303
hsa05414: Dilated cardiomyopathy	19	3.09E-04	0.407
hsa04080: Neuroactive ligand-receptor interaction	43	3.22E-04	0.425
hsa04310: Wnt signaling pathway	26	3.83E-04	0.504
hsa04970: Salivary secretion	19	4.19E-04	0.552
hsa04024: cAMP signaling pathway	33	5.36E-04	0.705
hsa04022: cGMP-PKG signaling pathway	28	5.96E-04	0.783
hsa04390: Hippo signaling pathway	26	0.001	1.957
hsa04261: Adrenergic signaling in cardiomyocytes	24	0.002	2.715

hsa05410: Hypertrophic cardiomyopathy (HCM)	16	0.003	3.896
hsa00230: Purine metabolism	28	0.003	3.993
hsa04360: Axon guidance	22	0.004	4.552
hsa04728: Dopaminergic synapse	22	0.004	4.997
hsa04974: Protein digestion and absorption	17	0.004	5.143
hsa04971: Gastric acid secretion	15	0.004	5.396
hsa04911: Insulin secretion	16	0.007	8.797
hsa04978: Mineral absorption	10	0.013	16.116
hsa04010: MAPK signaling pathway	34	0.014	17.354
hsa04972: Pancreatic secretion	16	0.016	18.816
hsa04512: ECM-receptor interaction	15	0.020	22.930
hsa05010: Alzheimer's disease	24	0.022	25.827
hsa04925: Aldosterone synthesis and secretion	14	0.024	27.827
hsa05030: Cocaine addiction	10	0.026	29.240
hsa04114: Oocyte meiosis	17	0.034	36.634
hsa04730: Long-term depression	11	0.036	38.326
hsa04510: Focal adhesion	27	0.040	41.270

Appendix III

Differentially expressed pathways identified by KEGG using DAVID analysis

These tables represent the differentially expressed genes identified in the isolated periventricular white matter, using KEGG pathway analysis, focussing on pathways of interest. These genes were classified as up-and down-regulated.

PI3K/AKT pathway (PVL compared to Control)

ProbeSet ID	Gene name	Gene Detail	FC	P-Value
211550_AT	EGFR	epidermal growth factor receptor	1.43	0.0004
225293_AT	COL27A1	collagen, type XXVII, alpha 1	1.66	0.0005
205291_AT	IL2RB	interleukin 2 receptor, beta	-1.62	0.0008
225288_AT	COL27A1	collagen, type XXVII, alpha 1	1.48	0.001
219393_S_AT	AKT3	v-akt murine thymoma viral oncogene homolog 3	1.33	0.002
225669_AT	IFNAR1	interferon (alpha, beta and omega) receptor 1	1.79	0.0035
202449_S_AT	RXRA	retinoid X receptor alpha	1.34	0.0035
208225_AT	FGFR2	fibroblast growth factor receptor 2	-1.51	0.0052
201984_S_AT	EGFR	epidermal growth factor receptor	1.55	0.0057
209542_X_AT	IGF1	insulin-like growth factor 1 (somatomedin C)	-1.51	0.007
211968_S_AT	HSP90AA1	heat shock protein 90kDa alpha (cytosolic), class A member 1	2.02	0.0075
1557354_AT	SOS1	SOS Ras/Rac guanine nucleotide exchange factor 1	1.42	0.0079
202404_S_AT	COL1A2	collagen, type I, alpha 2	-1.66	0.0085
210211_S_AT	HSP90AA1	heat shock protein 90kDa alpha (cytosolic), class A member 1	1.7	0.0102
200064_AT	HSP90AB1	heat shock protein 90kDa alpha (cytosolic), class B member 1	1.47	0.0102
201438_AT	COL6A3	collagen, type VI, alpha 3	-1.62	0.0103
209799_AT	PRKAA1	protein kinase, AMP-activated, alpha 1 catalytic subunit	-1.72	0.0106

211969_AT	HSP90AA1	heat shock protein 90kDa alpha (cytosolic), class A member 1	1.42	0.011
209341_S_AT	IKBKB	inhibitor of kappa light polypeptide gene enhancer in B-cells, kinase beta	1.38	0.0112
214328_S_AT	HSP90AA1	heat shock protein 90kDa alpha (cytosolic), class A member 1	1.27	0.0114
211804_S_AT	CDK2	cyclin-dependent kinase 2	-1.32	0.0134
208240_S_AT	FGF1	fibroblast growth factor 1 (acidic)	1.33	0.0152
236034_AT	ANGPT2	angiopoietin 2	1.25	0.0178
201108_S_AT	THBS1	thrombospondin 1	-2.01	0.0178
205923_AT	HLA-DQB1	major histocompatibility complex, class II, DQ beta 1	-1.47	0.0197
216896_AT	COL4A3	collagen, type IV, alpha 3 (Goodpasture antigen)	-1.21	0.02
201125_S_AT	ITGB5	integrin beta 5	1.37	0.0212
223943_S_AT	0	0	-1.45	0.0216
216893_S_AT	COL4A3	collagen, type IV, alpha 3 (Goodpasture antigen)	-1.48	0.0218
224965_AT	GNG2	guanine nucleotide binding protein (G protein), gamma 2	-1.47	0.0219
201109_S_AT	THBS1	thrombospondin 1	-1.32	0.0223
203638_S_AT	FGFR2	fibroblast growth factor receptor 2	-1.3	0.0224
209561_AT	THBS3	thrombospondin 3	1.33	0.024
212688_AT	PIK3CB	phosphatidylinositol-4,5-bisphosphate 3-kinase, catalytic subunit beta	1.25	0.0243
206254_AT	EGF	epidermal growth factor	1.64	0.025
209364_AT	BAD	BCL2-associated agonist of cell death	1.22	0.0261
202883_S_AT	PPP2R1B	protein phosphatase 2, regulatory subunit A, beta	1.24	0.0278
232555_AT	CREB5	cAMP responsive element binding protein 5	-1.36	0.0284
213523_AT	CCNE1	cyclin E1	1.3	0.0286
211980_AT	COL4A1	collagen, type IV, alpha 1	-1.72	0.0289
208228_S_AT	FGFR2	fibroblast growth factor receptor 2	-1.24	0.0289
211161_S_AT	COL3A1	collagen, type III, alpha 1	-1.51	0.0304
211964_AT	COL4A2	collagen, type IV, alpha 2	-1.28	0.0313

1557910_AT	HSP90AB 1	heat shock protein 90kDa alpha (cytosolic), class B member 1	1.21	0.0328
225066_AT	PPP2R2D	protein phosphatase 2, regulatory subunit B, delta	1.4	0.0331
205572_AT	ANGPT2	angiopoietin 2	1.33	0.0367
219304_S_AT	PDGFD	platelet derived growth factor D	-1.22	0.0379
207709_AT	PRKAA2	protein kinase, AMP-activated, alpha 2 catalytic subunit	-1.22	0.0392
214036_AT	EFNA5	ephrin-A5	1.29	0.0393
203639_S_AT	FGFR2	fibroblast growth factor receptor 2	-1.45	0.04
204627_S_AT	ITGB3	integrin beta 3	-1.53	0.0406
203685_AT	BCL2	B-cell CLL/lymphoma 2	1.29	0.0419
223573_S_AT	PPP2R2C	protein phosphatase 2, regulatory subunit B, gamma	1.41	0.0435
222073_AT	COL4A3	collagen, type IV, alpha 3 (Goodpasture antigen)	-1.92	0.0439
241565_AT	COL4A4	collagen, type IV, alpha 4	-1.27	0.044
1565484_X_AT	EGFR	epidermal growth factor receptor	1.29	0.0443
201505_AT	LAMB1	laminin, beta 1	-1.22	0.0444
211401_S_AT	FGFR2	fibroblast growth factor receptor 2	-1.41	0.0449
204524_AT	PDPK1	3-phosphoinositide dependent protein kinase 1	1.59	0.0451
225330_AT	IGF1R	insulin-like growth factor 1 receptor	1.28	0.0492
1568629_S_AT	PIK3R2	phosphoinositide-3-kinase, regulatory subunit 2 (beta)	1.2	0.0492

MAPK Pathway (PVL compared to Control)

ProbeSet ID	**Gene name**	**Gene Detail**	**FC**	**P-Value**
225185_AT	MRAS	muscle RAS oncogene homolog	1.75	0.0002
210189_AT	HSPA1L	heat shock 70kDa protein 1-like	1.48	0.0015
219393_S_AT	AKT3	v-akt murine thymoma viral oncogene homolog 3	1.33	0.002
208225_AT	FGFR2	fibroblast growth factor receptor 2	-1.51	0.0052
201984_S_AT	EGFR	epidermal growth factor receptor	1.55	0.0057

1557354_AT	SOS1	SOS Ras/Rac guanine nucleotide exchange factor 1	1.42	0.0079
201465_S_AT	JUN	jun proto-oncogene	1.33	0.0082
201763_S_AT	DAXX	death-domain associated protein	1.22	0.0082
228109_AT	RASGRF 2	Ras protein-specific guanine nucleotide-releasing factor 2	-1.56	0.0088
39402_AT	IL1B	interleukin 1 beta	-1.34	0.0102
205067_AT	IL1B	interleukin 1 beta	-1.35	0.0105
209341_S_AT	IKBKB	inhibitor of kappa light polypeptide gene enhancer in B-cells, kinase beta	1.38	0.0112
211105_S_AT	NFATC1	nuclear factor of activated T-cells, cytoplasmic, calcineurin-dependent 1	1.36	0.0125
206538_AT	MRAS	muscle RAS oncogene homolog	1.46	0.0127
201841_S_AT	HSPB1	heat shock 27kDa protein 1	2.07	0.013
222912_AT	ARRB1	arrestin, beta 1	1.58	0.0144
233694_AT	HSPA1L	heat shock 70kDa protein 1-like	2.26	0.0151
208240_S_AT	FGF1	fibroblast growth factor 1 (acidic)	1.33	0.0152
200799_AT	HSPA1A ; HSPA1B	heat shock 70kDa protein 1A; heat shock 70kDa protein 1B	1.41	0.0162
212180_AT	CRKL	v-crk avian sarcoma virus CT10 oncogene homolog-like	1.27	0.017
202948_AT	IL1R1	interleukin 1 receptor, type I	-1.29	0.0197
211550_AT	HLA-DQB1	major histocompatibility complex, class II, DQ beta 1	-1.47	0.0197
203638_S_AT	FGFR2	fibroblast growth factor receptor 2	-1.3	0.0224
202581_AT	HSPA1A ; HSPA1B	heat shock 70kDa protein 1A; heat shock 70kDa protein 1B	1.61	0.0226
34726_AT	CACNB3	calcium channel, voltage-dependent, beta 3 subunit	1.42	0.0226
200800_S_AT	HSPA1A ; HSPA1B	heat shock 70kDa protein 1A; heat shock 70kDa protein 1B	2.23	0.0234
208944_AT	TGFBR2	transforming growth factor beta receptor II	-1.52	0.0236
208687_X_AT	HSPA8	heat shock 70kDa protein 8	1.24	0.0239
206254_AT	EGF	epidermal growth factor	1.64	0.025
207876_S_AT	FLNC	filamin C, gamma	1.24	0.0259

214376_AT	MAPK10	mitogen-activated protein kinase 10	1.38	0.0278
208876_S_AT	PAK2	p21 protein (Cdc42/Rac)-activated kinase 2	-1.23	0.0288
208228_S_AT	FGFR2	fibroblast growth factor receptor 2	-1.24	0.0289
215561_S_AT	IL1R1	interleukin 1 receptor, type I	-1.69	0.0348
209332_S_AT	MAX	MYC associated factor X	1.26	0.0363
210482_X_AT	MAP2K5	mitogen-activated protein kinase kinase 5	1.2	0.0388
203639_S_AT	FGFR2	fibroblast growth factor receptor 2	-1.45	0.04
225662_AT	ZAK	sterile alpha motif and leucine zipper containing kinase AZK	1.91	0.0429
1565484_X_AT	EGFR	epidermal growth factor receptor	1.29	0.0443
211401_S_AT	FGFR2	fibroblast growth factor receptor 2	-1.41	0.0449
213603_S_AT	RAC2	ras-related C3 botulinum toxin substrate 2 (rho family, small GTP binding protein Rac2)	-1.21	0.046
227073_AT	MAP3K2	mitogen-activated protein kinase kinase kinase 2	-1.3	0.0478

FC: Fold Change

Antigen processing and presentation and Heat Shock Proteins (PVL compared to Control)

ProbeSet ID	**Gene name**	**Gene Detail**	**FC**	**P-Value**
205671_s_at	HLA-DOB	major histocompatibility complex, class II, DO beta (HLA-DOB)	-1.79	0.0009
210189_at	HSPA1L	heat shock protein family A (Hsp70) member 1 like (HSPA1L)	1.48	0.0015
210982_s_at	hla-dra	major histocompatibility complex, class II, DR alpha (HLA-DRA)	-1.71	0.0038
208306_x_at	HLA-DRB1	major histocompatibility complex, class II, DR beta 1 (HLA-DRB1)	-1.62	0.004
212671_s_at	hla-dqa1	major histocompatibility complex, class II, DQ alpha 1 (HLA-DQA1)	-2.93	0.0055
1567627_at	CD74	CD74 molecule (CD74)	-2.67	0.0068
211968_s_at	HSP90AA1	heat shock protein 90 alpha family class A member 1 (HSP90AA1)	2.02	0.0075

209728_at	HLA-DRB4	major histocompatibility complex, class II, DR beta 4 (HLA-DRB4)	-9.48	0.0086
210211_s_at	HSP90AA1	heat shock protein 90 alpha family class A member 1 (HSP90AA1)	1.7	0.0102
200064_at	HSP90AB1	heat shock protein 90 alpha family class B member 1 (HSP90AB1)	1.47	0.0102
211969_at	HSP90AA1	heat shock protein 90 alpha family class A member 1 (HSP90AA1)	1.42	0.011
214328_s_at	HSP90AA1	heat shock protein 90 alpha family class A member 1 (HSP90AA1)	1.27	0.0114
208812_x_at	HLA-C	major histocompatibility complex, class I, C (HLA-C)	-1.4	0.0145
233694_at	HSPA1L	heat shock protein family A (Hsp70) member 1 like (HSPA1L)	2.26	0.0151
214459_x_at	HLA-C	major histocompatibility complex, class I, C (HLA-C)	-1.34	0.016
200799_at	HSPA1A	heat shock protein family A (Hsp70) member 1A (HSPA1A)	1.41	0.0162
205758_at	CD8A	CD8a molecule (CD8A)	-1.28	0.0164
208428_at	tap2	transporter 2, ATP binding cassette subfamily B member (TAP2)	-1.39	0.0172
215193_x_at	HLA-DQB1	major histocompatibility complex, class II, DQ beta 1 (HLA-DQB1)	-2.08	0.0187
201422_at	IFI30	IFI30, lysosomal thiol reductase (IFI30)	-1.86	0.0194
209823_x_at	HLA-DQB1	major histocompatibility complex, class II, DQ beta 1 (HLA-DQB1)	-1.47	0.0197
208894_at	hla-dra	major histocompatibility complex, class II, DR alpha (HLA-DRA)	-1.6	0.0221
202581_at	HSPA1A	heat shock protein family A (Hsp70) member 1A (HSPA1A)	1.61	0.0226
200800_s_at	HSPA1A	heat shock protein family A (Hsp70) member 1A (HSPA1A)	2.23	0.0234
208687_x_at	HSPA8	heat shock protein family A (Hsp70) member 8 (HSPA8)	1.24	0.0239
213537_at	HLA-DPA1	major histocompatibility complex, class II, DP alpha 1 (HLA-DPA1)	-1.57	0.0252
212998_x_at	HLA-DQB1	major histocompatibility complex, class II, DQ beta 1 (HLA-DQB1)	-1.44	0.0253
210606_x_at	KLRD1	killer cell lectin like receptor D1 (KLRD1)	-1.22	0.0311

1557910_at	HSP90AB 1	heat shock protein 90 alpha family class B member 1 (HSP90AB1)	1.21	0.0328
209619_at	CD74	CD74 molecule (CD74)	-1.4	0.0355
218127_at	NFYB	nuclear transcription factor Y subunit beta (NFYB)	1.26	0.0405
209312_x_at	HLA-DQB1	major histocompatibility complex, class II, DQ beta 1 (HLA-DQB1)	-1.49	0.0454
226878_at	HLA-DOA	major histocompatibility complex, class II, DO alpha (HLA-DOA)	-1.24	0.0496

FC: Fold Change

Phagosome (PVL compared to Control)

ProbeSet ID	**Gene name**	**Gene Detail**	**FC**	**P-Value**
205671_S_AT	HLA-DOB	major histocompatibility complex, class II, DO beta	-1.79	0.0009
210982_S_AT	HLA-DRA	major histocompatibility complex, class II, DR alpha	-1.71	0.0038
208306_X_AT	HLA-DRB1	major histocompatibility complex, class II, DR beta 1	-1.62	0.004
212671_S_AT	HLA-DQA1; HLA-DQA2	major histocompatibility complex, class II, DQ alpha 1; major histocompatibility complex, class II, DQ alpha 2	-2.93	0.0055
210004_AT	OLR1	oxidized low density lipoprotein (lectin-like) receptor 1	-3.05	0.0078
209728_AT	HLA-DRB4	major histocompatibility complex, class II, DR beta 4	-9.48	0.0086
240990_AT	RAB5A	RAB5A, member RAS oncogene family	-1.43	0.0115
236527_AT	ATP6V0E1	ATPase, H+ transporting, lysosomal 9kDa, V0 subunit e1	1.43	0.0118
207446_AT	TLR6	toll-like receptor 6	-1.2	0.0127
208812_X_AT	HLA-C	major histocompatibility complex, class I, C	-1.4	0.0145

214459_X_AT	HLA-C	major histocompatibility complex, class I, C	-1.34	0.016
216951_AT	FCGR1A	Fc fragment of IgG, high affinity Ia, receptor (CD64)	-2.12	0.0164
208428_AT	TAP2	transporter 2, ATP-binding cassette, sub-family B (MDR/TAP)	-1.39	0.0172
201108_S_AT	THBS1	thrombospondin 1	-2.01	0.0178
215193_X_AT	HLA-DRB1; HLA-DRB3; HLA-DRB4; LOC105369230	major histocompatibility complex, class II, DR beta 1; major histocompatibility complex, class II, DR beta 3; major histocompatibility complex, class II, DR beta 4; HLA class II histocompatibility antigen, DRB1-7 beta chain	-2.08	0.0187
209823_X_AT	HLA-DQB1	major histocompatibility complex, class II, DQ beta 1	-1.47	0.0197
201125_S_AT	ITGB5	integrin beta 5	1.37	0.0212
208894_AT	HLA-DRA	major histocompatibility complex, class II, DR alpha	-1.6	0.0221
201109_S_AT	THBS1	thrombospondin 1	-1.32	0.0223
208422_AT	MSR1	macrophage scavenger receptor 1	-1.95	0.0225
221504_S_AT	ATP6V1H	ATPase, H+ transporting, lysosomal 50/57kDa, V1 subunit H	1.24	0.0233
209561_AT	THBS3	thrombospondin 3	1.33	0.024
1553917_AT	PIKFYVE	phosphoinositide kinase, FYVE finger containing	1.29	0.025
213537_AT	HLA-DPA1	major histocompatibility complex, class II, DP alpha 1	-1.57	0.0252
212998_X_AT	HLA-DQB1	major histocompatibility complex, class II, DQ beta 1	-1.44	0.0253
204627_S_AT	ITGB3	integrin beta 3	-1.53	0.0406
1565673_AT	FCGR2A	Fc fragment of IgG, low affinity IIa, receptor (CD32)	-2.5	0.0409
204006_S_AT	FCGR3A; FCGR3B	Fc fragment of IgG, low affinity IIIa, receptor (CD16a); Fc fragment of IgG,	-1.53	0.0434

		low affinity IIIb, receptor (CD16b)		
209312_X_AT	HLA-DRB1; HLA-DRB4; HLA-DRB5; LOC105369230	major histocompatibility complex, class II, DR beta 1; major histocompatibility complex, class II, DR beta 4; major histocompatibility complex, class II, DR beta 5; HLA class II histocompatibility antigen, DRB1-7 beta chain	-1.49	0.0454
226878_AT	HLA-DOA	major histocompatibility complex, class II, DO alpha	-1.24	0.0496

FC: Fold Change

GABAergic Synapse (Pre-lesion compared to control)

ProbeSet ID	Gene name	Gene Detail	FC	P-value
206456_AT	GABRA5	gamma-aminobutyric acid (GABA) A receptor, alpha 5	7.1	0.0002
216895_AT	GABRG3	gamma-aminobutyric acid (GABA) A receptor, gamma 3	1.78	0.0006
215531_S_AT	GABRA5	gamma-aminobutyric acid (GABA) A receptor, alpha 5	3.89	0.001
1555867_AT	GNG4	guanine nucleotide binding protein (G protein), gamma 4	2.57	0.0014
1557122_S_AT	GABRB2	gamma-aminobutyric acid (GABA) A receptor, beta 2	2.86	0.0015
1568612_AT	GABRG2	gamma-aminobutyric acid (GABA) A receptor, gamma 2	2.37	0.0019
214933_AT	CACNA1A	calcium channel, voltage-dependent, P/Q type, alpha 1A subunit	1.76	0.0026
233437_AT	GABRA4	gamma-aminobutyric acid (GABA) A receptor, alpha 4	1.91	0.0027
222005_S_AT	GNG3	guanine nucleotide binding protein (G protein), gamma 3	2.86	0.0038
232062_AT	ADCY1	adenylate cyclase 1 (brain)	1.52	0.0039
227830_AT	GABRB3	gamma-aminobutyric acid (GABA) A receptor, beta 3	2.24	0.0043
242344_AT	GABRB2	gamma-aminobutyric acid (GABA) A receptor, beta 2	10.45	0.0045
230255_AT	GABRD	gamma-aminobutyric acid (GABA) A receptor, delta	1.54	0.007
227817_AT	PRKCB	protein kinase C, beta	2.37	0.0076
1566513_A_AT	GNG4	guanine nucleotide binding protein (G protein), gamma 4	1.71	0.0081
215340_AT	ADCY1	adenylate cyclase 1 (brain)	2.21	0.0082
206849_AT	GABRG2	gamma-aminobutyric acid (GABA) A receptor, gamma 2	2.08	0.0082
209685_S_AT	PRKCB	protein kinase C, beta	2.04	0.009
230437_S_AT	PRKCB	protein kinase C, beta	1.54	0.0094
217280_X_AT	GABRA5	gamma-aminobutyric acid (GABA) A receptor, alpha 5	1.6	0.0095

206678_AT	GABRA1	gamma-aminobutyric acid (GABA) A receptor, alpha 1	5.31	0.0125
210454_S_AT	KCNJ6	potassium channel, inwardly rectifying subfamily J, member 6	1.23	0.014
229724_AT	GABRB3	gamma-aminobutyric acid (GABA) A receptor, beta 3	4.42	0.0152
228795_AT	PRKCB	protein kinase C, beta	1.87	0.0172
213245_AT	ADCY1	adenylate cyclase 1 (brain)	2.22	0.018
207352_S_AT	GABRB2	gamma-aminobutyric acid (GABA) A receptor, beta 2	1.44	0.0192
202125_S_AT	TRAK2	trafficking protein, kinesin binding 2	1.62	0.0206
204763_S_AT	GNAO1	guanine nucleotide binding protein (G protein), alpha activating activity polypeptide O	2.24	0.0216
208463_AT	GABRA4	gamma-aminobutyric acid (GABA) A receptor, alpha 4	2.04	0.022
202124_S_AT	TRAK2	trafficking protein, kinesin binding 2	1.37	0.0231
228831_S_AT	GNG7; LOC101929097	guanine nucleotide binding protein (G protein), gamma 7; uncharacterized LOC101929097	1.24	0.0252
203158_S_AT	GLS	glutaminase	1.87	0.0264
204762_S_AT	GNAO1	guanine nucleotide binding protein (G protein), alpha activating activity polypeptide O	1.78	0.029
242891_AT	ADCY5	adenylate cyclase 5	1.31	0.0308
235049_AT	ADCY1	adenylate cyclase 1 (brain)	1.41	0.0323
203159_AT	GLS	glutaminase	2.2	0.0333
227824_AT	PRKCB	protein kinase C, beta	1.77	0.0337
205850_S_AT	GABRB3	gamma-aminobutyric acid (GABA) A receptor, beta 3	1.42	0.034
236195_X_AT	PRKCG	protein kinase C, gamma	1.25	0.0397
235781_AT	CACNA1B	calcium channel, voltage-dependent, N type, alpha 1B subunit	1.84	0.0403

205184_AT	GNG4	guanine nucleotide binding protein (G protein), gamma 4	1.67	0.042
202742_S_AT	PRKACB	protein kinase, cAMP-dependent, catalytic, beta	1.33	0.0473
216651_S_AT	GAD2	glutamate decarboxylase 2	2.08	0.0476

FC: Fold Change

Calcium Signalling (Pre-lesion compared to control)

ProbeSet ID	**Gene name**	**Gene Detail**	**FC**	**P-value**
231783_AT	CHRM1	cholinergic receptor, muscarinic 1	1.84	0.0002
214217_AT	GRM5	glutamate receptor, metabotropic 5	1.78	0.0004
229029_AT	CAMK4	calcium/calmodulin-dependent protein kinase IV	2.74	0.0008
241871_AT	CAMK4	calcium/calmodulin-dependent protein kinase IV	3.31	0.0008
211925_S_AT	PLCB1	phospholipase C, beta 1 (phosphoinositide-specific)	2.73	0.0009
200623_S_AT	CALM2; CALM3	calmodulin 2 (phosphorylase kinase, delta); calmodulin 3 (phosphorylase kinase, delta)	2.11	0.001
215687_X_AT	PLCB1	phospholipase C, beta 1 (phosphoinositide-specific)	2.39	0.0011
1556583_A_AT	SLC8A1	solute carrier family 8 (sodium/calcium exchanger), member 1	3.21	0.0011
236013_AT	CACNA1E	calcium channel, voltage-dependent, R type, alpha 1E subunit	4.46	0.0012
205915_X_AT	GRIN1	glutamate receptor, ionotropic, N-methyl D-aspartate 1	1.74	0.0013
207577_AT	HTR4	5-hydroxytryptamine (serotonin) receptor 4, G protein-coupled	1.78	0.0013

210939_S_AT	GRM1	glutamate receptor, metabotropic 1	3.08	0.0013
244256_AT	CACNA1E	calcium channel, voltage-dependent, R type, alpha 1E subunit	4.11	0.0015
1565389_S_AT	GRM5	glutamate receptor, metabotropic 5	5.37	0.0017
214044_AT	RYR2	ryanodine receptor 2 (cardiac)	2.35	0.0018
206534_AT	GRIN2A	glutamate receptor, ionotropic, N-methyl D-aspartate 2A	1.68	0.0019
214933_AT	CACNA1A	calcium channel, voltage-dependent, P/Q type, alpha 1A subunit	1.76	0.0026
242488_AT	CHRM3	cholinergic receptor, muscarinic 3	1.65	0.0027
209281_S_AT	ATP2B1	ATPase, Ca++ transporting, plasma membrane 1	1.83	0.0031
221631_AT	CACNA1I	calcium channel, voltage-dependent, T type, alpha 1I subunit	1.58	0.0034
207235_S_AT	GRM5	glutamate receptor, metabotropic 5	1.85	0.0034
213688_AT	CALM1; CALM2	calmodulin 1 (phosphorylase kinase, delta); calmodulin 2 (phosphorylase kinase, delta)	1.6	0.0036
232062_AT	ADCY1	adenylate cyclase 1 (brain)	1.52	0.0039
205450_AT	PHKA1	phosphorylase kinase, alpha 1 (muscle)	-1.34	0.0044
1561615_S_AT	SLC8A1	solute carrier family 8 (sodium/calcium exchanger), member 1	2.35	0.0045
34846_AT	CAMK2B	calcium/calmodulin-dependent protein kinase II beta	2.1	0.006
202425_X_AT	PPP3CA	protein phosphatase 3, catalytic subunit, alpha isozyme	1.68	0.0065
210448_S_AT	P2RX5	purinergic receptor P2X, ligand gated ion channel, 5	1.48	0.0066
212930_AT	ATP2B1	ATPase, Ca++ transporting, plasma membrane 1	2.9	0.0068
207613_S_AT	CAMK2A	calcium/calmodulin-dependent protein kinase II alpha	7.37	0.0068

210781_X_AT	GRIN1	glutamate receptor, ionotropic, N-methyl D-aspartate 1	1.93	0.0074
227817_AT	PRKCB	protein kinase C, beta	2.37	0.0076
215340_AT	ADCY1	adenylate cyclase 1 (brain)	2.21	0.0082
1559633_A_AT	CHRM3	cholinergic receptor, muscarinic 3	1.78	0.0084
209685_S_AT	PRKCB	protein kinase C, beta	2.04	0.009
213222_AT	PLCB1	phospholipase C, beta 1 (phosphoinositide-specific)	3.9	0.0092
230437_S_AT	PRKCB	protein kinase C, beta	1.54	0.0094
213108_AT	CAMK2A	calcium/calmodulin-dependent protein kinase II alpha	1.72	0.0099
217140_S_AT	VDAC1	voltage-dependent anion channel 1	1.24	0.01
211483_X_AT	CAMK2B	calcium/calmodulin-dependent protein kinase II beta	1.69	0.01
200653_S_AT	CALM1; CALM2	calmodulin 1 (phosphorylase kinase, delta); calmodulin 2 (phosphorylase kinase, delta)	1.63	0.0104
208432_S_AT	CACNA1E	calcium channel, voltage-dependent, R type, alpha 1E subunit	1.62	0.0122
229876_AT	PHKA1	phosphorylase kinase, alpha 1 (muscle)	-1.65	0.0124
209956_S_AT	CAMK2B	calcium/calmodulin-dependent protein kinase II beta	5.14	0.0127
211125_X_AT	GRIN1	glutamate receptor, ionotropic, N-methyl D-aspartate 1	1.79	0.0135
1566739_AT	PLCE1	phospholipase C, epsilon 1	-1.54	0.0149
207309_AT	NOS1	nitric oxide synthase 1 (neuronal)	1.84	0.015
240650_AT	CACNA1E	calcium channel, voltage-dependent, R type, alpha 1E subunit	1.31	0.0162
228795_AT	PRKCB	protein kinase C, beta	1.87	0.0172
213245_AT	ADCY1	adenylate cyclase 1 (brain)	2.22	0.018
215267_S_AT	SLC8A2	solute carrier family 8 (sodium/calcium exchanger), member 2	1.22	0.0182
235213_AT	ITPKB	inositol-trisphosphate 3-kinase B	-1.37	0.0212

200622_X_AT	CALM2; CALM3	calmodulin 2 (phosphorylase kinase, delta); calmodulin 3 (phosphorylase kinase, delta)	1.71	0.0213
235518_AT	SLC8A1	solute carrier family 8 (sodium/calcium exchanger), member 1	1.49	0.0216
216098_S_AT	HTR7; HTR7P1	5-hydroxytryptamine (serotonin) receptor 7, adenylate cyclase-coupled; 5-hydroxytryptamine (serotonin) receptor 7 pseudogene 1	1.34	0.0234
209563_X_AT	CALM1; CALM2	calmodulin 1 (phosphorylase kinase, delta); calmodulin 2 (phosphorylase kinase, delta)	1.25	0.0237
32541_AT	PPP3CC	protein phosphatase 3, catalytic subunit, gamma isozyme	-1.29	0.0258
207557_S_AT	RYR2	ryanodine receptor 2 (cardiac)	2.75	0.0265
233498_AT	ERBB4	erb-b2 receptor tyrosine kinase 4	1.31	0.0268
32540_AT	PPP3CC	protein phosphatase 3, catalytic subunit, gamma isozyme	-1.36	0.0271
204506_AT	PPP3R1	protein phosphatase 3, regulatory subunit B, alpha	1.67	0.0274
206355_AT	GNAL	guanine nucleotide binding protein (G protein), alpha activating activity polypeptide, olfactory type	2.7	0.0286
209439_S_AT	PHKA2	phosphorylase kinase, alpha 2 (liver)	-1.25	0.0288
210404_X_AT	CAMK2B	calcium/calmodulin-dependent protein kinase II beta	2.33	0.0298
202429_S_AT	PPP3CA	protein phosphatase 3, catalytic subunit, alpha isozyme	2.51	0.0303
214348_AT	TACR2	tachykinin receptor 2	1.3	0.0309
235049_AT	ADCY1	adenylate cyclase 1 (brain)	1.41	0.0323
239132_AT	NOS1	nitric oxide synthase 1 (neuronal)	1.63	0.0332
227824_AT	PRKCB	protein kinase C, beta	1.77	0.0337
40562_AT	GNA11	guanine nucleotide binding protein (G protein), alpha 11 (Gq class)	1.26	0.0348

211985_S_AT	CALM1; CALM2	calmodulin 1 (phosphorylase kinase, delta); calmodulin 2 (phosphorylase kinase, delta)	1.26	0.0348
234729_AT	PHKG1	phosphorylase kinase, gamma 1 (muscle)	-1.25	0.0359
213924_AT	GNAL	guanine nucleotide binding protein (G protein), alpha activating activity polypeptide, olfactory type	1.46	0.0388
236195_X_AT	PRKCG	protein kinase C, gamma	1.25	0.0397
235781_AT	CACNA1B	calcium channel, voltage-dependent, N type, alpha 1B subunit	1.84	0.0403
210804_X_AT	SLC8A1	solute carrier family 8 (sodium/calcium exchanger), member 1	1.28	0.0419
203131_AT	PDGFRA	platelet-derived growth factor receptor, alpha polypeptide	1.63	0.0432
231916_AT	NOS1	nitric oxide synthase 1 (neuronal)	2.26	0.0436
202742_S_AT	PRKACB	protein kinase, cAMP-dependent, catalytic, beta	1.33	0.0473
239357_AT	ATP2B2	ATPase, Ca++ transporting, plasma membrane 2	2.4	0.0477
206356_S_AT	GNAL	guanine nucleotide binding protein (G protein), alpha activating activity polypeptide, olfactory type	1.6	0.0481

FC: Fold Change

Glutamatergic synapse (pre-lesion compared to control)

ProbeSet ID	Gene name	Gene Detail	FC	P-value
1565389_S_AT	GRM5	glutamate receptor, metabotropic 5	5.37	0.0017
227824_AT	PRKCB	protein kinase C, beta	1.77	0.0337
235049_AT	ADCY1	adenylate cyclase 1 (brain)	1.41	0.0323
205915_X_AT	GRIN1	glutamate receptor, ionotropic, N-methyl D-aspartate 1	1.74	0.0013
203159_AT	GLS	glutaminase	2.2	0.0333
210781_X_AT	GRIN1	glutamate receptor, ionotropic, N-methyl D-aspartate 1	1.93	0.0074
236195_X_AT	PRKCG	protein kinase C, gamma	1.25	0.0397
205358_AT	GRIA2	glutamate receptor, ionotropic, AMPA 2	1.72	0.0246
214217_AT	GRM5	glutamate receptor, metabotropic 5	1.78	0.0004
213793_S_AT	HOMER1	homer scaffolding protein 1	2.53	0.0037
211925_S_AT	PLCB1	phospholipase C, beta 1 (phosphoinositide-specific)	2.73	0.0009
204763_S_AT	GNAO1	guanine nucleotide binding protein (G protein), alpha activating activity polypeptide O	2.24	0.0216
204229_AT	SLC17A7	solute carrier family 17 (vesicular glutamate transporter), member 7	1.34	0.0168
1555867_AT	GNG4	guanine nucleotide binding protein (G protein), gamma 4	2.57	0.0014
204184_S_AT	ADRBK2	adrenergic, beta, receptor kinase 2	1.33	0.0104
213845_AT	GRIK2	glutamate receptor, ionotropic, kainate 2	1.32	0.0102
204762_S_AT	GNAO1	guanine nucleotide binding protein (G protein), alpha activating activity polypeptide O	1.78	0.029

241172_AT	GRIA2	glutamate receptor, ionotropic, AMPA 2	1.6	0.0043
208389_S_AT	SLC1A2	solute carrier family 1 (glial high affinity glutamate transporter), member 2	1.48	0.0423
203158_S_AT	GLS	glutaminase	1.87	0.0264
1566513_A_AT	GNG4	guanine nucleotide binding protein (G protein), gamma 4	1.71	0.0081
232062_AT	ADCY1	adenylate cyclase 1 (brain)	1.52	0.0039
239095_AT	GRIN2B	glutamate receptor, ionotropic, N-methyl D-aspartate 2B	2.1	0.0019
213222_AT	PLCB1	phospholipase C, beta 1 (phosphoinositide-specific)	3.9	0.0092
206730_AT	GRIA3	glutamate receptor, ionotropic, AMPA 3	2.54	0.0025
32540_AT	PPP3CC	protein phosphatase 3, catalytic subunit, gamma isozyme	-1.36	0.0271
227817_AT	PRKCB	protein kinase C, beta	2.37	0.0076
215687_X_AT	PLCB1	phospholipase C, beta 1 (phosphoinositide-specific)	2.39	0.0011
213245_AT	ADCY1	adenylate cyclase 1 (brain)	2.22	0.018
205184_AT	GNG4	guanine nucleotide binding protein (G protein), gamma 4	1.67	0.042
211602_S_AT	TRPC1	transient receptor potential cation channel, subfamily C, member 1	-1.63	0.0226
206534_AT	GRIN2A	glutamate receptor, ionotropic, N-methyl D-aspartate 2A	1.68	0.0019
209685_S_AT	PRKCB	protein kinase C, beta	2.04	0.009
230437_S_AT	PRKCB	protein kinase C, beta	1.54	0.0094
228795_AT	PRKCB	protein kinase C, beta	1.87	0.0172
202429_S_AT	PPP3CA	protein phosphatase 3, catalytic subunit, alpha isozyme	2.51	0.0303
202742_S_AT	PRKACB	protein kinase, cAMP-dependent, catalytic, beta	1.33	0.0473
208032_S_AT	GRIA3	glutamate receptor, ionotropic, AMPA 3	2.22	0.001

211125_X_AT	GRIN1	glutamate receptor, ionotropic, N-methyl D-aspartate 1	1.79	0.0135
207235_S_AT	GRM5	glutamate receptor, metabotropic 5	1.85	0.0034
32541_AT	PPP3CC	protein phosphatase 3, catalytic subunit, gamma isozyme	-1.29	0.0258
210411_S_AT	GRIN2B	glutamate receptor, ionotropic, N-methyl D-aspartate 2B	1.7	0.005
204506_AT	PPP3R1	protein phosphatase 3, regulatory subunit B, alpha	1.67	0.0274
242891_AT	ADCY5	adenylate cyclase 5	1.31	0.0308
209793_AT	GRIA1	glutamate receptor, ionotropic, AMPA 1	2.46	0.0325
215340_AT	ADCY1	adenylate cyclase 1 (brain)	2.21	0.0082
210939_S_AT	GRM1	glutamate receptor, metabotropic 1	3.08	0.0013
228831_S_AT	GNG7; LOC101929097	guanine nucleotide binding protein (G protein), gamma 7; uncharacterized LOC101929097	1.24	0.0252
214933_AT	CACNA1A	calcium channel, voltage-dependent, P/Q type, alpha 1A subunit	1.76	0.0026
210684_S_AT	DLG4	discs, large homolog 4 (Drosophila)	2.22	0.0134
222005_S_AT	GNG3	guanine nucleotide binding protein (G protein), gamma 3	2.86	0.0038
217565_AT	GRIA3	glutamate receptor, ionotropic, AMPA 3	1.88	0.0153
230144_AT	GRIA3	glutamate receptor, ionotropic, AMPA 3	2.47	0.003
202425_X_AT	PPP3CA	protein phosphatase 3, catalytic subunit, alpha isozyme	1.68	0.0065

FC: Fold Change

Phagosome (pre-lesion compared to control)

ProbeSet ID	Gene name	Gene Detail	FC	P-Value
211990_AT	HLA-DPA1	major histocompatibility complex, class II, DP alpha 1	-3.77	0.0324
1565673_AT	FCGR2A	Fc fragment of IgG, low affinity IIa, receptor (CD32)	-3.5	0.0391
208422_AT	MSR1	macrophage scavenger receptor 1	-3.13	0.0199
212671_S_AT	HLA-DQA1; HLA-DQA2	major histocompatibility complex, class II, DQ alpha 1; major histocompatibility complex, class II, DQ alpha 2	-2.8	0.0183
213537_AT	HLA-DPA1	major histocompatibility complex, class II, DP alpha 1	-2.72	0.0004
210004_AT	OLR1	oxidized low density lipoprotein (lectin-like) receptor 1	-2.28	0.0474
216951_AT	FCGR1A	Fc fragment of IgG, high affinity Ia, receptor (CD64)	-2.12	0.0372
1554406_A_AT	CLEC7A	C-type lectin domain family 7, member A	-1.95	0.016
1565674_AT	FCGR2A; FCGR2C	Fc fragment of IgG, low affinity IIa, receptor (CD32); Fc fragment of IgG, low affinity IIc, receptor for (CD32) (gene/pseudogene)	-1.95	0.0485
211991_S_AT	HLA-DPA1	major histocompatibility complex, class II, DP alpha 1	-1.93	0.0228
206313_AT	HLA-DOA	major histocompatibility complex, class II, DO alpha	-1.83	0.0238
217478_S_AT	HLA-DMA	major histocompatibility complex, class II, DM alpha	-1.79	0.0352
211654_X_AT	HLA-DQB1	major histocompatibility complex, class II, DQ beta 1	-1.76	0.0046
208894_AT	HLA-DRA	major histocompatibility complex, class II, DR alpha	-1.72	0.0266
210992_X_AT	FCGR2C	Fc fragment of IgG, low affinity IIc, receptor for (CD32) (gene/pseudogene)	-1.72	0.0326

211395_X_AT	FCGR2C	Fc fragment of IgG, low affinity IIc, receptor for (CD32) (gene/pseudogene)	-1.69	0.0092
226878_AT	HLA-DOA	major histocompatibility complex, class II, DO alpha	-1.64	0.0163
205671_S_AT	HLA-DOB	major histocompatibility complex, class II, DO beta	-1.64	0.0207
204006_S_AT	FCGR3A; FCGR3B	Fc fragment of IgG, low affinity IIIa, receptor (CD16a); Fc fragment of IgG, low affinity IIIb, receptor (CD16b)	-1.61	0.0368
210982_S_AT	HLA-DRA	major histocompatibility complex, class II, DR alpha	-1.54	0.0229
210889_S_AT	FCGR2B	Fc fragment of IgG, low affinity IIb, receptor (CD32)	-1.53	0.0161
201137_S_AT	HLA-DPB1	major histocompatibility complex, class II, DP beta 1	-1.47	0.0478
208812_X_AT	HLA-C	major histocompatibility complex, class I, C	-1.45	0.0125
208428_AT	TAP2	transporter 2, ATP-binding cassette, sub-family B (MDR/TAP)	-1.44	0.019
202307_S_AT	TAP1	transporter 1, ATP-binding cassette, sub-family B (MDR/TAP)	-1.44	0.0232
236203_AT	HLA-DQA1	major histocompatibility complex, class II, DQ alpha 1	-1.42	0.0372
1555756_A_AT	CLEC7A	C-type lectin domain family 7, member A	-1.41	0.0255
222385_X_AT	SEC61A1	Sec61 translocon alpha 1 subunit	-1.38	0.0067
214459_X_AT	HLA-C	major histocompatibility complex, class I, C	-1.36	0.0123
212320_AT	TUBB	tubulin, beta class I	-1.3	0.0283
208306_X_AT	HLA-DRB1	major histocompatibility complex, class II, DR beta 1	-1.27	0.0345
211799_X_AT	HLA-C	major histocompatibility complex, class I, C	-1.23	0.029
1569843_AT	DYNC1I1	dynein, cytoplasmic 1, intermediate chain 1	1.22	0.028

214762_AT	ATP6V1G2	ATPase, H+ transporting, lysosomal 13kDa, V1 subunit G2	1.45	0.0255
239132_AT	NOS1	nitric oxide synthase 1 (neuronal)	1.63	0.0332
207309_AT	NOS1	nitric oxide synthase 1 (neuronal)	1.84	0.015
231916_AT	NOS1	nitric oxide synthase 1 (neuronal)	2.26	0.0436

Antigen processing and presentation and HSP (pre-lesion compared to control)

ProbeSet ID	**Gene name**	**Gene Detail**	**FC**	**P-Value**
213537_at	HLA-DPA1	major histocompatibility complex, class II, DP alpha 1(HLA-DPA1)	-2.72	0.0004
214328_s_at	HSP90AA1	heat shock protein 90 alpha family class A member 1(HSP90AA1)	1.34	0.0028
211654_X_AT	HLA-DQB1	major histocompatibility complex, class II, DQ beta 1	-1.76	0.0046
211969_at	HSP90AA1	heat shock protein 90 alpha family class A member 1(HSP90AA1)	1.47	0.0087
214459_x_at	HLA-C	major histocompatibility complex, class I, C(HLA-C)	-1.36	0.0123
208812_x_at	HLA-C	major histocompatibility complex, class I, C(HLA-C)	-1.45	0.0125
211968_s_at	HSP90AA1	heat shock protein 90 alpha family class A member 1(HSP90AA1)	1.91	0.0127
226878_at	HLA-DOA	major histocompatibility complex, class II, DO alpha (HLA-DOA)	-1.64	0.0163
202963_AT	RFX5	regulatory factor X, 5 (influences HLA class II expression)	-1.37	0.0172
209619_at	CD74	CD74 molecule (CD74)	-1.57	0.0182

212671_s_at	hla-dqa1	major histocompatibility complex, class II, DQ alpha 1(HLA-DQA1)	-2.8	0.0183
201422_at	IFI30	IFI30, lysosomal thiol reductase (IFI30)	-1.66	0.0183
208428_AT	TAP2	transporter 2, ATP-binding cassette, sub-family B (MDR/TAP)	-1.44	0.019
210211_s_at	HSP90AA1	heat shock protein 90 alpha family class A member 1(HSP90AA1)	1.73	0.019
205671_s_at	HLA-DOB	major histocompatibility complex, class II, DO beta (HLA-DOB)	-1.64	0.0207
211991_S_AT	HLA-DPA1	major histocompatibility complex, class II, DP alpha 1	-1.93	0.0228
210982_s_at	hla-dra	major histocompatibility complex, class II, DR alpha (HLA-DRA)	-1.54	0.0229
202307_S_AT	TAP1	transporter 1, ATP-binding cassette, sub-family B (MDR/TAP)	-1.44	0.0232
206313_AT	HLA-DOA	major histocompatibility complex, class II, DO alpha	-1.83	0.0238
200064_at	HSP90AB1	heat shock protein 90 alpha family class B member 1(HSP90AB1)	1.28	0.0254
208894_at	hla-dra	major histocompatibility complex, class II, DR alpha (HLA-DRA)	-1.72	0.0266
211799_X_AT	HLA-C	major histocompatibility complex, class I, C	-1.23	0.029
211990_AT	HLA-DPA1	major histocompatibility complex, class II, DP alpha 1	-3.77	0.0324
208306_x_at	HLA-DRB1	major histocompatibility complex, class II, DR beta 1(HLA-DRB1)	-1.27	0.0345
217478_S_AT	HLA-DMA	major histocompatibility complex, class II, DM alpha	-1.79	0.0352
236203_AT	HLA-DQA1	major histocompatibility complex, class II, DQ alpha 1	-1.42	0.0372

208687_x_at	HSPA8	heat shock protein family A (Hsp70) member 8(HSPA8)	1.28	0.0424
201137_S_AT	HLA-DPB1	major histocompatibility complex, class II, DP beta 1	-1.47	0.0478
221891_X_AT	HSPA8	heat shock 70kDa protein 8	1.4	0.048
200799_at	HSPA1A	heat shock protein family A (Hsp70) member 1A(HSPA1A)	1.22	0.0488
208814_AT	HSPA4	heat shock 70kDa protein 4	1.24	0.0491

FC: Fold Change

Calcium Signalling Pathways (Pre-lesion compared to PVL)

ProbeSet ID	Gene name	Gene Detail	FC	P-Value
217623_AT	MYLK3	myosin light chain kinase 3	-3.29	0.0462
211492_S_AT	ADRA1A	adrenoceptor alpha 1A	-2.58	0.0103
206811_AT	ADCY8	adenylate cyclase 8 (brain)	-2.25	0.0022
1566739_AT	PLCE1	phospholipase C, epsilon 1	-2.15	0.0053
205450_AT	PHKA1	phosphorylase kinase, alpha 1 (muscle)	-1.53	0.0046
205125_AT	PLCD1	phospholipase C, delta 1	-1.48	0.0404
216836_S_AT	ERBB2	erb-b2 receptor tyrosine kinase 2	-1.45	0.0009
210930_S_AT	ERBB2	erb-b2 receptor tyrosine kinase 2	-1.44	0.0418
221864_AT	ORAI3	ORAI calcium release-activated calcium modulator 3	-1.43	0.0057
1557477_AT	STIM1	stromal interaction molecule 1	-1.43	0.0293
205410_S_AT	ATP2B4	ATPase, Ca++ transporting, plasma membrane 4	-1.4	0.0115
209439_S_AT	PHKA2	phosphorylase kinase, alpha 2 (liver)	-1.38	0.0076
203723_AT	ITPKB	inositol-trisphosphate 3-kinase B	-1.32	0.0055
235213_AT	ITPKB	inositol-trisphosphate 3-kinase B	-1.31	0.0353
1563466_AT	MYLK	myosin light chain kinase	-1.28	0.0298

32541_AT	PPP3CC	protein phosphatase 3, catalytic subunit, gamma isozyme	-1.24	0.0464
210804_X_AT	SLC8A1	solute carrier family 8 (sodium/calcium exchanger), member 1	1.21	0.0375
215267_S_AT	SLC8A2	solute carrier family 8 (sodium/calcium exchanger), member 2	1.26	0.0071
203110_AT	PTK2B	protein tyrosine kinase 2 beta	1.28	0.0339
240650_AT	CACNA1E	calcium channel, voltage-dependent, R type, alpha 1E subunit	1.29	0.024
214348_AT	TACR2	tachykinin receptor 2	1.33	0.0148
210637_AT	TACR1	tachykinin receptor 1	1.34	0.0279
232062_AT	ADCY1	adenylate cyclase 1 (brain)	1.36	0.0126
235049_AT	ADCY1	adenylate cyclase 1 (brain)	1.39	0.024
208432_S_AT	CACNA1E	calcium channel, voltage-dependent, R type, alpha 1E subunit	1.43	0.0234
221631_AT	CACNA1I	calcium channel, voltage-dependent, T type, alpha 1I subunit	1.44	0.0073
205915_X_AT	GRIN1	glutamate receptor, ionotropic, N-methyl D-aspartate 1	1.45	0.011
211805_S_AT	SLC8A1	solute carrier family 8 (sodium/calcium exchanger), member 1	1.46	0.0384
210448_S_AT	P2RX5	purinergic receptor P2X, ligand gated ion channel, 5	1.47	0.0125
216098_S_AT	HTR7; HTR7P1	5-hydroxytryptamine (serotonin) receptor 7, adenylate cyclase-coupled; 5-hydroxytryptamine (serotonin) receptor 7 pseudogene 1	1.49	0.0264
213688_AT	CALM1; CALM2	calmodulin 1 (phosphorylase kinase, delta); calmodulin 2 (phosphorylase kinase, delta)	1.59	0.0157
211125_X_AT	GRIN1	glutamate receptor, ionotropic, N-methyl D-aspartate 1	1.65	0.0409
213108_AT	CAMK2A	calcium/calmodulin-dependent protein kinase II alpha	1.67	0.0429

235518_AT	SLC8A1	solute carrier family 8 (sodium/calcium exchanger), member 1	1.69	0.019
209281_S_AT	ATP2B1	ATPase, Ca++ transporting, plasma membrane 1	1.75	0.007
242488_AT	CHRM3	cholinergic receptor, muscarinic 3	1.76	0.002
214217_AT	GRM5	glutamate receptor, metabotropic 5	1.77	0.001
206534_AT	GRIN2A	glutamate receptor, ionotropic, N-methyl D-aspartate 2A	1.77	0.0082
239132_AT	NOS1	nitric oxide synthase 1 (neuronal)	1.77	0.0351
204506_AT	PPP3R1	protein phosphatase 3, regulatory subunit B, alpha	1.78	0.0343
210781_X_AT	GRIN1	glutamate receptor, ionotropic, N-methyl D-aspartate 1	1.82	0.0182
200623_S_AT	CALM2; CALM3	calmodulin 2 (phosphorylase kinase, delta); calmodulin 3 (phosphorylase kinase, delta)	1.84	0.0281
230437_S_AT	PRKCB	protein kinase C, beta	1.85	0.0029
202425_X_AT	PPP3CA	protein phosphatase 3, catalytic subunit, alpha isozyme	1.85	0.0122
202425_X_AT	PPP3CA	protein phosphatase 3, catalytic subunit, alpha isozyme	1.85	0.0122
214596_AT	CHRM3	cholinergic receptor, muscarinic 3	1.88	0.0056
1561615_S_AT	SLC8A1	solute carrier family 8 (sodium/calcium exchanger), member 1	1.94	0.0151
207235_S_AT	GRM5	glutamate receptor, metabotropic 5	1.96	0.0038
34846_AT	CAMK2B	calcium/calmodulin-dependent protein kinase II beta	1.97	0.0169
215687_X_AT	PLCB1	phospholipase C, beta 1 (phosphoinositide-specific)	1.99	0.0046
214652_AT	DRD1	dopamine receptor D1	1.99	0.0187
1559633_A_AT	CHRM3	cholinergic receptor, muscarinic 3	2	0.004
231783_AT	CHRM1	cholinergic receptor, muscarinic 1	2.06	0.0000117
228795_AT	PRKCB	protein kinase C, beta	2.07	0.0162

203131_AT	PDGFRA	platelet-derived growth factor receptor, alpha polypeptide	2.09	0.004
227824_AT	PRKCB	protein kinase C, beta	2.14	0.03
227817_AT	PRKCB	protein kinase C, beta	2.18	0.0034
207957_S_AT	PRKCB	protein kinase C, beta	2.18	0.0045
207577_AT	HTR4	5-hydroxytryptamine (serotonin) receptor 4, G protein-coupled	2.2	0.0001
231916_AT	NOS1	nitric oxide synthase 1 (neuronal)	2.2	0.0445
211925_S_AT	PLCB1	phospholipase C, beta 1 (phosphoinositide-specific)	2.24	0.0018
235781_AT	CACNA1B	calcium channel, voltage-dependent, N type, alpha 1B subunit	2.29	0.0076
207309_AT	NOS1	nitric oxide synthase 1 (neuronal)	2.31	0.002
210939_S_AT	GRM1	glutamate receptor, metabotropic 1	2.34	0.0041
214044_AT	RYR2	ryanodine receptor 2 (cardiac)	2.35	0.0027
238546_AT	SLC8A1	solute carrier family 8 (sodium/calcium exchanger), member 1	2.37	0.0338
215340_AT	ADCY1	adenylate cyclase 1 (brain)	2.42	0.0117
209685_S_AT	PRKCB	protein kinase C, beta	2.42	0.0164
207053_AT	SLC8A1	solute carrier family 8 (sodium/calcium exchanger), member 1	2.62	0.0449
239357_AT	ATP2B2	ATPase, Ca++ transporting, plasma membrane 2	2.73	0.0382
229029_AT	CAMK4	calcium/calmodulin-dependent protein kinase IV	2.75	0.0014
1556583_A_AT	SLC8A1	solute carrier family 8 (sodium/calcium exchanger), member 1	2.76	0.004
238747_AT	CACNA1E	calcium channel, voltage-dependent, R type, alpha 1E subunit	3.01	0.0001
213245_AT	ADCY1	adenylate cyclase 1 (brain)	3.18	0.003
213222_AT	PLCB1	phospholipase C, beta 1 (phosphoinositide-specific)	3.73	0.0122

241871_AT	CAMK4	calcium/calmodulin-dependent protein kinase IV	3.93	0.0005
244256_AT	CACNA1E	calcium channel, voltage-dependent, R type, alpha 1E subunit	4.35	0.0009
1565389_S_AT	GRM5	glutamate receptor, metabotropic 5	4.93	0.0091
236013_AT	CACNA1E	calcium channel, voltage-dependent, R type, alpha 1E subunit	5.4	0.0003
242410_S_AT	CACNA1E	calcium channel, voltage-dependent, R type, alpha 1E subunit	5.6	8.77E-07
207613_S_AT	CAMK2A	calcium/calmodulin-dependent protein kinase II alpha	7.06	0.0085

Glutamatergic synapse (pre-lesion compared to PVL)

ProbeSet ID	**Gene name**	**Gene Detail**	**FC**	**P-Value**
206811_AT	ADCY8	adenylate cyclase 8 (brain)	-2.25	0.0022
1555240_S_AT	GNG12	guanine nucleotide binding protein (G protein), gamma 12	-1.59	0.0191
204647_AT	HOMER3	homer scaffolding protein 3	-1.29	0.0115
32541_AT	PPP3CC	protein phosphatase 3, catalytic subunit, gamma isozyme	-1.24	0.0464
224964_S_AT	GNG2	guanine nucleotide binding protein (G protein), gamma 2	1.22	0.0402
204184_S_AT	ADRBK2	adrenergic, beta, receptor kinase 2	1.29	0.0202
213664_AT	SLC1A1	solute carrier family 1 (neuronal/epithelial high affinity glutamate transporter, system Xag), member 1	1.33	0.0151
242891_AT	ADCY5	adenylate cyclase 5	1.35	0.0251
232062_AT	ADCY1	adenylate cyclase 1 (brain)	1.36	0.0126
235049_AT	ADCY1	adenylate cyclase 1 (brain)	1.39	0.024
204229_AT	SLC17A7	solute carrier family 17 (vesicular glutamate transporter), member 7	1.41	0.0219

205915_X_AT	GRIN1	glutamate receptor, ionotropic, N-methyl D-aspartate 1	1.45	0.011
213845_AT	GRIK2	glutamate receptor, ionotropic, kainate 2	1.48	0.0011
223943_S_AT	0	0	1.48	0.0067
210412_AT	GRIN2B	glutamate receptor, ionotropic, N-methyl D-aspartate 2B	1.49	0.0441
235527_AT	DLGAP1	discs, large (Drosophila) homolog-associated protein 1	1.53	0.049
241172_AT	GRIA2	glutamate receptor, ionotropic, AMPA 2	1.55	0.0153
1569290_S_AT	GRIA3	glutamate receptor, ionotropic, AMPA 3	1.6	0.0166
211125_X_AT	GRIN1	glutamate receptor, ionotropic, N-methyl D-aspartate 1	1.65	0.0409
217008_S_AT	GRM7	glutamate receptor, metabotropic 7	1.71	0.0055
214217_AT	GRM5	glutamate receptor, metabotropic 5	1.77	0.001
206534_AT	GRIN2A	glutamate receptor, ionotropic, N-methyl D-aspartate 2A	1.77	0.0082
204506_AT	PPP3R1	protein phosphatase 3, regulatory subunit B, alpha	1.78	0.0343
210781_X_AT	GRIN1	glutamate receptor, ionotropic, N-methyl D-aspartate 1	1.82	0.0182
210411_S_AT	GRIN2B	glutamate receptor, ionotropic, N-methyl D-aspartate 2B	1.83	0.003
230437_S_AT	PRKCB	protein kinase C, beta	1.85	0.0029
202425_X_AT	PPP3CA	protein phosphatase 3, catalytic subunit, alpha isozyme	1.85	0.0122
217565_AT	GRIA3	glutamate receptor, ionotropic, AMPA 3	1.87	0.0206
1555867_AT	GNG4	guanine nucleotide binding protein (G protein), gamma 4	1.94	0.0174
207235_S_AT	GRM5	glutamate receptor, metabotropic 5	1.96	0.0038
215687_X_AT	PLCB1	phospholipase C, beta 1 (phosphoinositide-specific)	1.99	0.0046
210684_S_AT	DLG4	discs, large homolog 4 (Drosophila)	1.99	0.0139
1566513_A_AT	GNG4	guanine nucleotide binding protein (G protein), gamma 4	2	0.0284
203158_S_AT	GLS	glutaminase	2.06	0.0198
228795_AT	PRKCB	protein kinase C, beta	2.07	0.0162

239095_AT	GRIN2B	glutamate receptor, ionotropic, N-methyl D-aspartate 2B	2.13	0.0015
227824_AT	PRKCB	protein kinase C, beta	2.14	0.03
227817_AT	PRKCB	protein kinase C, beta	2.18	0.0034
207957_S_AT	PRKCB	protein kinase C, beta	2.18	0.0045
211925_S_AT	PLCB1	phospholipase C, beta 1 (phosphoinositide-specific)	2.24	0.0018
210939_S_AT	GRM1	glutamate receptor, metabotropic 1	2.34	0.0041
208032_S_AT	GRIA3	glutamate receptor, ionotropic, AMPA 3	2.38	0.0005
215340_AT	ADCY1	adenylate cyclase 1 (brain)	2.42	0.0117
209685_S_AT	PRKCB	protein kinase C, beta	2.42	0.0164
222005_S_AT	GNG3	guanine nucleotide binding protein (G protein), gamma 3	2.62	0.0209
213793_S_AT	HOMER 1	homer scaffolding protein 1	2.66	0.0006
230144_AT	GRIA3	glutamate receptor, ionotropic, AMPA 3	2.66	0.0044
206730_AT	GRIA3	glutamate receptor, ionotropic, AMPA 3	2.94	0.0057
213245_AT	ADCY1	adenylate cyclase 1 (brain)	3.18	0.003
213222_AT	PLCB1	phospholipase C, beta 1 (phosphoinositide-specific)	3.73	0.0122
1565389_S_AT	GRM5	glutamate receptor, metabotropic 5	4.93	0.0091

WNT signalling pathway (pre-lesion compared to PVL)

ProbeSet ID	**Gene name**	**Gene Detail**	**FC**	**P-value**
226029_AT	VANGL2	VANGL planar cell polarity protein 2	-2.09	0.0152
212761_AT	TCF7L2	transcription factor 7-like 2 (T-cell specific, HMG-box)	-1.74	0.0223
1556006_S_AT	CSNK1A 1	casein kinase 1, alpha 1	-1.64	0.0229
232552_AT	DAAM1	dishevelled associated activator of morphogenesis 1	-1.6	0.0102

216511_S_AT	TCF7L2	transcription factor 7-like 2 (T-cell specific, HMG-box)	-1.54	0.0108
225745_AT	LRP6	LDL receptor related protein 6	-1.47	0.0381
229997_AT	VANGL1	VANGL planar cell polarity protein 1	-1.46	0.024
201868_S_AT	TBL1X	transducin (beta)-like 1X-linked	-1.45	0.0232
201465_S_AT	JUN	jun proto-oncogene	-1.43	0.0239
216035_X_AT	TCF7L2	transcription factor 7-like 2 (T-cell specific, HMG-box)	-1.42	0.0244
216037_X_AT	TCF7L2	transcription factor 7-like 2 (T-cell specific, HMG-box)	-1.39	0.0389
201614_S_AT	RUVBL1	RuvB-like AAA ATPase 1	-1.39	0.0478
212762_S_AT	TCF7L2	transcription factor 7-like 2 (T-cell specific, HMG-box)	-1.38	0.0345
229774_AT	CXXC4	CXXC finger protein 4	-1.36	0.0216
211105_S_AT	NFATC1	nuclear factor of activated T-cells, cytoplasmic, calcineurin-dependent 1	-1.31	0.0401
215310_AT	APC	adenomatous polyposis coli	-1.3	0.0307
212571_AT	CHD8	chromodomain helicase DNA binding protein 8	-1.3	0.0008
213400_S_AT	TBL1X	transducin (beta)-like 1X-linked	-1.29	0.0293
221016_S_AT	TCF7L1	transcription factor 7-like 1 (T-cell specific, HMG-box)	-1.27	0.0104
208867_S_AT	CSNK1A1	casein kinase 1, alpha 1	-1.24	0.045
32541_AT	PPP3CC	protein phosphatase 3, catalytic subunit, gamma isozyme	-1.24	0.0464
212759_S_AT	TCF7L2	transcription factor 7-like 2 (T-cell specific, HMG-box)	-1.22	0.0148
208866_AT	CSNK1A1	casein kinase 1, alpha 1	-1.21	0.0218
229154_AT	WNT10A	wingless-type MMTV integration site family, member 10A	1.25	0.0476
206459_S_AT	WNT2B	wingless-type MMTV integration site family, member 2B	1.28	0.0495
218318_S_AT	NLK	nemo-like kinase	1.34	0.0288
206213_AT	WNT10B	wingless-type MMTV integration site family, member 10B	1.51	0.0086
213108_AT	CAMK2A	calcium/calmodulin-dependent protein kinase II alpha	1.67	0.0429

204506_AT	PPP3R1	protein phosphatase 3, regulatory subunit B, alpha	1.78	0.0343
230437_S_AT	PRKCB	protein kinase C, beta	1.85	0.0029
202425_X_AT	PPP3CA	protein phosphatase 3, catalytic subunit, alpha isozyme	1.85	0.0122
34846_AT	CAMK2B	calcium/calmodulin-dependent protein kinase II beta	1.97	0.0169
215687_X_AT	PLCB1	phospholipase C, beta 1 (phosphoinositide-specific)	1.99	0.0046
228795_AT	PRKCB	protein kinase C, beta	2.07	0.0162
227824_AT	PRKCB	protein kinase C, beta	2.14	0.03
207957_S_AT	PRKCB	protein kinase C, beta	2.18	0.0045
227817_AT	PRKCB	protein kinase C, beta	2.18	0.0034
211925_S_AT	PLCB1	phospholipase C, beta 1 (phosphoinositide-specific)	2.24	0.0018
209685_S_AT	PRKCB	protein kinase C, beta	2.42	0.0164
204712_AT	WIF1	WNT inhibitory factor 1	3.19	0.0056
213222_AT	PLCB1	phospholipase C, beta 1 (phosphoinositide-specific)	3.73	0.0122
207613_S_AT	CAMK2A	calcium/calmodulin-dependent protein kinase II alpha	7.06	0.0085